

UC Irvine

UC Irvine Electronic Theses and Dissertations

Title

PEROVSKITE AND PEROVSKITE-LIKE MATERIALS FOR SOLUTION-PROCESSED THIN-FILM SOLAR CELLS

Permalink

<https://escholarship.org/uc/item/1p66d985>

Author

Fabian, David

Publication Date

2018

Peer reviewed|Thesis/dissertation

UNIVERSITY OF CALIFORNIA,
IRVINE

**PEROVSKITE AND PEROVSKITE-LIKE MATERIALS FOR SOLUTION-
PROCESSED THIN-FILM SOLAR CELLS**

DISSERTATION

submitted in partial satisfaction of the requirements
for the degree of

DOCTOR OF PHILOSOPHY

in Chemistry

by

David M. Fabian

Dissertation Committee:
Assistant Professor Shane Ardo, Chair
Associate Professor Matt Law
Professor Eric Potma

2018

Chapter 1 © 2014, 2015 David M. Fabian
Chapter 2 © 2016 Royal Society of Chemistry
Chapter 3 © 2018 David M. Fabian
Chapter 4 © 2018 Royal Society of Chemistry
Chapter 5 © 2018 David M. Fabian

TABLE OF CONTENTS

List of Figures	v
List of Tables	xiii
Acknowledgments.....	xiv
Curriculum Vitae	xv
Abstract of the Dissertation	xviii
Dissertation at a Glance	1
Chapter 1: Background, Deposition Procedure Development, and Novel Architectures of Perovskite Solar Cells.....	3
1.1 Introduction.....	3
1.2 Experimental.....	9
1.2.1 Preparation of MAPbX ₃ Solutions.....	9
1.2.2 Thin-Film Processing.....	10
1.2.2.1 Substrate Preparation and Metal–Oxide Materials Deposition.....	10
1.2.2.2 Perovskite Deposition Methods	11
1.2.3 Photovoltaic Device Preparation.....	13
1.2.4 Electrical Characterization.....	14
1.2.5 Mercury-Drop Top-Contact Electrode Setup.....	16
1.2.6 Thermal Stability Tests	16
1.2.7 Thin-Film Characterization.....	16
1.3 Results & Discussion	17
1.4 Conclusions.....	31
1.5 References.....	32
Chapter 2: Hybrid Organic–Inorganic Photovoltaics Based on Bismuth Iodide and 1,6-Hexanediammonium Dication	37
2.1 Introduction.....	37
2.2 Experimental.....	41
2.2.1 Preparation of MAPbI ₃ and HDABiI ₅ Solutions.....	41
2.2.2 Materials Processing	42
2.2.3 Device Fabrication	43
2.2.4 Thermal Stability Tests	44
2.2.5 Characterization	44
2.3 Results & Discussion	46
2.4 Conclusions.....	55
2.5 References.....	57
Chapter 3: Hybrid organic–inorganic bismuth–iodide materials incorporating divalent organic ligands for photovoltaics.....	61
3.1 Introduction.....	61

3.2 Experimental.....	66
3.2.1 Single-Crystal Growth and Measurement.....	66
3.2.1.1 Single-Crystal Growth.....	66
3.2.1.2 X-ray Data Collection and Structure Solution for $\text{EDA}_2\text{Bi}_2\text{I}_{10}$	67
3.2.1.3 X-ray Data Collection and Structure Solution for HDABiI_5	67
3.2.1.4 Structure Solution Definitions.....	68
3.2.2 Density Functional Theory Calculations for HDABiI_5	69
3.2.3 Preparation of Hybrid Organic–Inorganic Bismuth–Iodide Solutions.....	69
3.2.4 Materials Processing.....	70
3.2.5 Device Fabrication.....	71
3.2.6 Ultrafast Laser Spectroscopy.....	71
3.2.7 Characterization.....	72
3.3 Results & Discussion.....	75
3.4 Conclusions.....	99
3.5 References.....	101

Chapter 4: Demonstration of photovoltaic action and enhanced stability from a quasi-two-dimensional hybrid organic–inorganic copper–halide material incorporating divalent organic ligands.....105

4.1 Introduction.....	105
4.2 Experimental.....	107
4.2.1 Preparation of $(\text{HDA})_2\text{CuBr}_{6-x}\text{Cl}_x$ and $(\text{PA})_4\text{CuBr}_6$ Solutions.....	108
4.2.2 $(\text{HDA})_2\text{CuBr}_6$ Single-Crystal Growth.....	108
4.2.3 X-ray Data Collection and Structure Solution for $(\text{HDA})_2\text{CuBr}_6$	109
4.2.4 Materials Processing.....	109
4.2.5 Solar Cell Fabrication.....	110
4.2.6 Stability Tests.....	111
4.2.7 Materials Characterization.....	111
4.2.8 Electrical Characterization.....	113
4.3 Results & Discussion.....	114
4.4 Conclusions.....	130
4.5 References.....	131

Chapter 5: Low-dimensional lead–halide perovskite materials incorporating divalent organic ligands137

5.1 Introduction.....	137
5.2 Experimental.....	141
5.2.1 Preparation of Lead–Iodide Solutions.....	141
5.2.2 Materials Processing.....	142
5.2.3 Ultrafast Laser Spectroscopy.....	142
5.2.4 Characterization.....	144
5.3 Results & Discussion.....	145
5.4 Conclusions.....	154
5.5 References.....	156

LIST OF FIGURES

Figure 1.1. Levelized cost of energy values and Department of Energy cost goals for solar electricity.....	4
Figure 1.2. Best research-cell efficiencies of emerging photovoltaic technologies.....	5
Figure 1.3. (a) 1D and (b) 2D representation of general linking between organic moieties and inorganic moieties.....	6
Figure 1.4. (a) Mesostructured, (b) planar n–i–p, and (c) planar p–i–n architectures typically employed in perovskite photovoltaics.....	7
Figure 1.5. (a) Conventional spin-coat procedure for depositing perovskite precursor solution (e.g. MAPbI ₃ in DMF) on mesoporous metal oxide/compact TiO ₂ /fluorine-doped tin oxide. (b) Fast deposition crystallization spin-coat procedure, which incorporates an antisolvent (e.g. chlorobenzene) during the spin-coat process.....	11
Figure 1.6. (a) Illustration and (b) digital photograph images of the gas-solid crystallization method whereby methylammonium iodide powder is sprinkled on the PbI ₂ film to form MAPbI ₃ perovskite during heating at 150 °C.....	12
Figure 1.7. Digital photograph image of aqueous 2M HCl and zinc powder reacting to etch away the exposed fluorine-doped tin oxide.....	13
Figure 1.8. Digital photograph image of the photovoltaic device <i>J–V</i> measurement setup.....	15
Figure 1.9. Digital photograph image of the mercury-drop top-contact electrode setup.....	16
Figure 1.10. Current–voltage curves showing ohmic contacts of evaporated gold to a solution-deposited PEDOT:PSS thin film as well as liquid mercury to fluorine-doped tin–oxide and liquid mercury to PEDOT:PSS. Inset: zoomed-in area showing only slight differences in resistance for each contact.....	18
Figure 1.11. Three-electrode cyclic voltammetry at 50 mV/s of 1 mM ferrocene in acetonitrile with 100 mM tetra- <i>n</i> -butylammonium hexafluorophosphate. Working electrodes studied are different metal–oxide architectures on a fluorine-doped tin–oxide coated glass substrate, the counter electrode is platinum mesh, and the reference electrode is a saturated calomel electrode.....	19
Figure 1.12. Steady-state absorption spectra and photoluminescence emission spectra of PbI ₂ and MAPbI ₃ on fluorine-doped tin oxide. Insets are digital photograph images of the films.....	21
Figure 1.13. Depth profiling by fluorescence lifetime confocal microscopy imaging on MAPbI ₃ /mTiO ₂ /cTiO ₂ /FTO.....	22

Figure 1.14. Steady-state absorption spectra of an MAPbI₃ thin film on mTiO₂/cTiO₂/FTO. On left are digital photograph images of the film after treatment.....23

Figure 1.15. (a) Digital photograph images and (b) top-view scanning electron microscopy images of MAPbI₃ thin films on cTiO₂/FTO, for which MAPbI₃ was deposited via a conventional one-step spin-coating method or via a fast deposition crystallization technique for which chlorobenzene was used as the antisolvent. (c) Steady-state absorption spectra of the MAPbI₃/cTiO₂/FTO substrates shown in panel (a) as well as a spectrum of MAPbI₃/cTiO₂/FTO for which MAPbI₃ was deposited via fast deposition crystallization with toluene as the antisolvent. (d) Grazing-incidence X-ray diffraction patterns of the MAPbI₃/cTiO₂/FTO substrates shown in panel (a).....24

Figure 1.16. Reverse-bias voltage sweeps at 100 mV/s of the best-performing cells of devices 1, 2, and 3.....28

Figure 1.17. (a) Chronopotentiometry at open circuit and (b) chronoamperometry at short circuit (0 V vs. ref) of the best-performing perovskite cell of device 3.....29

Figure 1.18. Light-intensity-dependent measurements of the open-circuit voltage of a PV device. Inset: architectural layout of the cell (Au/PEDOT:PSS/MAPbI₃/mAl₂O₃/cTiO₂/FTO).....30

Figure 2.1. (a) The unit cell of lead-based organic–inorganic hybrid perovskite MAPbI₃. (b) Crystal structure of the inorganic framework of a bismuth-based organic–inorganic hybrid material, from the top-down view and side view.....38

Figure 2.2. (a) Cross-sectional scanning electron microscopy image of a representative HDABi₅ device, and (b) direct-bandgap and (c) indirect-bandgap Tauc plots of HDABi₅ deposited as thin films on FTO, and baseline corrected for the FTO substrate.....46

Figure 2.3. Top-view scanning electron microscopy image of (a) HDABi₅ and (b) MAPbI₃ deposited on mTiO₂/cTiO₂/FTO.....47

Figure 2.4. Ultraviolet photoemission spectra (He I) of HDABi₅/FTO for direct determination of the (a) work function and (b) valence-band maximum.....48

Figure 2.5. Energy-level diagram of spiro-OMeTAD/HDABi₅/TiO₂, where the VBM of HDABi₅ was determined by UPS measurement.....49

Figure 2.6. (a) Grazing-incidence XRD pattern and (b) XPS spectra of HDABi₅/mTiO₂/cTiO₂/FTO.....50

Figure 2.7. (a) Sequential X-ray photoelectron spectra of the Bi 4f region, which demonstrate increased signal attributed to Bi⁰ compared to signal attributed to Bi³⁺ concomitant with longer exposure to Al K_α X-ray radiation. (b) First scan and (c) second scan of the Bi 4f region, with Shirley backgrounds and peak fits shown for clarity.....50

Figure 2.8. XPS region scans of (a) Ti 2p and (b) O 1s binding energies for HDABi₅/mTiO₂/cTiO₂/FTO, where the intensities are normalized to the I 3d_{5/2} peak in Figure 2.6b. Small peak intensities indicate near-complete coverage of mTiO₂ by HDABi₅.....51

Figure 2.9. (a) *J–E* behavior with scan direction indicated by the arrows and (b) chronoamperometry under 0.8 Suns, and (c) IPCE action spectrum for a complete Au/spiro-OMeTAD/HDABi₅/mTiO₂/cTiO₂/FTO device. Inset in panel (a) is a digital photograph image of the device.....53

Figure 2.10. Side-view representation of the layer-by-layer architecture of the complete photovoltaic device.....54

Figure 2.11. Transmission-mode UV–Vis electronic absorption spectra of (a) HDABi₅ and (b) MAPbI₃ films on mTiO₂/cTiO₂/FTO. Inset in panel b shows absorption onsets in greater detail and with the same axes units as the main graph.....55

Figure 2.12. Plan-view SEM images of MAPbI₃ (top row, a–d) and HDABi₅ (bottom row, e–h) thin films deposited on TiO₂ via a simple one-step deposition (a, e), hot-casting (b, f), fast-deposition crystallization (c, g), or a novel “drop-heat-spin” technique that has been pioneered (d, h).....56

Figure 3.1. Electromagnetic radiation spectrum, with approximate positions of probing wavelengths of X-band time-resolved microwave conductivity, time-resolved terahertz, and transient absorption spectroscopic techniques and abilities of each technique to probe free carriers and/or excitons.....63

Figure 3.2. (a) A representation of the general linking of organic dications to one-dimensional bismuth–halide chains. (b) A representation of the organic dication crystal motif in dicationic organic–inorganic bismuth–halide materials, where the A²⁺ groups serve as “crystal fasteners” between one-dimensional bismuth–halide chains to enhance inter-chain conductivity, σ65

Figure 3.3. Molecular structure of EDA₂Bi₂I₁₀ • 5H₂O, with thermal ellipsoids drawn at the 50% probability level.....75

Figure 3.4. (a) A digital photograph image of a single crystal of (EDA)₂Bi₂I₁₀ • 5H₂O. (b) A segment of the (EDA)₂Bi₂I₁₀ • 5H₂O crystal structure unit cell, with bond distances labeled. (c) The complete (EDA)₂Bi₂I₁₀ • 5H₂O unit cell.....75

Figure 3.5. Molecular structure of HDABi₅, with thermal ellipsoids drawn at the 50% probability level.....77

Figure 3.6. (a) 1 x 1 x 3 unit cell structure of HDABi₅ with orientation in the [110] direction. (b) The same structure as displayed in panel (a) but rotated 90°. (c) The same structure as displayed in panel (b) with the organic HDA²⁺ groups removed. Hydrogens are omitted in each panel for clarity.....78

Figure 3.7. X-ray diffraction patterns of HDABiI ₅ predicted from the resolved single-crystal structure compared to powders scraped off of thin films measured using a synchrotron source.....	80
Figure 3.8. HSE06+SOC band structures of HDABiI ₅ . The valence-band maximum is set to 0 eV.....	81
Figure 3.9. (a) Calculated optical absorption spectrum and (b) calculated spectroscopic limited maximum efficiency of HDABiI ₅	82
Figure 3.10. Optical bandgap as a function of number of carbons in the diammonium group for the hybrid bismuth–halide materials (hydra)BiI ₅ (0 carbons), EDABiI ₅ (2 carbons), BDABiI ₅ (4 carbons), HDABiI ₅ (6 carbons), and DDDABiI ₅ (12 carbons).....	83
Figure 3.11. UV–Vis electronic absorption spectra of a series of organic–inorganic hybrid bismuth–halide thin films, which range in structural dimensionality from zero-dimensional to two-dimensional.....	85
Figure 3.12. Grazing-incidence X-ray diffraction patterns of thjn films of HDABiI ₅ and (PA) ₂ BiI ₅ on FTO.....	86
Figure 3.13. Grazing-incidence X-ray diffraction patterns of thin films of (PA) ₂ BiI ₅ processed in the conventional 4:1 DMF:DMSO solvent mixture and processed in an alternative acetonitrile (MeCN) with 15 wt. % butylamine.....	87
Figure 3.14. (a) Grazing-incidence X-ray diffraction patterns of a thjn film of (FA _{0.75} CS _{0.25}) ₃ Bi ₂ I ₉ on fluorine-doped tin–oxide-coated glass and the calculated powder pattern of analogous (MA) ₃ Bi ₂ I ₉ . (b) Single-crystal structure of analogous MA ₃ Bi ₂ I ₉ , recreated from a .cif file provided by Kamminga and coworkers.....	87
Figure 3.15. Time-resolved microwave conductivity traces of a thin film of HDABiI ₅ on a quartz substrate. Excitation laser fluence is shown in the legend in parentheses with units of photons/cm ²	89
Figure 3.16. Time-resolved microwave conductivity traces of a thin film of bpyBiI ₅ on a quartz substrate. Excitation laser fluence is shown in the legend in parentheses with units of photons/cm ²	90
Figure 3.17. Time-resolved microwave conductivity traces of a (FA _{0.75} CS _{0.25}) ₃ Bi ₂ I ₉ thin film of on a quartz substrate. Excitation laser fluence is shown in the legend in parentheses with units of photons/cm ²	91
Figure 3.18. Transient absorption spectra of a thin film of HDABiI ₅ using 450 nm laser excitation, with t = 0 indicating where the magnitude of ΔmOD integrated over wavelength was the largest.....	92

Figure 3.19. (a) Transient absorption spectra at $t = 0$ and (b) kinetic traces of thin films of one-dimensional HDABiI₅, supposed one-dimensional bpyBiI₅, and zero-dimensional (FA_{0.75}CS_{0.25})₃Bi₂I₉ using 450 nm laser excitation.....92

Figure 3.20. (a) Absorptance + reflectance spectra of HDABiI₅ and (PA)₂BiI₅ thin films deposited on glass using a conventional one-step deposition and using a fast deposition crystallization with chlorobenzene as antisolvent. (b) Digital photograph images of the thin films corresponding to each absorptance spectrum.....93

Figure 3.21. Plan-view scanning electron microscopy images of thin films of HDABiI₅/mTiO₂/cTiO₂/FTO (panels (a) and (b)) and (PA)₂BiI₅/mTiO₂/cTiO₂/FTO (panels (c) and (d)).....94

Figure 3.22. Absorption spectra and steady-state emission spectra of thin films of HDABiI₅ and (PA)₂BiI₅ using 400 nm excitation.....95

Figure 3.23. Steady-state emission spectra of thin films of (a) HDABiI₅ and (b) (PA)₂BiI₅ using 400 nm excitation – 500 nm excitation.....95

Figure 3.24. (a) Temperature-dependent thermogravimetric analysis of HDABiI₅ powder and (PA)₂BiI₅ powder. (b) Isothermal thermogravimetric analysis at 200 °C as a function of time.....96

Figure 3.25. (a) $J-E$ behavior for solar cells consisting of Au/spiro-OMeTAD/Bi/TiO_x/FTO, where Bi is HDABiI₅ or (PA)₂BiI₅. (b) Digital photograph images of the solar cells containing HDABiI₅ and (PA)₂BiI₅. (c) Chronoamperometry measurements of (PA)₂BiI₅ and HDABiI₅.....97

Figure 3.26. (a) Grazing-incidence X-ray diffraction patterns of HDABiI₅ and mixed organic dicationic (HDA-PhDA)BiI₅ thin films normalized to the 011 peak at ~12 °. (b) Grazing-incidence X-ray diffraction patterns of a 95%-5% (HDA-PhDA)BiI₅ thin film before and after thermal treatment at 200 °C for 19 h. (c) Transmission-mode electronic absorption spectra of mixed organic dicationic (HDA-PhDA)BiI₅ thin films before and after thermal treatment at 200°C for 19 h.....98

Figure 3.27. Through-plane conductivity $J-E$ measurements of HDABiI₅ (100-0) and the mixed-dication (HDA-PhDA)BiI₅ (95-5, 85-15, 75-25) thin films.....99

Figure 4.1. Unit cell crystal structure of (HDA)₂CuBr₆ showing the vertical alternation of copper (light blue)–bromide layers separated by hexanediammonium dications. Hydrogens are omitted for clarity. Shown on the right is a CuBr₆ octahedral unit with the measured Cu–Br bond lengths.....114

Figure 4.2. (a) Transmission-mode electronic absorbance spectra and steady-state photoluminescence emission spectra ($\lambda_{\text{ex}} \approx 340$ nm) of thin films of (HDA)₂CuBr₆ and (PA)₄CuBr₆. (b) Normalized steady-state photoluminescence emission spectra ($\lambda_{\text{ex}} \approx 400$ nm) of thin films of (HDA)₂CuBr₆ and (PA)₄CuBr₆, showing a broad tailing region due to emission from an electronic transition with $\lambda_{\text{max}} \approx 580$ nm. (c) Steady-state photoluminescence excitation spectra of

(HDA)₂CuBr₆ and (PA)₄CuBr₆ probed at emission peak wavelengths and at 580 nm, with the absorbance spectra of (HDA)₂CuBr₆ and (PA)₄CuBr₆ overlaid.....116

Figure 4.3. (a) Indirect-bandgap Tauc plots of copper–halide hybrid organic–inorganic thin films deposited on glass and incorporating HDA²⁺ with varying halide compositions or PA⁺. (b) Digital photograph image of representative freshly-prepared (HDA)₂CuBr_{6-x}Cl_x thin films deposited on glass, with $x = 0, 1,$ and 2117

Figure 4.4. Direct-bandgap Tauc plots of copper–halide hybrid organic–inorganic thin films deposited on glass and incorporating HDA²⁺ with varying halide compositions or PA⁺.....118

Figure 4.5. Digital photograph images of freshly-prepared (HDA)₂CuBr_{6-x}Cl_x with $x = 0, 1,$ and $2,$ and (PA)₄CuBr₆ thin films deposited in the mesostructured assembly, Cu/mTiO₂/cTiO₂/FTO, where Cu is the copper–halide light absorber material.....119

Figure 4.6. X-ray photoelectron spectra of the Cu 2p_{3/2} region of thin films of (a) (HDA)₂CuBr₆ and (b) (PA)₂CuBr₄ on FTO. Best fits to the Cu 2p_{3/2} peaks are shown.....119

Figure 4.7. X-ray photoelectron spectra of the (a) Cu 2p region and the (b) Cl 2p region of copper–halide hybrid organic–inorganic thin films each deposited on FTO. Intensities in panel (a) are normalized to the Cu 2p_{3/2} peak that corresponds to Cu²⁺.....120

Figure 4.8. Best fits to the Cu 2p_{3/2} peaks of the X-ray photoelectron spectra of thin films of (a) (HDA)₂CuBr₆ and (b) (PA)₄CuBr₆ thin films each deposited on FTO following continued X-ray exposure.....121

Figure 4.9. Scans of the (a), (d) C 1s, (b), (e) N 1s, and (c), (f) Br 3p core level binding energy regions for thin films of (HDA)₂CuBr₆ and (PA)₄CuBr₆, each deposited on FTO.....122

Figure 4.10. Grazing-incidence X-ray diffraction patterns of thin films of (a) (HDA)₂CuBr₆ and (b) (PA)₄CuBr₆ when freshly-prepared and after exposure to 100 °C and ~50% relative humidity for 16 h. # denote peaks associated with the underlying FTO substrate.....123

Figure 4.11. Powder X-ray diffraction patterns and thin-film X-ray diffraction patterns for (a) (HDA)₂CuBr₆ and (b) (PA)₄CuBr₆.....123

Figure 4.12. (a) Transmission-mode absorption spectra of thin films of HDA₂CuBr₆ and (PA)₄CuBr₆ freshly-prepared and after exposure to 100 °C and ~50% relative humidity for 16 h, each corrected for background scattering. Inset: Digital photograph images of the thin films before and after exposure. (b) Normalized absorbance at 500 nm as a function of time for copper–halide perovskite thin films at room temperature and 50% relative humidity. Inset: Digital photograph image of (PA)₄CuBr₆ after 6 days and HDA₂CuBr₆ after 12 days.....124

Figure 4.13. (a) Temperature-dependent thermogravimetric analysis of (HDA)₂CuBr₆, (PA)₄CuBr₆, and (DA)₄CuBr₆ powders. (b) Isothermal thermogravimetric analysis at 150 °C as a function of time.....125

Figure 4.14. a) Temperature-dependent thermogravimetric analysis of HDABr ₂ , PABr, and DABr precursor powders. (b) Isothermal thermogravimetric analysis at 250 °C as a function of time.....	126
Figure 4.15. Powder XRD of (a) (HDA) ₂ CuBr ₆ and (b) (PA) ₄ CuBr ₆ during moisture stability tests at the indicated number of days into the tests.....	126
Figure 4.16. Cross-sectional scanning electron micrograph of a representative solar cell containing (HDA) ₂ CuBr ₅ Cl as the photoactive layer.....	127
Figure 4.17. Energy-dispersive X-ray spectroscopy mapping data of a thin-film cross section of (HDA) ₂ CuBr ₆ /mTiO ₂ /cTiO ₂ /FTO.....	127
Figure 4.18 (a) <i>J</i> – <i>E</i> behavior for solar cells consisting of Au/spiro-OMeTAD/Cu/TiO ₂ /FTO, where Cu is (HDA) ₂ CuBr ₆ or (HDA) ₂ CuBr ₅ Cl. Inset: digital photograph image of a complete solar cell. (b) Impedance spectroscopy data, presented as a Mott–Schottky plot, for a solar cell consisting of Au/spiro-OMeTAD/(HDA) ₂ CuBr ₅ Cl/TiO ₂ /FTO, and with the calculated flat-band potential (<i>E</i> _{FB}) and dopant density (<i>N</i> _A). Inset: standard Randles circuit used to model the impedance spectroscopy data.....	128
Figure 4.19. Low-intensity X-ray photoelectron spectra of the cutoff region to determine work functions of copper–halide hybrid organic–inorganic materials each deposited on FTO.....	129
Figure 4.20. X-ray photoelectron valence-band spectra of copper–halide hybrid organic–inorganic materials each deposited on FTO showing (a) the entire valence-band region and (b) the valence-band position relative to the work function of the copper standard (set to 0.0 eV).....	130
Figure 4.21. Energy-level diagram of (HDA) ₂ CuBr _{6-x} Cl _x thin films, with <i>x</i> = 0, <i>x</i> = 1, and <i>x</i> = 2, as well as a (PA) ₄ CuBr ₆ thin film, each deposited on a fluorine-doped tin–oxide-coated glass substrate. The conduction-band minimum of TiO ₂ and valence-band maximum of spiro-OMeTAD were taken from a report by Chilvery et al.....	131
Figure 5.1. Proposed structure of the two-dimensional lead–halide perovskite ethylenediamine lead iodide (EDAPbI ₄) viewed along the plane of the <i>n</i> =1 sheets of PbI ₆ octahedra.....	137
Figure 5.2. (a) A schematic representation of time-resolved terahertz spectroscopy. (b) A diagram of the experimental setup of TRTS.....	139
Figure 5.3. (a) UV–Visible absorption spectra and (b) steady-state emission spectra (<i>λ</i> _{ex} = 400 nm) of hybrid lead–halide material thin films.....	145
Figure 5.4. (a) Time-resolved photoluminescence kinetic traces and (b) time-resolved photoluminescence emission spectra of hybrid lead–halide thin films at 410 nm excitation.....	146

Figure 5.5. Steady-state emission spectra of (a) EDAPbI ₄ and (b) BDAPbI ₄ , and (c) HDAPbI ₄ thin films showing no spectral shifts when varying the excitation wavelength.....	147
Figure 5.6. Grazing-incidence XRD patterns of hybrid lead–halide material thin films incorporating either ethylenediamine, butanediamine, or hexanediamine.....	148
Figure 5.7. Transient absorption (a) kinetic traces and (b) spectra of a thin film of EDAPbI ₄ at 400 nm excitation.....	148
Figure 5.8. Transient absorption (a) kinetic traces and (b) spectra of a thin film of BDAPbI ₄ at 400 nm excitation.....	149
Figure 5.9. Transient absorption (a) kinetic traces and (b) spectra of a thin film of HDAPbI ₄ at 400 nm excitation.....	149
Figure 5.10. Transient absorption (a) kinetic traces and (b) spectra of a thin film of EDAPbI ₄ at 500 nm excitation.....	150
Figure 5.11. Transient absorption (a) kinetic traces and (b) spectra of a thin film of BDAPbI ₄ at 500 nm excitation.....	150
Figure 5.12. Transient absorption (a) kinetic traces and (b) spectra of a thin film of HDAPbI ₄ at 500 nm excitation.....	151
Figure 5.13. Terahertz pump scans showing the charge-carrier kinetics of the hybrid lead–halide material thin films.....	151
Figure 5.14. (a) Transient absorption spectra of a freshly-prepared MAPbBr ₃ thin film excited with 520 nm laser light.....	152
Figure 5.15. Transient absorption spectra of a MAPbBr ₃ thin film that has been stored in a container in air for roughly three months.....	153
Figure 5.16. Transient absorption spectra of a freshly-prepared BDAPbI ₄ thin film at 485 nm excitation, probing the exciton bleach peak at 496 nm.....	153
Figure 5.17. Terahertz probe scans of thin films of (a) MAPbBr ₃ , (b) EDAPbI ₄ , (c) BDAPbI ₄ , and (d) HDAPbI ₄	154

LIST OF TABLES

Table 1.1. Promising MAPbX ₃ perovskite PV devices. Deposition method refers to how the perovskite layer is deposited, FDC = fast deposition crystallization, V_{OC} = open-circuit voltage, I_{SC} = short-circuit current, J_{SC} = short-circuit current density, FF = fill factor, PCE = power conversion efficiency.....	27
Table 2.1. Approximate percent surface elemental composition (excluding hydrogen) of HDABi ₅ /mTiO ₂ /cTiO ₂ /FTO calculated from XPS region scans.....	52
Table 3.1. Organic groups incorporated in dicationic hybrid organic–inorganic bismuth–halide materials for enhanced-conductivity PVs.....	66
Table 3.2. Crystallographic data for EDA ₂ Bi ₂ I ₁₀ •5H ₂ O.....	76
Table 3.3. Crystallographic data for HDABi ₅	79
Table 3.4. Optical bandgaps and corresponding digital images of a series of dicationic hybrid organic–inorganic bismuth–iodide thin films.....	84
Table 4.1. Crystallographic data for (HDA) ₂ CuBr ₆	115

ACKNOWLEDGMENTS

I would like to thank my parents, Debbie and Dave, and my three sisters, Laura, Sarah, and Becky, for all their love and support in everything I have set my mind to over the years. I would also like to thank my undergraduate advisor, Kristin Wustholz, who welcomed me into her group at the start of my junior year and taught me the importance of great science writing. I thank my doctoral advisor, Shane Ardo, for taking a chance with me and believing in me enough to give me essentially full autonomy in the research I wanted to pursue. I also thank the faculty on my committee for their guidance and for being incredibly brilliant representations of the world-class faculty we have in the Department of Chemistry at UCI. I would like to thank all my friends for keeping me sane throughout the PhD process by reminding me that I do have a life outside of school. Lastly, many “thank you’s” go to my fiancé, Kelly, whose unconditional love and support reminds me that I not only have *something* to live for (that is, a rewarding career), but also *someone* to live for.

I would also like to thank sources of funding that have helped support me and my research throughout my graduate school tenure: 1) the National Science Foundation Graduate Research Fellowship under Grant number DGE-1321846, 2) the DOE, Office of Science, Office of Workforce Development for Teachers and Scientists, Office of Science Graduate Student Research (SCGSR) program under contract number DE-SC0014664, the 2017 UC MEXUS-CONACYT Collaborative Research Grant under Grant number UCM-208101, and the School of Physical Sciences at the University of California, Irvine.

CURRICULUM VITAE

David M. Fabian

david.m.fabian13@gmail.com | 973-618-6652
714 Turtle Crest Dr, Irvine, CA 92603

EDUCATION

Ph.D., *Physical Chemistry*, University of California, Irvine
GPA: 3.97/4.00

Irvine, CA
July 2018

B.S., *Chemistry*, College of William & Mary
GPA: 3.43/4.00

Williamsburg, VA
May 2013

AWARDS

DOE Office of Science Graduate Research Award (2017 – 2018)
NSF Graduate Research Fellowship (2014 – 2018)
UCI School of Physical Sciences Travel Fund Award (2016)
UCI Associated Graduate Students Travel Grant (2016)
Electrochemical Society Travel Grant (2016)
UC Irvine Chemistry Department Teaching Award (2014)

RESEARCH EXPERIENCE

University of California, Irvine: Department of Chemistry

Irvine, CA

Advisor: Shane Ardo

Jan. 2014 – Present

Synthesize and characterize hybrid organic–inorganic materials for solution-processed thin-film solar cells. Fabricate thin-film solar cells and use materials characterization instrumentation including X-ray photoelectron spectroscopy, X-ray diffraction, and scanning electron microscopy. Analyze fundamental electrochemical and photophysical phenomena of thin-film solar cells. Designed and built unique X-band time-resolved microwave conductivity system with input from two experts in the field, Dr. Dennis Friedrich and Dr. Garry Rumbles.

National Renewable Energy Laboratory: Spectroscopy & Photoscience Group

Golden, CO

Mentor: Matthew Beard

Sep. 2017 – Mar. 2018

Synthesize and characterize hybrid organic–inorganic copper–halide, bismuth–halide and lead–halide perovskite materials for solution-processed thin-film solar cells. Analyze fundamental photophysical phenomena of hybrid organic–inorganic material thin films using time-resolved laser spectroscopic techniques including transient absorption, photoluminescence, microwave conductivity, and terahertz spectroscopy.

College of William & Mary: Department of Chemistry

Williamsburg, VA

Advisor: Kristin Wustholz

Sep. 2011 – May 2013

Investigated applications of surface-enhanced Raman spectroscopy (SERS) to the conservation of historical artworks. Synthesized silver nanoparticles to use as enhancing substrates for SERS analysis and developed novel detection methodologies for SERS-based analysis of artist materials. Developed techniques for the identification of blue and yellow colorants using SERS.

TEACHING EXPERIENCE

University of California, Irvine: Department of Chemistry

Irvine, CA

Teaching Assistant, Analytical Chemistry & General Chemistry

Sep. 2013 – Mar. 2014

Head Teaching Assistant, Analytical Chemistry

Mar. 2014 – June 2014

Demonstrated the ability to create and uphold effective student–teacher relationships and impart information and scientific knowledge through excellent instructional and written communication skills. Provided thorough feedback to students by way of grading lab reports each week. Held office hours weekly to provide further assistance to students.

College of William & Mary: Department of Chemistry

Williamsburg, VA

Teaching Assistant, Physical Chemistry

Jan. 2013 – May 2013

Offered dynamic instruction to assist students in successfully completing laboratory procedures. Instructed and supervised students in the use of computational chemistry software as well as spectroscopic techniques including infrared spectroscopy, nuclear magnetic resonance spectroscopy, and mass spectrometry.

INDUSTRY EXPERIENCE

Merck & Co., Inc.

Summit, NJ

Merck Manufacturing Division, Science Intern

June 2012 – Aug. 2012

Worked as part of a pharmaceutical stability project management team that oversaw laboratory testing of several contract research organizations (CROs). Performed an extensive analysis of employee time cards from CROs and developed a schedule forecasting model that continues to serve as a tool for dividing up CRO workload. Improved the performance and functionality of the database used to record and forecast project hours. Collaborated with colleagues on a similar project management team based in West Point, PA and facilitated the harmonization of forecasting models by offering changes to improve their model.

PUBLICATIONS

10. DM Fabian, AM Ganose, JW Ziller, DO Scanlon, MC Beard, S Ardo; “Hybrid organic–inorganic bismuth–halide materials incorporating divalent organic ligands for photovoltaics,” *ACS Applied Materials & Interfaces*, **2018**, in preparation.

9. DM Fabian, JW Ziller, S Ardo; “Demonstration of photovoltaic action and enhanced stability from a quasi-two-dimensional hybrid organic–inorganic copper–halide material incorporating divalent organic ligands,” *Journal of Materials Chemistry A*, **2018**, in preparation.

8. G Krueper, JM Cardon, J Angsono, K Tkacz, DM Fabian, H-Y Chen, S Ardo; “Synergistic effect of electrolyte cations on the rate of electron transfer between dye molecules anchored to TiO₂ nanocrystallites cast as mesoporous thin films”, *ACS Energy Letters*, submitted.

7. SP Dunfield, DT Moore, TR Klein, DM Fabian, JA Christians, AG Dixon, B Dou, S Ardo, MC Beard, SE Shaheen, JJ Berry, MFAM van Hest; “Curtailling Perovskite Processing Limitations via Lamination at the Perovskite/Perovskite Interface”, *ACS Energy Letters*, **2018**, 3(5), 1192-1197.

6. W White, CD Sanborn, DM Fabian, S Ardo; “Conversion of visible light into ionic power using photoacid-dye-sensitized bipolar ion-exchange membranes,” *Joule*, **2017**, 2(1), 94-109.

5. W White, CD Sanborn, RS Reiter, DM Fabian, S Ardo; “Observation of photovoltaic action from photoacid-modified Nafion due to light-driven ion transport,” *Journal of the American Chemical Society*, **2017**, 139(34), 11726-11733.

4. DM Fabian, S Ardo; “Hybrid organic–inorganic solar cells based on bismuth iodide and 1,6-hexanediammonium dication,” *Journl of Materials Chemistry A*, **2016**, 4(18), 6837-6841. (*invited; included in Emerging Investigators Special Issue and Themed Collection*)

3. DM Fabian, S Hu, N Singh, FA Houle, T Hisatomi, K Domen, FE Osterloh, S Ardo; “Particle suspension reactors and materials for solar-driven water splitting,” *Energy & Environmental Science*, **2015**, 8(10), 2825-2850. (*awarded front cover art*)

2. HE Mayhew, DM Fabian, SA Svoboda, KL Wustholz; “Surface-enhanced Raman spectroscopy studies of yellow organic dyestuffs and lake pigments in oil paint,” *Analyst*, **2013**, 138, 4493-4499. (*invited*)

1. LH Oakley, DM Fabian, HE Mayhew, SA Svoboda, KL Wustholz; “Pretreatment Strategies for SERS Analysis of Indigo and Prussian Blue in Aged Painted Surfaces,” *Analytical Chemistry*, **2012**, 84(18), 8006-8012.

PRESENTATIONS

5. DM Fabian, S Ardo; “Perovskite-Like Photovoltaics Incorporating Organic Dications”, 2016 MRS Fall Meeting, Nov. 27 – Dec. 2, 2016, Boston, MA.

4. DM Fabian, S Ardo; “Hybrid Organic/Inorganic Bismuth-Based Materials for Solution-Processed Thin-Film Photovoltaics”, 229th Electrochemical Society Meeting, May 29 – Jun. 2, 2016, San Diego, CA. (*invited*)

3. DM Fabian, S Ardo; “XPS and UPS analysis of solution-processed hybrid organic–inorganic bismuth materials”, 2016 Kratos Analytical North American Users Meeting, May 23, 2016, Irvine, CA.
2. DM Fabian, HE Mayhew, SA Svoboda, KL Wustholz, “Surface-enhanced Raman Spectroscopy of Oil Paints in Historic Artworks,” Undergraduate Science Symposium, Feb. 22, 2013, Williamsburg, VA.
1. DM Fabian, “An Improved Forecasting Model for Increasing Efficiency and Productivity of CRO Testing Labs”, Merck Summer Intern/Co-op Poster Fair, Aug. 7, 2012, Rahway, NJ.

MENTORING & OUTREACH

Mentor – Ardo Laboratories

Irvine, CA

Apr. 2015 – Present

Advised one Master’s student, two undergraduate students, and one high school student on conducting research in the Ardo Laboratories. Supervised laboratory work, discussed research results, and offered guidance for successful completion of their laboratory experiments.

“Juice from Juice”: making solar cells using blackberries

Irvine, CA

Nov. 2013 – Present

Instruct audiences of middle school students, high school students, and teachers on making dye-sensitized solar cells from commercially-available materials. Effectively communicate and demonstrate science as well as encourage younger audiences to pursue further studies in STEM disciplines.

UCI Center for Solar Energy: Sustainable Foods Fair

Irvine, CA

Apr. 2016

Engaged in informing UC Irvine students and the public about solar energy research conducted in the Ardo Group and about the importance of sustainable energy.

AFFILIATIONS

American Chemical Society (2012 – Present)

Materials Research Society (2013 – Present)

Electrochemical Society (2016 – Present)

ABSTRACT OF THE DISSERTATION

Perovskite and Perovskite-Like Materials for Solution-Processed Thin-Film Solar Cells

By

David Fabian

Doctor of Philosophy in Chemistry

University of California, Irvine, 2018

Professor Shane Ardo, Chair

Lead-halide-based hybrid organic-inorganic perovskite materials (APbX_3) have recently garnered increased attention among researchers worldwide as promising thin-film photovoltaic materials. Laboratory-scale solar cells incorporating APbX_3 materials as the light absorber have demonstrated impressive efficiencies of $> 20\%$, but commercialization of solar cells based on solution-cast materials and with only low-temperature processing steps is in-part limited by toxicity and instability of the photoactive materials even under ambient conditions. Specifically, APbX_3 contains toxic lead and is not stable in ambient conditions in part because AX dissociates into two water-soluble, low-boiling point species.

Therefore, the goal of my doctoral thesis project was to replace the organic monocationic salts in perovskite materials with non-volatile and less water-soluble analogs in the form of organic dicationic salts. Using this rationale, I have demonstrated the use of novel perovskite-like bismuth-halide and copper-halide materials as the photoactive layer in solar cells, which contain hexanediammonium dications (HDA^{2+}) that serve as the organic crystal fastener. I have elucidated structure-property relationships of these and related materials with different organic linkers through measurement of crystal structure, powder and thin-film characterization of the materials,

and long-term thermal and moisture stability. I have also studied these materials using ultrafast spectroscopy techniques to elucidate energy-transport and charge-transport dynamics of these materials as thin films. Efficient photovoltaic devices featuring a dicationic metal–halide material that does not contain lead may offer a more environmentally-friendly, stable alternative to the APbX_3 photovoltaic devices that currently dominate emerging photovoltaic technology research.

DISSERTATION AT A GLANCE

Chapter 1 highlights the development of deposition procedures and novel architectures for lead–halide perovskite solar cells. A proof-of-concept demonstration of the use of a mercury drop as a top-contact electrode in high-throughput experimentation was shown. The best method for depositing the compact TiO_2 blocking layer was determined. The most promising solution-deposition method to reproducibly fabricate high-quality thin films was discovered. Three promising devices, one of which had a particularly novel architecture in that it employed a layer of p-type PEDOT:PSS on top of the perovskite layer, boasted PCEs of $> 1.3\%$.

Chapter 2 demonstrates use of a hybrid organic–inorganic material containing trivalent bismuth and HDA^{2+} (HDABiI_5) as the photoactive layer in solution-processed solar cells. These proof-of-concept photovoltaics demonstrated a stable open-circuit photovoltage of 384 ± 12 mV and steady-state short-circuit photocurrent density of 0.101 ± 0.020 mA/cm². In comparison to the widely studied lead–halide-based perovskites, the bismuth-based materials had superior coverage on mesoporous TiO_2 layers as determined by scanning electron microscopy. Moreover, thermal stability tests demonstrated that these bismuth-based materials were stable at higher temperatures than those for comparable lead-based materials.

In Chapter 3, a library of dicationic hybrid organic–inorganic bismuth–iodide thin films were prepared and characterized in order to understand structure–property relationships. Ultrafast laser spectroscopic techniques were employed to study hybrid organic–inorganic bismuth–iodide thin films. A comparative study was performed on HDABiI_5 vs. propylammonium bismuth pentaiodide, $(\text{PA})_2\text{BiI}_5$, a material that incorporates two propylammonium monocations (PA^+) per formula unit that together are about the same size as HDA^{2+} . Preliminary results on mixed dicationic organic moieties incorporating conjugated organic PhDA^{2+} groups were also obtained.

In Chapter 4, new copper–halide perovskite-like materials containing HDA²⁺ demonstrated superior stability to heat and moisture treatments in comparison to an analogous copper–halide perovskite material containing PA⁺. Electronic absorption spectra taken of the materials were consistent with an indirect optical bandgap of ~1.8 eV, making them well-suited for application as the photoactive layer in the top cell of a tandem solar cell with silicon. A champion single-junction solar cell containing the dicationic material as the photoactive layer exhibited an open-circuit photovoltage in excess of 200 mV and a short-circuit photocurrent density of ~30 $\mu\text{A}/\text{cm}^2$.

Chapter 5 presents an analysis on a series of low-dimensional lead–halide perovskite materials incorporating alkylammonium dications of varying alkyl chain length. Absorption, photoluminescence, and ultrafast laser spectroscopy data of thin films of the materials showed trends that support structural data obtained by X-ray diffraction. Exciton binding energies were determined to be ~100-160 meV for the series of materials. The two-dimensional lead–halide perovskite material incorporating butanediammonium dications exhibited the longest free-carrier lifetimes.

CHAPTER 1: BACKGROUND, DEPOSITION PROCEDURE DEVELOPMENT, AND NOVEL ARCHITECTURES OF PEROVSKITE SOLAR CELLS

1.1 Introduction

It is evident that the finite supply of fossil fuels is leading to impending energy crises and fossil fuel consumption associated with human activity is causing worldwide pollution problems. In order to resolve these prominent societal issues, research into generating useful power from renewable energy sources such as wind, hydroelectric, geothermal, biomass, and solar needs to be prioritized. The amount of accessible energy directly from the Sun exceeds all other renewable energy sources,¹ and thus it can be argued that the most impactful renewable energy technologies lie in the solar market. For this reason, commercialized technologies that directly convert clean, renewable sunlight into electricity, e.g. photovoltaics (PVs), are becoming vastly important.

In recent years, PVs have become promising technologies due to improvements in PV materials quality and lowered costs.² Crystalline silicon (c-Si) PVs have cornered the solar market for over 50 years due to their high crystal quality, robustness, and relatively low cost compared to other commercialized PV materials.³ However, in order for a PV technology to be cost-competitive with current fossil fuel-based grid electric power throughout the U.S., it is necessary that PV costs are brought down further. In 2011, the U.S. Department of Energy launched an initiative to spur innovative efforts to re-establish the U.S. as a leader in solar energy technologies. The goal of the initiative is to drive the average price of utility-scale PV modules down to \$0.06/kWh by 2020 and to \$0.03/kWh by 2030 (Figure 1.1).⁴ The PV market is currently ahead of the pace, as the 2020 utility-scale module price target of \$0.06/kWh was reached in September 2017.⁵ In order to uproot the established electricity industry and transform it into a solar-dominated industry, however, more

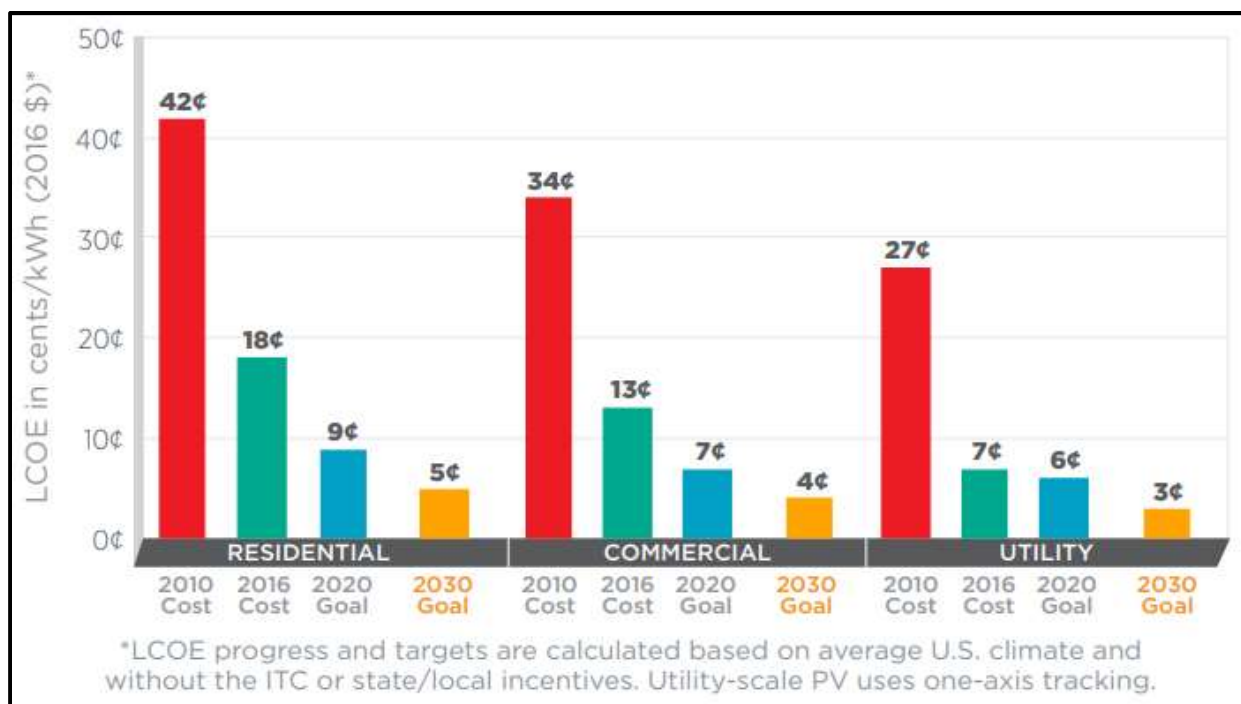


Figure 1.1. Levelized cost of energy values and Department of Energy cost goals for solar electricity.

than just cost-competitive PV technologies are needed; emerging PV technologies have to be substantially cheaper than current grid electric power to make the removal of established electricity infrastructure economically feasible.

The halide perovskite is a specific class of materials that has been utilized in next-generation PVs as an effective light absorber and charge transport material.⁶ Perovskite PVs have an advantage over c-Si PVs in that they can be solution-processed at low temperatures, meaning they are less expensive to fabricate.⁷ Based on materials and manufacturing costs, a utility-scale perovskite PV module operating at 16% efficiency is projected to cost \$0.05-0.08/kWh.⁸

Halide perovskite materials of the form $APbX_3$ (where A^+ is an organic monocation, Pb^{II} is lead, and X^- is a halide like iodide, bromide, chloride) were first introduced as light absorbers in solar cells in 2009, when Miyasaka and colleagues used methylammonium lead iodide perovskite ($MAPbI_3$) in a dye-sensitized solar cell and reported a 3.8% power conversion

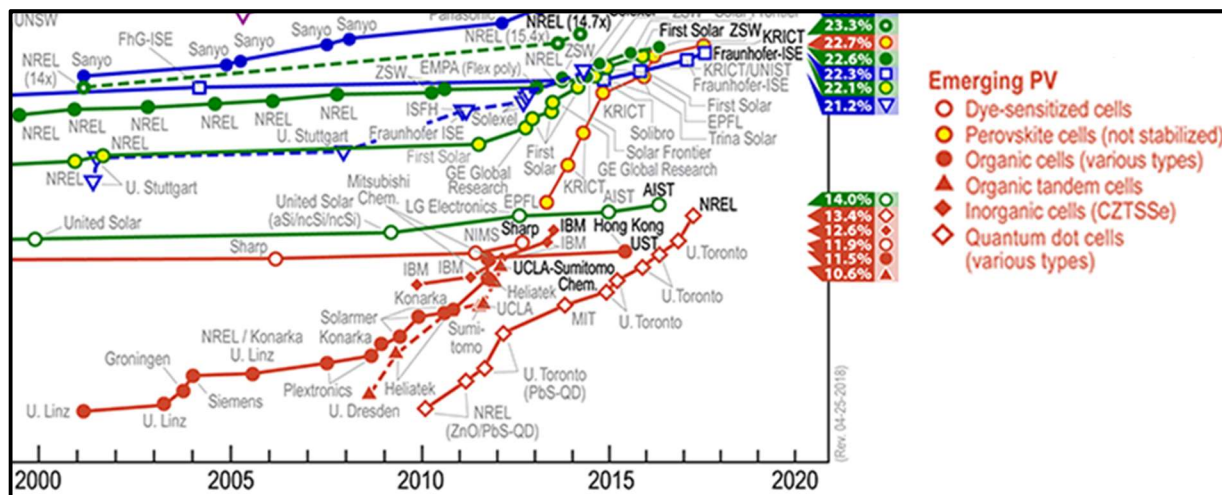


Figure 1.2. Best research-cell efficiencies of emerging photovoltaic technologies (red traces).

efficiency (PCE).⁹ Three years later Miyasaka, Snaith, and colleagues reported a solar cell with 10% PCE and since then, research and development into these materials has soared.¹⁰ As of 2018, APbX₃ PVs have achieved laboratory efficiencies of > 22% (Figure 1.2).¹¹ These promising efficiencies can be explained by the numerous desirable properties of APbX₃ as a PV absorber material. APbX₃ perovskites have a near-ideal bandgap for terrestrial PV use, high optical absorption, benign grain boundaries, shallow-level defects, and small effective masses for charge-carriers.^{12,13} APbX₃ boasts high charge-carrier conductivity through PbX₆ octahedra arranged in a three-dimensional (3D) lattice. In addition, the A group in APbX₃ contributes to dielectric and ferroelectric properties and sets a low energetic barrier for reorientation of the A group within the structure.¹⁴

Despite all these promising PV properties, the rapid growth rate of halide perovskite PV materials came at the expense of several critical aspects that today, still remain unoptimized. The critical unanswered fundamental question that I address in my work is whether PV stable, efficient, *and* non-toxic visible-light-absorbing perovskite materials can be demonstrated. The halide perovskites APbX₃, ASnX₃, and mixtures thereof are innately unstable in ambient conditions.^{13,15}

APbX₃ materials are not stable in part because AX dissociates into two water-soluble, low-boiling point species (e.g. when AX = CH₃NH₃⁺X⁻, CH₃NH₂ and HX are formed). ASnX₃ materials are not stable in air, as Sn²⁺ readily oxidizes to Sn⁴⁺.¹⁶ In addition, PVs when in operation can reach temperatures of > 45 °C after a few minutes of sunlight exposure, which is beyond the sublimation point of both CH₃NH₂ and HX.¹⁷ Exposure to light and dry air has also been reported to rapidly decompose APbX₃ and ASnX₃, especially when employed in mesostructured assemblies.¹⁸ This means that for large-scale development, stringent atmospheric conditions are required for synthesis and fabrication, which necessitates additional manufacturing and safety costs. Perovskite materials are also ionically unstable, which results in current–voltage hysteresis. Vacancy-assisted migration of iodide ions in the perovskite crystal was suggested to be an important factor contributing to the observed hysteresis.¹⁹ Moreover, several APbX₃-like materials do not form 3D crystals and instead form one-dimensional (1D) or two-dimensional (2D) crystals,^{20–24} which more easily allows ingress of molecules that degrade the cells. These 1D and 2D materials are also problematic because inter-chain and inter-sheet spacing precludes rapid conduction between the inorganic regions (Figure 1.3), which adversely affects overall solar cell performance.

Halide perovskite PVs commonly take the form of one of three general architectures as shown in Figure 1.4: mesostructured, planar n–i–p (commonly referred to as “regular”), and planar p–i–

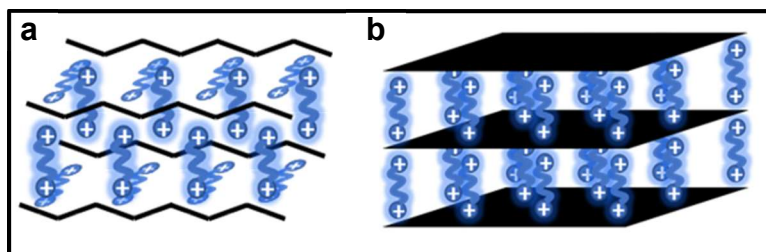


Figure 1.3. (a) 1D and (b) 2D representation of general linking between organic moieties (blue) and inorganic (black) moieties. Shown are divalent organic groups, although monovalent organic groups are also common.

n (commonly referred to as “inverted”). The mesostructured architecture was adopted from dye-sensitized solar cells and the planar p–i–n architecture was adopted from organic solar cells.^{25,26} As of

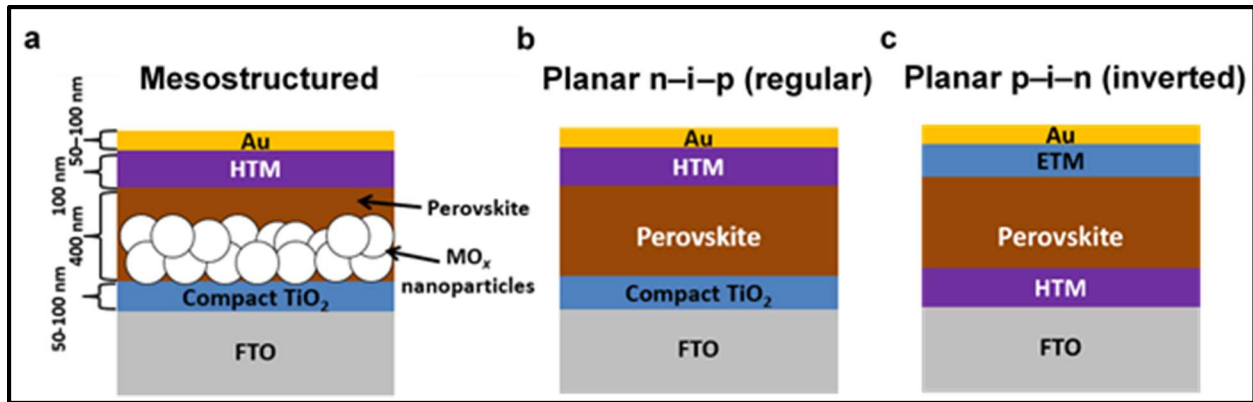


Figure 1.4. (a) Mesostructured, (b) planar n-i-p, and (c) planar p-i-n architectures typically employed in perovskite photovoltaics. Labeled thicknesses are approximate. FTO = fluorine doped tin oxide, MO_x = metal oxide, HTM = hole transport material, ETM = electron transport material.

2018, PCEs for PVs employing each architecture have exceeded 19%.^{11,27,28} The only compositional difference between the mesostructured and planar architectures is the presence of a mesoporous metal oxide nanoparticle layer. The metal oxide used can be semiconducting TiO_2 , ZnO , SnO_2 , etc. or even insulating Al_2O_3 , ZrO_2 , MgO , etc.

In early perovskite PV demonstrations, the mesostructured architecture was exclusively employed.^{9,10,29} However, because PVs incorporating insulating metal oxide nanoparticles demonstrated comparable PCEs to those incorporating semiconducting metal oxide nanoparticles, it became evident that there is efficient charge-carrier transport through the perovskite absorber layer itself and that the metal oxide nanoparticle layer may merely serve as a scaffold to allow for more effective perovskite crystal nucleation and growth.¹⁰ In September 2013, Snaith and colleagues demonstrated that the mesoporous layer was unnecessary for high-performance perovskite PVs. Snaith and coworkers deposited the perovskite layer via dual-source thermal evaporation of methylammonium iodide and lead chloride, and they reported PVs with PCEs of >15%.³⁰ As a result, many questions arose as to the precise role of the metal oxide layer.

There is no one perovskite PV architecture that stands out as boasting the highest-efficiency devices. There are several methods presented in the literature for depositing the dense, crystalline

compact TiO₂ layer in n-i-p perovskite solar cells; four of these methods were compared by Huang and colleagues.³¹ Common methods include chemical bath deposition, sol-gel method, spin-coating, screen-printing, and spray-pyrolysis.^{32,33} There are also several TiO₂ precursor materials used, which include TiCl₄, titanium isopropoxide, and titanium diisopropoxide bis(acetylacetonate), and commercially-available blocking layer titania pastes.³¹

Another drawback of halide perovskite PVs is the high cost of commercially-available p-type hole transport materials, which are used in the regular n-i-p architecture, and n-type electron transport materials, which are used in the inverted p-i-n architecture. Although poly(3,4-ethylenedioxythiophene):poly(styrenesulfonate) (PEDOT:PSS) is a p-type hole transport material commonly used in inverted p-i-n solar cells, it is not employed in regular n-i-p solar cells because of solvent incompatibility issues. In the n-i-p architecture, the p-type hole transport material is deposited on top of the intrinsic perovskite layer, which means the solvent used for the hole transport material solution must not degrade the underlying perovskite layer during deposition. For PEDOT:PSS solutions, water is the optimal solvent and water, like many polar solvents, readily decomposes the perovskite by solubilizing the organic component, which compromises the stability and integrity of the perovskite structure.³⁴

Demonstrations of single-junction perovskite PVs with efficiencies > 20% make them competitive options for large-scale deployment.³⁵ In order to scale up the PV fabrication process, innovative materials deposition methods are needed. Inkjet printing is not amenable to the deposition of many high-quality semiconductor materials, because high-vacuum chemical-vapor-deposition processes are often required, deposited material precursors must be homogeneous, and the solvents for the inks must have a low vapor pressure so that regions do not dry prematurely. These are not problems for perovskite materials, however. First, perovskite materials result in

efficient solar cells even when deposited by solution-based techniques. Second, mixing is not crucial to obtaining homogeneous perovskite thin films; for example, studies have shown that PbI_2 can be deposited into a mesoporous metal-oxide support and dried, and then subsequently immersed into an alcohol solution of MAI to form MAPbI_3 nanocrystallites that result in a > 15% efficient solar cell.²⁹ Third, ABX_3 perovskite materials are often deposited from high-boiling point solvents with low vapor pressures, such as *N,N'*-dimethylformamide (DMF) (153 °C), dimethylsulfoxide (DMSO) (189 °C), *N*-methyl-2-pyrrolidone (203 °C), or γ -butyrolactone (204 °C),³⁶ so that the crystallites can form prior to evaporation of the solvent. Perovskite materials can therefore be interrogated using combinatorial printing and screening to investigate small compositional changes and an extremely fine map of the crystallographic structures and bandgap energies.

1.2 Experimental

1.2.1 Preparation of MAPbX_3 Solutions

All chemicals were used as received. Methylammonium iodide (MAI) was synthesized by slow addition of 6.5 mL of hydriodic acid (47% in water, stabilized with 1.5% hypophosphorous acid, Sigma-Aldrich) at room temperature to 6 mL of methylamine (40 wt. % in methanol, TCI America) at 0 °C with stirring, followed by continued stirring for 1 hr. MAI precipitate was recovered by evaporation of solvents at 50 °C under reduced pressure. To purify MAI, the precipitate was dissolved in ethanol, recrystallized from diethyl ether, and finally vacuum dried at 60 °C for 12 h. MAPbI_3 solution was then prepared by mixing MAI and PbI_2 (99%, Sigma-Aldrich) powders in approximately a 1:1 mole ratio, but with MAI in slight excess, in anhydrous *N,N*-dimethylformamide (DMF) at 70 °C inside a nitrogen-filled glovebox. For mixed-halide MAPbI_3 .

$x\text{Cl}_x$ solutions, PbI_2 was replaced with PbCl_2 (98%, Sigma-Aldrich) and powders were mixed in approximately a 3:1 ratio of MAI to PbCl_2 . MAPbX_3 solutions were stored in the glovebox until use and were used within one week of preparation.

1.2.2 Thin-Film Processing

1.2.2.1 Substrate Preparation and Metal–Oxide Materials Deposition

All steps of materials deposition and photovoltaic device fabrication were performed in air with 40–60% relative humidity, unless noted otherwise. All thermal treatments were performed using a hot plate. Fluorine-doped tin oxide coated glass (FTO) substrates were cleaned as follows: 1) sonicated in Alconox solution, 2) rinsed with deionized water, 3) rinsed with ethanol, 4) sonicated in ethanol, and 5) dried with nitrogen. To deposit the compact TiO_2 (cTiO_2) layer, a solution of titanium diisopropoxide bis(acetylacetonate) was pipetted onto a cleaned FTO substrate and then the substrate was spun at 2000 rpm (2000 rpm/s acceleration) for 60 s. The substrate was subsequently dried at 125 °C and then sintered at 550 °C for 30 min. Nanoparticles of TiO_2 were synthesized following a procedure by Ito et al.³⁷ The nanoparticle solution was used as is and was deposited via blade coating to form a microns thick mesoporous TiO_2 (mTiO_2) layer for fluorescence imaging microscopy. For all other thin-film preparation and measurements, the nanoparticle solution was further diluted in ethanol at a weight ratio of 1:3.5 TiO_2 nanoparticle solution:ethanol. Mesoporous γ -phase Al_2O_3 nanoparticles (mAl_2O_3) were used in place of mTiO_2 in some thin films and devices. mAl_2O_3 suspensions were prepared by mixing γ -phase Al_2O_3 nanoparticles, <50 nm particle size, 20 wt% in isopropanol (Sigma Aldrich) in a solution of ethyl cellulose, ethanol, and terpineol. The mTiO_2 or mAl_2O_3 layer was deposited by spin coating this

solution at 500 rpm (500 rpm/s acceleration) for 5 s and then 5000 rpm (5000 rpm/s acceleration) for 25 s, then dried at 125 °C, and then sintered at 550 °C for 30 min.

For metal–oxide film coverage measurements, a 2M TiCl_4 solution was prepared via slow addition of TiCl_4 (99%, Strem Chemicals) to deionized water. This solution was further diluted with deionized water to make a 200 mM bath. TiCl_4 deposition was carried out following a procedure adapted from Yella and coworkers.³⁸ Briefly, cTiO_2/FTO substrates were submerged in the TiCl_4 bath kept at 70 °C for 30 minutes to allow for a thin capping layer of TiO_2 to form on the substrate. TiO_2 thin films were rinsed with water, rinsed with ethanol, dried with a flow of N_2 , and dried further in air at 100 °C for 60 minutes.

1.2.2.2 Perovskite Deposition Methods

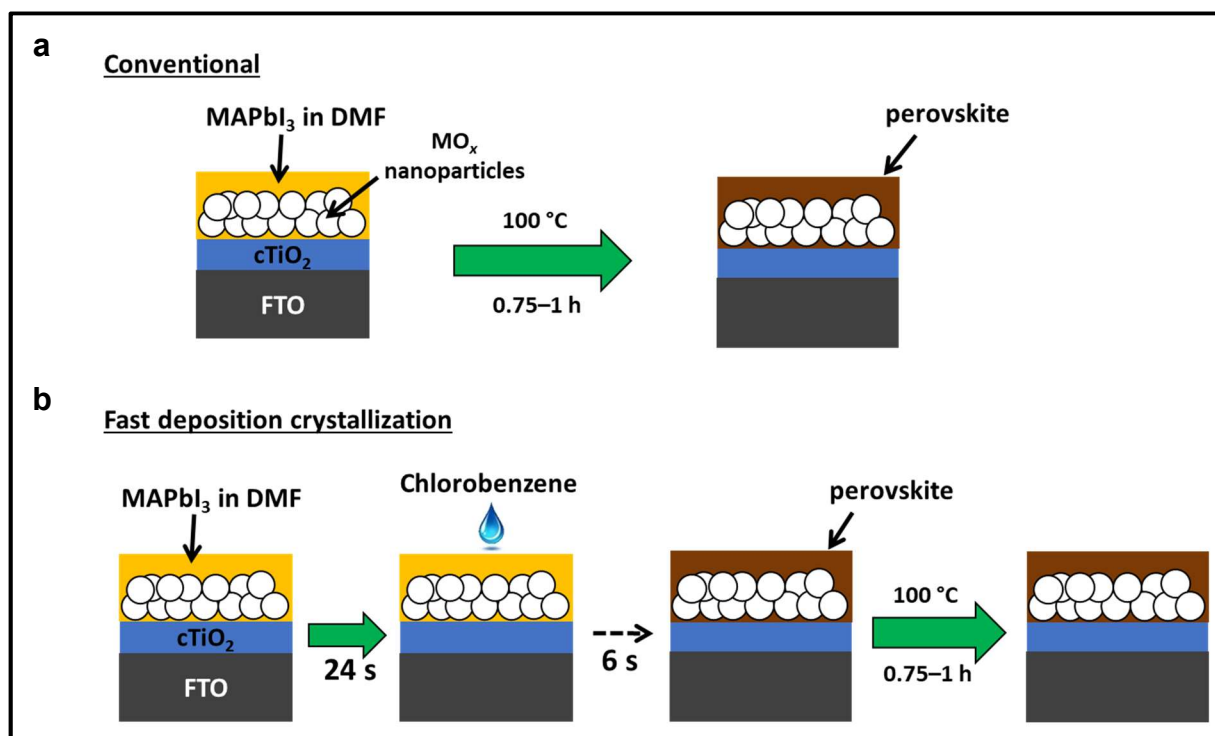


Figure 1.5. (a) Conventional spin-coat procedure for depositing perovskite precursor solution (e.g. MAPbI_3 in DMF) on mesoporous metal oxide (MO_x)/compact TiO_2 (cTiO_2)/fluorine-doped tin oxide (FTO). (b) Fast deposition crystallization (FDC) spin-coat procedure, which incorporates an antisolvent (e.g. chlorobenzene) during the spin-coat process.

A conventional one-step spin-coating method was adapted from the method of Lee and coworkers,¹⁰ in which a filtered solution of MAPbI₃ in DMF was dropped on top of a metal-oxide(MO_x)-coated FTO substrate and then was spun at 2000 rpm (with 2000 rpm/s acceleration) for 60 seconds using a spin coater. After spinning was complete, the substrate was

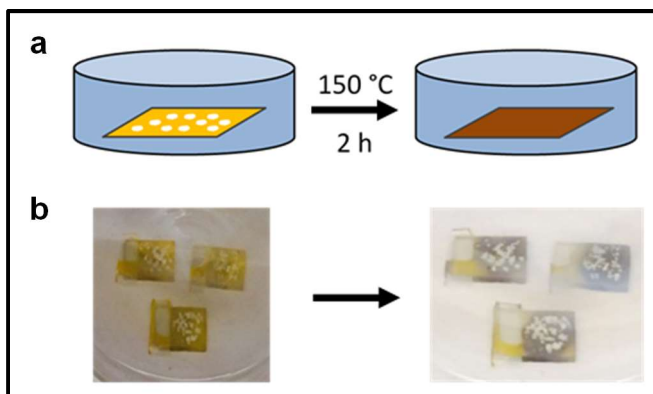


Figure 1.6. (a) Illustration and (b) digital photograph images of the gas-solid crystallization method whereby methylammonium iodide (MAI) powder is sprinkled on the PbI₂ film to form MAPbI₃ perovskite during heating at 150 °C.

quickly transferred to a hot plate that was preheated to 100 °C and annealed for 45-60 minutes to ensure that all DMF evaporated. This conventional spin-coat method is shown pictorially in Figure 1.5a. Other deposition methods that were tested include fast deposition crystallization (FDC) (Figure 1.5b),³⁹ sequential deposition,⁴⁰ gas-solid crystallization (Figure 1.6),⁴¹ vapor-assisted solution process,⁴² and hot-casting.⁴³

For the FDC method (shown pictorially in Figure 1.5b), the MAPbX₃ solution was instead spun at 6000 rpm for 30 seconds total, and 6 seconds before the end of the spin process, anhydrous chlorobenzene (CB) or toluene was dropped onto the film while the substrate was spinning. The faint yellow film immediately turned dark brown, indicating formation of the MAPbX₃ perovskite structure during the spinning process. For the hot-cast method, a substrate was heated to 130 °C and the perovskite solution was kept at 70 °C. Then, the substrate was quickly transferred to the spin coater, perovskite solution was dispensed, and immediately after dispensing, the substrate was spun at 4000 rpm (4000 rpm/s acceleration) for 6 s. The faint yellow film turned dark brown while the substrate was spinning, characteristic of perovskite formation. Shortly thereafter, the hole

transport material was deposited or, in cases where no hole transport material was used, the substrate was transferred to the glovebox for thermal evaporation of the gold top contact.

1.2.3 Photovoltaic Device Preparation

After an FTO-coated glass substrate was cut to a size of 1 inch x 1 inch, roughly one-third of the FTO was etched with aqueous 2M HCl and zinc powder in order to prevent device shunting upon contact to the top Au electrode of the device (Figure 1.7). To etch the FTO, roughly two-thirds of the FTO was covered with masking tape, zinc powder was sprinkled onto the exposed FTO, and aqueous 2M HCl was



Figure 1.7. Digital photograph image of aqueous 2M HCl and zinc powder reacting to etch away the exposed fluorine-doped tin oxide.

dispensed and spread around the exposed FTO. The HCl and zinc powder were allowed to react for approximately 3 min, and then the FTO was rinsed with deionized water followed by ethanol and finally dried with a flow of N₂. After performing the cleaning steps listed above (*1.2.2.1 Substrate Preparation and Metal–Oxide Materials Deposition*), substrates were further cleaned using an O₂ plasma treatment for 10 min. During the deposition of the compact TiO₂ (cTiO₂) layer and the mesoporous MO_x layer via spin coating, one of the corners as well as roughly one-half of the etched region were masked with scotch tape.

Following deposition of MAPbX₃ per one of the protocols described above (Perovskite Deposition Methods subsection), a 50 mM solution of 2,2',7,7'-tetrakis(N,N'-di-p-methoxyphenylamine)-9,9'-spirobifluorene (spiro-OMeTAD) dissolved in chlorobenzene with additives of 17.5 μL 4-tert-butylpyridine and 37.5 μL lithium bis(trifluoromethane)sulfonimide in

acetonitrile (170 mg/mL) was deposited by spin coating at 3000 rpm (3000 rpm/s acceleration) for 60 s. For devices incorporating PEDOT:PSS as the hole transport material (HTM) instead of spiro-OMeTAD, PEDOT:PSS pellets were dispersed in isopropanol at ~1 wt. % via vortexing and sonication using an ultrasonic bath and ultrasonic horn. PEDOT:PSS solution was deposited by spin coating at 2000 rpm (2000 rpm/s acceleration) for 60 s. The MAPbX₃ and spiro-oMeTAD HTM layers were deposited without masking via spin coating. Afterward, a razor blade was used to scratch off the previously masked areas. Finally, the devices were transferred into a nitrogen-filled glovebox and 80 nm of gold was thermally evaporated (custom, Law Group) in either a 3 x 3 array of dots or two rectangular strips that slightly overlap where the FTO had been etched away. The evaporated gold served as the top-contact anode. For current density vs. voltage ($J-V$) measurements, a masked area of 0.25 cm² was illuminated by an ELH lamp of ~1 Sun light intensity (calibrated with a Si diode).

1.2.4 Electrical Characterization

For electrochemical measurements performed outside the glovebox, including mercury drop electrode measurements and metal-oxide film coverage measurements, a Biologic Science VSP-300 was used. For mercury drop electrode and Au electrode conductivity measurements of thin films, two-electrode cyclic voltammetry was performed vs. E_{ref} by scanning from 0 V to +0.2 V to -0.2 V to 0 V at a scan rate of 100 mV s⁻¹. The inner o-ring area in which the mercury drop was placed was 0.032 cm² and the Au dot had an area of 0.085 cm². For studies on TiO₂ film coverage on FTO-coated glass substrates, thin films immersed in an electrolyte containing 1 mM ferrocene and 100 mM tetra-*n*-butylammonium hexafluorophosphate in acetonitrile. An aqueous KCl-saturated calomel electrode (SCE) was used as the potential-sensing reference electrode, and

a platinum mesh electrode and the FTO served as the current-carrying counter and working electrodes, respectively. Three-electrode cyclic voltammetry was then performed vs. E_{SCE} by scanning from 0 V to +1.2 V to -1.2 V to 0 V at a scan rate of 50 mV s^{-1} .

For electrochemical measurements performed inside the glovebox, including photovoltaic device $J-V$ measurements and light-intensity-dependent measurements, a Gamry

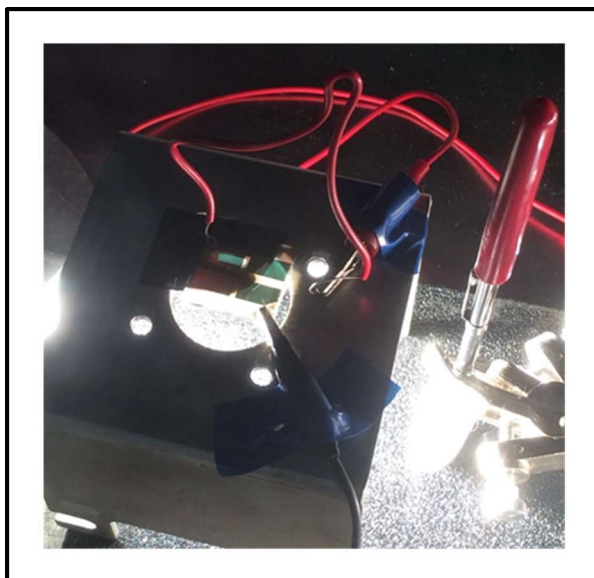


Figure 1.8. Digital photograph image of the photovoltaic device $J-V$ measurement setup.

Instruments Reference 600TM Potentiostat was used. For device $J-V$ measurements, two-electrode cyclic voltammetry was performed vs. E_{ref} by scanning from 0 V to +1 V (under reverse bias) to -1 V (under forward bias) to 0 V (under reverse bias) at a scan rate of 100 mV s^{-1} . The gold electrode of the device was gently contacted with a looped tinned copper wire that was connected to an alligator clip wired to the potentiostat. Another alligator clip wired to the potentiostat was contacted to the FTO-coated glass substrate (Figure 1.8). Devices were masked so that only one “cell” (i.e. one gold pad) was exposed to light. Cells were light-soaked for 5 minutes prior to running cyclic voltammetry. Current densities were calculated by dividing the current passed through the potentiostat by the unmasked area of the device. For light-intensity-dependent measurements, the ELH lamp position was varied to obtain light intensities ranging from ~ 0.2 to ~ 1 sun. Chronopotentiometry was performed for each light intensity and V_{OC} values were recorded 60 s after the ELH lamp was turned on.

1.2.5 Mercury-Drop Top-Contact Electrode Setup

Liquid mercury was dropped inside an O-ring placed on top of the film to be measured (Figure 1.9). A platinum wire connected to a soldering aid (which was in electrical contact to an alligator clip of the potentiostat) was carefully submerged into the mercury drop. A washer was carefully submerged into the mercury drop. A washer was contacted to the FTO substrate, which was in electrical contact with a bolt, followed by an alligator clip of the potentiostat.

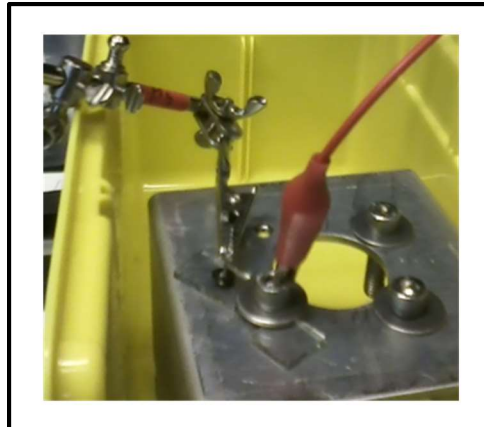


Figure 1.9. Digital photograph image of the mercury-drop top-contact electrode setup.

1.2.6 Thermal Stability Tests

Thermal stability tests were performed in air for MAPbI₃ thin films deposited on mTiO₂/cTiO₂/FTO per the protocols above, but using a 70 °C annealing temperature for 60 min. Then, a UV–Vis absorption spectrum was acquired. The hot plate temperature was raised from the processing temperature (70 °C) to 90 °C, held for 10 min, and a UV–Vis absorption spectrum of the thin film was acquired. Then, the temperature was raised to 100 °C, held for 10 min, and another UV–Vis absorption spectrum was acquired. This procedure was repeated up to 200 °C as such: 1) the processing temperature was raised by 20 °C, 2) the temperature was held for 10 min, and 3) a UV–Vis absorption spectrum was acquired.

1.2.7 Thin-Film Characterization

Ultraviolet–visible light (UV–Vis) absorption measurements were carried out using an Agilent Cary 60 spectrophotometer. Photoluminescence (PL) measurements were performed using

a Cary Eclipse fluorescence spectrophotometer. For fluorescence imaging microscopy measurements, a 438 nm laser source (Spectra-Physics MaiTai HP) was used to excite the sample and emission intensity at 650-750 nm was detected and imaged using an Olympus IX81 confocal laser scanning microscope. Scanning electron microscopy (SEM) images were acquired on a FEI Magellan 400L XHR. Grazing incidence X-ray diffraction (GIXRD) data were collected using a Rigaku Smartlab diffractometer with Cu K α radiation and in parallel beam geometry.

1.3 Results & Discussion

To assess the feasibility of using an inkjet printer system to print combinatorial libraries of various perovskite material compositions, a mobile, non-destructive, easily deposited and removed top-contact electrode would be beneficial for performing rapid $J-V$ measurements on PV device stacks. Because mercury is a liquid metal, it has been used as an electrode in electrochemical measurements. The use of a mercury drop top-contact electrode would significantly lower the cost of a high-throughput PV device performance testing system. Mercury is much less expensive than typical noble metals used, such as gold, and does not require time-consuming vacuum-based deposition techniques that evaporated metal contacts require for forming an electrode. A drawback, however, is that mercury forms an amalgam with lead, which would cause decomposition of the perovskite layer upon contact with the mercury drop. Therefore, in order to prevent perovskite decomposition, a pinhole-free selective contact between the perovskite layer and mercury drop is necessary.

A proof-of-concept demonstration of the use of a mercury drop as a top-contact electrode was performed and results are shown in Figure 1.10. White-light illumination from an ELH lamp was incident through the FTO side of each sample. It is evident that liquid mercury forms an ohmic

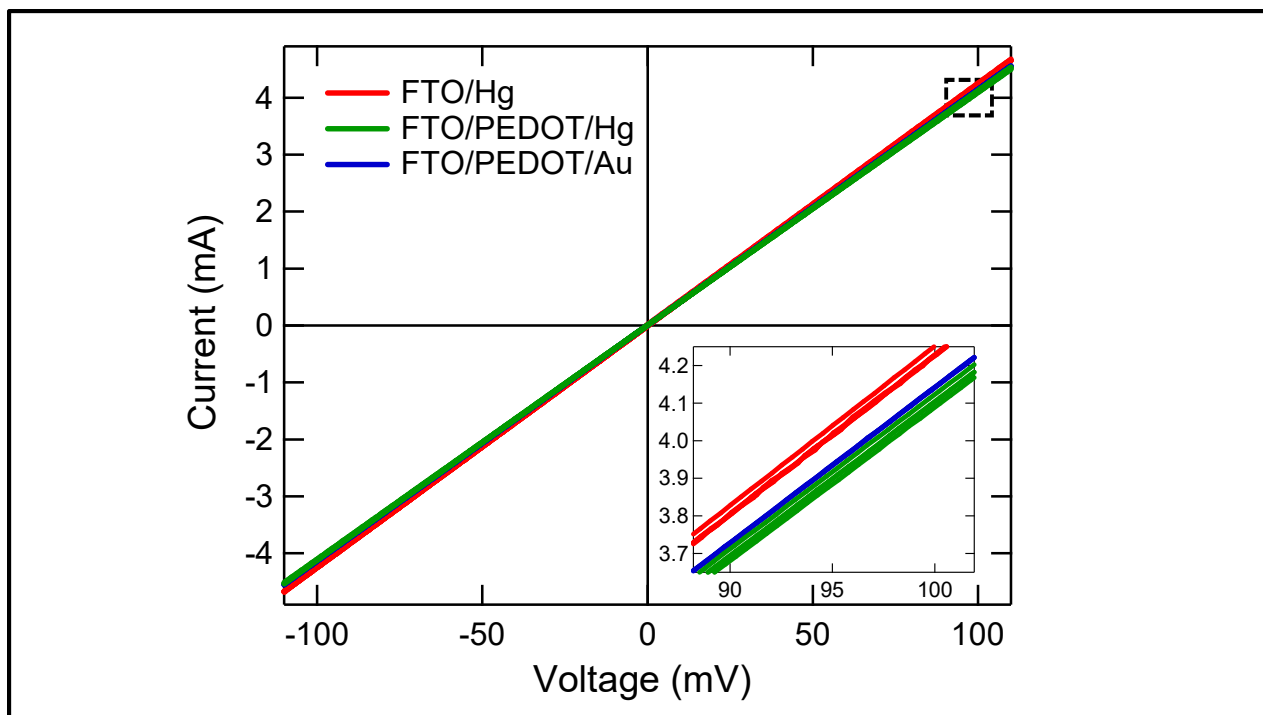


Figure 1.10. Current–voltage curves showing ohmic contacts of evaporated gold to a solution-deposited PEDOT:PSS thin film (blue trace) as well as liquid mercury to fluorine-doped tin–oxide (red trace) and liquid mercury to PEDOT:PSS (green trace). Inset: zoomed-in area (denoted by dashed box) showing only slight differences in resistance for each contact.

contact with PEDOT:PSS (green trace), as gold does (blue trace). In addition, there is minimal resistance when PEDOT:PSS is used as a hole transport material, which is depicted by the small difference in the slope of the red trace vs. the green trace. The resistance of FTO/Hg is 23.5Ω , the resistance of FTO/PEDOT:PSS/Au is 24.1Ω , and the resistance of FTO/PEDOT:PSS/Hg is 24.2Ω . Therefore, a high-throughput experimental setup using a mercury drop top-contact electrode would afford a reasonable low-cost method to evaluate individual PV device stacks.

The cTiO_2 layer serves as the hole-blocking layer in n–i–p perovskite PVs. Surface coverage of cTiO_2 on the underlying substrate is vital to perovskite PV performance. As it is the first layer deposited in n–i–p perovskite PVs, the deposition quality of the cTiO_2 layer is a key factor in resulting PV performance. If the cTiO_2 layer has pinholes, they often persist upon deposition of other material layers and result in a shunting pathway for electronic charges. For this

reason, determining the most effective precursor and deposition method for the cTiO₂ layer is crucial.

Cyclic voltammetry was employed to assess the hole-blocking effectiveness of different metal–oxide architectures commonly used in regular n–i–p perovskite PVs. To accomplish this, cyclic voltammetry measurements were conducted using the perovskite as the working electrode in contact with an acetonitrile electrolyte containing ferrocene (Fc) as the conformal redox-active contact. Fc is frequently used as a standard for calibrating redox potentials in non-aqueous electrochemistry, for which the one-electron reduction potential for Fc⁺⁰ is ~0.5 V vs. SCE.⁴⁴ In this experiment, working electrodes with different metal–oxide architectures on FTO were submerged in 1 mM Fc and 100 mM tetra-*n*-butylammonium hexafluorophosphate in acetonitrile that had been degassed with argon. Three-electrode cyclic voltammetry at 50 mV/s was performed

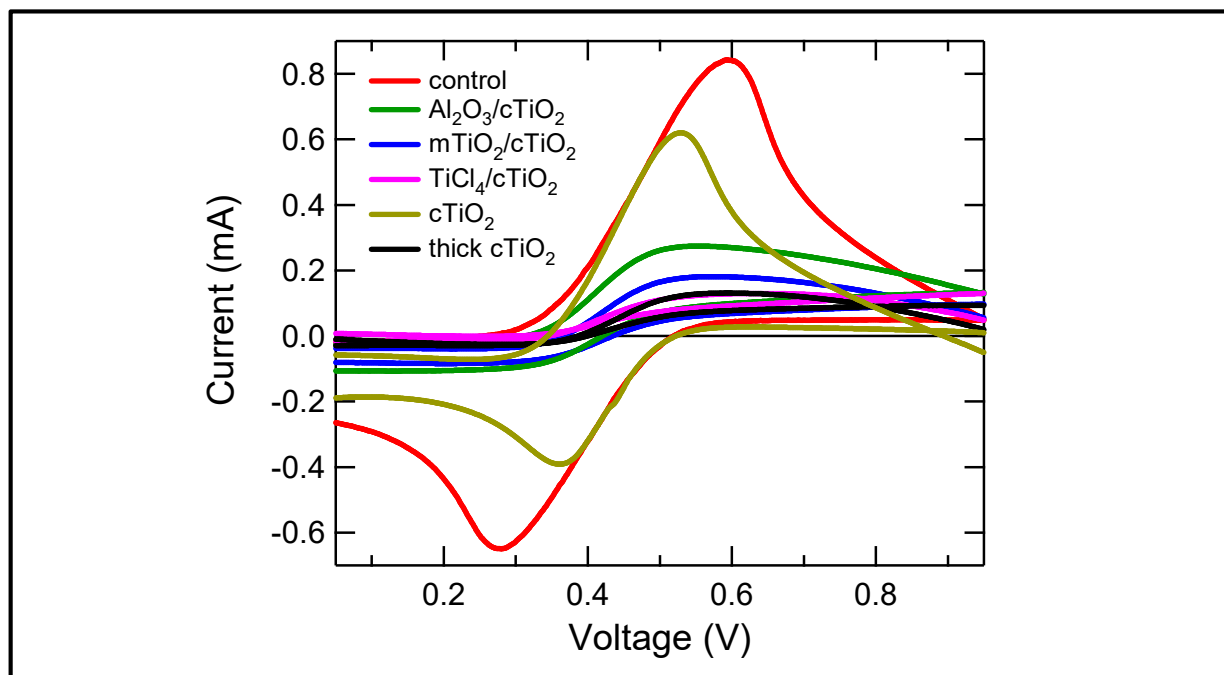


Figure 1.11. Three-electrode cyclic voltammetry at 50 mV/s of 1 mM ferrocene in acetonitrile with 100 mM tetra-*n*-butylammonium hexafluorophosphate. Working electrodes studied are different metal–oxide architectures on a fluorine-doped tin–oxide coated glass substrate, the counter electrode is platinum mesh, and the reference electrode is a saturated calomel electrode. control = FTO.

for each working electrode and voltammograms are shown in Figure 1.11. For the electrode labeled ‘thick cTiO₂’ (black trace), the cTiO₂ solution was spun-coat using 2000 rpm (2000 rpm/s acceleration) instead of 4000 rpm (4000 rpm/s acceleration) used for all other electrodes. Single-electron transfer of Fc⁺⁰ was first monitored on an FTO substrate as a control. For subsequent films containing TiO₂ in various architectures, the suppression of this single-electron transfer reaction was calculated based on the area under the curve in relation to the control FTO substrate. The cTiO₂ film (gold trace) resulted in 26% suppression, mAl₂O₃/cTiO₂ (green trace) resulted in 51% suppression, mTiO₂/cTiO₂ (blue trace) resulted in 79% suppression, TiCl₄/cTiO₂ (pink trace) resulted in 84% suppression, and thick cTiO₂ (black trace) resulted in 85% suppression. It is evident that the thick cTiO₂ and TiCl₄/cTiO₂ films promoted superior film coverage on FTO. However, TiCl₄ treatment resulted in the precipitation of large TiO₂ particles, which introduces larger surface roughness and thus poorer subsequent perovskite coverage and film smoothness. For this reason, a slower spin-coat speed (2000 rpm with 2000 rpm/s acceleration) was determined to be the best method for depositing the compact TiO₂ blocking layer for future preparation of thin films and fabrication of perovskite PVs.

Strong absorption of visible light and efficient charge separation and extraction are essential properties for PV materials. In order to understand the photophysical, structural, and morphological properties of MAPbI₃, a series of characterizations were performed on MAPbI₃ thin films. Figure 1.12 displays steady-state absorption and steady-state photoluminescence (PL) emission spectra of MAPbI₃ and PbI₂. Non-zero absorbance values at longer wavelengths than the absorption onsets correspond to scattering of incident excitation light. Scattering can be due to film roughness or differences in refractive index between the film and air. The absorption onset of a PbI₂ thin film was observed at 540 nm, corresponding to a 2.3 eV optical band gap, and the film

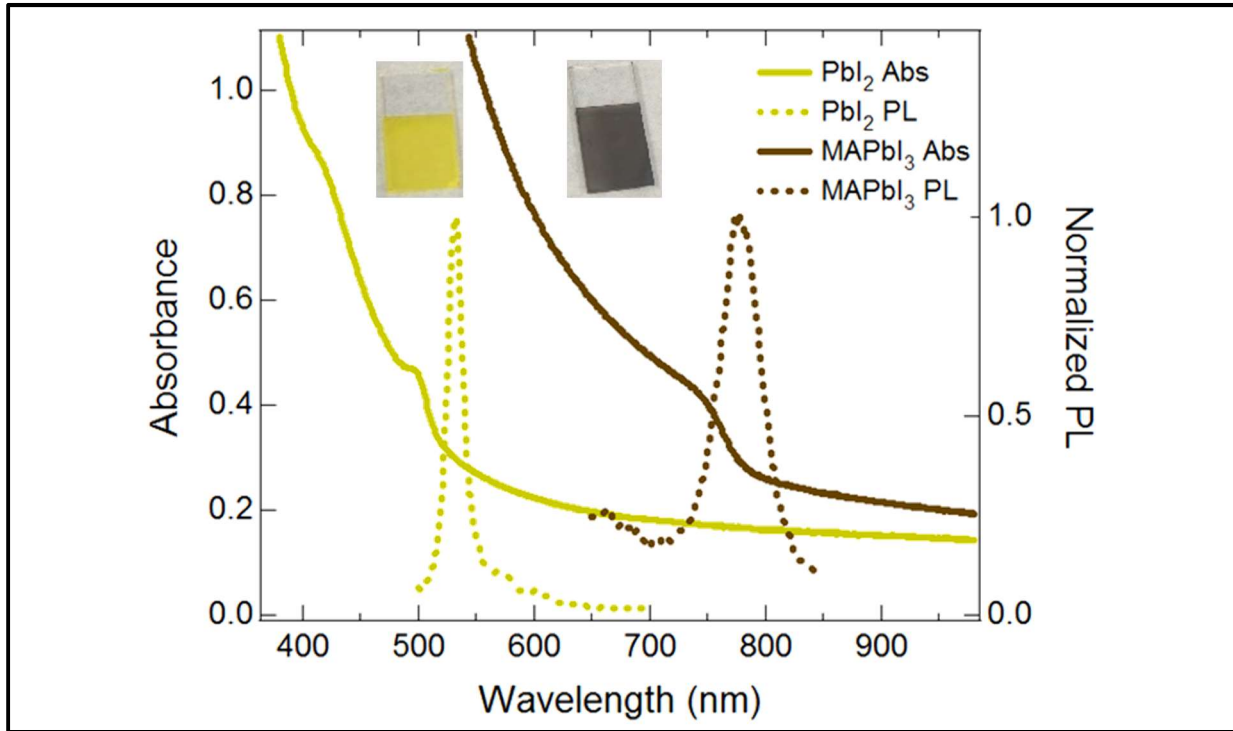


Figure 1.12. Steady-state absorption spectra (solid traces) and photoluminescence emission spectra (dashed traces) of PbI₂ (gold traces) and MAPbI₃ (brown traces) on fluorine-doped tin oxide. Insets are digital photograph images of the films.

exhibited a vibrant yellow color. The MAPbI₃ thin film was dark brown in color, exhibiting an absorption onset at 800 nm, which corresponds to a 1.55 eV optical bandgap. Maximum PL emission occurred at 532 nm and 780 nm for the PbI₂ and MAPbI₃ thin films, respectively. MAPbI₃ also exhibits PL at the band edge, which suggests that MAPbI₃ has a small exciton binding energy that results in efficient free-carrier generation.⁴⁵

Excitation wavelength (λ_{exc}) was chosen to be significantly above the bandgap of each material. λ_{exc} used for PbI₂ was 385 nm and λ_{exc} used for MAPbI₃ was 485 nm. PL emission maxima are at ~530 nm and ~780 nm for PbI₂ and MAPbI₃, respectively (Figure 1.12), and emission peaks were independent of the excitation wavelength for both PbI₂ and MAPbI₃. The PL emission peaks are located at the absorption onsets, i.e. band edges, of each material. Band-edge emission is commonly observed for inorganic semiconductor materials like PbI₂, and is also

observed for the hybrid organic–inorganic material MAPbI₃. Small Stokes shifts have recently been shown to indicate photon recycling in perovskite materials.⁴⁶ This therefore provides fundamental rationale for the high PL quantum yields and long charge-carrier lifetimes observed in perovskite materials.⁴⁷

Despite the recent boom in halide perovskite materials research, published results on fluorescence imaging of these materials have been limited to only a few groups.^{48,49} In this work, a new technique to the halide perovskite research field, termed depth profile fluorescence imaging, was explored. Figure 1.13 depicts fluorescence microscopy images, as a function of position of the point of focus, for a MAPbI₃ thin film on a thick mesostructured TiO₂ scaffold deposited by blade coating. “Surface” represents the depth at which the fluorescence was largest, and all other depths were relative to the surface. The remaining images were acquired at focus depths either above the surface (positive values) or below the surface (negative values). Emission intensity was imaged at 650-750 nm to avoid imaging emission from any excess PbI₂ in the crystal. Definition

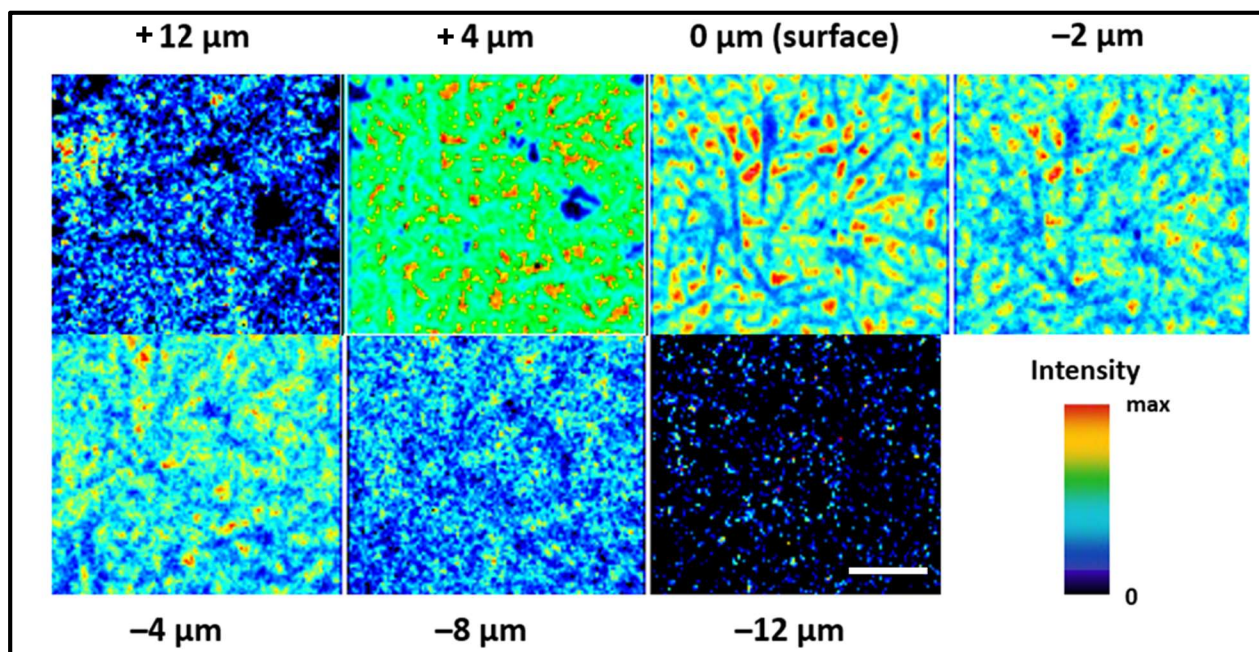


Figure 1.13. Depth profiling by fluorescence lifetime confocal microscopy imaging on MAPbI₃/mTiO₂/cTiO₂/FTO. Scale bar = 20 μm.

in the MAPbI₃ structures became most apparent in the “surface” image. As the focal point of the laser moved deeper into the film, the emission decreased, and at 12 μm into the surface, no significant emission was detected. It is conjectured that perovskite crystals present at the surface of the film are larger than crystals within the mTiO₂ pores and these larger crystallites contribute to higher-intensity fluorescence. Larger crystallites will have smaller relative amounts of defects that serve as non-radiative recombination pathways, and thus are expected to exhibit higher-intensity PL.

The thermal stability of an MAPbI₃ thin film on mTiO₂/cTiO₂/FTO was tested and the results are displayed in Figure 1.14. The absorption onset is observed at ~800 nm (~1.55 eV) and is characteristic of the MAPbI₃. This onset marks the lowest-energy direct-bandgap transition of MAPbI₃, for which the valence band maximum is composed of I 5p and Pb 6s orbital antibonding states and the conduction band minimum is composed of Pb 6p states. Thermal degradation is

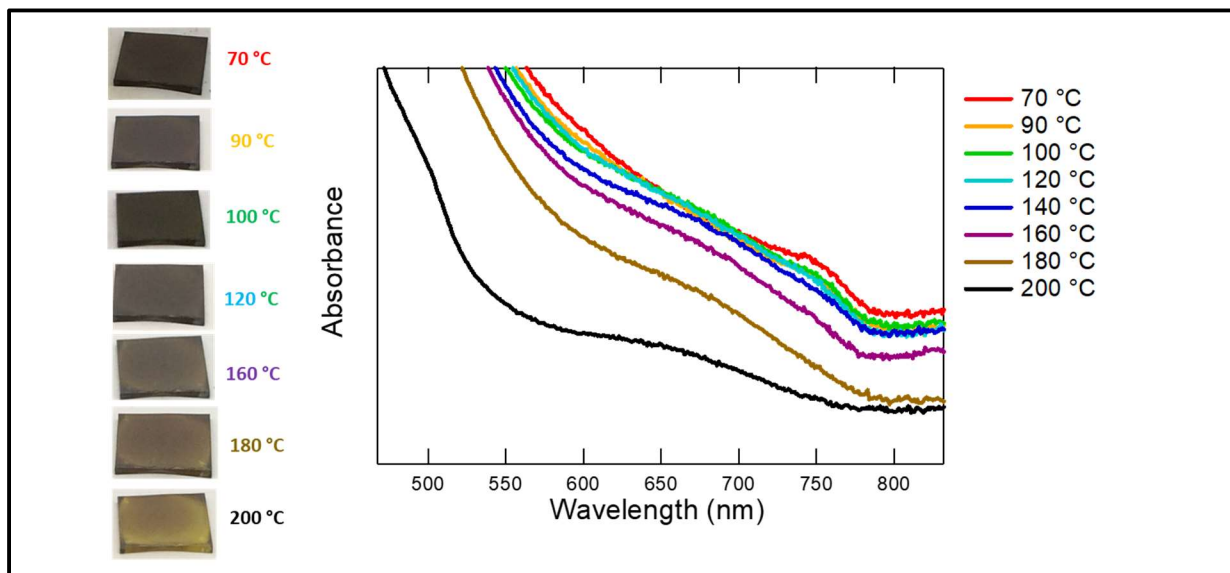


Figure 1.14. Steady-state absorption spectra of an MAPbI₃ thin film on mTiO₂/cTiO₂/FTO. The film was annealed at 70 °C for 60 minutes (red trace) and measured, and then the temperature was raised and then held at each subsequent temperature for 10 minutes, and another absorption spectrum was acquired. On left are digital photograph images of the film after treatment at the specified temperature.

observed starting after the 160 °C treatment, which can be noted by the flattening of the absorption onset (purple trace) and early signs of yellowing of the film in the digital photograph image. There is significant degradation after the thermal treatment of 200 °C, as there is significant absorption loss (black trace) and obvious yellowing of the film. The yellowing can be attributed to structural decomposition of the MAPbI₃ perovskite into PbI₂ upon loss of deprotonated MA and HI due to sublimation.

Due to the nature of layer-by-layer solution-processing as well as the conditions by which the perovskite crystal forms and grows, there is a great deal of variability in PV device

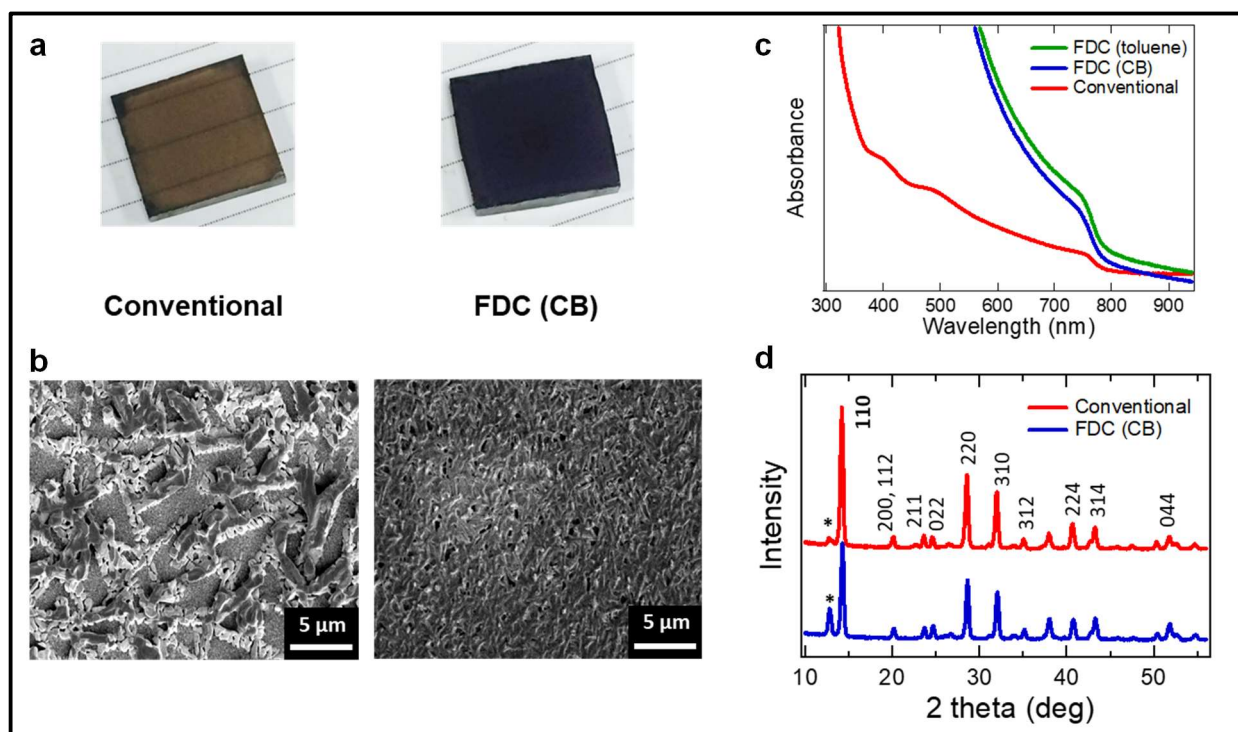


Figure 1.15. (a) Digital photograph images and (b) top-view scanning electron microscopy images of MAPbI₃ thin films on cTiO₂/FTO, for which MAPbI₃ was deposited via a conventional one-step spin-coating method (conventional) or via a fast deposition crystallization technique for which chlorobenzene was used as the antisolvent (FDC (CB)). (c) Steady-state absorption spectra of the MAPbI₃/cTiO₂/FTO substrates shown in panel (a) (red trace and green trace) as well as a spectrum of MAPbI₃/cTiO₂/FTO for which MAPbI₃ was deposited via fast deposition crystallization with toluene as the antisolvent. (d) Grazing-incidence X-ray diffraction patterns of the MAPbI₃/cTiO₂/FTO substrates shown in panel (a). Peaks labeled with asterisks denote residual PbI₂.

performance, even when processing procedures are nominally identical.⁵⁰ When MAPbI₃ is solution-deposited on the same substrate (in this case, cTiO₂/FTO), there are clear differences in film morphology and absorption properties depending on how perovskite crystal formation and growth is induced (Figure 1.15). Digital photograph images of MAPbI₃/cTiO₂/FTO substrates show clear differences that are dependent on processing procedures used (Figure 1.15a). MAPbI₃ thin films deposited via a conventional one-step spin-coating method¹⁰ (conventional) were a transparent brown color whereas MAPbI₃ thin films deposited via a fast deposition crystallization technique for which chlorobenzene was used as the antisolvent³⁹ (FDC (CB)) were a semi-transparent black color. These appearance differences can be explained by the superior surface coverage of MAPbI₃ on the underlying cTiO₂ layer when the FDC (CB) method is employed, which results in denser, smoother thin films than those deposited using the conventional method.

Differences in film morphology can be viewed in the plan-view SEM images in Figure 1.15b. Absorption spectra support the images in Figures 1.15a and 1.15b in that the absorption onset is sharper and the thin films absorb more light in the visible wavelength region (Figure 1.15c). The grazing-incidence XRD patterns shown in Figure 1.15d confirm crystallization of both thin films in the tetragonal phase (space group: I4/mcm, Z=4)⁵¹ and lattice constants are $a = b = 8.90 \text{ \AA}$, $c = 12.64 \text{ \AA}$. The MAPbI₃ (110) lattice plane corresponds to the most conductive carrier transport direction,⁵² and thus the (110) preferential orientation of the PbI₆ framework is beneficial to MAPbI₃ solar cell performance.⁵³ All peaks are attributable to MAPbI₃ perovskite except for the peak labeled with an asterisk at 12.8°, which corresponds to the (001) plane of PbI₂. This peak is slightly more prominent in the film processed by FDC (CB), which can be explained by partial solubility of MAPbI₃ to residual CB in the film during annealing, resulting in decomposition to

PbI₂. Therefore, the FDC method was the most successful method used to reproduce data of high-quality films from literature reports.

Complete perovskite PV devices adopting a wide range of architectures and processing conditions were fabricated and tested. Three promising devices, one of which had a novel architecture (device **2**), are shown in Table 1.1. For device **1**, MAPbI_{3-x}Cl_x was hot-cast on mAl₂O₃/cTiO₂/FTO as described in the experimental section (*1.2.2.2 Perovskite Deposition Methods*). Shortly thereafter, substrates were transferred into the glovebox for thermal evaporation of the gold top contact without deposition of a hole transport material. The best-performing cell of the device exhibited a PCE of 1.31 %. Device **2** has an architecture not previously reported in the literature. PEDOT:PSS was employed as a p-type HTM on top of the MAPbI₃ layer deposited via the FDC method. The best-performing cell of the device exhibited a PCE of 2.33 %. Device **3**, which featured an architecture of Au/spiro-OMeTAD/MAPbI_{3-x}Cl_x/mAl₂O₃/cTiO₂/FTO, produced the highest-efficiency cell of 2.53 %. Devices with the same architecture as device **3** but with mAl₂O₃ replaced by mTiO₂ did not perform as well. These observations are potentially due to faster recombination rates at the MAPbI₃-mTiO₂ interface than at the MAPbI₃-mAl₂O₃ interface.

Reverse-bias voltage sweeps of the best-performing cell of each device are displayed in Figure 1.16. Although the cell of device **3** had the lowest J_{SC} of the group of cells, it had the highest V_{OC} and FF. A non-zero slope in reverse bias (i.e. negative potentials) indicates the presence of shunts. Shunting can also occur when a device contains pinholes, which is an almost unavoidable issue for solution-processed materials. Most devices tested exhibited significant shunting, including devices **1** and **2**, due to a less-than-optimal device architecture. Device **3**, however, does not exhibit significant shunting, as the slope of the voltage sweep under reverse-bias conditions is nearly zero. This supports the SEM image shown in Figure 1.15b that indicates high surface

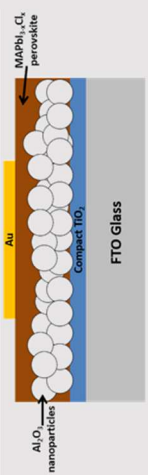
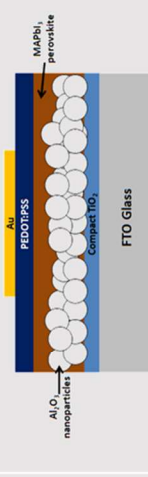
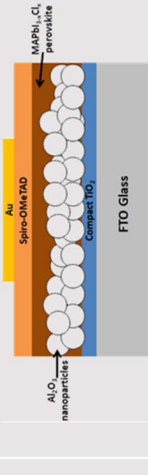
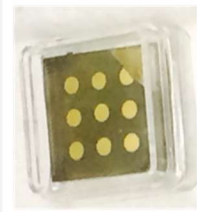


Device #	1	2	3
Architecture			
Deposition method	Hot-cast	FDC	FDC
V_{OC}	382 mV	556 mV	780 mV
I_{SC}	0.6885 mA	1.02 mA	0.945 mA
Area	0.085 cm ²	0.085 cm ²	0.15 cm ²
J_{SC}	8.1 mA cm ⁻²	12.0 mA cm ⁻²	6.3 mA cm ⁻²
FF	0.43	0.35	0.52
PCE	1.31 %	2.33 %	2.53 %
			

Table 1.1. Promising MAPbX₃ perovskite PV devices. Deposition method refers to how the perovskite layer is deposited, FDC = fast deposition crystallization, V_{OC} = open-circuit voltage, I_{SC} = short-circuit current, J_{SC} = short-circuit current density, FF = fill factor, PCE = power conversion efficiency.

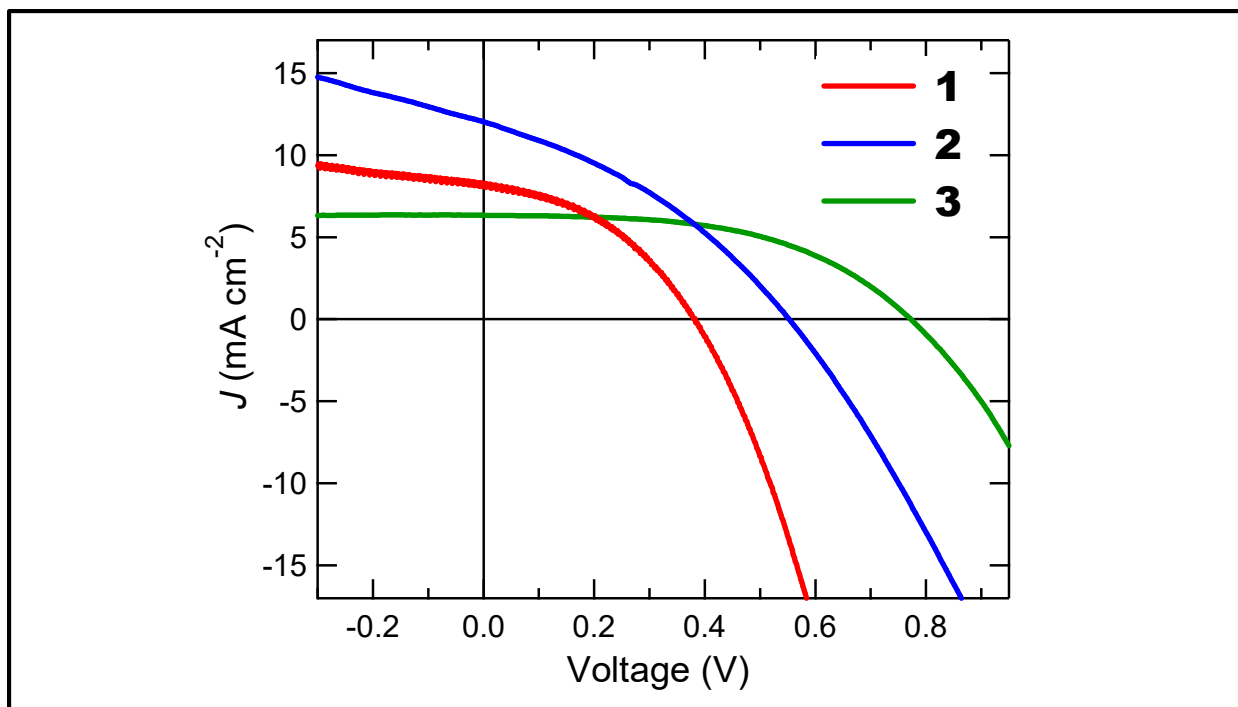


Figure 1.16. Reverse-bias voltage sweeps at 100 mV/s of the best-performing cells of devices **1**, **2**, and **3**.

coverage in the FDC-prepared MAPbI₃ film. Linear sloped behavior under large forward bias (i.e. positive potentials) indicates series resistance in the device, which is primarily due to material layer thicknesses that are too large. Some series resistance is unavoidable, due to the multilayer nature of the device by which charge-transfer resistances are present at each material layer interface.

Device **3** was further characterized by chronopotentiometry and chronoamperometry in order to determine the stability of V_{OC} and J_{SC} values over time under 1 sun illumination. Figure 1.17a and Figure 1.17b show V_{OC} and J_{SC} tracking, respectively. The V_{OC} of the cell exhibits a rapid onset and plateaus after ~ 1 min (Figure 1.17a). The J_{SC} , on the other hand continues to increase even after ~ 2 minutes (Figure 1.17b). For this reason, cells were light-soaked for 5 minutes prior to measurement of J - V characteristics in order to obtain stable photocurrent output from the cell.

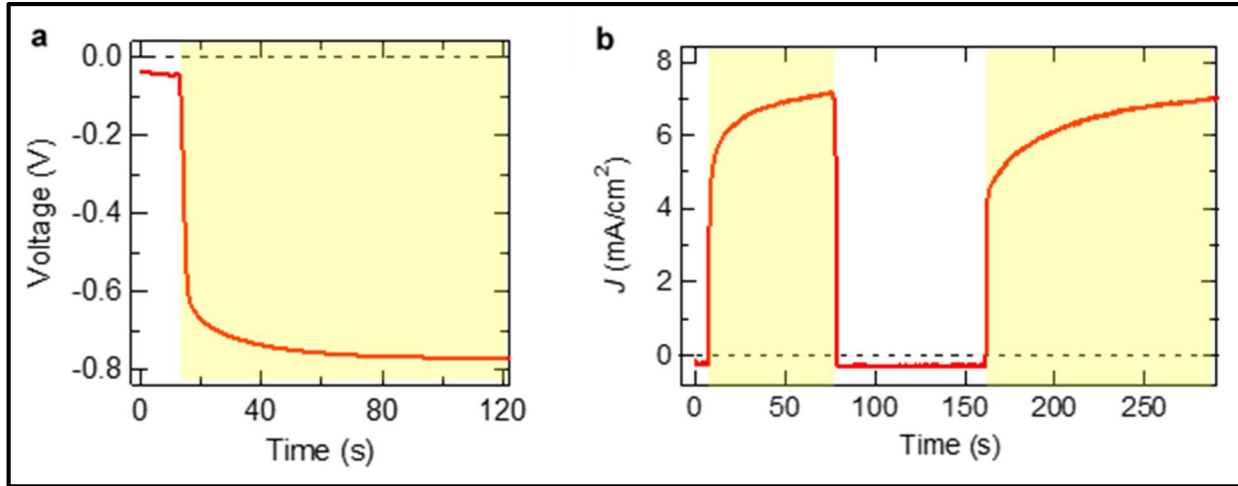


Figure 1.17. (a) Chronopotentiometry at open circuit and (b) chronoamperometry at short circuit (0 V vs. ref) of the best-performing perovskite cell of device **3**. Regions highlighted in yellow represent time when the cell was under illumination.

For perovskite PVs incorporating a mesostructured TiO₂ layer, it has been shown that recombination kinetics deviate from first order, which is attributed to a dominant trap-assisted recombination mechanism due to TiO₂ trap states.⁵⁴⁵⁵ This observed behavior was tested in perovskite PVs incorporating a mesostructured Al₂O₃ layer. Figure 1.18 shows the V_{OC} values of a PV cell with the architecture Au/PEDOT:PSS/MAPbI₃/mAl₂O₃/cTiO₂/FTO as a function of the natural log of light intensity, with light intensity ranging from 0.2 suns to 1 sun. As expected, the V_{OC} has a linear dependence to the natural log of the light intensity, with a slope of 35.2 mV. Because the slope is greater than kT/q , which is 26 mV at room temperature, this suggests that a component of recombination in the device is attributed to trap-assisted recombination, is the dominant recombination mechanism. which could be due to Al₂O₃ crystal impurities that form trap states in the Al₂O₃ layer.⁵⁶ The ideality factor (IF) of the device is $35.2 \text{ mV} / 26 \text{ mV} = 1.35$. An ideal pn-junction device has an IF of 1 and an ideal pin-junction device has an IF of 2.⁵⁷ An IF between 1 and 2 suggests hybrid behavior.

Light-intensity-dependent measurements presented in Figure 1.18. For data points corresponding to lower light intensity, the slope is closer to 26 mV (i.e. IF is closer to 1), and for

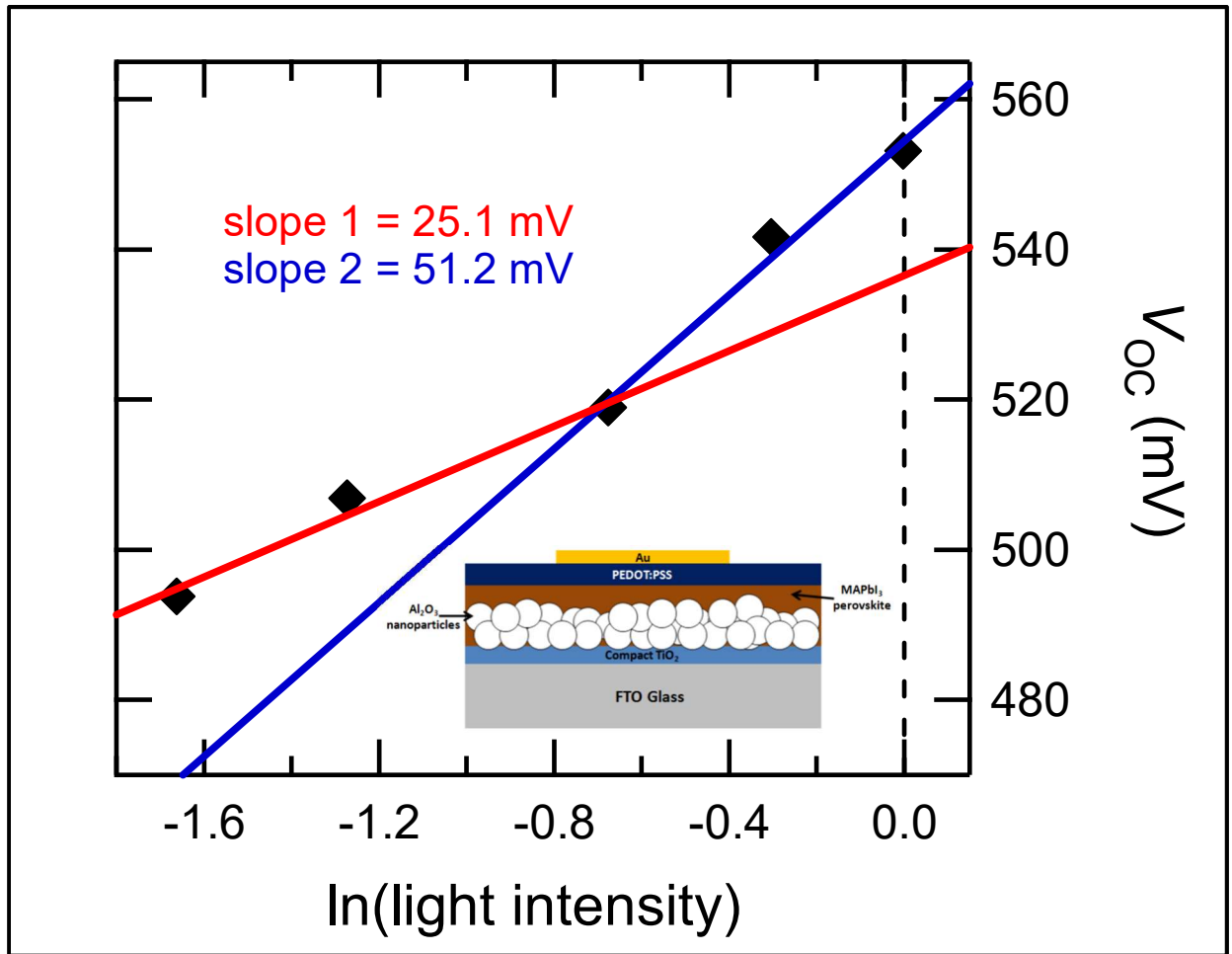


Figure 1.18. Light-intensity-dependent measurements of the open-circuit voltage of a PV device. Inset: architectural layout of the cell (Au/PEDOT:PSS/MAPbI₃/mAl₂O₃/cTiO₂/FTO).

data points corresponding to higher light intensity, the slope is closer to 52 mV (i.e. IF is closer to 2). This is expected for a lightly-doped material like MAPbI₃.⁵⁸ Under low light, the charge-carrier kinetics of a lightly-doped material were pseudo-first order, corresponding to an IF of ~ 1 , but under high light, the dark concentrations of electrons and holes are much lower than the concentrations of photogenerated electrons and holes, and therefore the kinetics were pseudo-second order, corresponding to an IF of ~ 2 .⁵⁷

1.4 Conclusions

A proof-of-concept demonstration of the use of a mercury drop as a top-contact electrode showed that liquid mercury forms an ohmic contact with PEDOT:PSS as gold does, meaning that a high-throughput experimental setup using liquid mercury would afford a reasonable low-cost method to evaluate individual PV device stacks. Cyclic voltammetry was employed to assess the hole-blocking effectiveness of different metal–oxide architectures commonly used in regular n–i–p perovskite PVs, from which it was determined that a slower spin-coat speed (2000 rpm with 2000 rpm/s acceleration) is the best method for depositing the compact TiO₂ blocking layer. The hybrid organic–inorganic material MAPbI₃, like the all-inorganic PbI₂, exhibits PL at the band edge, which suggests that MAPbI₃ has a small exciton binding energy that results in efficient free-carrier generation. From fluorescence lifetime confocal microscopy imaging data, it was conjectured that perovskite crystals present at the surface of the film are larger than crystallites within the mTiO₂ pores and these larger crystallites contribute to higher-intensity fluorescence.

The FDC method was the most successful method used to reproducibly fabricate high-quality thin films. Three promising devices, one of which had a particularly novel architecture in that it employed a layer of p-type PEDOT:PSS on top of the perovskite layer, boasted PCEs of > 1.3%. It was determined from light-intensity-dependent measurements that the MAPbI₃ thin film was lightly doped. The charge-carrier kinetics of a lightly-doped material were pseudo-first order under low light, but under high light, the dark concentrations of electrons and holes are much lower than the concentrations of photogenerated electrons and holes, and therefore the kinetics were pseudo-second order.

1.5 References

- (1) Perez, R.; Perez, M. *IEA/SHC Sol. Updat.* **2009**, *50*, 2–3.
- (2) SunShot Vision Study <http://energy.gov/eere/sunshot/sunshot-vision-study> (accessed Oct 25, 2015).
- (3) Zhang, S.; Yang, X.; Numata, Y.; Han, L. *Energy Environ. Sci.* **2013**, *6*, 1443.
- (4) SunShot 2030 Fact Sheet https://www.energy.gov/sites/prod/files/2016/12/f34/SunShot2030FactSheet-12_16.pdf (accessed May 28, 2018).
- (5) 2020 Utility-Scale Solar Goal Achieved <https://www.energy.gov/eere/solar/articles/2020-utility-scale-solar-goal-achieved> (accessed May 28, 2018).
- (6) Cui, J.; Yuan, H.; Li, J.; Xu, X.; Shen, Y.; Lin, H.; Wang, M. *Sci. Technol. Adv. Mater.* **2015**, *16*, 036004.
- (7) Sum, T. C.; Mathews, N. *Energy Environ. Sci.* **2014**, *7*, 2518–2534.
- (8) Song, Z.; McElvany, C. L.; Phillips, A. B.; Celik, I.; Krantz, P. W.; Waththage, S. C.; Liyanage, G. K.; Apul, D.; Heben, M. J. *Energy Environ. Sci.* **2017**, *10*, 1297–1305.
- (9) Kojima, A.; Teshima, K.; Shirai, Y.; Miyasaka, T. *J. Am. Chem. Soc.* **2009**, *131*, 6050–6051.
- (10) Lee, M. M.; Teuscher, J.; Miyasaka, T.; Murakami, T. N.; Snaith, H. J. *Science* **2012**, *338*, 643–647.
- (11) Research Cell Efficiency Records <https://www.energy.gov/eere/solar/downloads/research-cell-efficiency-records> (accessed May 28, 2018).
- (12) Yin, W.; Shi, T.; Yan, Y. *Adv. Mater.* **2014**, *26*, 4653–4658.
- (13) Saparov, B.; Mitzi, D. B. *Chem. Rev.* **2016**, *116*, 4558–4596.
- (14) Frost, J. M.; Butler, K. T.; Brivio, F.; Hendon, C. H.; van Schilfgaarde, M.; Walsh, A. *Nano*

- Lett.* **2014**, *14*, 2584–2590.
- (15) Slavney, A. H.; Smaha, R. W.; Smith, I. C.; Ja, A.; Umeyama, D.; Karunadasa, H. I. *Inorg. Chem.* **2017**, *56*, 46–55.
- (16) Cotton, F. A.; Wilkinson, G. *Advanced Inorganic Chemistry: A Comprehensive Text. Advanced Inorganic Chemistry*, 1972, 657–669.
- (17) Abate, A.; Paek, S.; Giordano, F.; Correa Baena, J. P.; Saliba, M.; Gao, P.; Matsui, T.; Ko, J.; Zakeeruddin, S. M.; Dahmen, K. H.; Hagfeldt, A.; Grätzel, M.; Mohammad K., N. *Energy Environ. Sci.* **2015**, *8*, 2946–2953.
- (18) Aristidou, N.; Sanchez-Molina, I.; Chotchuangchutchaval, T.; Brown, M.; Martinez, L.; Rath, T.; Haque, S. A. *Angew. Chem Int. Ed.* **2015**, *54*, 8208–8212.
- (19) Eames, C.; Frost, J. M.; Barnes, P. R. F.; O'Regan, B. C.; Walsh, A.; Islam, M. S. *Nat. Commun.* **2015**, *6*, 7497.
- (20) Liang, K.; Mitzi, D. B.; Prikas, M. T. *Chem. Mater.* **1998**, *10*, 403–411.
- (21) Mitzi, D. B.; Chondroudis, K.; Kagan, C. R. *Inorg. Chem.* **1999**, *38*, 6246–6256.
- (22) Mitzi, D. B. *Inorg. Chem.* **2000**, *39*, 6107–6113.
- (23) Smith, I. C.; Hoke, E. T.; Solis-Ibarra, D.; McGehee, M. D.; Karunadasa, H. I. *Angew. Chemie - Int. Ed.* **2014**, *53*, 11232–11235.
- (24) Cao, D.; Stoumpos, C. C.; Farha, O. K.; Hupp, J. T.; Kanatzidis, M. G. *J. Am. Chem. Soc.* **2015**, *137*, 7843–7850.
- (25) Meng, L.; You, J.; Guo, T.-F. F.; Yang, Y. *Acc. Chem. Res.* **2015**, *49*, acs.accounts.5b00404.
- (26) You, J.; Yang, Y. (Michael); Hong, Z.; Song, T.; Meng, L.; Liu, Y.; Jiang, C.; You, J.; Yang, Y. M.; Hong, Z.; Song, T.; Meng, L. *Appl. Phys. Lett.* **2014**, *105*, 183902.
- (27) Ye, S.; Rao, H.; Zhao, Z.; Zhang, L.; Bao, H.; Sun, W.; Li, Y.; Gu, F.; Wang, J.; Liu, Z.;

- Bian, Z.; Huang, C. *J. Am. Chem. Soc.* **2017**, *139*, 7504–7512.
- (28) Seok, S. I.; Grätzel, M.; Park, N.-G. *Small* **2018**, 1704177.
- (29) Burschka, J.; Pellet, N.; Moon, S.-J.; Humphry-Baker, R.; Gao, P.; Nazeeruddin, M. K.; Grätzel, M. *Nature* **2013**, *499*, 316–319.
- (30) Liu, M.; Johnston, M. B.; Snaith, H. J. *Nature* **2013**, *501*, 395–398.
- (31) Zhang, C.; Luo, Y.; Chen, X.; Ou-yang, W.; Chen, Y.; Sun, Z. *Appl. Surf. Sci.* **2016**, *388*, 82–88.
- (32) Heo, J. H.; Im, S. H.; Noh, J. H.; Mandal, T. N.; Lim, C.; Chang, J. A.; Lee, Y. H.; Kim, H.; Sarkar, A.; Nazeeruddin, K.; Gra, M. *Nat. Photonics* **2013**, 1–6.
- (33) Dualeh, A.; Moehl, T.; Tétreault, N.; Teuscher, J.; Gao, P.; Nazeeruddin, M. K.; Grätzel, M. *ACS Nano* **2014**, *8*, 362–373.
- (34) Leijtens, T.; Eperon, G. E.; Noel, N. K.; Habisreutinger, S. N.; Petrozza, A.; Snaith, H. J. *Adv. Energy Mater.* **2015**, *5*, 1500963.
- (35) Green, M. A.; Hishikawa, Y.; Dunlop, E. D.; Levi, D. H.; Hohl-Ebinger, J.; Ho-Baillie, A. W. Y. *Prog. Photovoltaics Res. Appl.* **2018**, *26*, 3–12.
- (36) Eperon, G. E.; Burlakov, V. M.; Docampo, P.; Goriely, A.; Snaith, H. J. *Adv. Funct. Mater.* **2014**, *24*, 151–157.
- (37) Ito, S.; Murakami, T. N.; Comte, P.; Liska, P.; Grätzel, C.; Nazeeruddin, M. K.; Grätzel, M. *Thin Solid Films* **2008**, *516*, 4613–4619.
- (38) Yella, A.; Heiniger, L. P.; Gao, P.; Nazeeruddin, M. K.; Grätzel, M. *Nano Lett.* **2014**, *14*, 2591–2596.
- (39) Xiao, M.; Huang, F.; Huang, W.; Dkhissi, Y.; Zhu, Y.; Etheridge, J.; Gray-Weale, A.; Bach, U.; Cheng, Y.-B.; Spiccia, L. *Angew. Chemie - Int. Ed.* **2014**, *126*, 10056–10061.

- (40) Burschka, J.; Pellet, N.; Moon, S.-J.; Humphry-Baker, R.; Gao, P.; Nazeeruddin, M. K.; Grätzel, M. *Nature* **2013**, *499*, 316–319.
- (41) Hao, F.; Stoumpos, C. C.; Liu, Z.; Chang, R. P. H.; Kanatzidis, M. G. *J. Am. Chem. Soc.* **2014**, *136*, 16411–16419.
- (42) Chen, Q.; Zhou, H.; Hong, Z.; Luo, S.; Duan, H.-S.; Wang, H.-H.; Liu, Y.; Li, G.; Yang, Y. *J. Am. Chem. Soc.* **2014**, *136*, 622–625.
- (43) Nie, W.; Tsai, H.; Asadpour, R.; Blancon, J.; Neukirch, A. J.; Gupta, G.; Crochet, J. J.; Chhowalla, M.; Tretiak, S.; Alam, M. A.; Wang, H.; Mohite, A. D. *Science* **2015**, *347*, 522–525.
- (44) Gagne, R. R.; Koval, C. A.; Lisensky, G. C. *Inorg. Chem.* **1980**, *19*, 2854–2855.
- (45) D’Innocenzo, V.; Grancini, G.; Alcocer, M. J. P.; Kandada, A. R. S.; Stranks, S. D.; Lee, M. M.; Lanzani, G.; Snaith, H. J.; Petrozza, A. *Nat. Commun.* **2014**, *5*, 1–6.
- (46) Yamada, T.; Aharen, T.; Kanemitsu, Y. *Phys. Rev. Lett.* **2018**, *120*, 57404.
- (47) DeQuilettes, D. W.; Koch, S.; Burke, S.; Paranjli, R. K.; Shropshire, A. J.; Ziffer, M. E.; Ginger, D. S. *ACS Energy Lett.* **2016**, *1*, 438–444.
- (48) Wen, X.; Sheng, R.; Ho-baillie, A. W. Y.; Benda, A.; Woo, S.; Ma, Q.; Huang, S.; Green, M. A. *J. Phys. Chem. Lett.* **2014**, *5*, 3849–3853.
- (49) DeQuilettes, D. W.; Vorpahl, S. M.; Stranks, S. D.; Nagaoka, H.; Eperon, G. E.; Ziffer, M. E.; Snaith, H. J.; Ginger, D. S. *Science* **2015**, *348*, 683–686.
- (50) Agarwal, S.; Nair, P. R. *J. Appl. Phys.* **2017**, *122*.
- (51) Amat, A.; Mosconi, E.; Ronca, E.; Quarti, C.; Umari, P.; Nazeeruddin, M. K.; Grätzel, M.; De Angelis, F. *Nano Lett.* **2014**.
- (52) Ishii, A.; Jena, A. K.; Miyasaka, T. *APL Mater.* **2014**, *2*, 091102.

- (53) Docampo, P.; Hanusch, F. C.; Giesbrecht, N.; Angloher, P.; Ivanova, A.; Bein, T. *APL Mater.* **2014**, *2*.
- (54) Bi, D.; Yang, L.; Boschloo, G.; Hagfeldt, A.; Johansson, E. M. J. *J. Phys. Chem. Lett.* **2013**, *4*, 1532–1536.
- (55) Bi, D.; Moon, S.-J.; Häggman, L.; Boschloo, G.; Yang, L.; Johansson, E. M. J.; Nazeeruddin, M. K.; Grätzel, M.; Hagfeldt, A. *RSC Adv.* **2013**, *3*, 18762–18766.
- (56) Sherkar, T. S.; Momblona, C.; Avila, J.; Sessolo, M.; Bolink, H. J.; Koster, L. J. A. *ACS Energy Lett.* **2017**, *2*, 1214–1222.
- (57) Sze, S. M.; Ng, K. K. *Physics of Semiconductor Devices*; 3rd ed.; Wiley: Hoboken, 2007.
- (58) Laban, W. A.; Etgar, L. *Energy Environ. Sci.* **2013**, *6*, 3249.

CHAPTER 2: HYBRID ORGANIC–INORGANIC PHOTOVOLTAICS BASED ON BISMUTH IODIDE AND 1,6-HEXANEDIAMMONIUM DICATION

** In part a compilation of one publication¹*

2.1 Introduction

Lead–halide perovskite (APbX_3) photovoltaics offer a potential low-cost alternative to established silicon photovoltaic technologies, as most of the components can be deposited from solution using conventional spin-coating methods.^{2,3} However, issues with lead toxicity and APbX_3 instability remain at the forefront of current research. Though the lead component in the perovskite material is earth-abundant, lead halides are considered probable carcinogens, and due to their moderate solubility in water, lead halides could potentially leach into water supplies, which would deter use of APbX_3 photovoltaics.⁴ Moreover, alkylammonium halide (AX) dissociates into HX and alkylamine (A) which are both particularly volatile, and thus APbX_3 films degrade in humid or high-temperature conditions, leaving behind a film of PbX_2 .⁵ Lastly, many APbX_3 photovoltaic architectures suffer from hysteresis during cyclic voltammetry measurements, which has resulted in inaccurate and typically inflated efficiency values.^{4,6}

These undesired properties of APbX_3 motivate the investigation of a replacement for lead that would allow for equally as inexpensive and more environmentally benign photovoltaics, assuming they exhibit similar favorable optoelectronic properties. APbX_3 materials feature a three-dimensional lattice of lead halide that participates in charge-carrier conduction,⁷ and small monocationic alkylammonium groups that occupy the cavities of the lead iodide lattice, which have been suggested to result in slow charge-carrier recombination.⁸ Although studies on APbX_3 materials for solar cell applications were first published in 2009,⁹ the more general class of hybrid

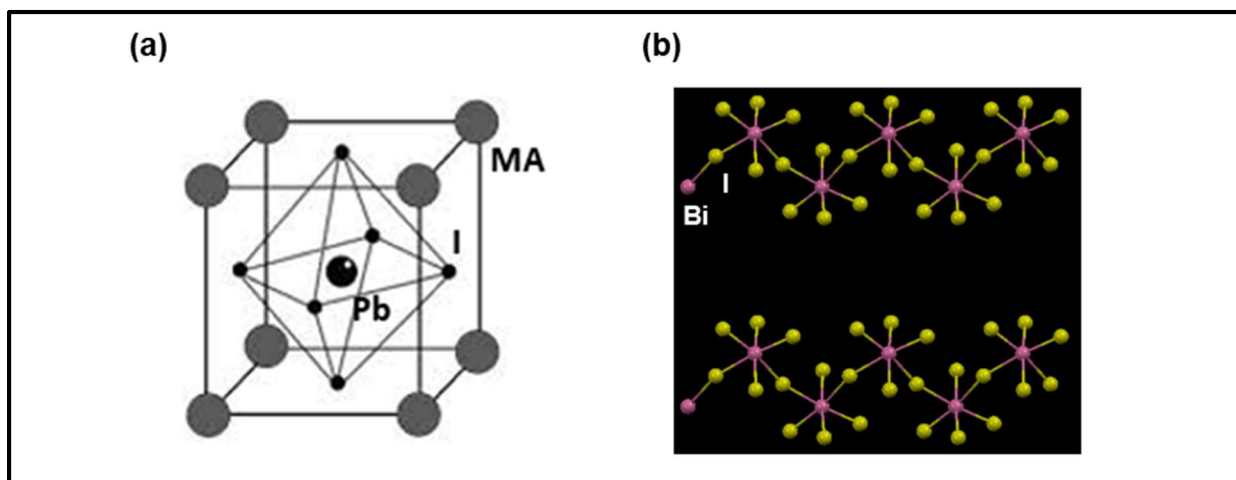


Figure 2.1. (a) The unit cell of lead-based organic–inorganic hybrid perovskite MAPbI₃. Reproduced from Cheng, Z.; Lin, J. *CrystEngComm* **2010**, *12*, 2646–2662 with permission of The Royal Society of Chemistry. (b) Crystal structure of the inorganic framework of a bismuth-based organic–inorganic hybrid material, from the top-down view (top) and side view (bottom).

organic–inorganic materials, which range from zero-dimensional to three-dimensional systems, had been investigated for years before intense study began on three-dimensional APbX₃-based systems.^{10–12} For example, since the late 1990s, bismuth-containing hybrid organic–inorganic materials have shown potential as semiconductors and are candidates for optoelectronic devices.^{11–17} In 1998, Mousdis et al. reported a crystal structure for HDABiI₅ (where bismuth is in the 3+ oxidation state and HDA²⁺ = 1,6-hexanediammonium, [H₃NC₆H₁₂NH₃]²⁺), but this group never investigated HDABiI₅ as a photoactive material in solar cells. This discovery is analogous to that of MAPbI₃ (where MA⁺ is the methylammonium cation), which was first discovered by Mitzi and colleagues in 1998 but only recently was used in solar cells that today achieve > 20% efficiency.^{18,19}

Figure 2.1 depicts differences in the crystal structures of lead-based (Figure 2.1a) and bismuth-based (Figure 2.1b) organic–inorganic hybrid materials.^{20,21} In lead-based MAPbI₃ the lead iodide network forms a lattice in three dimensions, whereas for the bismuth-based materials the bismuth–iodide network forms chains that extend in one dimension (shown in Figure 2.1b) or

binuclear clusters that render the material zero-dimensional. If a small dicationic organic group is incorporated into the structure, it is hypothesized that the chains may be close enough to each other to provide long-range charge transport in three dimensions similar to that observed in MAPbI₃.

Dicationic alkyldiammonium bismuth–halide materials like HDABiI₅ are noteworthy because of reported single-crystal structural resolution, thin-film X-ray diffraction (XRD) patterns that suggest preferred crystal orientation, and electronic absorption spectra that suggest an optical bandgap of ~2.0 eV.^{11,13} Unlike the three-dimensional lead–halide lattice that forms in APbX₃, the metal–halide network of dicationic alkyldiammonium bismuth–halide materials is composed of one-dimensional zig-zag chains of distorted BiX₆ octahedra,¹¹ and it has been suggested that the role of the organic groups is to serve as molecular fasteners.²² Moreover, Bi³⁺ is the only stable and nontoxic cation with the same 6s²6p⁰ electronic configuration as Pb²⁺, which is important because the favorable electronic properties of APbX₃ materials, such as long carrier lifetimes and shallow trap states, are in part due to the contributions of Pb²⁺ to both the conduction band (6p orbitals) and valence band (6s orbitals).^{23,24} While Mousdis et al. and Mitzi et al. have previously synthesized and crystallographically characterized HDABiI₅,^{11,13} analysis of photovoltaic performance when incorporated as the photoactive layer in a solar cell has not previously been presented, thus motivating the work presented herein.

Recently, zero-dimensional (0D) A₃Bi₂I₉ perovskite-like materials, where the A groups are MA⁺, K⁺, Rb⁺, or Cs⁺, have been examined as lead-free candidate solar absorbers that were stable in humid air and were shown to exhibit excited-state lifetimes on the order of nanoseconds.^{25–28} Notably, a solar cell incorporating 0D Cs₃Bi₂I₉ with an efficiency exceeding 1 % was reported.²⁸ Moreover, the all-inorganic BiI₃ was synthesized with phase purity and exhibited photoluminescence, but no solar cells were fabricated.²⁹ In a separate study a year later,

Hamdeh and colleagues reported a BiI₃ solar cell with an efficiency just over 1 %.³⁰ A Bi-containing double perovskite, Cs₂AgBiBr₆, has been reported to be more heat-stable and moisture-stable than APbX₃, which then led to the synthesis and computational design of novel families of double perovskites, Cs₂BiMX₆ and Cs₂SbMX₆, where M = Cu, Ag, or Au. These materials exhibited high conductivities and tunable band gaps in the visible range.³¹ These observations suggest that lower-dimensional dication-containing Bi-halide hybrid materials warrant further investigation.

The presence of a well-defined crystal structure that includes organic groups of varying size allows a unique opportunity to tune transport intra-chain in one-dimensional bismuth-halide materials. This strategy has been employed in a somewhat related application to fabricate superlattices of quantum dots for electronics and solar cell applications.^{32,33} However, there are many differences in the strategy for quantum dots (versus for the hybrid organic-inorganic materials described herein): (i) each quantum dot is a separate crystallite with poor-defined surface termination to the organic linkers, (ii) most times single organic linkers are not thought to bridge individual quantum dots but form clusters of organic groups between the quantum dots,³⁴ (iii) there is poor order in quantum dot films because the organic linker is not considered crystalline, (iv) quantum dots do not bind well to metal-oxide layers without intentionally introducing linkers between them, and (v) overall photovoltaic performance is often inhibited due to surface trap states being responsible for rapid recombination.³⁵ In hybrid organic-inorganic materials, the organic group is innately incorporated as part of the crystallite and is therefore directed anisotropically, which provides unique opportunities to carefully and controllably tune the ability for charges to transport between individual chains. In this regard, the bandgap, the conductivity, moisture stability and ultimately, device performance can be varied by modifying the nature of the organic

groups, and the strength of the intra-crystallite and inter-crystallite electronic interactions.³⁶ With the use of relatively small dications, it is hypothesized that these properties will be most optimized.

2.2 Experimental

2.2.1 Preparation of MAPbI₃ and HDABiI₅ Solutions

All chemicals were used as received. Methylammonium iodide (MAI) was synthesized by slow addition of 6.5 mL of hydriodic acid (47% in water, stabilized with 1.5% hypophosphorous acid, Sigma-Aldrich) at room temperature to 6 mL of methylamine (40 wt. % in methanol, TCI America) at 0 °C with stirring, followed by continued stirring for 1 hr. MAI precipitate was recovered by evaporation of solvents at 50 °C with a rotary evaporator. To purify MAI, the precipitate was dissolved in ethanol, recrystallized from diethyl ether, and finally vacuum dried at 60 °C for 12 h. MAPbI₃ solution was then prepared by mixing MAI and PbI₂ (99%, Sigma-Aldrich) powders at approximately a 1:1 mole ratio, but with MAI in slight excess, in anhydrous *N,N*-dimethylformamide (DMF) at 70 °C inside a nitrogen-filled glovebox. The MAPbI₃ solution was stored in the glovebox until use and was used within one week of preparation.

To synthesize 1,6-hexanediamine dihydriodide (HDA•2HI), 260.9 mg of 1,6-hexanediamine (98+%, Alfa Aesar) was dissolved in 5 mL methanol, and then 1 mL hydriodic acid was added slowly at 0 °C with stirring, followed by stirring for an additional 30 min. HDA•2HI precipitate was recovered by evaporation of solvents at 40 °C with a rotary evaporator. The precipitate was rinsed with diethyl ether, and vacuum dried at 60 °C for 12 h. HDABiI₅ solution was then prepared by mixing HDA•2HI and BiI₃ (99%, Sigma-Aldrich) powders at an approximately 1:1 mole ratio, but with HDA•2HI in slight excess, in anhydrous DMF at 70 °C

inside a nitrogen-filled glovebox. The HDABiI₅ solution was stored in the glovebox until use and was used within one week of preparation.

2.2.2 Materials Processing

All steps of materials deposition and device fabrication were performed in air with 40–60% relative humidity and as described below, unless noted otherwise. All thermal treatments were performed using a hot plate. Fluorine-doped tin oxide coated glass (FTO) substrates were cleaned as follows: 1) sonication in Alconox solution, 2) rinse with deionized water, 3) rinse with ethanol, 4) sonication in ethanol, and 5) dry with nitrogen. A compact TiO₂ (cTiO₂) layer was deposited by pipetting a solution of titanium diisopropoxide bis(acetylacetonate) on a cleaned FTO substrate and then the substrate was spun at 2000 rpm (2000 rpm/s acceleration) for 60 s. The substrate was subsequently dried at 125 °C and then sintered at 550 °C for 30 min. Nanoparticles of TiO₂ were synthesized following a procedure by Ito et al.³⁷ The nanoparticle solution was further diluted in ethanol at a ratio of 1:3.5 TiO₂ nanoparticle solution:ethanol, w/w to make a mesoporous TiO₂ (mTiO₂) suspension. The mTiO₂ layer was deposited by spin coating this solution at 500 rpm (500 rpm/s acceleration) for 5 s and then 5000 rpm (5000 rpm/s acceleration) for 25 s, followed by drying at 125 °C, and then sintering at 550 °C for 30 min. The substrates were allowed to cool to room temperature. Unless otherwise noted, a conventional spin-coat deposition method was adapted from Kim et al.³⁸ and used for both MAPbI₃ and HDABiI₅. For this method, a filtered MAPbI₃ or HDABiI₅ solution in DMF was pipetted on top of the mTiO₂-coated FTO substrate and then the substrate was spun at 2000 rpm (2000 rpm/s acceleration) for 60 s, followed by rapid transfer to a hot plate that was preheated to 100 °C and subsequent annealing at 100 °C for 30 min.

Other procedures for depositing the photoactive layer (i.e. MAPbI₃ or HDABiI₅) that have been tested include a fast-deposition crystallization (FDC) method, a hot-casting method, and a “drop-heat-spin” (DHS) method that was pioneered as part of the work presented herein. All deposition procedures are described in the experimental section of Chapter 1 (*1.2.2.2 Perovskite Deposition Methods*) except the DHS method. For the DHS method, a substrate was placed on a hot plate set at 70 °C and the substrate was allowed to reach thermal equilibrium with the hot plate. A solution containing the precursors for the photoactive layer was kept at 70 °C during that time. The solution was dispensed on the substrate at a volume of 17.5 μA/cm² and the dispensed solution was heated on the substrate at 70 °C for 2 min. Then, the substrate was quickly transferred to a spin coater and spun at 3000 rpm (3000 rpm/s acceleration) for 60 s. The resulting film was annealed at 100 °C for 60 min.

2.2.3 Device Fabrication

Prior to the FTO cleaning step, a region of the FTO film was etched using 2 M HCl and Zn powder in order to prevent device shunting upon contact to the device top Au electrode. After performing the cleaning steps listed above (*Materials Processing* subsection), FTO substrates were further cleaned using an O₂ plasma treatment for 10 min. Following deposition of HDABiI₅ per the protocol described above (*Materials Processing* subsection), a 50 mM solution of 2,2',7,7'-tetrakis(*N,N'*-di-*p*-methoxyphenylamine)-9,9'-spirobifluorene (spiro-OMeTAD) dissolved in chlorobenzene with additives of 17.5 μL 4-*tert*-butylpyridine and 37.5 μL lithium bis(trifluoromethane)sulfonimide in acetonitrile (170 mg/mL) was deposited by spin coating at 3000 rpm (3000 rpm/s acceleration) for 60 s. The devices were then transferred into a nitrogen-filled glovebox and 80 nm of Au was thermally evaporated onto the devices at a base pressure of

5×10^{-6} mbar. The complete devices had an architecture of Au/spiro-OMeTAD/HDABiI₅/mTiO₂/cTiO₂/FTO.

2.2.4 Thermal Stability Tests

Thermal stability tests were performed in air for MAPbI₃ and HDABiI₅ thin films deposited on mTiO₂/cTiO₂/FTO per the protocols above (Materials Processing and Device Fabrication subsections). Then, a transmission-mode ultraviolet–visible (UV–Vis) optical absorption spectrum was acquired. The hot plate temperature was raised from the processing temperature (100 °C) in 20 °C increments and held at each temperature for 10 min, up to 200 °C. After each temperature treatment step, a UV–Vis absorption spectrum was acquired. For the HDABiI₅ thin film (Figure 4a), the temperature was raised in a final step to 300 °C and held for 10 min, followed by acquisition of a UV–Vis absorption spectrum.

2.2.5 Characterization

UV–Vis absorption measurements were carried out using an Agilent Cary 60 spectrophotometer. Tauc plots were constructed from measured UV–Vis spectra. Spectra were baseline-subtracted for long-wavelength scattering, and bandgap energies were determined from best-fit lines of the data near the absorption onset. Scanning electron microscopy (SEM) images were acquired on a FEI Magellan 400L XHR using 15 kV accelerating voltage and 0.8 nA beam current. Grazing-incidence X-ray diffraction (XRD) data were collected using a Rigaku Smartlab diffractometer with Cu K_α radiation and in parallel beam geometry. X-ray photoelectron spectroscopy (XPS) measurements and ultraviolet photoelectron spectroscopy (UPS) measurements were performed using a Kratos AXIS Supra photoelectron spectrometer using Al

K_{α} radiation. For XPS measurements, two separate spots on the sample were evaluated to confirm matching peak intensities for binding energy scans of C 1s, N 1s, Bi 4f, I 3d, Ti 2p, and O 1s. XPS data were analyzed using CasaXPS Processing Software and the peaks were fit to Gaussian–Lorentzian (80/20) curves. UPS measurements were performed with an unfiltered He I (21.22 eV) gas discharge lamp, and Fermi edge calibration was performed with a sputter-cleaned Ag standard to ensure that all energies were referenced to a common Fermi level (0 eV). SEM, grazing-incidence XRD, XPS, and UPS work was performed in the UC Irvine Materials Research Institute (IMRI).

An ELH-type W–halogen lamp was used inside a nitrogen-filled glovebox as a source of simulated solar illumination. Before measurement of device J – E behavior and chronoamperometry, the light intensity was roughly approximated to be 1 Sun using a calibrated Si photodiode (ThorLabs, Inc., FDS100) positioned at the location of the device. Based on the integrated photocurrent of devices determined from the product of the incident-photon-to-current efficiency (IPCE) values and the air mass 1.5 global (AM1.5G) solar photon flux spectrum at 1 Sun intensity, however, the simulated solar illumination for measurement of J – E behavior and chronoamperometry was more accurately determined to be 0.8 Suns (i.e. the steady-state photocurrent density measured by the ELH lamp was 0.115 mA/cm^2 , and the integrated photocurrent density measured by the IPCE setup was 0.143 mA/cm^2 , and so $0.115 / 0.143 = 0.8$). Cyclic voltammetry measurements (at a scan rate of 100 mV s^{-1}) and chronoamperometry measurements were performed using a Gamry Reference 600 Potentiostat. The diode quality factor of a device was measured by evaluating the dependence of the open-circuit photovoltage on light intensity. The light intensity was varied by adjusting the position of the lamp source with respect to the position of the tested device. The data were fit to the Shockley diode equation by the method

of least squares and the diode quality factor was determined to be ~ 1.3 . IPCE action spectra were determined using a Cornerstone 260 monochromator equipped with a 100 W APEX2 Xe arc lamp, and an NREL-calibrated Si solar cell as the reference.

2.3 Results & Discussion

It has been demonstrated that issues of stability and conductivity can in part be mitigated through use of new photovoltaic bismuth–halide “perovskite-like” materials that specifically incorporate organic dications within their crystallites. These materials are considered “perovskite-like” because, like perovskites, they are hybrid organic–inorganic materials, but the materials do not adopt the perovskite structure. More details on the implications of this classification are provided in Chapter 3. HDABiI₅ was determined out of a library of hybrid organic–inorganic

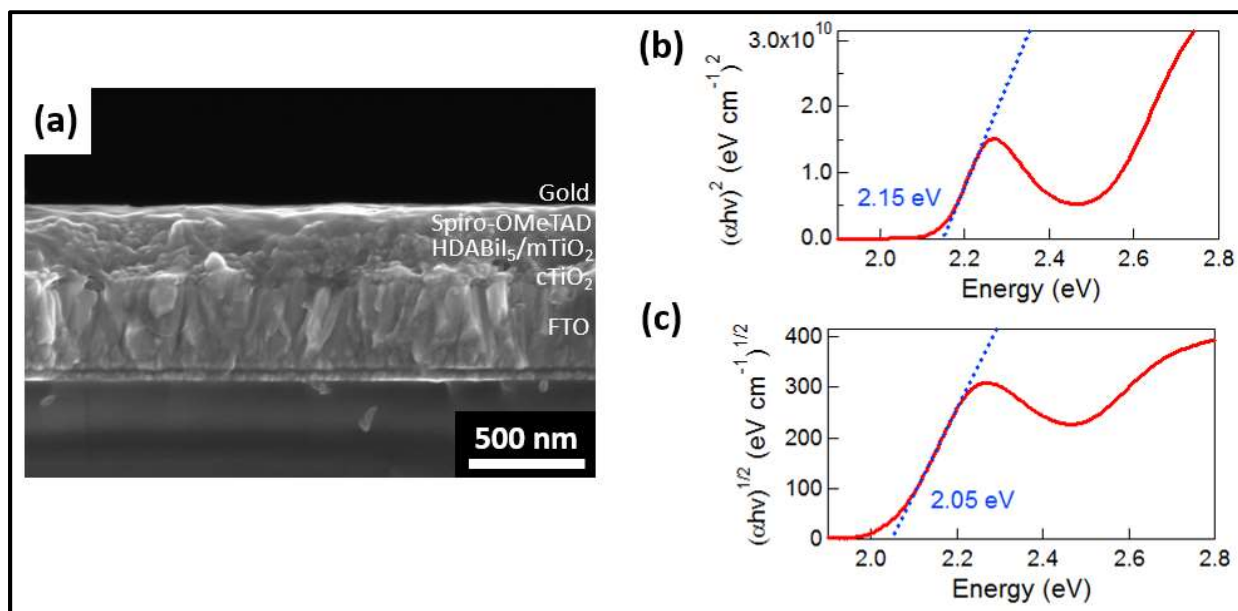


Figure 2.2. (a) Cross-sectional scanning electron microscopy image of a representative HDABiI₅ device, and (b) direct-bandgap and (c) indirect-bandgap Tauc plots of HDABiI₅ deposited as thin films on FTO, and baseline corrected for the FTO substrate. D. M. Fabian and S. Ardo, *J. Mater. Chem. A*, 2016, **4**, 6837 – Reproduced by permission of The Royal Society of Chemistry

bismuth–halide materials containing organic dications to be the ideal material candidate of its class for PV use in terms of closest-to-ideal bandgap and high crystal quality when cast as a thin film.

Scanning electron microscopy (SEM) images of a cross section of a complete HDABiI₅ device revealed that the HDABiI₅-coated mesoporous TiO₂ nanoparticle layer (HDABiI₅/mTiO₂) was 200–250 nm thick (Figure 2.2a), which is comparable to the thickness of state-of-the-art mesostructured perovskite solar cells.³⁹ Top-down SEM images (Figure 2.2a) showed crystal morphology and near-complete surface coverage of mTiO₂ by HDABiI₅. The majority of HDABiI₅ crystal grains appeared to range in size between 200 nm and 400 nm with no preferential orientation in the plane of the deposited film. Also, HDABiI₅ covered the mTiO₂ layer to a greater extent than APbX₃ processed by the same method (Figure 2.3). The transmission-mode ultraviolet–visible (UV–Vis) absorption spectrum of an HDABiI₅ thin film displayed as Tauc plots are shown in Figure 2.2b and 2.2c and both suggest that the optical bandgap of HDABiI₅ is ~2.1 eV with a lowest-energy indirect transition of 2.05 eV and a lowest-energy direct transition of 2.15 eV.

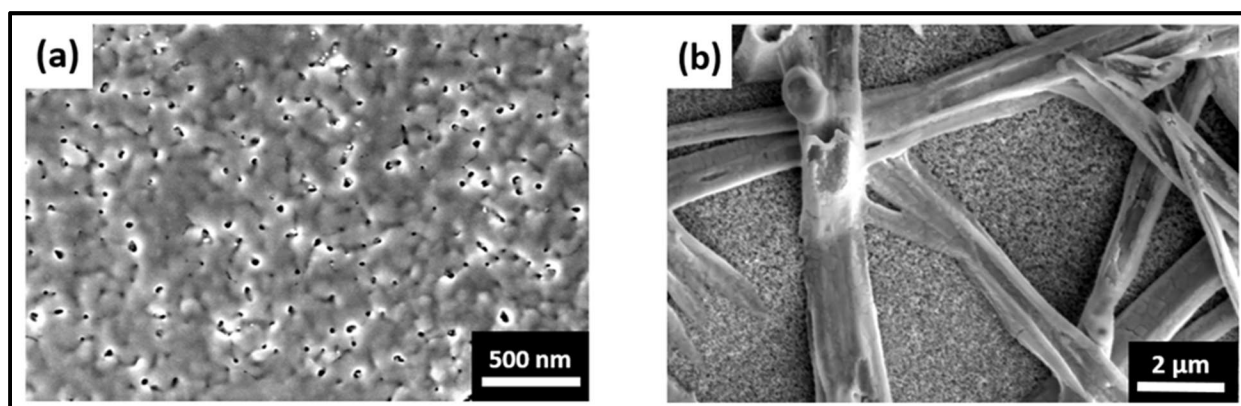


Figure 2.3. Top-view scanning electron microscopy image of (a) HDABiI₅ and (b) MAPbI₃ deposited on mTiO₂/cTiO₂/FTO. Overall surface coverage of MAPbI₃ on mTiO₂ is poor compared to that of HDABiI₅ on mTiO₂. D. M. Fabian and S. Ardo, *J. Mater. Chem. A*, 2016, **4**, 6837 – Reproduced by permission of The Royal Society of Chemistry

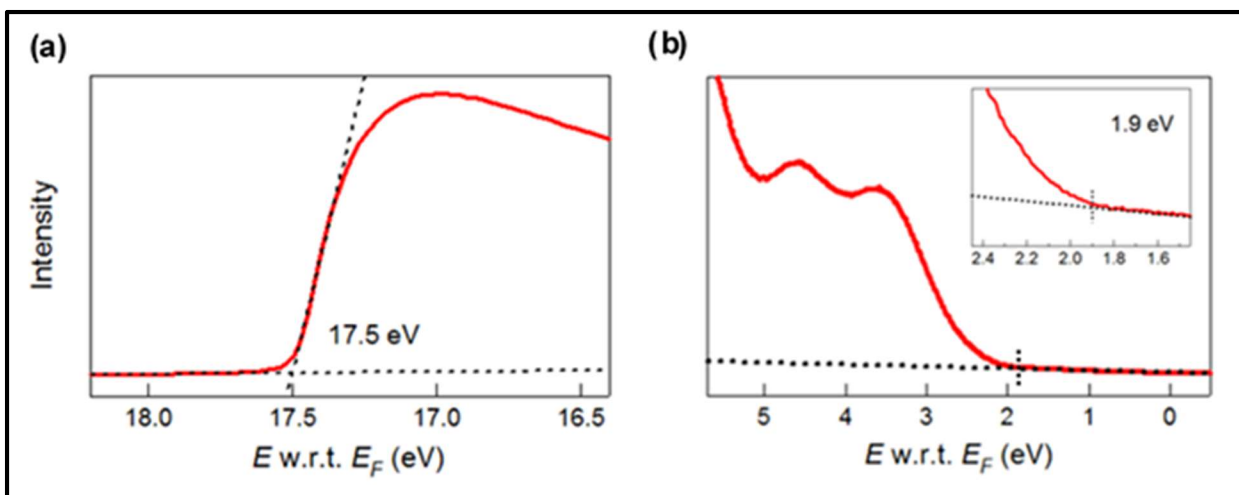


Figure 2.4. Ultraviolet photoemission spectra (He I) of HDABi₅/FTO for direct determination of the (a) work function and (b) valence-band maximum. D. M. Fabian and S. Ardo, *J. Mater. Chem. A*, 2016, **4**, 6837 – Reproduced by permission of The Royal Society of Chemistry

Information on the electronic band structure of HDABi₅ was elucidated from ultraviolet photoemission spectroscopy (UPS) measurements (Figure 2.4). The work function and valence band maximum were measured to be approximately -3.7 ± 0.1 eV and -5.6 ± 0.2 eV *versus* vacuum, respectively. The work function was calculated by subtracting the high-binding-energy cutoff at 17.5 eV (Figure 2.4a) from the He I radiation energy of 21.2 eV ($17.5 (\pm 0.1)$ eV $- 21.2$ eV = -3.7 ± 0.1 eV *versus* vacuum). In a similar manner performed by Schulz et al. for a bare MAPbI₃ surface,⁴⁰ the low-energy tail of the UPS spectrum was used to determine the position of the VBM as 1.9 ± 0.1 eV below the Fermi level (Figure 2.4b), and therefore the VBM was calculated to be $-3.7 (\pm 0.1)$ eV $- 1.9 (\pm 0.1)$ eV = -5.6 ± 0.2 eV *versus* vacuum. Considering the calculated optical bandgap of ~ 2.1 eV (Figure 2.2b and 2.2c), the conduction band minimum is therefore approximately -3.5 eV *versus* vacuum. It is evident, therefore, that the Fermi level of HDABi₅ lies close to the conduction band and signifying that HDABi₅ is an n-type semiconductor.

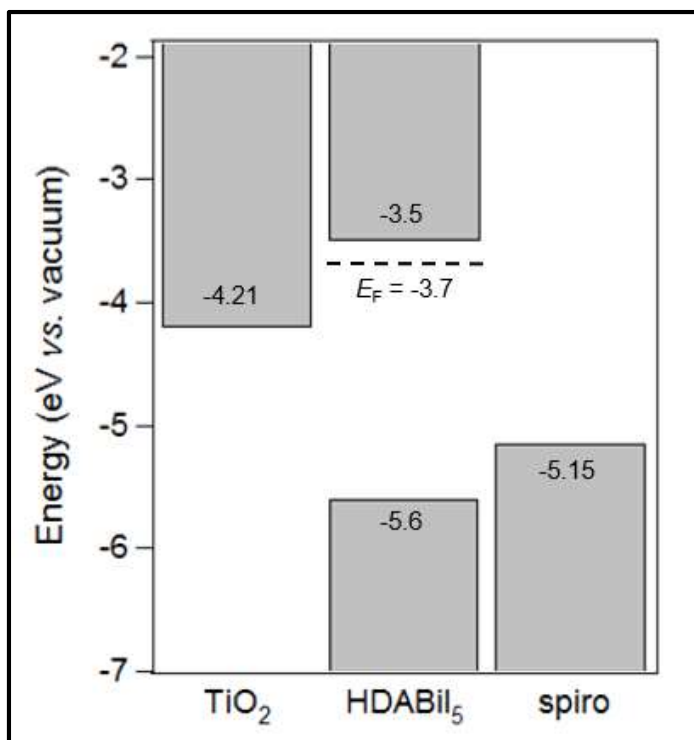


Figure 2.5. Energy-level diagram of spiro-OMeTAD/HDABi₅/TiO₂, where the VBM of HDABi₅ was determined by UPS measurement. D. M. Fabian and S. Ardo, *J. Mater. Chem. A*, 2016, **4**, 6837 – Reproduced by permission of The Royal Society of Chemistry

An energy-level diagram is displayed as Figure 2.5, where the calculated CBM (−3.5 eV), VBM (−5.6 eV), and Fermi level (−3.7 eV) are depicted. The electronic band gap of the widely studied lead-halide-based perovskites has been shown to be 0.1 eV larger than the optical band gap,⁴⁰ and thus the CBM of HDABi₅ may in fact lie at an energy closer to the vacuum level. The CBM of TiO₂ (−4.21 eV *versus* vacuum) was taken from a report by Xu et al.,⁴¹ and the VBM of spiro-OMeTAD (−5.15 eV *versus* vacuum) was taken from a report by Nguyen et

al.⁴² The spiro-OMeTAD/HDABi₅ and HDABi₅/TiO₂ interfaces are responsible for combined photovoltage losses of greater than 1 V, and so use of a hole-transporting material with a more negative VBM and an electron-transporting material with a less negative CBM may result in a device with a larger photovoltage.

Figure 2.6a displays a grazing-incidence XRD pattern of HDABi₅ infiltrated into an mTiO₂ layer on top of a cTiO₂-coated FTO substrate (HDABi₅/mTiO₂/cTiO₂/FTO). The XRD pattern of the solution-deposited HDABi₅ film matches the pattern determined by Mitzi et al. for an HDABi₅ film deposited using a single source thermal ablation technique.⁴³ HDABi₅

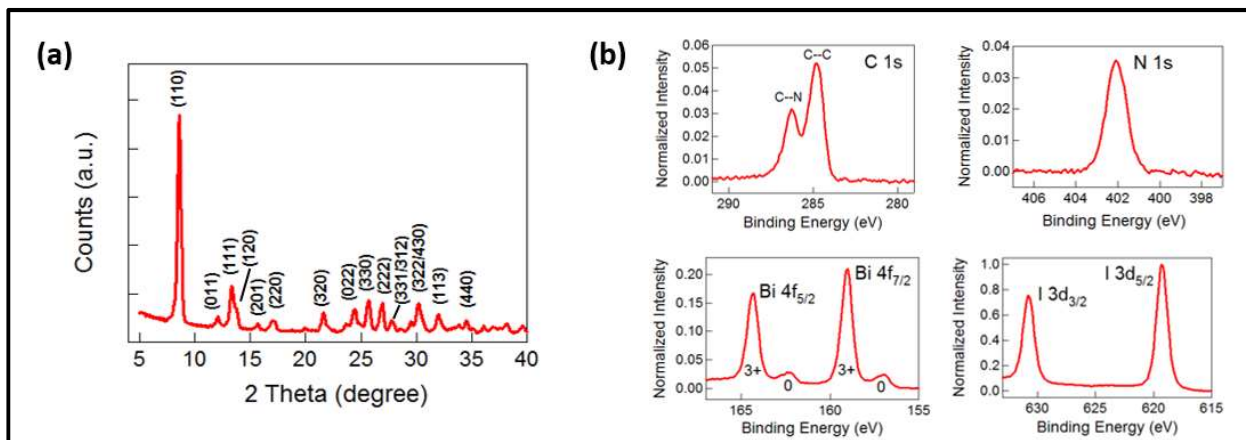


Figure 2.6. (a) Grazing-incidence XRD pattern and (b) XPS spectra of HDABi₅/mTiO₂/cTiO₂/FTO. D. M. Fabian and S. Ardo, *J. Mater. Chem. A*, 2016, **4**, 6837 – Reproduced by permission of The Royal Society of Chemistry

crystallizes in a primitive orthorhombic crystal structure, with lattice constants that match those determined for an HDABi₅ single crystal by Mousdis et al. ($a = 15.2 \text{ \AA}$, $b = 14.4 \text{ \AA}$, $c = 8.7 \text{ \AA}$).¹¹ It is evident from grazing-incidence XRD that the (110) plane is orientated in the plane of the underlying substrate. It is conjectured that the bismuth–iodide chains participate in carrier conduction along the (110) plane, similar to the facilitated carrier conduction along the (110) plane in the lead–halide network of APbX₃.⁷

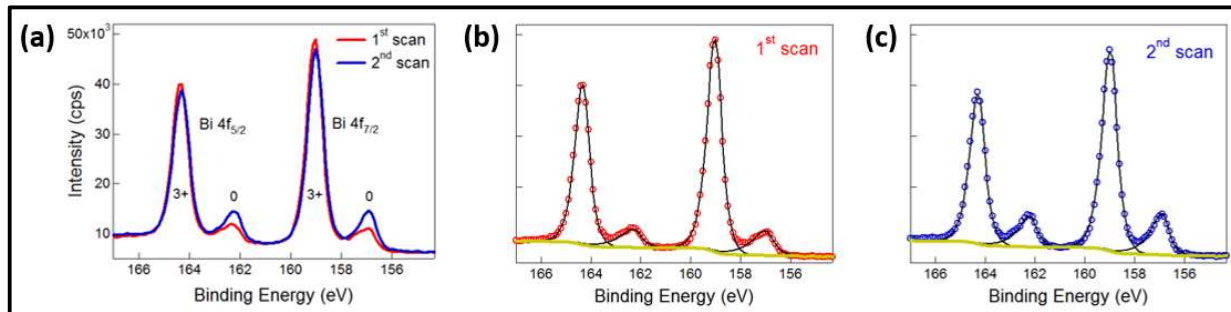


Figure 2.7. (a) Sequential X-ray photoelectron spectra of the Bi 4f region, which demonstrate increased signal attributed to Bi⁰ compared to signal attributed to Bi³⁺ concomitant with longer exposure to Al K_α X-ray radiation. (b) First scan (red circles) and (c) second scan (blue circles) of the Bi 4f region, with Shirley backgrounds (gold curves) and peak fits (black curves) shown for clarity. D. M. Fabian and S. Ardo, *J. Mater. Chem. A*, 2016, **4**, 6837 – Reproduced by permission of The Royal Society of Chemistry

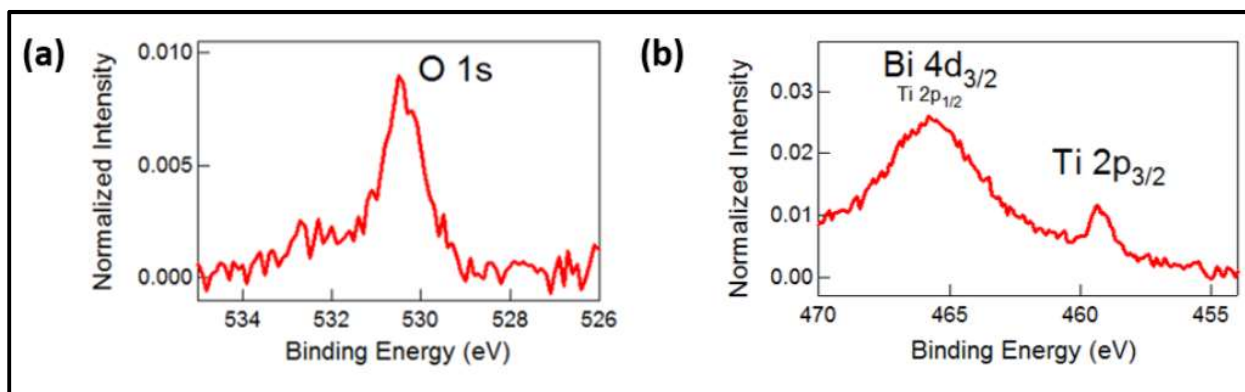


Figure 2.8. XPS region scans of (a) Ti 2p and (b) O 1s binding energies for HDABi₅/mTiO₂/cTiO₂/FTO, where the intensities are normalized to the I 3d_{5/2} peak in Figure 2.6b. Small peak intensities indicate near-complete coverage of mTiO₂ by HDABi₅. D. M. Fabian and S. Ardo, *J. Mater. Chem. A*, 2016, **4**, 6837 – Reproduced by permission of The Royal Society of Chemistry

The speciation of the near-surface atoms was characterized by X-ray photoelectron spectroscopy (XPS) (Figure 2.6b). Scans of the C 1s core level binding energy reveal the presence of two peaks, corresponding to both C–C and C–N bonds in the organic HDA²⁺ groups.⁴⁴ Bi 4f core level binding energy scans indicate that Bi species exist predominantly in the 3+ oxidation state, and a small amount as Bi⁰, which is suggested to be induced in part during measurement of the XPS spectra. The first XPS Bi 4f region scan displayed in Figure 2.6b is also displayed in Figure 2.7 (red traces) and was the first scan acquired for the sample. A subsequent Bi 4f scan was acquired immediately afterward and is also shown in Figure 2.7 (blue traces). For each scan, an emission current of 20 mA was used, and two sweeps were performed. Based on peak fitting to Gaussian–Lorentzian (80:20) curves, percent concentration of Bi⁰ was determined to be ~15% in the first scan and ~20% in the second scan. This suggests that some Bi⁰ species formed as degradation during X-ray radiation, and that some Bi⁰ was most likely present on the surface of the as-deposited HDABi₅. No Bi⁰ peaks could be resolved by grazing-incidence XRD, suggesting that any Bi⁰ present at the surface of the as-deposited film existed as isolated atoms or small amorphous clusters.

Table 2.1. Approximate percent surface elemental composition (excluding hydrogen) of HDABi₅/mTiO₂/cTiO₂/FTO calculated from XPS region scans. D. M. Fabian and S. Ardo, *J. Mater. Chem. A*, 2016, 4, 6837 – Reproduced by permission of The Royal Society of Chemistry

Element	Composition (%)
Carbon	47.2
Nitrogen	12.3
Bismuth	7.4
Iodine	31.1
Titanium	0.6
Oxygen	1.4

Ti 2p and O 1s peaks were negligible indicating near-complete coating of mTiO₂ by HDABi₅. Approximate elemental composition was determined based on regions scans of HDABi₅/mTiO₂/cTiO₂/FTO. To take into account the contribution of the Ti 2p_{1/2} peak that is overlapped by the Bi 4d_{3/2} peak, the overall peak area of Ti was approximated as the Ti 2p_{3/2} peak area multiplied by 1.5, since the Ti 2p_{1/2} to Ti 2p_{3/2} area ratio is expected to be 1:2 (Figure 2.8).⁴⁵ The percent composition of Ti was determined to be 0.6 atom % (Table 2.1). Approximate percent elemental composition at the surface of HDABi₅/mTiO₂/cTiO₂/FTO (Table 2.1), which was calculated based on region scans, indicates ~98% coating of mTiO₂ by HDABi₅.

Complete photovoltaic devices with the architecture Au/spiro-OMeTAD/HDABi₅/mTiO₂/cTiO₂/FTO, where spiro-OMeTAD is 2,2',7,7'-tetrakis(*N,N'*-di-*p*-methoxyphenylamine)-9,9'-spirobifluorene, were fabricated and their photovoltaic performance was evaluated (Figure 2.9). A side-view representation of the complete device architecture is shown in Figure 2.10. Current density *versus* potential (*J-E*) behavior of a device with an active area of 0.25 cm² was measured (Figure 2.9a). In the reverse scan direction (indicated by the left-

facing arrow), the device exhibited a short-circuit photocurrent density (J_{SC}) of 0.124 mA/cm², an open-circuit photovoltage (V_{OC}) of 403 mV (384 ± 12 mV over two samples), and a fill factor of 0.43, which yielded a sunlight-to-electricity power-conversion efficiency of 0.027%.

The device exhibited a stable steady-state J_{SC} of 0.115 mA/cm² (0.101 ± 0.020 mA/cm² over two samples), as shown in chronoamperometry data (Figure 2.9b), which is consistent with the hysteresis observed in the J - E behavior shown in Figure 3a. The incident-photon-to-current efficiency (IPCE) action spectrum reached a maximum value at 400 nm (Figure 2.9c). In the range of 340 – 450 nm, the HDABiI₅ material embedded in the mTiO₂ layer converted incident photons to electrical current with > 2% external quantum yield (EQY). The non-zero EQY onset at ~600 nm coincides with the absorption onset of the material, and thus supports the calculated optical bandgap of ~2.1 eV. The integrated J_{SC} was determined to be 0.143 mA/cm² (as shown in 2.2.5 *Characterization* of the experimental section), which suggests that the illumination intensity used in J - E and chronoamperometry measurements (Figure 2.9a and 2.9b) was approximately 0.8 Suns. EQY values for HDABiI₅ devices were small in comparison to those of state-of-the-art APbX₃ devices, for which > 80% EQY has been achieved across a spectral region of 400–700 nm.⁴⁶

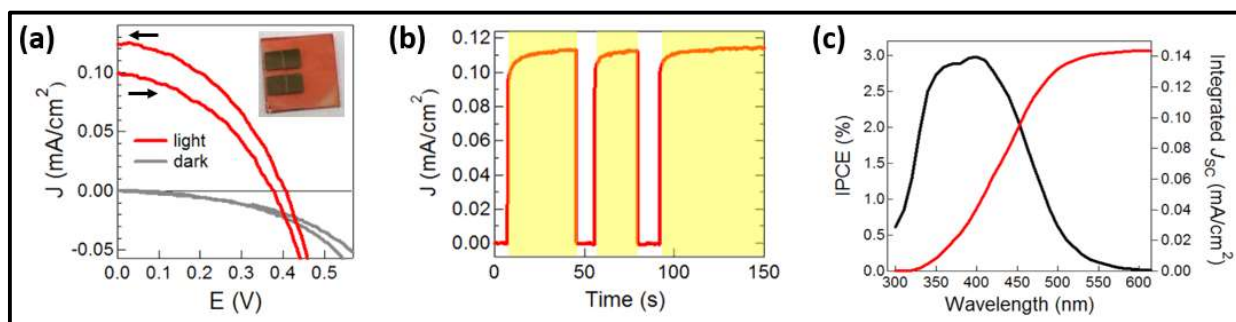


Figure 2.9. (a) J - E behavior with scan direction indicated by the arrows and (b) chronoamperometry under 0.8 Suns, and (c) IPCE action spectrum for a complete Au/spiro-OMeTAD/HDABiI₅/mTiO₂/cTiO₂/FTO device. Inset in panel (a) is a digital photograph image of the device. Yellow regions in panel (b) indicate time periods of illumination. D. M. Fabian and S. Ardo, *J. Mater. Chem. A*, 2016, **4**, 6837 – Reproduced by permission of The Royal Society of Chemistry

HDABiI₅ devices thus require optimization of film thickness, film quality, dopant density, trap-state density, and selective contact engineering to achieve larger J_{SC} values.

Accelerated thermal stability studies were performed on thin films of HDABiI₅ as well as MAPbI₃ (where MA is methylammonium) perovskites, each deposited on mTiO₂/cTiO₂/FTO. Transmission-mode UV–Vis absorption spectra of HDABiI₅ thin films were nearly unchanged up to 200 °C, which suggests that there was negligible thermal degradation at this temperature (Figure 2.11a). At 300 °C there was noticeable loss in HDABiI₅ material noted by a decrease in absorbance; however, there was no significant structural change in the film (i.e. features of the absorption spectrum did not change shape and there was no change in film color). This behavior is in contrast with that observed for an MAPbI₃ thin film (Figure 2.11b) where following treatment at 160 °C (Figure 2.11b, red), there was noticeable color change of the film from brown to yellow–brown. By 200 °C (Fig 2.11b, green), the film was bright yellow, suggesting a significant loss of MAI and degradation to PbI₂, a semiconductor with a 2.3 eV bandgap (which corresponds to an absorption onset of ~540 nm) (Figure 2.11b, inset).⁴⁷ These data are consistent with the fact that HDA of HDABiI₅, which is a solid at room temperature and has a boiling point > 200 °C, is considerably less volatile than MA of MAPbI₃, which is a gas at room temperature.

A more compact and conformal photoactive thin-film layer will aid in forming conformal and defect-free interfaces with the electron-selective and

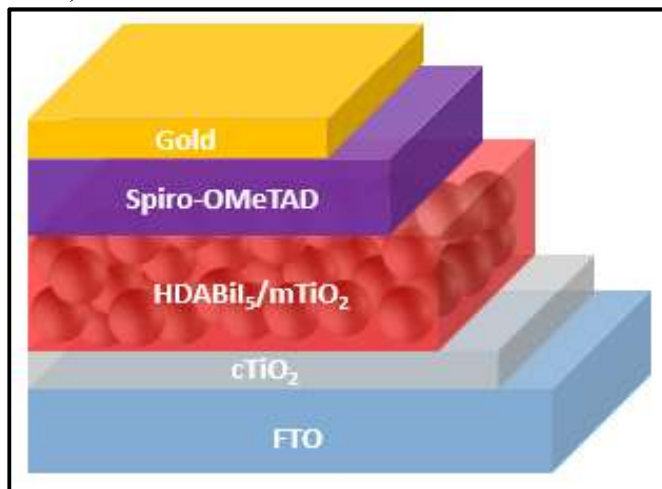


Figure 2.10. Side-view representation of the layer-by-layer architecture of the complete photovoltaic device. D. M. Fabian and S. Ardo, *J. Mater. Chem. A*, 2016, **4**, 6837 – Reproduced by permission of The Royal Society of Chemistry

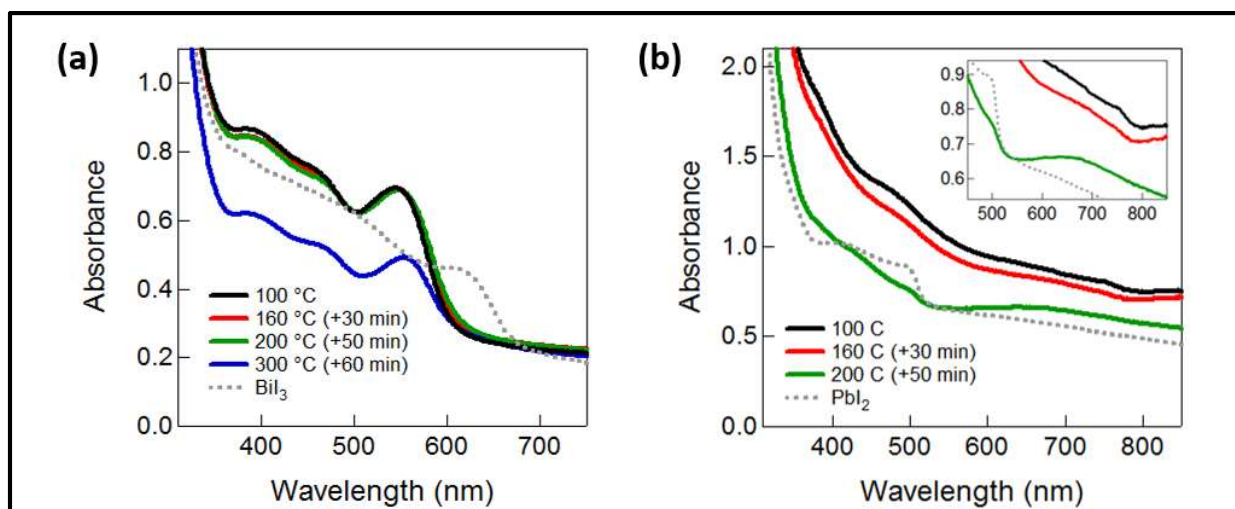


Figure 2.11. Transmission-mode UV–Vis electronic absorption spectra of (a) HDABi₅ and (b) MAPbI₃ films on mTiO₂/cTiO₂/FTO. Inset in panel b shows absorption onsets in greater detail and with the same axes units as the main graph. D. M. Fabian and S. Ardo, *J. Mater. Chem. A*, 2016, 4, 6837 – Reproduced by permission of The Royal Society of Chemistry

hole-selective contacts in solar cells. Therefore, several methods have been investigated for depositing HDABi₅ as well as MAPbI₃ thin films. Plan-view SEM micrographs of MAPbI₃ and HDABi₅ thin films deposited by several solution-based methods are shown in Figure 2.12. The deposition procedure that consistently yielded high surface coverage, well-controlled film thickness, and large crystal grains determined by SEM is the fast deposition-crystallization (FDC) procedure (panels c and g), which is the technique that consistently has been employed for preparing solar cells following publication of this work.^{1,46}

We have also tested processing techniques including a simple one-step deposition (panels a and e) and hot-casting (panels b and f).^{48,49} It is evident in panels a and e that the simple one-step deposition results in poor surface coverage on the underlying TiO₂. The hot-casting technique results in relatively large grains of APbI₃ (panel b), but the surface coverage is also poor. The micrograph in panel f suggests that hot-casting of HDABi₅ results in incomplete crystal formation. A new deposition technique has recently been pioneered termed “drop-heat-spin,” or DHS, (panels d and h) which yields thin films with large grains and higher surface coverage on TiO₂ than the

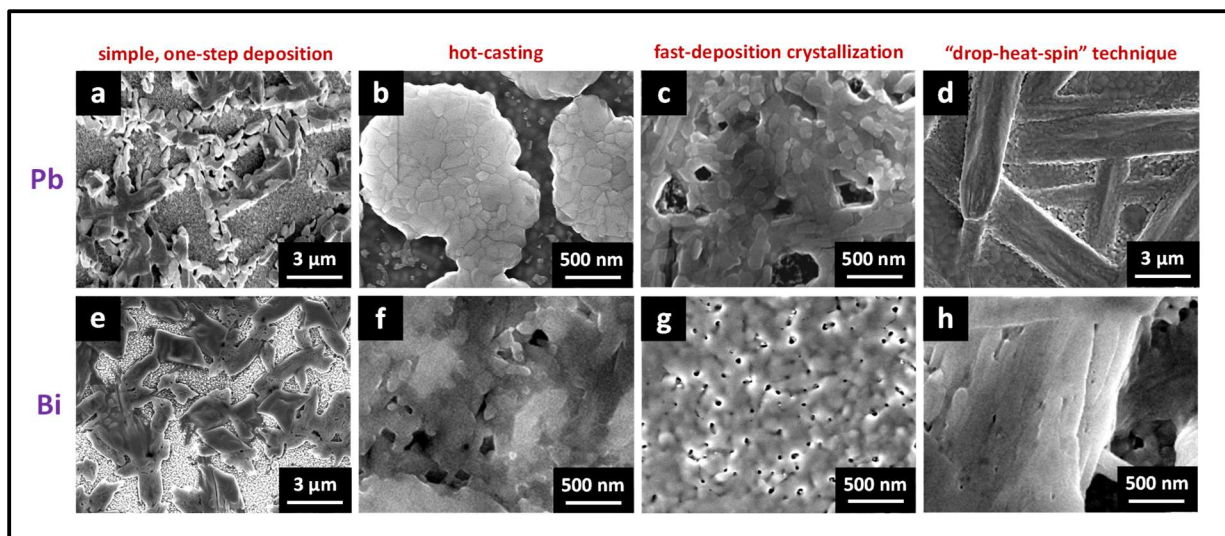


Figure 2.12. Plan-view SEM images of MAPbI₃ (top row, a–d) and HDABi₅ (bottom row, e–h) thin films deposited on TiO₂ via a simple one-step deposition (a, e), hot-casting (b, f), fast-deposition crystallization (c, g), or a novel “drop-heat-spin” technique that has been pioneered (d, h). D. M. Fabian and S. Ardo, *J. Mater. Chem. A*, 2016, **4**, 6837 – Reproduced by permission of The Royal Society of Chemistry

FDC procedure. This technique is described in detail in the experimental section (2.2.2 *Materials Processing*). However, lack of reproducibility in structural properties and film thickness using the DHS method rendered the FDC procedure a superior deposition method for reproducible photoactive layers.

2.4 Conclusions

A hybrid organic–inorganic material, HDABi₅, containing less toxic bismuth and more stable dicationic 1,6-hexanediammonium groups was synthesized and characterized. The electronic absorption spectrum of HDABi₅ was consistent with a material whose optical bandgap is ~2.1 eV and ultraviolet photoemission spectroscopy data suggest that the material is n-type. Grazing-incidence XRD data confirmed crystallinity and preferential orientation of HDABi₅. XPS data confirmed the surface elemental composition of HDABi₅ as well as near-complete coverage of the underlying mesoporous TiO₂ nanoparticle layer by HDABi₅.

Photoelectrochemical measurements showed that an HDABiI₅ device exhibited a steady-state short-circuit photocurrent density of ~100 $\mu\text{A}/\text{cm}^2$ and a stable open-circuit photovoltage of almost 400 mV under 0.8 Suns illumination. Thermal stability tests suggested that HDABiI₅ is more robust than MAPbI₃, which is thought to be attributed to decreased volatility of the deprotonated organic 1,6-hexanediamine group, compared to the deprotonated organic methylamine group of MAPbI₃. These results suggest that design of alternative structures with metal valency other than two may allow combinations of organic cationic groups and metal cores necessary for stable and nontoxic solution-processed photovoltaic materials. In terms of film quality and reproducibility it was determined that the fast-deposition crystallization procedure was a superior method for photoactive layer deposition in future device fabrication.

2.5 References

- (1) Fabian, D. M.; Ardo, S. *J. Mater. Chem. A* **2016**, *4*, 6837–6841.
- (2) Burschka, J.; Pellet, N.; Moon, S.-J.; Humphry-Baker, R.; Gao, P.; Nazeeruddin, M. K.; Grätzel, M. *Nature* **2013**, *499*, 316–319.
- (3) Stranks, S. D.; Eperon, G. E.; Grancini, G.; Menelaou, C.; Alcocer, M. J. P.; Leijtens, T.; Herz, L. M.; Petrozza, A.; Snaith, H. J. *Science* **2013**, *342*, 341–344.
- (4) Grätzel, M. *Nat. Mater.* **2014**, *13*, 838–842.
- (5) Frost, J. M.; Butler, K. T.; Brivio, F.; Hendon, C. H.; van Schilfgaarde, M.; Walsh, A. *Nano Lett.* **2014**, *14*, 2584–2590.
- (6) Snaith, H. J.; Abate, A.; Ball, J. M.; Eperon, G. E.; Leijtens, T.; Noel, N. K.; Stranks, S. D.; Wang, J. T.; Wojciechowski, K.; Zhang, W. *J. Phys. Chem. Lett.* **2014**, *5*, 1511–1515.
- (7) Ishii, A.; Jena, A. K.; Miyasaka, T. *APL Mater.* **2014**, *2*, 091102.
- (8) Motta, C.; El-Mellouhi, F.; Kais, S.; Tabet, N.; Alharbi, F.; Sanvito, S. *Nat. Commun.* **2015**,

- 6, 7026.
- (9) Kojima, A.; Teshima, K.; Shirai, Y.; Miyasaka, T. *J. Am. Chem. Soc.* **2009**, *131*, 6050–6051.
- (10) Papavassiliou, G. C. *Prog. Solid State Chem.* **1997**, *25*, 125–270.
- (11) Mousdis, G. A.; Papavassiliou, G. C.; Terzis, A.; Raptopoulou, C. P. *Z. Naturforsch.* **1998**, *53b*, 927–931.
- (12) Mitzi, D. B. *Inorg. Chem.* **2000**, *39*, 6107–6113.
- (13) Mitzi, D. B.; Brock, P. *Inorg. Chem.* **2001**, *40*, 2096–2104.
- (14) Lindsjö, M.; Fischer, A.; Kloo, L. *Zeitschrift für Anorg. und Allg. Chemie* **2005**, *631*, 1497–1501.
- (15) Hrizi, C.; Samet, A.; Abid, Y.; Chaabouni, S.; Fliyou, M.; Koumina, A. *J. Mol. Struct.* **2011**, *992*, 96–101.
- (16) Hrizi, C.; Trigui, A.; Abid, Y.; Chniba-Boudjada, N.; Bordet, P.; Chaabouni, S. *J. Solid State Chem.* **2011**, *184*, 3336–3344.
- (17) Hrizi, C.; Chaari, N.; Abid, Y.; Chniba-Boudjada, N.; Chaabouni, S. *Polyhedron* **2012**, *46*, 41–46.
- (18) Liang, K.; Mitzi, D. B.; Prikas, M. T. *Chem. Mater.* **1998**, *10*, 403–411.
- (19) Green, M. A.; Hishikawa, Y.; Dunlop, E. D.; Levi, D. H.; Hohl-Ebinger, J.; Ho-Baillie, A. W. Y. *Prog. Photovoltaics Res. Appl.* **2018**, *26*, 3–12.
- (20) Kazim, S.; Nazeeruddin, M. K.; Gratzel, M.; Ahmad, S. *Angew. Chem. Int. Ed.* **2014**, *53*, 2812–2824.
- (21) Cheng, Z.; Lin, J. *CrystEngComm* **2010**, *12*, 2646–2662.
- (22) Kodzasa, T.; Ushijima, H.; Matsuda, H.; Kamata, T. *Mol. Cryst. Liq. Cryst.* **2000**, *343*, 71–

75.

- (23) Umebayashi, T.; Asai, K.; Kondo, T.; Nakao, A. *Phys. Rev. B* **2003**, *67*, 155405.
- (24) Slavney, A. H.; Hu, T.; Lindenberg, A. M.; Karunadasa, H. I. *J. Am. Chem. Soc.* **2016**, *138*, 2138–2141.
- (25) Lyu, M.; Yun, J. H.; Cai, M.; Jiao, Y.; Bernhardt, P. V.; Zhang, M.; Wang, Q.; Du, A.; Wang, H.; Liu, G.; Wang, L. *Nano Res.* **2016**, *9*, 692–702.
- (26) Lehner, A. J.; Fabini, D. H.; Evans, H. A.; Hébert, C.-A.; Smock, S. R.; Hu, J.; Wang, H.; Zwanziger, J. W.; Chabinyk, M. L.; Seshadri, R. *Chem. Mater.* **2015**, *27*, 7137–7148.
- (27) Hoye, R.; Brandt, R. E.; Osherov, A.; Stevanovic, V.; Stranks, S. D.; Wilson, M. W. B.; Kim, H.; Akey, A. J.; Kurchin, R. C.; Poindexter, J. R.; Wang, E. N.; Bawendi, M. G.; Bulovic, V.; Buonassisi, T. *Chem. - A Eur. J.* **2016**, *22*, 2605–2610.
- (28) Park, B. W.; Philippe, B.; Zhang, X.; Rensmo, H.; Boschloo, G.; Johansson, E. M. J. *Adv. Mater.* **2015**, *27*, 6806–6813.
- (29) Brandt, R. E.; Kurchin, R. C.; Hoye, R. L. Z.; Poindexter, J. R.; Wilson, M. W. B.; Sulekar, S.; Lenahan, F.; Yen, P. X. T.; Stevanovi??, V.; Nino, J. C.; Bawendi, M. G.; Buonassisi, T. *J. Phys. Chem. Lett.* **2015**, *6*, 4297–4302.
- (30) Hamdeh, U. H.; Nelson, R. D.; Ryan, B. J.; Bhattacharjee, U.; Petrich, J. W.; Panthani, M. G. *Chem. Mater.* **2016**, *28*, 6567–6574.
- (31) Volonakis, G.; Filip, M. R.; Haghghirad, A. A.; Sakai, N.; Wenger, B.; Snaith, H. J.; Giustino, F. *J. Phys. Chem. Lett.* **2016**, *7*, 1254–1259.
- (32) Kagan, C. R.; Murray, C. B. *Nat. Nanotechnol.* **2015**, *10*, 1013–1026.
- (33) Yuan, M.; Liu, M.; Sargent, E. H. *Nat. Energy* **2016**, *2*, 16016.
- (34) Nozik, A. J.; Beard, M. C.; Luther, J. M.; Law, M.; Ellingson, R. J.; Johnson, J. C.; Arrays,

- Q. D. *Chem. Rev.* **2010**, *110*, 6873–6890.
- (35) McDaniel, H.; Kuposov, A. Y.; Pandey, A.; Fuke, N.; Klimov, V. I. US 20140275544 A1, 2014.
- (36) Mali, S. S.; Shim, C. S.; Hong, C. K. *NPG Asia Mater.* **2015**, *7*, e208.
- (37) Ito, S.; Murakami, T. N.; Comte, P.; Liska, P.; Grätzel, C.; Nazeeruddin, M. K.; Grätzel, M. *Thin Solid Films* **2008**, *516*, 4613–4619.
- (38) Kim, H.-S.; Lee, C.-R.; Im, J.-H.; Lee, K.-B.; Moehl, T.; Marchioro, A.; Moon, S.-J.; Humphry-Baker, R.; Yum, J.-H.; Moser, J. E.; Grätzel, M.; Park, N.-G. *Sci. Rep.* **2012**, *2*, 591.
- (39) Salim, T.; Sun, S.; Abe, Y.; Krishna, A.; Grimsdale, A. C.; Lam, Y. M. *J. Mater. Chem. A* **2014**, *3*, 8943–8969.
- (40) Schulz, P.; Edri, E.; Kirmayer, S.; Hodes, G.; Cahen, D.; Kahn, A. *Energy Environ. Sci.* **2014**, *7*, 1377–1381.
- (41) Xu, Y.; Schoonen, M. A. A. *Am. Mineral.* **2000**, *85*, 543–556.
- (42) Nguyen, W. H.; Bailie, C. D.; Unger, E. L.; McGehee, M. D. *J. Am. Chem. Soc.* **2014**, *136*, 10996–11001.
- (43) Mitzi, D. B.; Prikas, M. T.; Chondroudis, K. *Chem. Mater.* **1999**, *11*, 542–544.
- (44) Moulder, J. F.; Stickle, W. F.; Sobol, P. E.; Bomben, K. D. *Handbook of X-ray Photoelectron Spectroscopy*, 1995, 261.
- (45) Watts, J. F.; Wolstenholme, J. *An Introduction to Surface Analysis by XPS and AES*; 1st ed.; John Wiley & Sons Ltd.: Chichester, 2003.
- (46) Xiao, M.; Huang, F.; Huang, W.; Dkhissi, Y.; Zhu, Y.; Etheridge, J.; Gray-Weale, A.; Bach, U.; Cheng, Y.-B.; Spiccia, L. *Angew. Chemie - Int. Ed.* **2014**, *126*, 10056–10061.

- (47) Ferreira da Silva, A.; Veissid, N.; An, C. Y.; Pepe, I.; Barros de Oliveira, N.; Batista da Silva, A. V. *Appl. Phys. Lett.* **1996**, *69*, 1930.
- (48) Lee, M. M.; Teuscher, J.; Miyasaka, T.; Murakami, T. N.; Snaith, H. J. *Science* **2012**, *338*, 643–647.
- (49) Nie, W.; Tsai, H.; Asadpour, R.; Blancon, J.; Neukirch, A. J.; Gupta, G.; Crochet, J. J.; Chhowalla, M.; Tretiak, S.; Alam, M. A.; Wang, H.; Mohite, A. D. *Science* **2015**, *347*, 522–525.

CHAPTER 3: HYBRID ORGANIC–INORGANIC BISMUTH–IODIDE MATERIALS INCORPORATING DIVALENT ORGANIC LIGANDS FOR PHOTOVOLTAICS

** In part a compilation of one publication in preparation¹*

3.1 Introduction

A series of solution-processed hybrid organic–inorganic bismuth–iodide materials have been developed where the organic monocations used in typical perovskite materials are replaced with non-volatile and less water-soluble analogs in the form of organic dications, thus expanding the suite of hybrid organic–inorganic materials. Through an understanding of fundamental electronic, photophysical, and photochemical properties, promising hybrid organic–inorganic bismuth–iodide photoactive materials can be determined. This would ultimately afford facile processing of robust and environmentally-friendly photoactive materials for low-cost, high-efficiency tandem PVs with market-dominating silicon absorbers.²

Ultrafast and nanosecond and longer transient spectroscopies are commonly employed for the study of photophysical properties of hybrid organic–inorganic materials.^{3–8} These techniques can provide a fundamental understanding of the small photocurrents observed with bismuth–iodide organic-dication-containing photoactive layers in PVs. Broadband ultrafast transient absorption spectroscopy has been employed to understand the charge-carrier dynamics of APbX₃, and data suggest that their photophysical properties are comparable to state-of-the-art bulk gallium arsenide (GaAs).⁷ Furthermore, the advantage of APbX₃ over GaAs, is that high-efficiency APbX₃ PVs can be solution processed in air at low temperatures.⁹ If the charge-carrier mobilities are low (i.e. less than 0.0001 cm² V⁻¹ s⁻¹), as they are predicted to be in hybrid organic–inorganic bismuth–halide materials, then time-resolved microwave conductivity (TRMC) can determine in a non-contact

fashion the carrier mobility while such small mobilities are too small for detection by time-resolved terahertz spectroscopy (TRTS).¹⁰ TRMC results on the nanosecond and longer timescale have shown that charge separation occurs at both the APbX₃/electron-transport-layer junction and the APbX₃/hole-transport-layer junction, and that charge recombination is significantly slower on TiO₂ than on Al₂O₃.¹¹ TRMC measurements and time-resolved photoluminescence (TRPL) spectroscopy measurements each on the nanosecond and longer timescale have also shown that larger perovskite crystal grains, which are typical of planar, thin-film PVs, exhibit slower trap-mediated charge recombination and higher mobilities than those of mesostructured assemblies, due to the fewer number of grain boundaries in planar PVs.¹² Time-correlated single-photon counting (TCSPC) fluorescence measurements have corroborated the deleterious influence of grain boundaries on charge-carrier lifetimes.^{13,14} In Figure 3.1, the spectrum of electromagnetic radiation is shown indicating the probing wavelength regions of X-band TRMC, TRTS, and transient absorption, as well as the type of charge carrier(s) each spectroscopic technique probes. While transient absorption spectroscopy probes free carriers and excitons, the individual effects of each remain convoluted.¹⁵ On the other hand, TRMC and TRTS typically probe only free carriers, and so the contribution of excitons to the signal can be understood qualitatively through acquisition of both transient absorption and TRMC or TRTS data.

The hybrid organic–inorganic bismuth–iodide material HDABiI₅ reported on in Chapter 2 can be considered “perovskite-like” because, like perovskites, they are hybrid organic–inorganic materials, but the materials do not adopt the perovskite structure. Goldschmidt’s tolerance factor (*t*) provides a necessary condition for the formation of a perovskite crystal structure.¹⁶ The tolerance factor equation is a formula relating the ionic radii of each component in the structure as such:

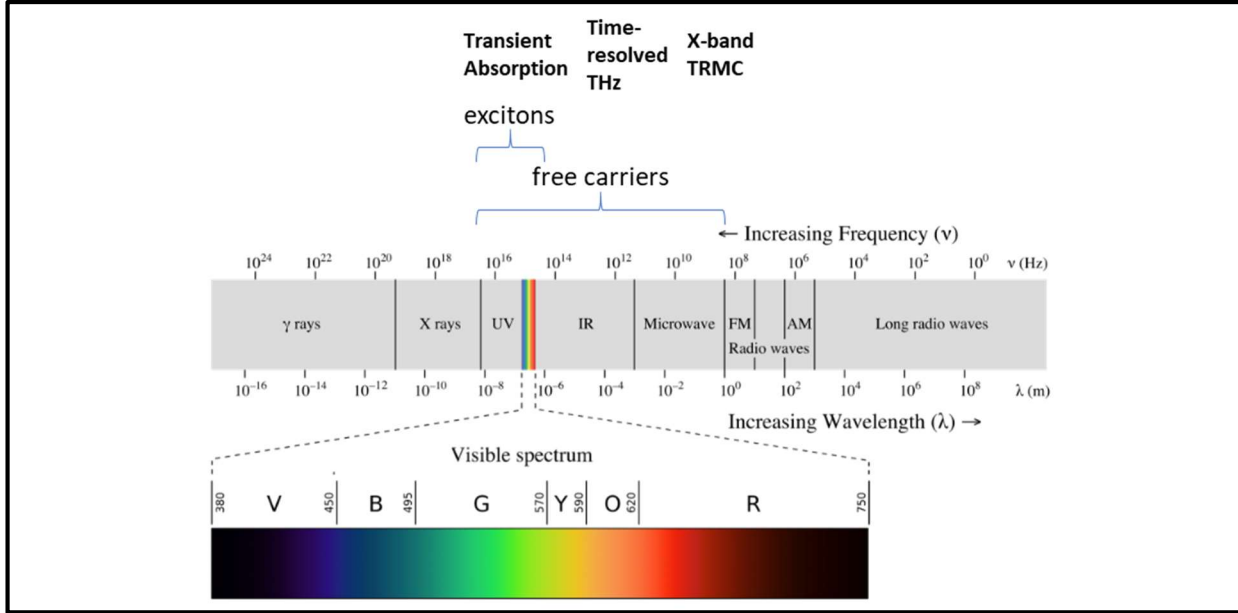


Figure 3.1. Electromagnetic radiation spectrum, with approximate positions of probing wavelengths of X-band time-resolved microwave conductivity, time-resolved terahertz, and transient absorption spectroscopic techniques and abilities of each technique to probe free carriers and/or excitons.

Adapted from https://upload.wikimedia.org/wikipedia/commons/3/30/EM_spectrumrevised.png.

$$t = \frac{R_A + R_X}{\sqrt{2}(R_B + R_X)} \quad (\text{Equation 2.1})$$

where R_A , R_B , and R_X are the ionic radii of A^+ , B^{2+} and X^- , respectively. For nearly all perovskite oxides and halides, $0.74 < t < 1.28$.¹⁷ This is not the single criterion for perovskite structure formation, however, as other factors that affect whether or not a perovskite structure will form include geometric requirements and lattice constant relationships.¹⁶ The majority of materials that form perovskite structures also have a B^{2+} to X^- radius ratio of $0.414 < R_B/R_X < 0.732$. In addition, the ratio of A^+ to X^- (R_A/R_X) should be significantly larger than 0.732 in order to satisfy 12-fold coordination of the A^+ group. Otherwise, a small R_A/R_X results in a decreased effective number of X^- ions around A^+ , which results in distortion of the perovskite lattice.¹⁶

The ionic radii of Bi^{3+} and I^- in HDABiI_5 are 1.03 Å, and 2.2 Å, respectively. In order to fit the criterion of $0.74 < t < 1.28$, the ionic radius of HDA^{2+} must be in the range of 1.18–3.65 Å. The ionic radius of MA^+ is 2.17 Å and HDA^{2+} is much larger (approximately 4 times larger) than MA^+ . Based on this rationale, therefore, HDABiI_5 will not form a perovskite structure. This also supports the fact that the material consists of chains of bismuth–iodide octahedra (i.e. the inorganic network is one-dimensional) and not a lattice of octahedra (i.e. the inorganic network is three-dimensional), and this is due to the organic moiety, HDA^{2+} , being too large. This reasoning prompted the investigation of a potential intra-crystallite fastener in the form of a small conjugated dicationic organic moiety to incorporate in the hybrid organic–inorganic bismuth–iodide crystal structure, following the linking strategy depicted in Figure 3.2a. These moieties have been shown to increase the anisotropic conductivity of materials.¹⁸ Even if this moiety is too large for the material to form a perovskite structure, this moiety could enhance charge-carrier conduction between the chains of bismuth–iodide octahedra.

The orientation of the active inorganic network of these materials is also important for rapid conduction, and it has been hypothesized that crystallite orientation can be controlled based on the organic crystal fasteners used.¹⁹ HDABiI_5 has a preferred orientation in the [110] direction when deposited as a thin film, indicating that the Bi–I chains are parallel to the substrate surface, which is not ideal for charge-carrier collection. This suggests that thin-film in-plane conductivity is significantly higher than through-plane conductivity. Since the material layers in PVs stack parallel to the substrate, high through-plane conductivity is vital to high-performance PVs. A substitution of some or all of the HDA^{2+} groups with small conjugated organic groups such as *p*-phenylenediammonium dication (PhDA^{2+}) could enhance through-plane conductivity and, as a result, increase photocurrents in bismuth–iodide thin-film PVs (Figure 3.2b).

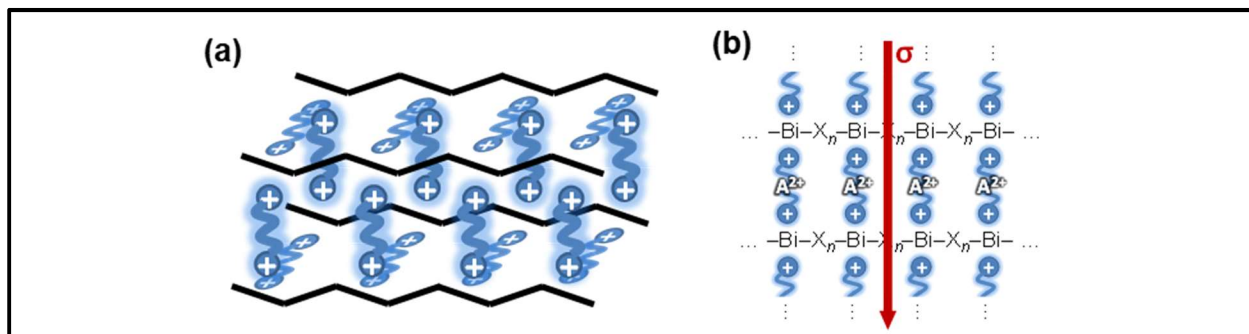


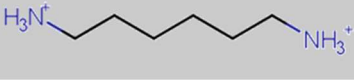
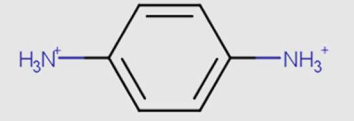
Figure 3.2. (a) A representation of the general linking of organic dications to one-dimensional bismuth–halide chains. (b) A representation of the organic dication crystal motif in dicationic organic–inorganic bismuth–halide materials, where the A^{2+} groups serve as “crystal fasteners” between one-dimensional bismuth–halide chains to enhance inter-chain conductivity, σ .

Because the bismuth–iodide network is one-dimensional, the structures are quantum-confined and are expected to have large exciton binding energies. By reducing the size of the organic moiety and/or by incorporating conjugated, polarizable molecular groups, it is conjectured that the exciton binding energies in these materials can be significantly reduced.^{20,21} Mixtures of dicationic organic groups also allow fine tuning of the unit cell size. Incorporating a smaller organic moiety favorably decreases the bandgap of the material, but based on observations of film quality, if the organic moiety is too small, the one-dimensional bismuth–iodide structure instead crystallizes as a zero-dimensional structure.

Preliminary results from Chapter 2 indicated that HDABiI₅ exhibits superior film quality, PV performance, and stability in comparison to the widely-studied 3D lead–iodide material MAPbI₃ when processed under ambient conditions. Based on the promising results presented in Chapter 2 on HDABiI₅, other lead-free bismuth–iodide materials that require two positive charges in the unit cell for charge neutrality were targeted. The overall goal of the research presented in this chapter was to identify stable, highly-conductive, and non-toxic hybrid organic–inorganic bismuth–iodide materials for use in solution-processed PVs. In this chapter, work presented in Chapter 2 on the novel use of HDABiI₅ as a PV material was expanded upon. A series of dicationic

hybrid organic–inorganic bismuth–iodide thin films were prepared and characterized in order to understand structure–property relationships. Ultrafast laser spectroscopic techniques were employed to study hybrid organic–inorganic bismuth–iodide thin films. A comparative study was performed

Table 3.1. Organic groups incorporated in dicationic hybrid organic–inorganic bismuth–halide materials for enhanced-conductivity PVs.

Neutral Species	Dication Representation
Hexanediamine	
Phenylenediamine	

on HDABiI₅ vs. propylammonium bismuth pentaiodide, (PA)₂BiI₅, a material that incorporates two propylammonium monocations (PA⁺) per formula unit that together are about the same size as HDA²⁺. Preliminary results on mixed dicationic organic moieties incorporating conjugated organic PhDA²⁺ groups were also obtained. The two organic groups used in these mixed dicationic bismuth–iodide materials are displayed in Table 3.1.

3.2 Experimental

3.2.1 Single-Crystal Growth and Measurement

3.2.1.1 Single-Crystal Growth

Single crystals of (EDA)₂Bi₂I₁₀•5H₂O were grown by vapor diffusion of acetonitrile into a 0.5 M solution of ethylenediamine (EDA), aqueous concentrated hydriodic acid (HI), and BiI₃ in N,N-dimethylformamide (DMF). The solution contained EDA, HI, and BiI₃ in a molar ratio of 1:2:1, with HI in slight excess to ensure complete conversion of EDA and BiI₃ into the final product. Single crystals of HDABiI₅ were grown by vapor diffusion of dichloromethane into a 0.5 M solution of 1:1 HDAl₂:BiI₃, with HDAl₂ in slight excess to ensure there was no residual BiI₃, in a solvent mixture of 4:1 (v/v) DMF:dimethylsulfoxide (DMSO).

3.2.1.2 X-ray Data Collection and Structure Solution for $(EDA)_2Bi_2I_{10}\cdot 5H_2O$

An orange crystal of approximate dimensions 0.123 x 0.128 x 0.272 mm was mounted on a glass fiber and transferred to a Bruker SMART APEX II diffractometer. The APEX2²² program package was used to determine the unit-cell parameters and for data collection (10 sec/frame scan time for a sphere of diffraction data). The raw frame data was processed using SAINT²³ and SADABS²⁴ to yield the reflection data file. Subsequent calculations were carried out using the SHELXTL²⁵ program. The diffraction symmetry was $2/m$ and the systematic absences were consistent with the monoclinic space groups Cc and $C2/c$. It was later determined that space group $C2/c$ was correct.

The structure was solved by dual-space methods and refined on F^2 by full-matrix least-squares techniques. The analytical scattering factors²⁶ for neutral atoms were used throughout the analysis. Hydrogen atoms were included using a riding model. The molecule was dimeric consisting of two half-dimers. One molecule was located about an inversion center while the other was located on a two-fold rotation axis. There were five molecules of water solvent present.

Least-squares analysis yielded $wR2 = 0.0395$ and $Goof = 1.210$ for 261 variables refined against 7836 data (0.77\AA), $R1 = 0.0208$ for those 7508 data with $I > 2.0\sigma(I)$.

3.2.1.3 X-ray Data Collection and Structure Solution for $HDABiI_5$

A red crystal of approximate dimensions 0.125 x 0.127 x 0.276 mm was mounted on a glass fiber and transferred to a Bruker SMART APEX II diffractometer. The APEX2²² program package was used to determine the unit-cell parameters and for data collection (10 sec/frame scan time for a sphere of diffraction data). The raw frame data was processed using SAINT²³ and

SADABS²⁴ to yield the reflection data file. Subsequent calculations were carried out using the SHELXTL²⁵ program. The diffraction symmetry was *mmm* and the systematic absences were consistent with the orthorhombic space groups *Pnma* and *Pna2₁*. It was later determined that space group *Pna2₁* was correct.

The structure was solved by dual space methods and refined on F^2 by full-matrix least-squares techniques. The analytical scattering factors²⁶ for neutral atoms were used throughout the analysis. Hydrogen atoms were included using a riding model. It was necessary to refine carbon atoms isotropically (presumably due to high absorption). The complex formed an extended structure.

Least-squares analysis yielded $wR2 = 0.0646$ and $Goof = 1.150$ for 100 variables refined against 3940 data (0.78 Å), $R1 = 0.0282$ for those 3844 data with $I > 2.0\sigma(I)$. The structure was refined as an inversion twin.

3.2.1.4 Structure Solution Definitions

$$wR2 = [\Sigma[w(F_o^2 - F_c^2)^2] / \Sigma[w(F_o^2)^2]]^{1/2}$$

$$R1 = \Sigma||F_o| - |F_c|| / \Sigma|F_o|$$

$Goof = S = [\Sigma[w(F_o^2 - F_c^2)^2] / (n-p)]^{1/2}$ where n is the number of reflections and p is the total number of parameters refined.

The thermal ellipsoid plot is shown at the 50% probability level. For $(EDA)_2Bi_2I_{10} \cdot 5H_2O$, symmetry-equivalent water molecules were omitted for clarity.

3.2.2 Density Functional Theory Calculations for HDABiI₅

All density functional theory (DFT) calculations were performed using the Vienna *Ab initio*

Simulation Package (VASP), employing the projector augmented-wave (PAW) method to describe the interactions and between valence and core electrons. A Γ -centered $2 \times 2 \times 1$ k -point sampling mesh was found to achieve convergence to within 1 meV/atom. The plane wave energy cutoff was converged to 10 meV/atom, with a cutoff of 400 eV found to be sufficient. To prevent errors arising from Pulay stress, the cutoff energy was raised to 520 eV during geometry relaxations. The structures were deemed converged when the forces on each atom totaled less than 10 meV/Å.

Geometry relaxations were performed using the PBEsol functional, a version of the Perdew Burke and Ernzerhof (PBE) functional revised for solids. PBEsol has been shown to accurately reproduce the structure parameters of many materials containing post-transition metal cations. To avoid errors arising from the systematic band gap underestimation in generalized gradient approximation functionals such as PBEsol, the Heyd--Scuseria--Ernzerhof hybrid functional (HSE06) was employed for density of states, band structure and optics calculations. In addition, spin-orbit coupling (SOC) was treated explicitly to account for the relativistic effects on the bismuth valence electrons. This combination of HSE06+SOC has previously been shown to reproduce the electronic properties of a large number of solar absorber materials. The optical response was calculated using density functional perturbation theory (DFPT) within the transversal approximation, in which only direct valence to conduction band transitions are considered.

3.2.3 Preparation of Hybrid Organic-Inorganic Bismuth-Iodide Solutions

All chemicals were used as received. Diammonium iodide salts were synthesized by slow addition of hydriodic acid (47% in water, stabilized with 1.5% hypophosphorous acid, Sigma-Aldrich) to the diamine of choice dissolved in methanol. The hydriodic acid to diamine molar ratio

was 2:1, with hydriodic acid in slight excess. As an example, to synthesize 1,6-hexanediamine dihydriodide (HDA•2HI), 260.9 mg of 1,6-hexanediamine (98+%, Alfa Aesar) was dissolved in 5 mL methanol, and then 1 mL hydriodic acid was added slowly at 0 °C with stirring, followed by stirring for an additional 30 min. HDA•2HI precipitate was recovered by evaporation of solvents at 40 °C with a rotary evaporator. The precipitate was rinsed with diethyl ether, and vacuum dried at 60 °C for at least 12 h. HDABiI₅ solution was then prepared by mixing HDA•2HI and BiI₃ (99%, Sigma-Aldrich) powders at an approximately 1:1 mole ratio, with HDA•2HI in slight excess, in an anhydrous mixture of 4:1 (v/v) DMF:DMSO at 70 °C inside a nitrogen-filled glovebox. The HDABiI₅ solution was stored in the glovebox until use and was used within one week of preparation.

3.2.4 Materials Processing

All steps of materials deposition and device fabrication were performed in air with 40–60% relative humidity and as described below, unless noted otherwise. All thermal treatments were performed using a hot plate. Fluorine-doped tin oxide coated glass (FTO) substrates were cleaned as follows: 1) sonication in Alconox solution, 2) rinse with deionized water, 3) rinse with ethanol, 4) sonication in ethanol, and 5) dry with nitrogen. A compact TiO₂ (cTiO₂) layer was deposited by pipetting a solution of titanium diisopropoxide bis(acetylacetonate) on a cleaned FTO substrate and then the substrate was spun at 2000 rpm (2000 rpm/s acceleration) for 60 s. The substrate was subsequently dried at 125 °C and then sintered at 550 °C for 30 min. Nanoparticles of TiO₂ were synthesized following a procedure by Ito et al.²⁷ The nanoparticle solution was further diluted in ethanol at a ratio of 1:3.5 TiO₂ nanoparticle solution:ethanol, w/w to make a mesoporous TiO₂ (mTiO₂) suspension. The mTiO₂ layer was deposited by spin coating this solution at 500 rpm

(500 rpm/s acceleration) for 5 s and then 5000 rpm (5000 rpm/s acceleration) for 25 s, followed by drying at 125 °C, and then sintering at 550 °C for 30 min. The substrates were allowed to cool to room temperature. Unless otherwise noted, a conventional spin-coat method was adapted from Kim et al.²⁸ and used for depositing the hybrid organic–inorganic bismuth–iodide solutions that served as the photoactive layer. For this method, a filtered solution in 4:1 (v/v) DMF:DMSO was pipetted on top of the mTiO₂-coated FTO substrate and then the substrate was spun at 3000 rpm (3000 rpm/s acceleration) for 60 s, followed by rapid transfer to a hot plate that was preheated to 100 °C and subsequent annealing at 100 °C for 30 min. In some cases, the fast-deposition crystallization (FDC) method was employed for depositing the photoactive layer, which was described in the experimental section of Chapter 1 (*1.2.2.2 Perovskite Deposition Methods*). For all deposition methods, the photoactive layer solution was dispensed on the substrate at a volume of 17.5 μL/cm².

3.2.5 Device Fabrication

Prior to the FTO cleaning step, a region of the FTO film was etched using 2 M HCl and Zn powder in order to prevent device shunting upon contact to the device top Au electrode. After performing the cleaning steps listed above (*Materials Processing* subsection), FTO substrates were further cleaned using an O₂ plasma treatment for 10 min. Following deposition of HDABiI₅ or (PA)₂BiI₅ per the protocol described above (*Materials Processing* subsection), a 50 mM solution of 2,2',7,7'-tetrakis(*N,N'*-di-*p*-methoxyphenylamine)-9,9'-spirobifluorene (spiro-OMeTAD) dissolved in chlorobenzene with additives of 17.5 μL 4-*tert*-butylpyridine and 37.5 μL lithium bis(trifluoromethane)sulfonimide in acetonitrile (170 mg/mL) was deposited by spin coating at 3000 rpm (3000 rpm/s acceleration) for 60 s. The devices were then transferred into a nitrogen-

filled glovebox and 80 nm of Au was thermally evaporated onto the devices at a base pressure of 5×10^{-6} mbar.

3.2.6 Ultrafast Laser Spectroscopy

Time-resolved microwave conductivity (TRMC) measurements were performed in a standard system that has been extensively reported elsewhere.²⁹ Briefly, a sample is mounted in a microwave cavity, a microwave probe beam is coupled to the cavity through the use of waveguides, and the microwave frequency is tuned to obtain resonance with the cavity. A short pump laser pulse is used to photoexcite the sample (~ 5 ns, Nd:YAG pumped OPO system: Spectra Physics QuantaRay/GWU PremiScan) and the transient change in absorption of the microwave probe is measured as a function of time after the pump pulse. TRMC data was analyzed in Igor Pro using custom software. Each photoconductance transient was fit using a convolution between the instrument response function and a double-exponential decay. Samples were measured under ambient conditions.

Transient absorption (TA) measurements were performed using a Coherent Libra Ti:sapphire ultrafast laser (800 nm, pulse duration ~ 100 fs, ~ 4 mJ/pulse, and 1 KHz repetition rate) and a Helios Ultrafast System pump-probe TA spectrometer. In this system, the 800 nm fundamental beam is split into two beams, one of which becomes the pump beam and the other becomes the probe beam. One beam is sent to a TOPAS optical parametric amplifier to generate the pump pulse with a tunable wavelength, and its intensity is attenuated by two neutral density filters. The other beam is focused into a sapphire crystal to generate a white light continuum probe beam. The pump-probe delay is tuned by a delay line (Thorlabs). The pump and probe beams are

focused and overlapped onto the sample. The probe beam size is $\sim 130 \mu\text{m}$ and the pump beam size is $\sim 1 \text{ mm}$. Samples were measured under ambient conditions.

3.2.7 Characterization

High-resolution synchrotron powder diffraction data were collected using beamline 11-BM at the Advanced Photon Source (APS) at Argonne National Laboratory using a calibrated wavelength of 0.41417 \AA . Discrete detectors covering an angular range from -6 to $16^\circ 2\theta$ are scanned over a $34^\circ 2\theta$ range, with data points collected every $0.001^\circ 2\theta$ and scan speed of $0.01^\circ/\text{s}$. Data are collected while continually scanning the diffractometer 2θ arm. A mixture of NIST standard reference materials, Si (SRM 640c) and Al_2O_3 (SRM 676) is used to calibrate the instrument, where the Si lattice constant determines the wavelength for each detector. Corrections are applied for detector sensitivity, 2θ offset, small differences in wavelength between detectors, and the source intensity, as noted by the ion chamber before merging the data into a single set of intensities evenly spaced in 2θ . For ease of data presentation, 2θ values were adjusted as if Cu K_α radiation (1.5406 \AA) was used.

Grazing-incidence XRD data were collected using a Rigaku Smartlab diffractometer with Cu K_α radiation and in parallel beam geometry. Transmission and reflection spectra were obtained using an integrating sphere in a Shimadzu UV-3600 ultraviolet-visible-near-infrared spectrophotometer. Absorption was calculated by assuming $\text{Absorbance} = 1 - \text{Transmittance} - \text{Reflectance}$. Steady-state photoluminescence (PL) was measured with a Horiba Jobin Yvon Model FL-1039/40 Fluorolog, a Horiba Jobin Yvon iHR320 spectrograph, and a Horiba Jobin Yvon SPEX Instruments S.A. Group Spectrum One G35 CCD camera. A monochromatized Xe lamp was used as the excitation source. Scanning electron microscopy images were acquired on a FEI

Magellan 400L XHR using 15 kV accelerating voltage and 0.8 nA beam current. X-ray photoelectron spectroscopy (XPS) measurements were performed using a Kratos AXIS Supra photoelectron spectrometer using Al K_{α} radiation. XPS data were analyzed using CasaXPS Processing Software. Thermogravimetric analysis data were obtained using a TGA Q500 by TA Instruments.

An ELH-type W-halogen lamp was used inside a nitrogen-filled glovebox as a source of simulated solar illumination. Before measurement of device $J-E$ behavior, chronoamperometry, and through-plane conductivity measurements, the light intensity was roughly approximated to be 1 Sun using a calibrated Si photodiode (ThorLabs, Inc., FDS100) positioned at the location of the device. 2-electrode cyclic voltammetry measurements (at a scan rate of 100 mV s⁻¹), chronoamperometry measurements, and through-plane conductivity measurements were performed using a Gamry Reference 600 Potentiostat.

Transmission, reflection, steady-state PL, TRMC, TAS, and some of the grazing-incidence XRD measurements were performed in the Chemistry and Nanoscience Center at the National Renewable Energy Laboratory. SEM, XPS, and some of the grazing-incidence XRD work was performed in the UC Irvine Materials Research Institute (IMRI).

formed binuclear clusters of $\text{Bi}_2\text{I}_{10}^{4-}$ with two EDA^{2+} groups and five water molecules associated with each cluster. This represents the first report of the crystal structure of $(\text{EDA})_2\text{Bi}_2\text{I}_{10}\cdot 5\text{H}_2\text{O}$. Figure 3.4a shows a digital photograph image of the single crystal, Figure 3.4b displays bond distances of a segment of the $(\text{EDA})_2\text{Bi}_2\text{I}_{10}\cdot 5\text{H}_2\text{O}$ unit cell, and Figure 3.4c shows the complete

Table 3.2. Crystallographic data for $\text{EDA}_2\text{Bi}_2\text{I}_{10} \cdot 5\text{H}_2\text{O}$.

$\text{EDA}_2\text{Bi}_2\text{I}_{10} \cdot 5\text{H}_2\text{O}$	
Empirical formula	$\text{C}_4 \text{H}_{30} \text{Bi}_2 \text{I}_{10} \text{N}_4 \text{O}_5$
Formula weight	1901.28
Temperature	88(2) K
Crystal system	Monoclinic
Space group	$\text{C}2/\text{c}$
a	41.2157(16)
b	8.4359(3)
c	20.0255(8)
α	90°
β	$100.1235(5)^\circ$
γ	90°
Volume	6854.3(5)
Z	8
Calculated density	3.685 g/cm^3
Absorption coefficient	19.282 mm^{-1}
F(000)	6544
Crystal size	0.272 x 0.128 x 0.123 mm
Crystal color	orange
θ range for data collection	2.008 to 27.484°
Index ranges	$-53 \leq h \leq 53, -10 \leq k \leq 10, -26 \leq l \leq 26$
Reflections collected/unique/observed	39710/7836
Completeness to $\theta = 25.50^\circ$	99.9 %
Absorption correction	Semi-empirical from equivalents

unit cell. Bond angles and bond distances of the bismuth–iodide clusters are very similar to a previous report by Hrizi et al. on $\text{PhDA}_2\text{Bi}_2\text{I}_{10}\cdot 4\text{H}_2\text{O}$.³⁰

Table 3.2 shows crystallographic information pertaining to the $(\text{EDA})_2\text{Bi}_2\text{I}_{10}\cdot 5\text{H}_2\text{O}$ single crystal. The resolved crystal structure does not represent how the material crystallizes as a thin film, however, as the waters evaporate out of the crystal during the annealing step. Therefore, this information is not particularly useful for further analysis related to thin-film material properties.

Single-crystal XRD data of HDABiI_5 confirmed the crystal structure (Figure 3.5) and supported the role of the organic dication (white, blue) as intra-crystallite fastener between iodides (green) coordinated to bismuth(III) ions (yellow) on one-dimensional chains.^{10,12,33} The chains of bismuth–iodide octahedra align along the (110) plane, as indicated by the red plane in Figure 3.6a, which shows a $1 \times 1 \times 3$ unit cell structure of HDABiI_5 . The bismuth–iodide chains are oriented

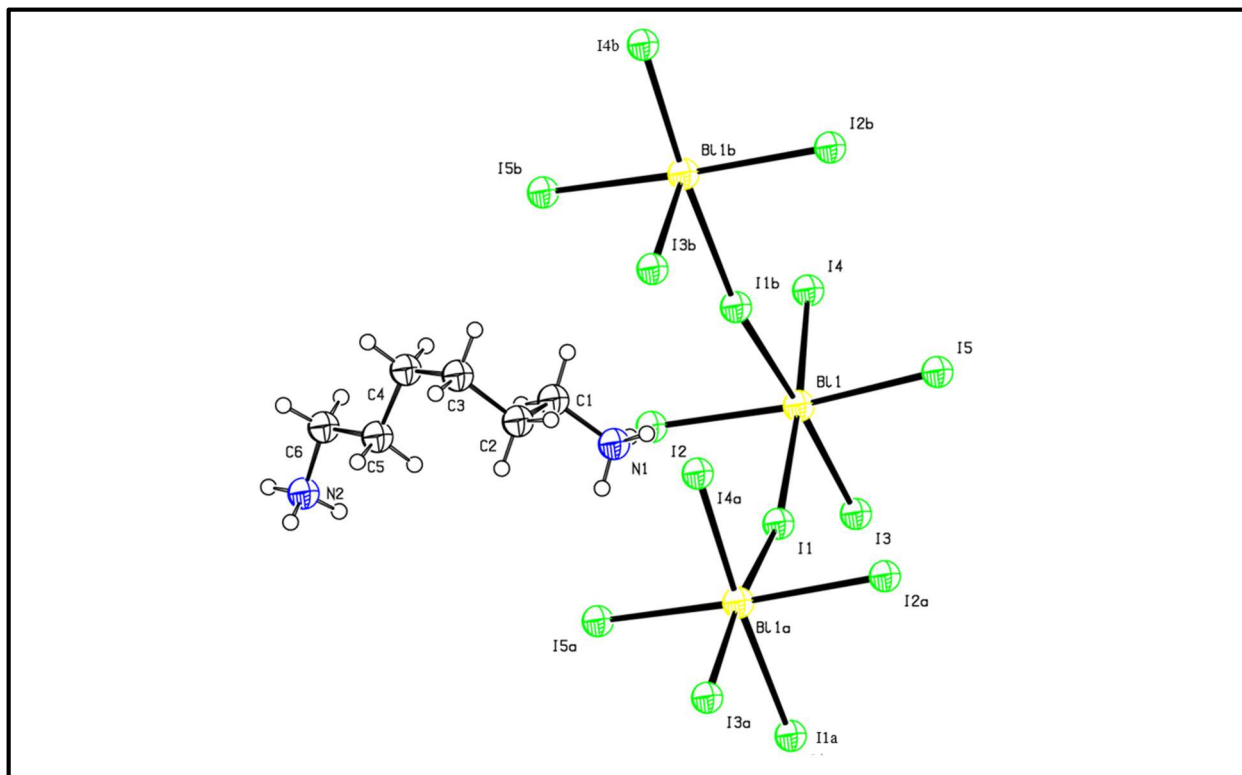


Figure 3.5. Molecular structure of HDABiI_5 , with thermal ellipsoids drawn at the 50% probability level and where green = iodine, yellow = bismuth, blue = nitrogen, white = carbon, and red = oxygen.

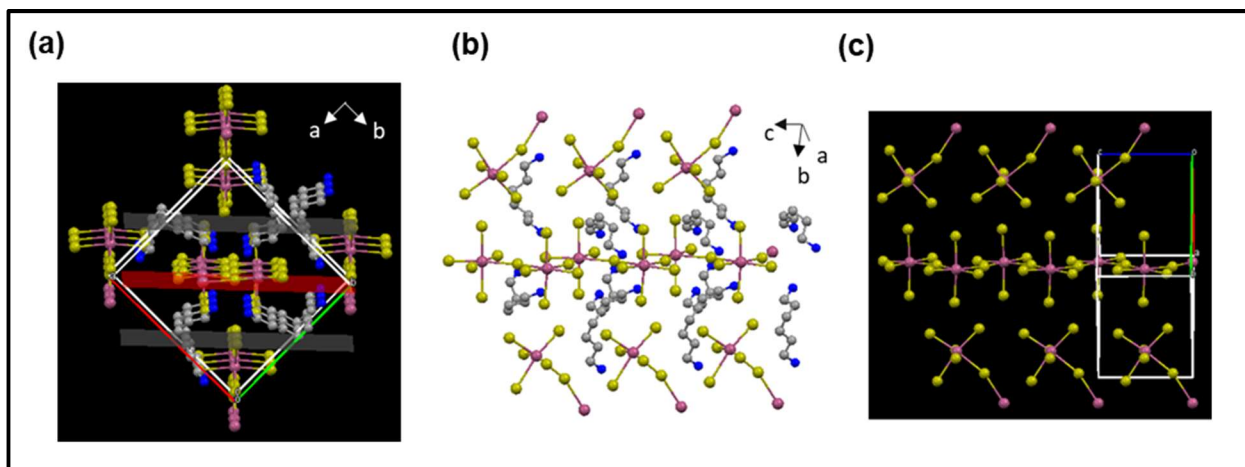


Figure 3.6. (a) $1 \times 1 \times 3$ unit cell structure of HDABiI₅ with orientation in the [110] direction. The red plane indicates the (110) plane, the gray planes indicate (220) planes, purple spheres = bismuth, gold spheres = iodide, gray spheres = carbon, and blue spheres = nitrogen. (b) The same structure as displayed in panel (a) but rotated 90°. (c) The same structure as displayed in panel (b) with the organic HDA²⁺ groups removed. Hydrogens are omitted in each panel for clarity.

along the c-axis (i.e. perpendicular to the plane of the page). The organic HDA²⁺ groups in the HDABiI₅ structure are “c”-shaped, supporting the notion that there is some bonding interaction between terminal amine groups of HDA²⁺ and iodides of BiI₅²⁻ that is causing the HDA²⁺ groups to bend.

In Figure 3.6b, the same structure is displayed but rotated 90° and Figure 3.6c is also the same structure but with the HDA²⁺ groups omitted. Figures 3.6b and 3.6c highlight the inorganic BiI₅²⁻ framework of HDABiI₅ through which rapid charge-carrier conduction takes place.¹⁰ Since the inorganic framework is only one-dimensional, charge-carrier conduction is conjectured to be much faster intra-chain along the c-axis than inter-chain along the a-axis and b-axis. Table 3.3 shows crystallographic information pertaining to the HDABiI₅ single crystal.

Synchrotron XRD was performed on HDABiI₅ powders scraped off of thin films (Figure 3.7, red trace) The diffraction patterns are consistent with the calculated powder pattern based on single-crystal data (Figure 3.7, black trace). The similarity in diffraction patterns confirms that the

HDABiI₅ single crystal that grows in solution has the same structure as the HDABiI₅ thin film that crystallizes during annealing.

To guide experimental design, density functional theory (DFT) calculations were performed to determine the structural stability, bandgap, and optical absorption spectrum of

Table 3.3. Crystallographic data for HDABiI₅.

HDABiI ₅	
Empirical formula	[C ₆ H ₁₈ Bi I ₅ N ₂] _∞
Formula weight	961.70
Temperature	128(2) K
Crystal system	Orthorhombic
Space group	Pna2 ₁
a	15.0653(13)
b	14.1204(12)
c	8.6201(8)
α	90 °
β	90 °
γ	90 °
Volume	1833.7(3)
Z	4
Calculated density	3.484 g/cm ³
Absorption coefficient	18.012 mm ⁻¹
F(000)	1664
Crystal size	0.276 x 0.127 x 0.125 mm
Crystal color	red
θ range for data collection	1.977 to 27.100°
Index ranges	-19 ≤ h ≤ 19, -18 ≤ k ≤ 17, -11 ≤ l ≤ 11
Reflections collected/unique	18044/3940
Completeness to θ = 25.50°	99.7 %
Absorption correction	Semi-empirical from equivalents

HDABi₅ (Figure 3.8). The HSE06 functional was employed with SOC effects explicitly included for all calculations. HSE06 is a hybrid DFT functional that generally performs well for these perovskite-halide and bismuth-halide-type materials.³³

The indirect band gap of HDABi₅ was calculated to be 2.01 eV and the direct band gap

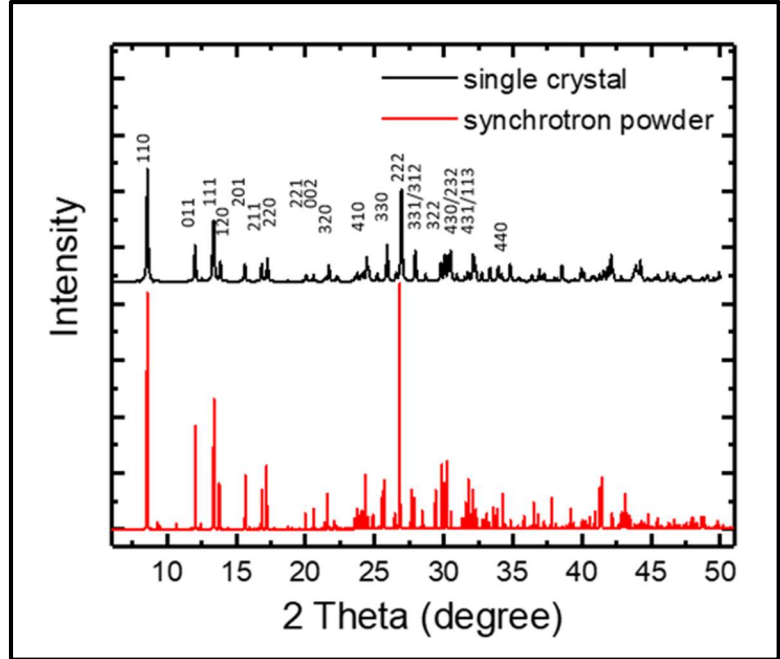


Figure 3.7. X-ray diffraction patterns of HDABi₅ predicted from the resolved single-crystal structure (black trace) compared to powders scraped off of thin films measured using a synchrotron source (red trace).

was calculated to be 2.03 eV, which shows very good agreement with previously published experimental measurements (presented in Chapter 2) of 2.05 eV and 2.15 eV, respectively.³² Inclusion of SOC was important due to the large effect it has on the bandgap of hybrid lead/bismuth-halide materials, since SOC has a large impact on the electronic structure of heavy 6p ions.³⁴ SOC lowers the calculated bandgap of HDABi₅ by 0.68 eV. The calculated non-parabolic effective masses of the valence band maximum and conduction band minimum are smaller for electrons than holes: for holes these are 0.79 m_0 and 5.80 m_0 , respectively, and for the electrons these are 0.57 m_0 and 2.08 m_0 , respectively.

The calculated optical absorption spectrum agrees well with previously published absorption data presented in Chapter 2. Specifically, HDABi₅ shows a similarly large absorption coefficient just above the band gap, indicating strong optical absorption (Figure 3.9a). Strong

optical absorption is quite surprising for a one-dimensional hybrid organic–inorganic material.³⁵ For this reason, the calculated spectroscopic limited maximum efficiency (SLME),^{36–38} which is a metric to predict the maximum solar cell efficiency considering the direct/indirect nature of the band gap, the

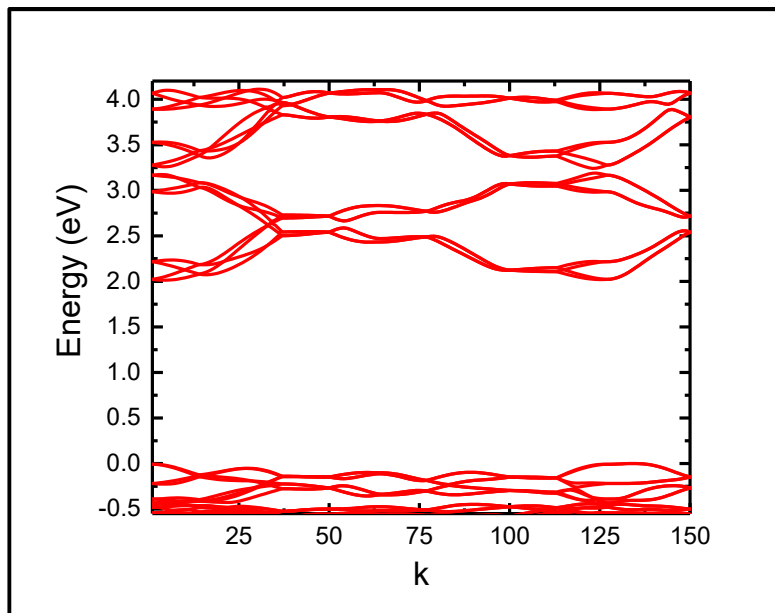


Figure 3.8. HSE06+SOC band structures of HDABiI₅. The valence-band maximum is set to 0 eV.

strength of optical absorption, and the thickness of the film, is > 20% for film thicknesses of > ~250 nm (Figure 3.9b). This is close to the Shockley-Queisser limit of 21.6 % for a material with a band gap of 2.05 eV. Unfortunately, these calculations can only be performed for materials whose crystal structures have been experimentally resolved from single-crystal XRD. At this time, HDABiI₅ is the only dicationic bismuth–halide material that does not contain water molecules for which single crystals suitable for structural resolution have been successfully grown.

A series of bismuth–iodide materials that contain organic dications and exhibit photovoltaic action were studied in order to elucidate the role that dicationic organic crystal fasteners have on the materials properties and performance as the photoactive layer in PVs. Table 3.4 lists optical bandgaps of these materials as thin films obtained from Ultraviolet–Visible (UV–Vis) electronic absorption data. The materials investigated were dicationic bismuth–iodide compounds which included those with alkyldiammonium groups with carbon-chain lengths of 2 (ethylenediamine, EDA), 4 (1,4-butanediamine, BDA), 6 (1,6-hexanediamine, HDA), or 12 (1,12-

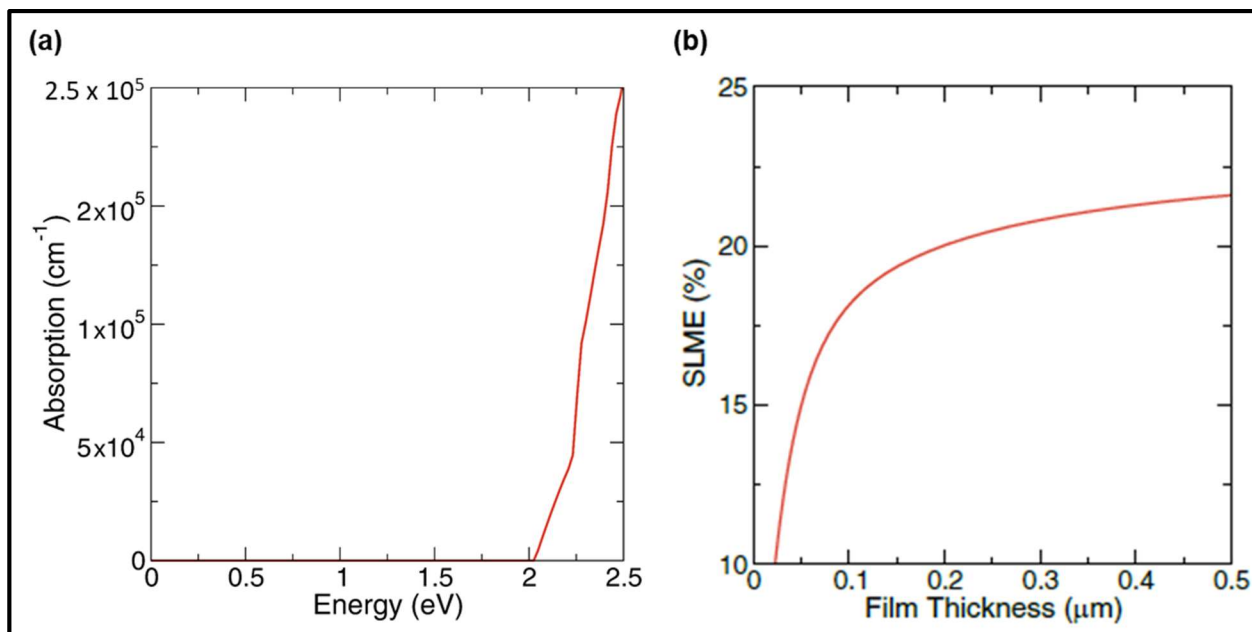


Figure 3.9. (a) Calculated optical absorption spectrum and (b) calculated spectroscopic limited maximum efficiency of HDABi₅.

dodecanediamine, DDDA), urea, phenylenediamine (PhDA), or hydrazine (hydra) as the organic moiety. The lowest bandgap material, determined by UV–Vis absorption, was hexanediammonium bismuth pentaiodide HDABi₅, which has an lowest-energy indirect bandgap transition of ~ 2.05 eV.³²

For carbon-chain lengths of 0–6, the optical bandgap decreases with increasing number of carbons, but increases for the 12-carbon chain (Figure 3.10). This suggests there is an optimal distance at which the bismuth–iodide chains prefer to be separated to absorb the most visible light and maintain the desired one-dimensional inorganic structural network. All bismuth–iodide-based films except EDABi₅ and (hydra)BiI₅ appeared smooth and transparent. It is conjectured that the organic dications serve as molecular fasteners, holding the crystal in place and keeping the bismuth–iodide chains intact.³⁹ For the case of EDABi₅ and (hydra)BiI₅, however, it is hypothesized that the organic dications are not large enough to maintain the structural integrity of

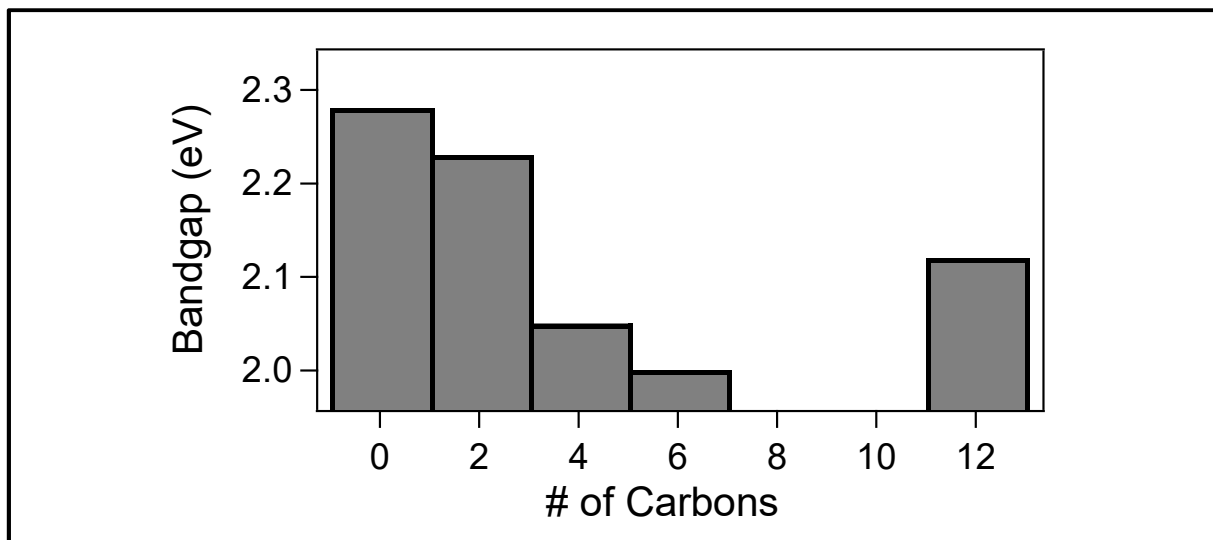


Figure 3.10. Optical bandgap as a function of number of carbons in the diammonium group for the hybrid bismuth–halide materials (hydra)BiI₅ (0 carbons), EDABiI₅ (2 carbons), BDABiI₅ (4 carbons), HDABiI₅ (6 carbons), and DDDABiI₅ (12 carbons).

the bismuth–iodide chains. As a result, the bismuth–iodide chains do not form and the resulting films scatter light significantly.

In the search for promising hybrid organic–inorganic PV absorbers, structural dimensionality has an important role in setting the material bandgap, charge-carrier effective masses, and optical absorption.³⁵ Generally, as structural dimensionality of the material decreases, bandgap increases.³⁵ Figure 3.11 depicts this trend in UV–Vis electronic absorption spectra of a series of hybrid organic–inorganic bismuth–iodide materials.


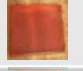





The structure of bismuth(III) iodide (BiI₃) is two-dimensional, and thus it has the longest-wavelength absorption onset (i.e. smallest band gap) of the series of materials. However, the BiI₃ thin film is a much weaker photoabsorber than the hybrid organic–inorganic materials, which suggests that the interaction between organic and inorganic moieties in these materials enhances absorption. EDA₂Bi₂I₁₀ and (FA_{0.75}Cs_{0.25})₃Bi₂I₉, where FA is formamidinium, have significantly blue-shifted absorption onsets in comparison to HDABiI₅. This discrepancy suggests that

EDA₂Bi₂I₁₀ and (FA_{0.75}Cs_{0.25})₃Bi₂I₉ are not one-dimensional materials like HDABiI₅,³² but are in fact zero-dimensional materials.

The absorption onset of 4,4'-bipyridinium bismuth iodide (bpyBiI₅) is intermediate between EDA₂Bi₂I₁₀ and (FA_{0.75}Cs_{0.25})₃Bi₂I₉ vs. HDABiI₅. The absorption onset of (PA)₂BiI₅ is gradual unlike those of the other materials presented in Figure 3.11. It is conjectured that the (PA)₂BiI₅ thin film is composed of a mix of two phases, one of which is one-dimensional and the other that is zero-dimensional. This is corroborated by

the XRD data of thin films presented in Figure 3.12. The XRD pattern of the HDABiI₅ thin film matches the patterns of the single crystal and powder presented in Figure 3.12, indicating a one-dimensional framework of corner-sharing bismuth–iodide octahedra. For the XRD pattern of (PA)₂BiI₅ (blue trace), however, there is a dominant peak at ~7.4° that can not be indexed to (PA)₂BiI₅ with a one-dimensional framework of corner-sharing octahedra. This un-indexed peak is postulated to be due to a zero-dimensional phase of the material.

Table 3.4. Optical bandgaps and corresponding digital images of a series of dicationic hybrid organic–inorganic bismuth–iodide thin films. HDA = 1,6-hexanediamine bismuth iodide, BDA = 1,4-butanediamine bismuth iodide, DDDA = 1,12-dodecanediamine bismuth iodide, PhDA = *p*-phenylenediamine bismuth iodide, EDA = 1,2-ethanediamine bismuth iodide, and hydra = hydrazine bismuth iodide.

Material	Optical Bandgap (eV)	
HDA	2.05	
BDA	2.10	
DDDA	2.17	
urea	2.21	
PhDA	2.24	
EDA	2.28	
hydra	2.33	

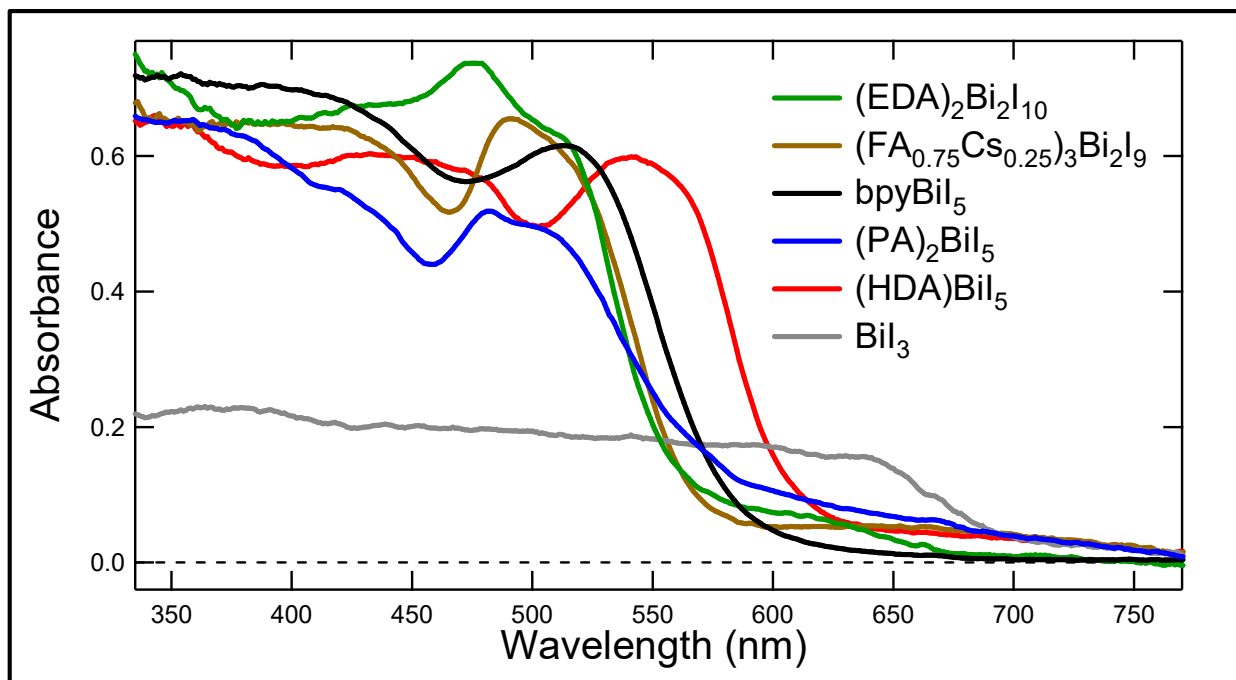


Figure 3.11. UV-Vis electronic absorption spectra of a series of organic-inorganic hybrid bismuth-halide thin films, which range in structural dimensionality from zero-dimensional to two-dimensional.

Spin-coat deposition of thin films in low-viscosity, low-boiling-point solvents has been shown to result in dense, pinhole-free, uniform thin films for high-efficiency perovskite solar cells.⁴⁰ A similar method was employed for the deposition of $(\text{PA})_2\text{BiI}_5$ with the goal of obtaining phase-pure $(\text{PA})_2\text{BiI}_5$ that is isostructural to the one-dimensional HDABiI_5 . The low-boiling-point solvent, acetonitrile, with 15 wt. % butylamine was used to dissolve $(\text{PA})_2\text{BiI}_5$, and $(\text{PA})_2\text{BiI}_5$ was spun-coat to obtain a dense, uniform film. The film was significantly more red in color than films processed using 4:1 DMF:DMSO, which appear more orange in color. There were no differences, however, in the resulting XRD patterns of thin films (Figure 3.13).

The grazing-incidence XRD pattern of a $(\text{FA}_{0.75}\text{Cs}_{0.25})_3\text{Bi}_2\text{I}_9$ thin film matches the calculated powder pattern for the single-crystal structure of $(\text{MA})_3\text{Bi}_2\text{I}_9$ reported by Kamminga and coworkers (Figure 3.14).⁴¹ $(\text{FA}_{0.75}\text{Cs}_{0.25})_3\text{Bi}_2\text{I}_9$ is a novel formulation and the 75%/25% FA/Cs mixed-cation organic moiety was chosen because: 1) FA and Cs are more stable alternatives to

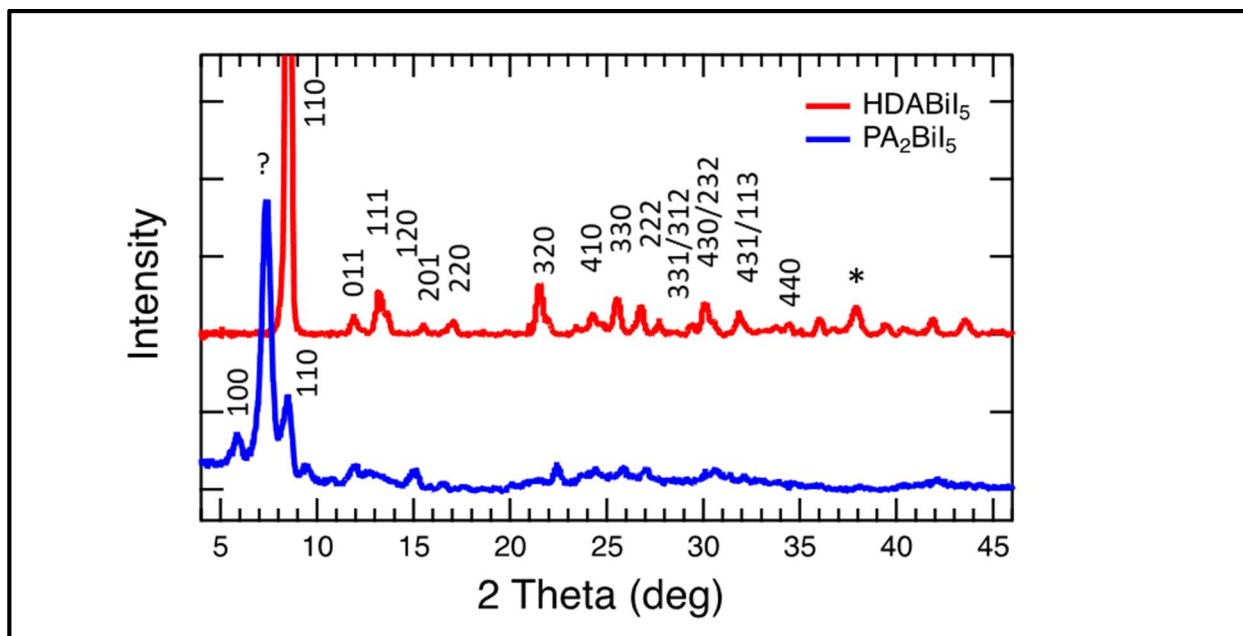


Figure 3.12. Grazing-incidence X-ray diffraction patterns of thin films of HDABi₅ (red trace) and (PA)₂Bi₅ (blue trace) on FTO.

MA as the organic moiety and 2) the 75%/25% FA/Cs mixture results in approximately the same average ionic radius as MA. This would yield a unit cell with approximately the same lattice constants and XRD peaks as long as the inorganic moieties are isostructural. In fact, this is the case, as the peak positions for the gold and gray traces are nearly identical. The inorganic framework was determined by Kamminga and coworkers to be zero-dimensional and the framework consists of face-sharing binuclear clusters of bismuth–iodide octahedra.⁴¹

Since the XRD patterns are nearly identical, it can be concluded that (FA_{0.75}Cs_{0.25})₃Bi₂I₉ is isostructural to (MA)₃Bi₂I₉ and consists of zero-dimensional face-sharing binuclear clusters of

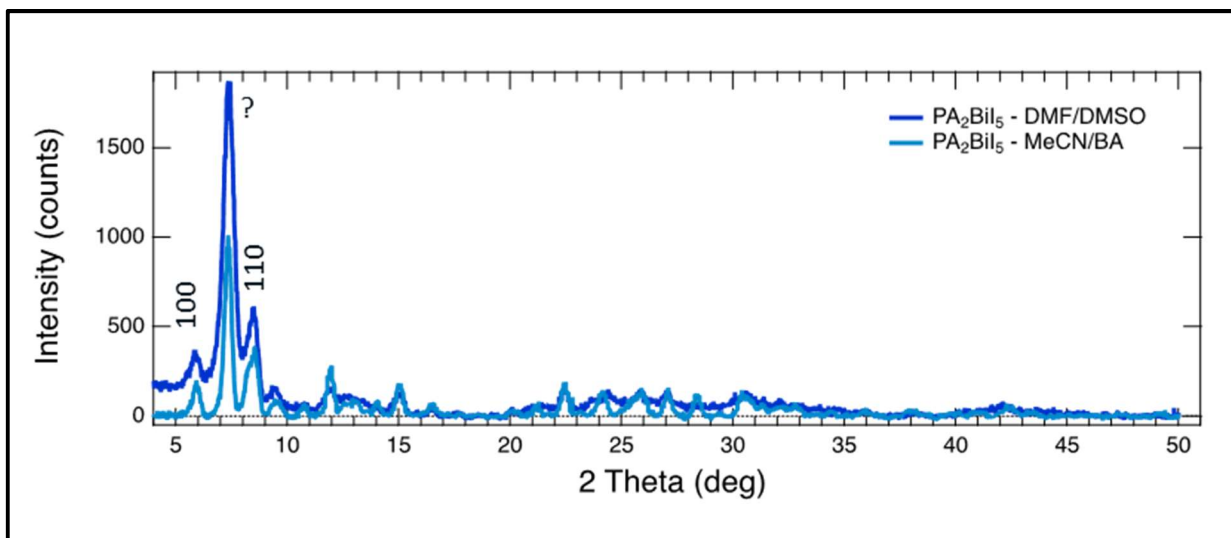


Figure 3.13. Grazing-incidence X-ray diffraction patterns of thin films of $(\text{PA})_2\text{BiI}_5$ processed in the conventional 4:1 DMF:DMSO solvent mixture and processed in an alternative acetonitrile (MeCN) with 15 wt. % butylamine (BA).

bismuth-iodide octahedra. This provides rationale as to why $(\text{FA}_{0.75}\text{Cs}_{0.25})_3\text{Bi}_2\text{I}_9$ has the shortest-wavelength absorption onset of the series. Because the absorption onset of $(\text{EDA})_2\text{Bi}_2\text{I}_{10}$ is in approximately the same position as that of $(\text{FA}_{0.75}\text{Cs}_{0.25})_3\text{Bi}_2\text{I}_9$, it is likely that $(\text{EDA})_2\text{Bi}_2\text{I}_{10}$ is a zero-dimensional material, but instead consists of edge-sharing binuclear clusters of bismuth-

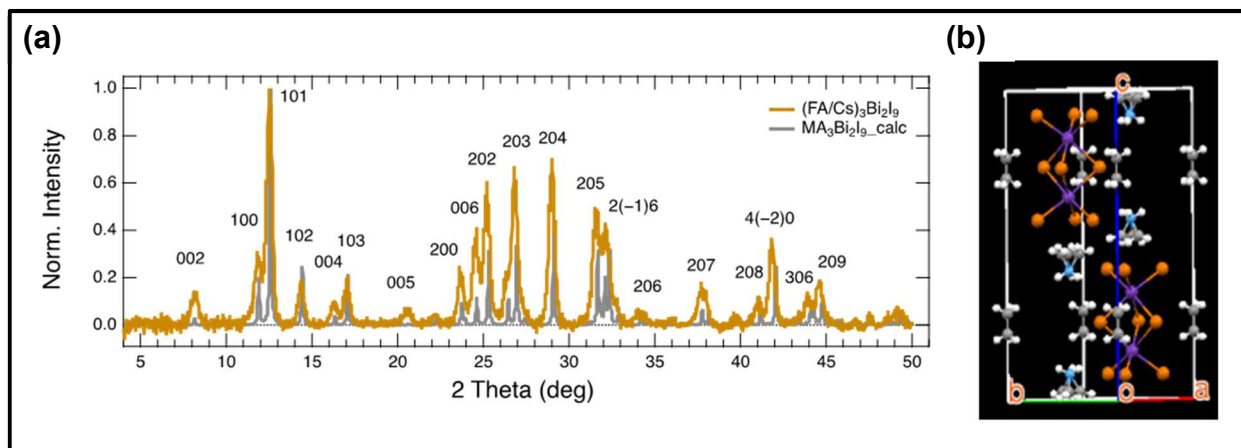


Figure 3.14. (a) Grazing-incidence X-ray diffraction patterns of a thin film of $(\text{FA}_{0.75}\text{Cs}_{0.25})_3\text{Bi}_2\text{I}_9$ on fluorine-doped tin-oxide-coated glass (gold trace) and the calculated powder pattern of analogous $(\text{MA})_3\text{Bi}_2\text{I}_9$ (gray trace). (b) Single-crystal structure of analogous $\text{MA}_3\text{Bi}_2\text{I}_9$, recreated from a .cif file provided by Kamminga and coworkers.

iodide octahedra, as was determined for the hydrated form of the material, $(\text{EDA})_2\text{Bi}_2\text{I}_{10}\cdot 5\text{H}_2\text{O}$, for which the single-crystal structure is shown earlier in this chapter (Figure 3.3).

Ultrafast laser spectroscopic techniques were employed to characterize the photophysical properties of hybrid bismuth–iodide thin films. In TRMC, photogeneration of mobile charge carriers in the sample leads to an increase of the transient photoconductance, and consequently to the enhanced absorption of microwave power by the sample.⁴² Thus, charge-carrier dynamics can be probed with TRMC. Figures 3.15, 3.16, and 3.17 show fluence-dependent TRMC kinetic traces of HDABiI₅, $(\text{FA}_{0.75}\text{Cs}_{0.25})_3\text{Bi}_2\text{I}_9$, and bpyBiI₅, respectively. It is observed from the kinetic traces of the HDABiI₅ thin film that there is a fast component and a slow component, which have lifetimes of $\tau_1 = 10.3$ ns and $\tau_2 = 315.7$ ns, respectively, based on a global fitting to a biexponential decay function (Figure 3.15). The fast decay component can be attributed to carrier trapping, and the slow decay component are most likely attributed to carrier recombination.⁴³ The kinetic traces for a bpyBiI₅ thin film are shown in Figure 3.16 and global fitting to a biexponential decay function yields lifetimes of $\tau_1 = 8.0$ ns and $\tau_2 = 352.2$ ns, very similar to the lifetimes calculated for HDABiI₅. These comparable lifetimes suggest that bpyBiI₅, like HDABiI₅, is composed of one-dimensional chains of bismuth–iodide octahedra. The charge-carrier recombination lifetimes in the range of 300-400 ns for HDABiI₅ and bpyBiI₅ are comparable to those of state-of-the-art methylammonium lead iodide (MAPbI₃)

In Figure 3.17, it is evident that the carrier lifetimes of the $(\text{FA}_{0.75}\text{Cs}_{0.25})_3\text{Bi}_2\text{I}_9$ thin film are faster than the instrument response (i.e. the cavity ring-down time), which is expected to be roughly 5 ns. The drastic difference in the kinetics of $(\text{FA}_{0.75}\text{Cs}_{0.25})_3\text{Bi}_2\text{I}_9$ vs. HDABiI₅ supports the conclusion that the inorganic framework of $(\text{FA}_{0.75}\text{Cs}_{0.25})_3\text{Bi}_2\text{I}_9$ is zero-dimensional.

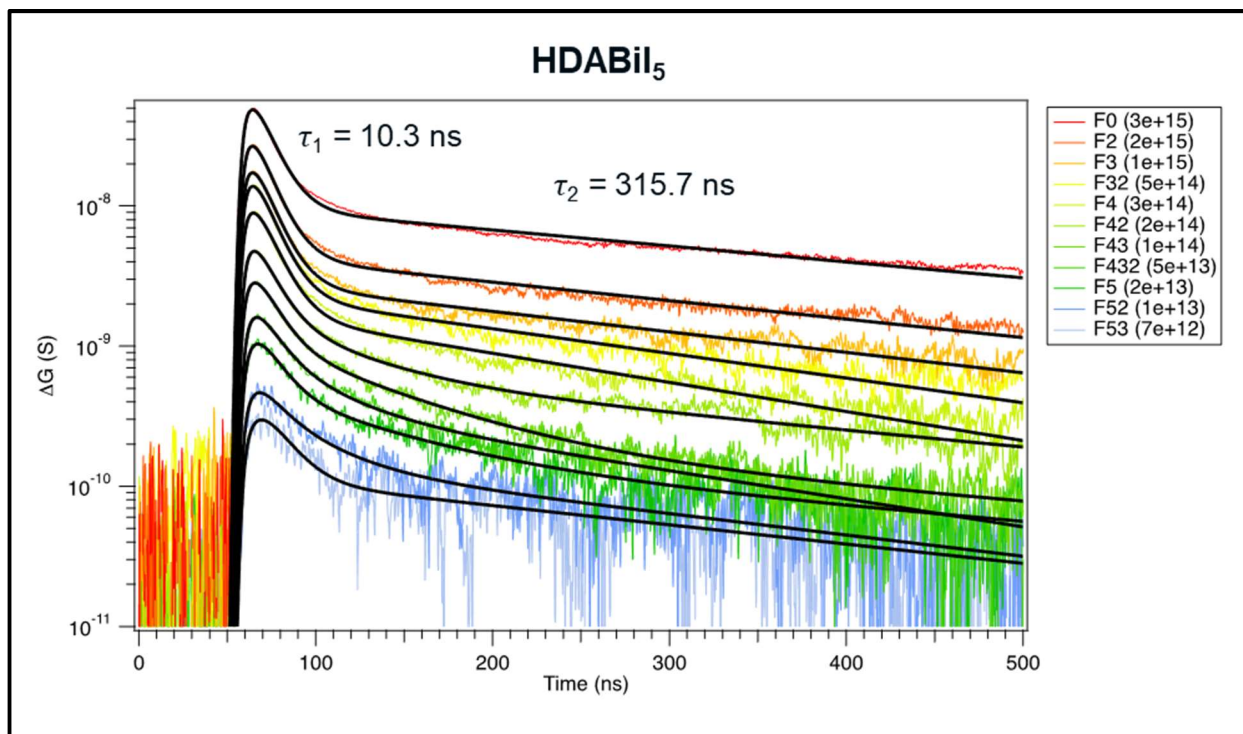


Figure 3.15. Time-resolved microwave conductivity traces of a thin film of HDABi₅ on a quartz substrate. Excitation laser fluence is shown in the legend in parentheses with units of photons/cm².

Transmission-mode transient absorption (TA) measurements were performed on a thin film of HDABi₅ on a quartz substrate (Figure 3.18). The spectra are described by an absorption–bleach–absorption pattern that follows the pattern of the second derivative of the steady-state absorption spectrum (black dashed trace). This indicates the presence of a trapped-carrier-induced Stark effect and stable exciton formation, which is common for materials with low structural dimensionality such as quantum dots and hybrid bismuth–halide materials.⁴⁴ The exciton binding energy can be estimated as the difference in the exciton-induced absorption (exciton IA) features, which for HDABi₅ is 310 meV. This happens to be 100 meV higher than that of the zero-dimensional MA₃Bi₂I₉. This may seem counterintuitive based on inorganic dimensionality, but for the case of MA₃Bi₂I₉ the binuclear clusters of bismuth–iodide octahedra separated by much small MA⁺ cations in comparison to bulky HDA²⁺ dications for the case of HDABi₅. TA spectra at t =

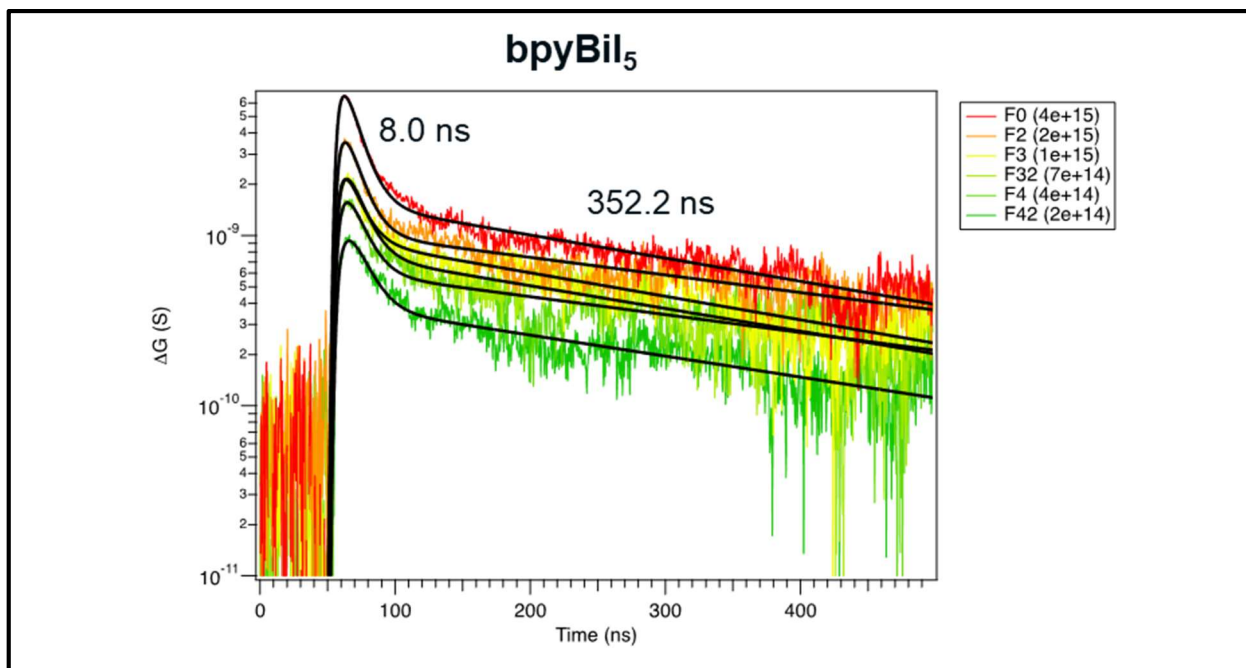


Figure 3.16. Time-resolved microwave conductivity traces of a thin film of bpyBiI₅ on a quartz substrate. Excitation laser fluence is shown in the legend in parentheses with units of photons/cm².

0 and TA kinetic traces using 450 nm laser excitation of one-dimensional HDABiI₅ (red traces), supposed one-dimensional bpyBiI₅ (black traces) and zero-dimensional (FA_{0.75}Cs_{0.25})₃Bi₂I₉ (gold traces) are shown in Figure 3.19. The spectrum of each material (Figure 3.19a) follows an absorption–bleach–absorption pattern, as observed with HDABiI₅, which makes sense as the materials have confined inorganic dimensionalities that cause the materials to be excitonic. In Figure 3.19b, TA kinetic traces of each material are shown. The kinetic traces were probed at the peak corresponding to the long-wavelength exciton IA feature for each material. Fitting to a biexponential decay function yields lifetimes of $\tau_1 = 23$ ps and $\tau_2 = 2.9$ ns for HDABiI₅, $\tau_1 = 11$ ps and $\tau_2 = 2.5$ ns for bpyBiI₅, and $\tau_1 = 42$ ps and $\tau_2 = 79$ ps for (FA_{0.75}Cs_{0.25})₃Bi₂I₉. Indeed, the long-lived component of the kinetic traces (τ_2) follow the trend of the inorganic structural dimensionalities of each material much like the TRMC data (Figures 3.15, 3.16, and 3.17). For the

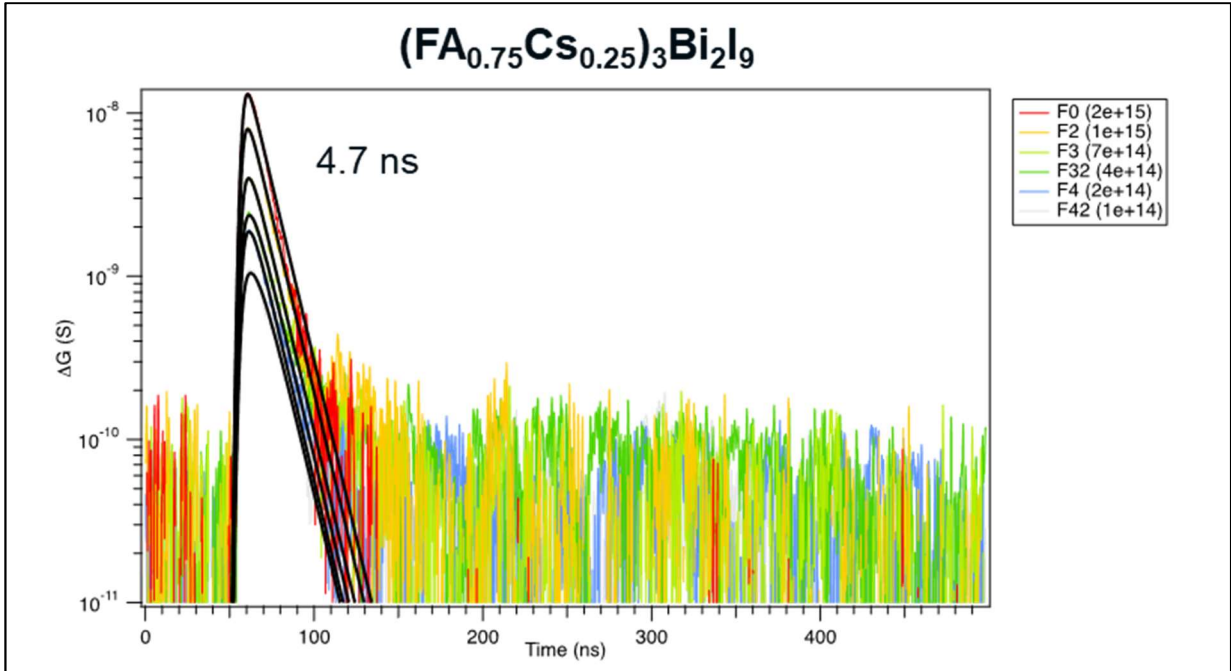


Figure 3.17. Time-resolved microwave conductivity traces of a $(\text{FA}_{0.75}\text{Cs}_{0.25})_3\text{Bi}_2\text{I}_9$ thin film on a quartz substrate. Excitation laser fluence is shown in the legend in parentheses with units of photons/cm².

one-dimensional materials HDABiI₅ and bpyBiI₅, the lifetimes of exciton IA are longer than 2 ns, and the exciton IA lifetime for the zero-dimensional $(\text{FA}_{0.75}\text{Cs}_{0.25})_3\text{Bi}_2\text{I}_9$ is significantly shorter.

The determination of an ideal solution deposition method for the series of hybrid bismuth-iodide materials under investigation is not trivial. It became apparent during the study of these materials that not one solution deposition method yielded the highest-quality film for each material. This is evident in the data presented in Figure 3.20. Under the assumption that the sum of absorptance, transmittance, and reflectance equals 1, the y-axis of Figure 3.20a could also be expressed as absorptance + reflectance. Assuming nominally identical thicknesses, absorptance should be constant regardless of deposition method. It is clear that reflectance is higher for the HDABiI₅ film processed using the FDC method with chlorobenzene as the antisolvent ('HDA_CB-freeze') than the film processed by the one-step deposition technique ('HDA_1-step'). This is evident by the fact that y-values at longer wavelengths than the absorption onset (i.e. >

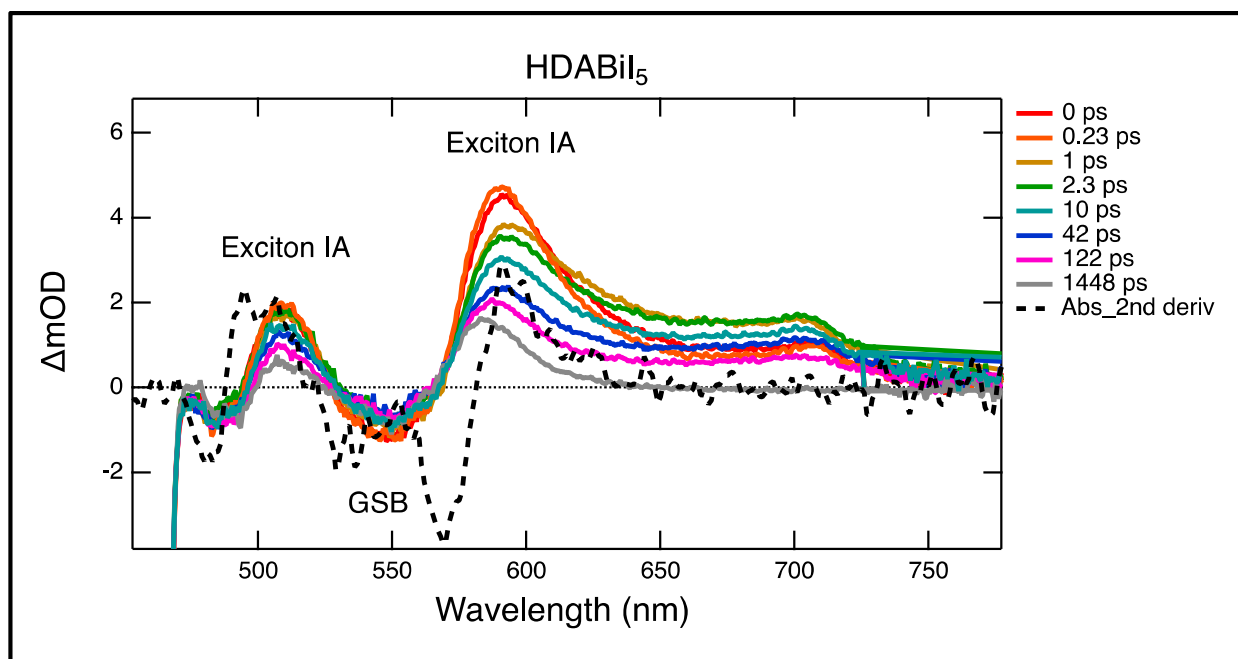


Figure 3.18. Transient absorption spectra of a thin film of HDABiI₅ using 450 nm laser excitation, with $t = 0$ indicating where the magnitude of ΔmOD integrated over wavelength was the largest (red trace). The black dashed trace is the second derivative of the steady-state absorption spectrum. Exciton IA = exciton-induced absorption, GSB = ground-state bleaching.

~625 nm) for ‘HDA_CB-freeze’ are larger than those for ‘HDA_1-step’. However, the opposite is true for (PA)₂BiI₅ (blue traces). The difference in absorption onset wavelength between HDABiI₅

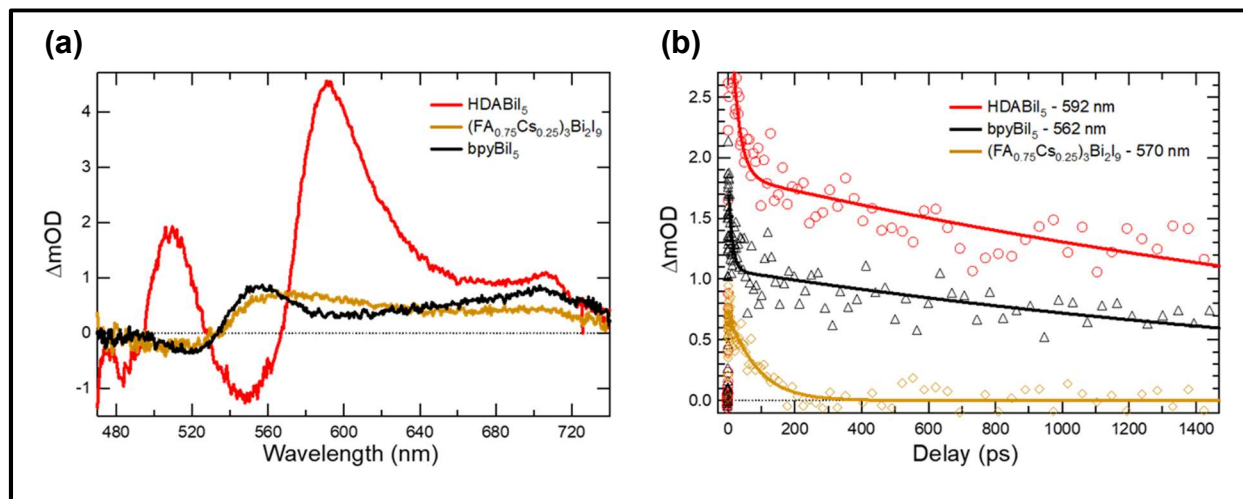


Figure 3.19. (a) Transient absorption spectra at $t = 0$ and (b) kinetic traces of thin films of one-dimensional HDABiI₅ (red traces), supposed one-dimensional bpyBiI₅ (black traces), and zero-dimensional (FA_{0.75}Cs_{0.25})₃Bi₂I₉ (gold traces) using 450 nm laser excitation.

and $(\text{PA})_2\text{BiI}_5$ can explain the clear difference in film color (Figure 3.20b).

The disparity in absorption onset and film color can also be explained through differences in thin-film coverage. It is evident from plan-view SEM images of HDABiI_5 (Figure 3.21a and 3.21b) and $(\text{PA})_2\text{BiI}_5$ that even though both material thin films consist of lamellar microstructures, surface coverage of HDABiI_5 on a TiO_2/FTO substrate is far superior than for $(\text{PA})_2\text{BiI}_5$. The reason for this discrepancy is still unknown, but it is conjectured that the organic dicationic HDA^{2+} groups fasten the chains of bismuth–iodide octahedra together more effectively than the organic monocationic PA^+ groups.

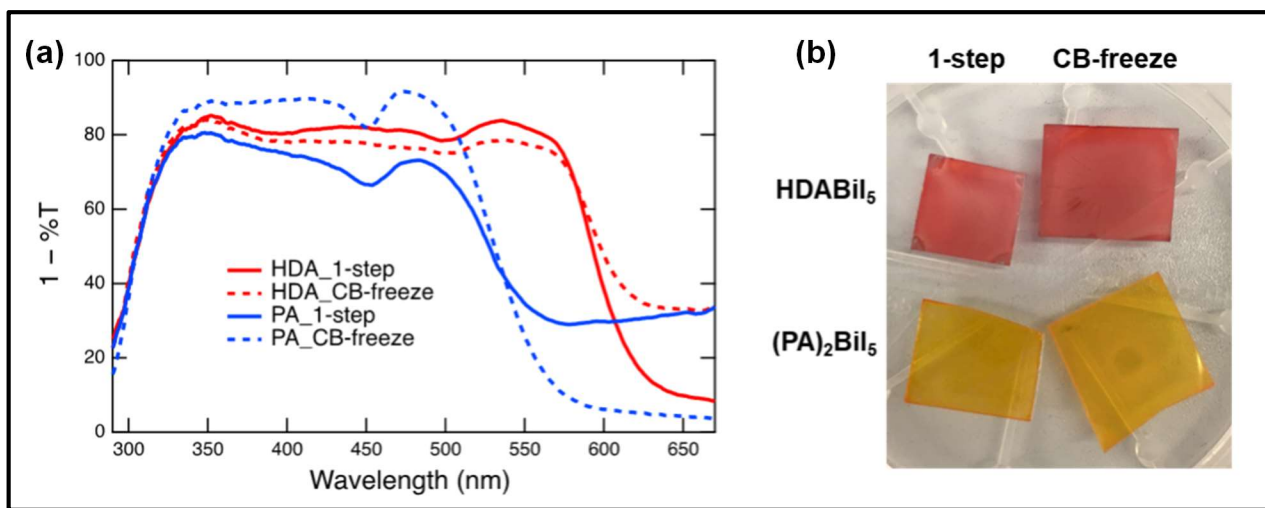


Figure 3.20. (a) Absorbance + reflectance spectra of HDABiI_5 (HDA, red traces) and $(\text{PA})_2\text{BiI}_5$ (PA_2 , blue traces) thin films deposited on glass using a conventional one-step deposition (solid traces) and using a fast deposition crystallization with chlorobenzene as antisolvent (CB-freeze). (b) Digital photograph images of the thin films corresponding to each absorbance spectrum.

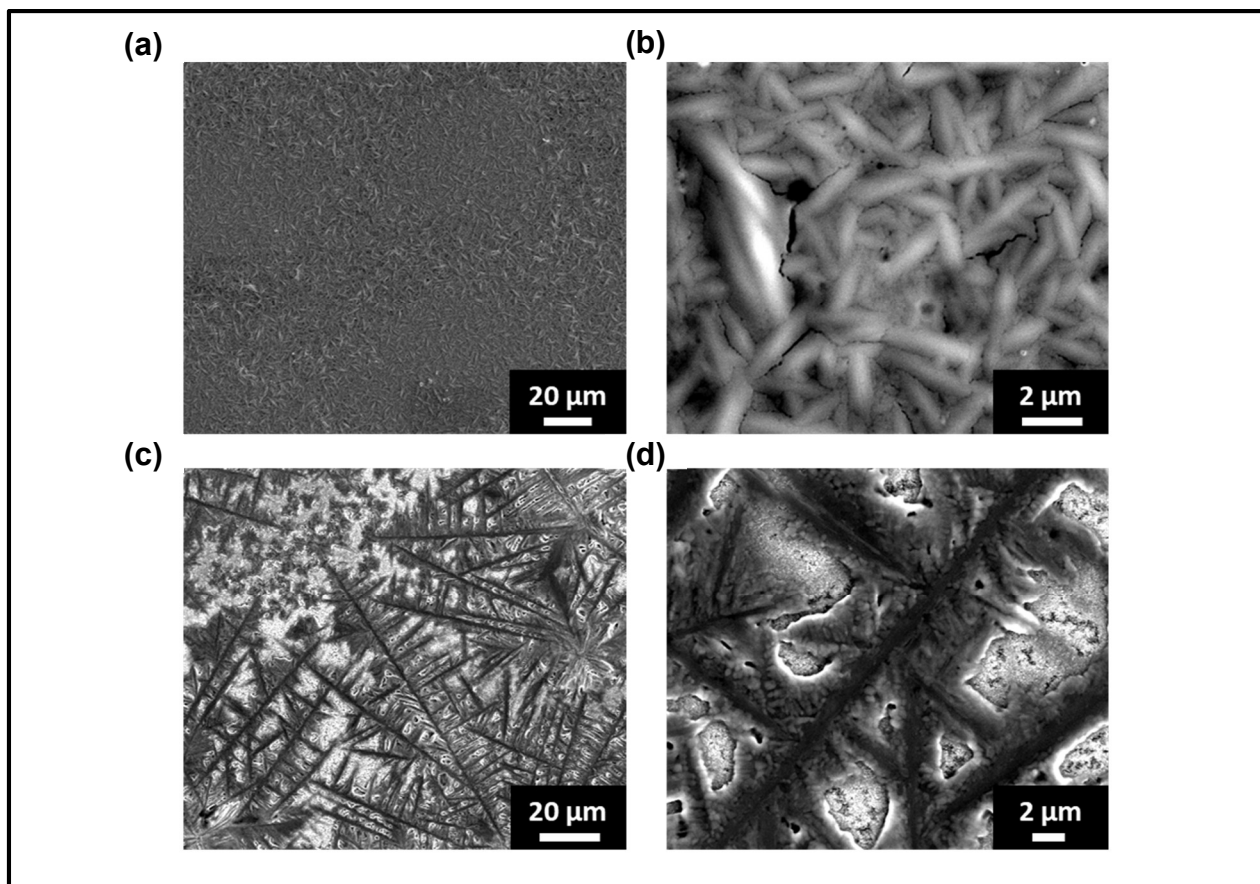


Figure 3.21. Plan-view scanning electron microscopy images of thin films of HDABiI₅/mTiO₂/cTiO₂/FTO (panels (a) and (b)) and (PA)₂BiI₅/mTiO₂/cTiO₂/FTO (panels (c) and (d)).

Absorption and steady-state emission spectra of thin films of HDABiI₅ and (PA)₂BiI₅ are displayed in Figure 3.22. The more gradual and blue-shifted absorption onset of (PA)₂BiI₅ compared to HDABiI₅ supports the XRD data that the (PA)₂BiI₅ film is composed of a mix of one-dimensional and zero-dimensional phases. Emission is present at the band edge of both materials, suggesting that the emission is not from intra-gap trap states. It is also evident in Figure 3.23 that there is no wavelength-dependent response to the emission of each film, indicating that the observed signal is not due to Raman scattering. Some overlap between the incident excitation light and the emission signal is apparent for 480 nm and 500 nm excitation of the (PA)₂BiI₅ film (Figure 3.23b).

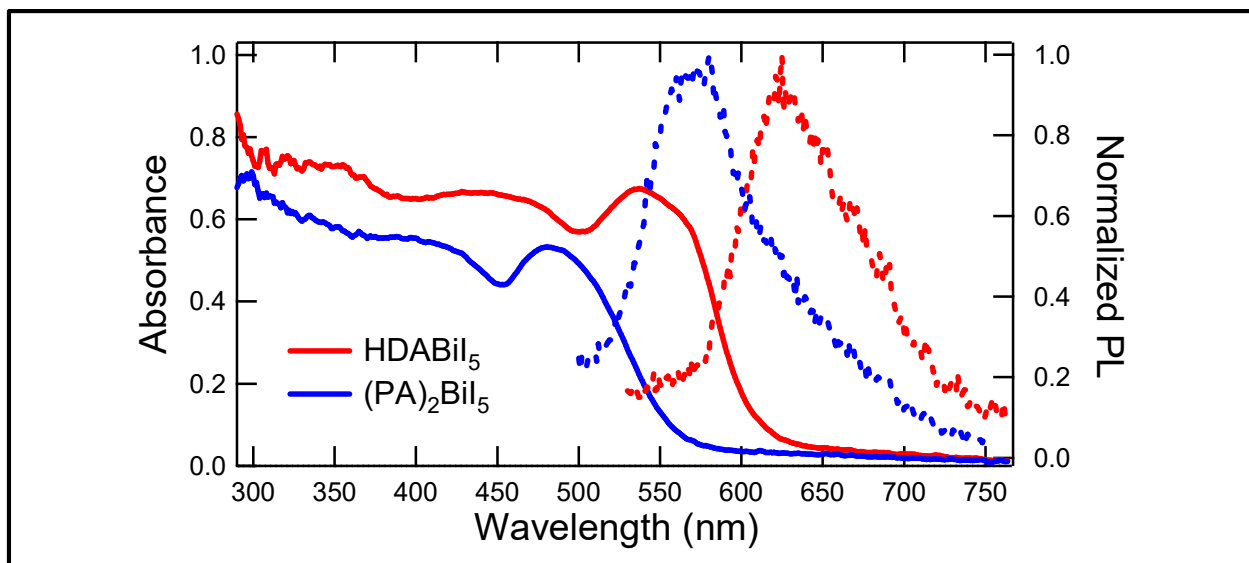


Figure 3.22. Absorption spectra (solid traces) and steady-state emission spectra (dashed traces) of thin films of HDABi₅ (red traces) and (PA)₂Bi₅ (blue traces) using 400 nm excitation.

The thermal stability of HDABi₅ and (PA)₂Bi₅ powders were assessed by thermogravimetric analysis (TGA) (Figure 3.24). The onset of significant mass loss occurs at a lower temperature for (PA)₂Bi₅ (< 250 °C) than for HDABi₅ (> 300 °C), which is depicted in the derivative plots (dash-dotted traces) of Figure 3.24a. It is also evident in Figure 3.24a that there is a non-zero slope of the mass loss curve of (PA)₂Bi₅ (blue solid trace) even at temperatures below 200 °C whereas the mass loss curve of HDABi₅ is flat (red solid trace). This difference is accentuated in the ramp and hold TGA data displayed in Figure 3.24b. The temperature in the

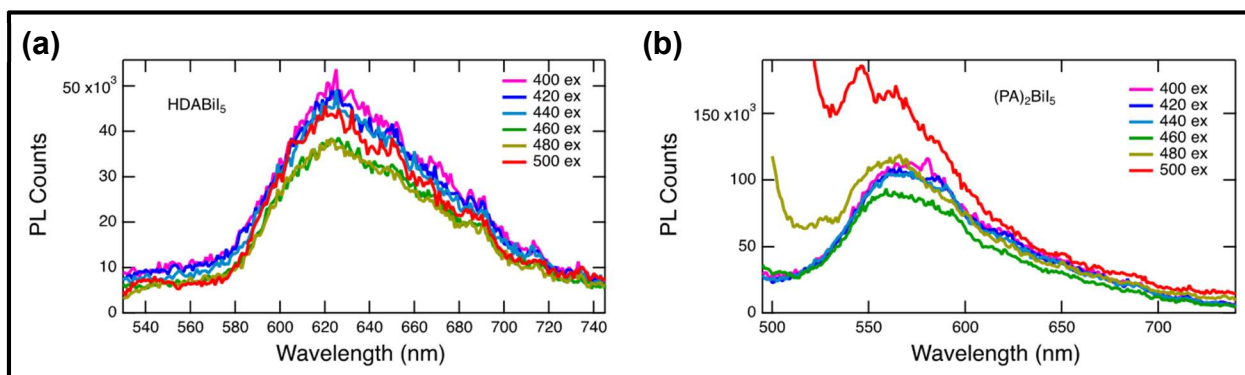


Figure 3.23. Steady-state emission spectra of thin films of (a) HDABi₅ and (b) (PA)₂Bi₅ using 400 nm excitation (pink traces) – 500 nm excitation (red traces).

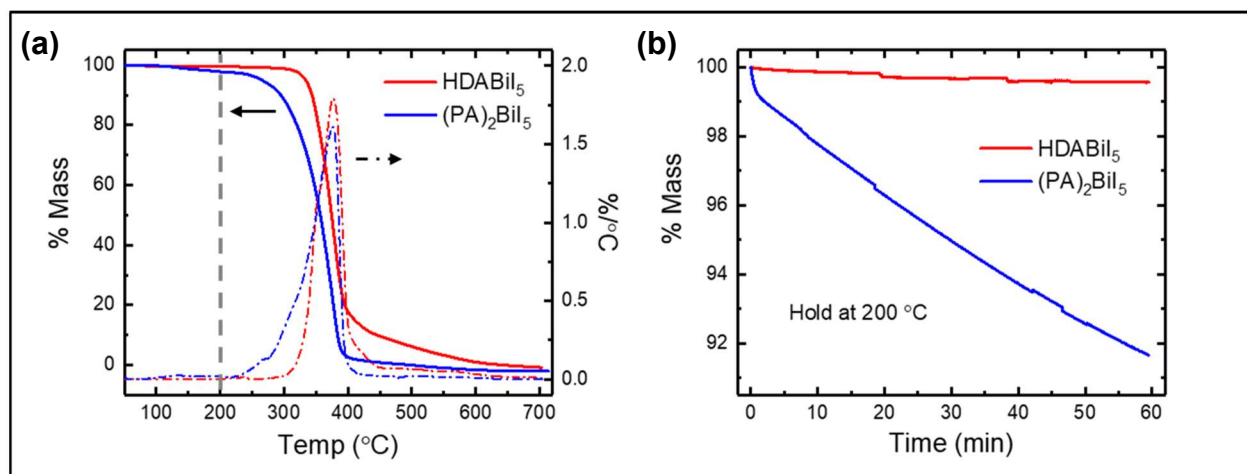


Figure 3.24. (a) Temperature-dependent thermogravimetric analysis of HDABi₅ powder (red traces) and (PA)₂Bi₅ powder (blue traces). The solid curves correspond to the % mass remaining (left axis) and the dash-dotted curves correspond to the derivative of the % mass with respect to temperature (right axis). The gray dotted vertical line corresponds to the temperature used in panel b. (b) Isothermal thermogravimetric analysis at 200 °C as a function of time.

TGA chamber was ramped to 200 °C and then held and monitored at 200 °C. After 1 hour, the (PA)₂Bi₅ powder sample had ~8% mass loss, whereas HDABi₅ had ~0.5% mass loss. The greater thermal stability of HDABi₅ compared to (PA)₂Bi₅ can be rationalized by differences in boiling points of the organic precursors. The boiling point of HDA is 204 °C and the boiling point of PA is 49 °C. In addition, part of the superior stability of HDABi₅ could be explained by the molecular fasterner effect, where organic dicationic HDA²⁺ groups give HDABi₅ more structural rigidity than the organic monocationic PA⁺ groups for (PA)₂Bi₅.

Photovoltaics (PV) devices containing (PA)₂Bi₅ as the photoactive layer were fabricated with an n–i–p architecture of FTO/cTiO₂/mTiO₂/(PA)₂Bi₅/spiro-OMeTAD/Au. PV devices were fabricated in a similar manner as those containing HDABi₅ presented in Chapter 2. (PA)₂Bi₅-containing PV devices were measured using two-electrode cyclic voltammetry and exhibited significant shunting, as indicated by the *J–E* curve of the (PA)₂Bi₅-containing device measured in the light passing through the origin (Figure 3.25a). Incomplete surface coverage of (PA)₂Bi₅ on the underlying TiO₂ layer results in shunting pathways for electronic charges (Figure 3.21).

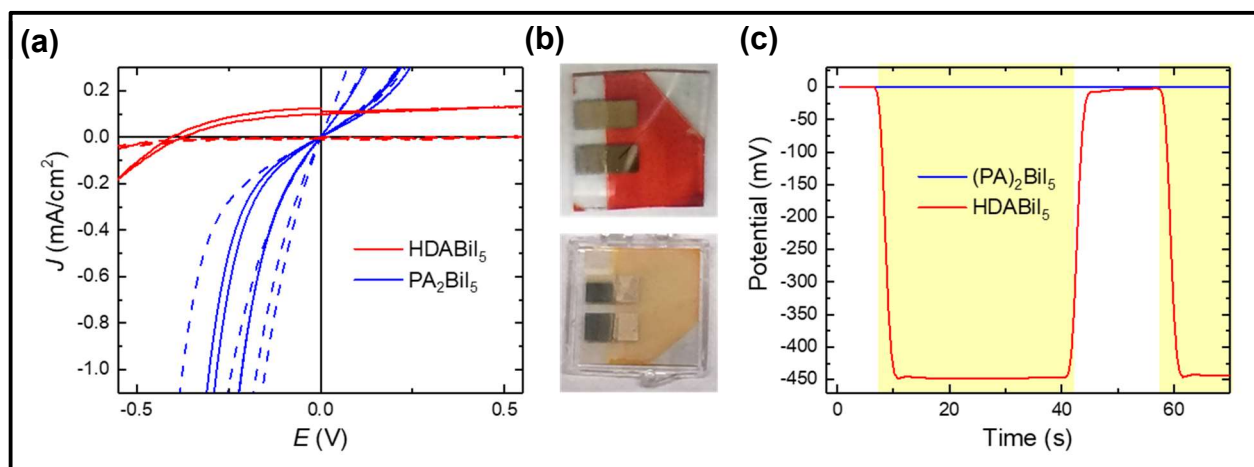


Figure 3.25. (a) J - E behavior for solar cells consisting of Au/spiro-OMeTAD/Bi/TiO_x/FTO, where Bi is HDABiI₅ (red trace) or (PA)₂BiI₅ (blue trace) and where dashed traces are measurements performed in the dark and solid traces are measurements performed under 1 Sun illumination. (b) Digital photograph images of the solar cells containing HDABiI₅ (top) and (PA)₂BiI₅ (bottom). (c) Chronoamperometry measurements of (PA)₂BiI₅ (blue trace) and HDABiI₅ (red trace). Yellow shaded regions indicate periods of time the solar cells were under 1 Sun illumination.

Because the (PA)₂BiI₅-containing devices have shunting pathways, negligible photocurrent (Figure 3.25c) and therefore negligible sunlight-to-electricity power-conversion efficiency was observed.

PhDA²⁺ was targeted as a small conjugated organic moiety to incorporate into hybrid bismuth-halide solar cells. Small conjugated organic moieties were investigated, because the one-dimensional hybrid bismuth-halide thin films prefer a (110) orientation on an FTO substrate, which aligns the chains of bismuth-iodide octahedra in parallel to the substrate surface (i.e. in plane). Small conjugated organic groups could therefore assist in charge-carrier conduction through the plane of the thin film. At first, an attempt at synthesizing and isolating stable PhDABiI₅ proved challenging. Following deposition of a thin film of PhDABiI₅,

XRD measurements were carried out and no XRD peaks were obtained. It is hypothesized that the PhDA²⁺ groups favorably π -stack, which disrupts formation of a crystalline structure of PhDABiI₅. As a result, mixed-dication bismuth-halide materials, for which the mole percentage

of PhDA^{2+} did not exceed 25%, were explored. Figure 3.26a displays grazing-incidence XRD data of HDABiI_5 as well as 95%-5%, 85%-15%, and 75%-25% mixtures of organic dications HDA^{2+} and PhDA^{2+} incorporated as the organic moiety in hybrid bismuth–halide materials, denoted $(\text{HDA-PhDA})\text{BiI}_5$. With increasing amount of PhDA^{2+} , the (110) orientation became less favorable, further indicating that PhDA^{2+} groups were detrimental to the integrity of the one-

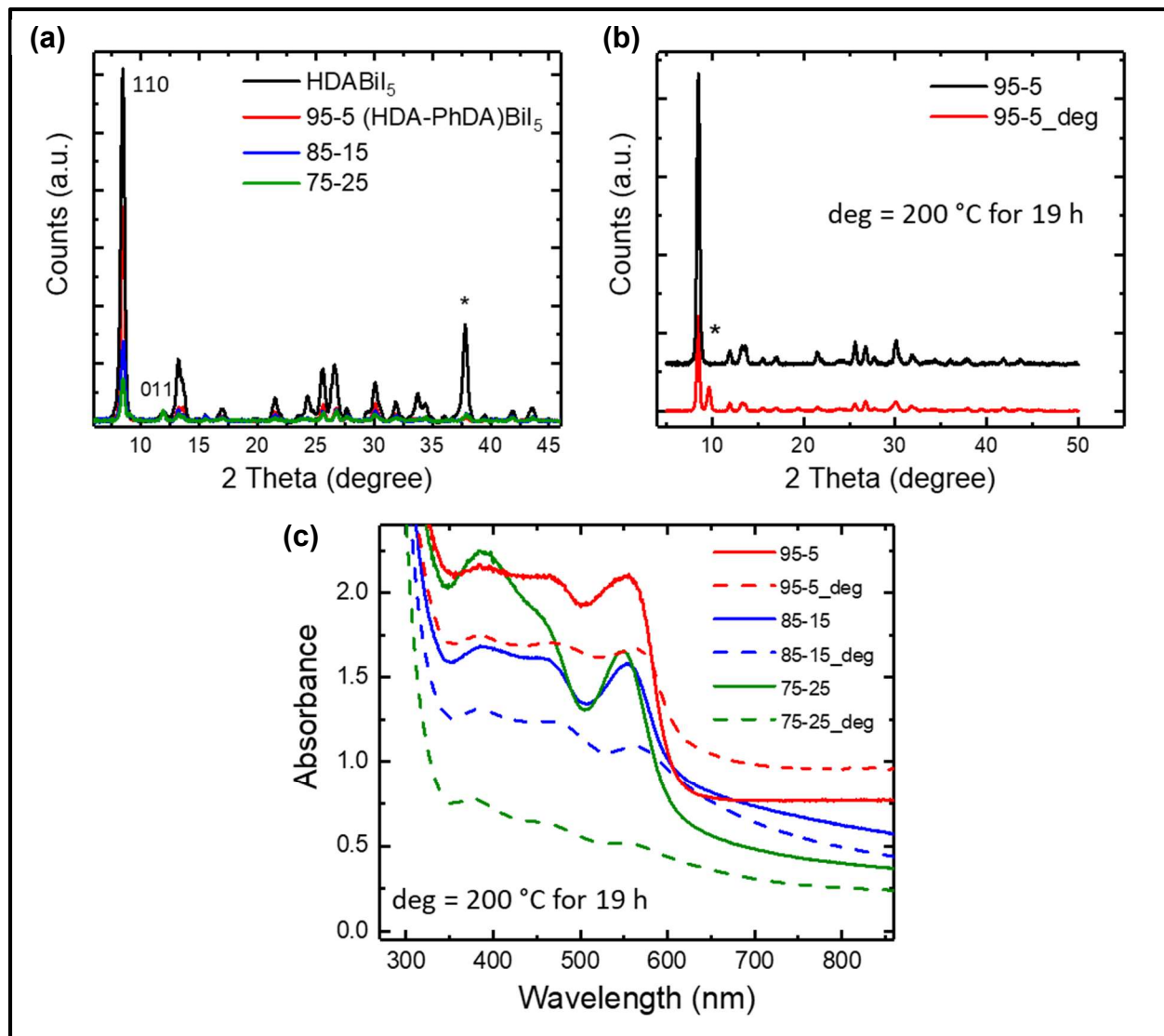


Figure 3.26. (a) Grazing-incidence X-ray diffraction patterns of HDABiI_5 and mixed organic dicationic $(\text{HDA-PhDA})\text{BiI}_5$ thin films normalized to the 011 peak at $\sim 12^\circ$. (b) Grazing-incidence X-ray diffraction patterns of a 95%-5% $(\text{HDA-PhDA})\text{BiI}_5$ thin film before and after thermal treatment at 200°C for 19 h. (c) Transmission-mode electronic absorption spectra of mixed organic dicationic $(\text{HDA-PhDA})\text{BiI}_5$ thin films before and after thermal treatment at 200°C for 19 h.

dimensional hybrid bismuth–halide structure. It is not apparent that incorporation of PhDA²⁺ adversely affects overall material stability, as noted by Figure 3.26b. A film of 95-5 (HDA-PhDA)BiI₅ is completely stable at 200 °C for 19 h. The only difference in XRD patterns before and after this thermal treatment was a peak that emerged at ~9.5 °, which cannot be attributed to decomposition to BiI₃. Absorption spectra of the series of mixed-dication bismuth–halide material thin films before and after thermal treatment were acquired and are displayed in Figure 3.26c. Percent absorbance losses at 500 nm for each thin film were determined to be 14.2%, 15.1%, and 57.9% for the 95-5, 85-15, and 75-25 (HDA-PhDA)BiI₅, respectively. Therefore, 95-5 and 85-15 (HDA-PhDA)BiI₅ have been deemed strong candidates for enhanced conductivity hybrid bismuth–halide PVs.

To assess the conductivity of the mixed-dication bismuth–halide materials, through-plane conductivity measurements were

carried out on devices with the architecture FTO/Bi/Au, where Bi was the photoactive hybrid bismuth–halide thin film (Figure 3.27). Preparing solution-deposited films for through-plane conductivity measurement can be quite difficult as pinhole-free films are required in order to prevent shunting by way of Au being in contact with FTO. It is

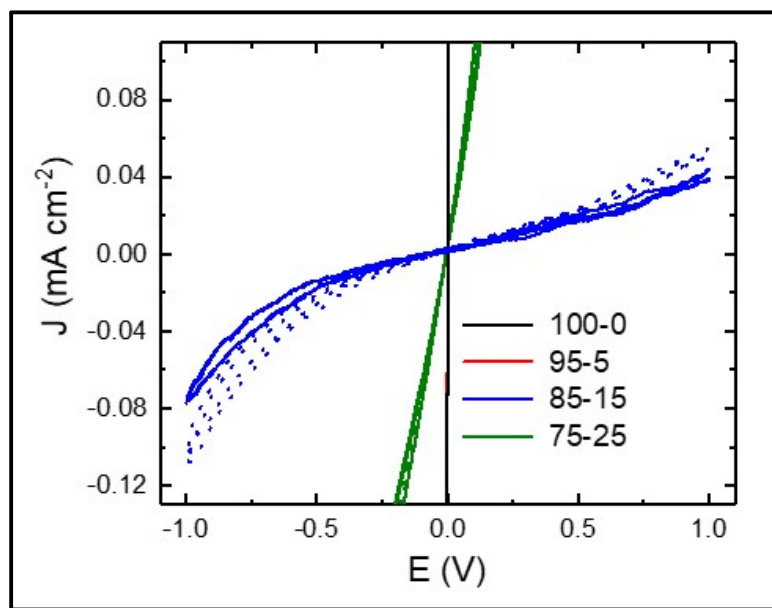


Figure 3.27. Through-plane conductivity J - E measurements of HDABiI₅ (100-0) and the mixed-dication (HDA-PhDA)BiI₅ (95-5, 85-15, 75-25) thin films. The blue solid trace is a measurement of 85-15 (HDA-PhDA)BiI₅ conducted in the dark and the blue dashed trace is a measurement conducted under 1 Sun illumination.

apparent that the devices containing HDABiI₅ (100-0) and 95-5 (HDA-PhDA)BiI₅ exhibited significant shunting and the device containing 75-25 (HDA-PhDA)BiI₅ exhibited appreciable shunting. This is not representative of the conductivity of the hybrid bismuth–halide material layer, as the path of least resistance for current to flow is from FTO to Au or vice versa. The FTO/85-15 (HDA-PhDA)BiI₅/Au device, however, behaves as expected. This suggests that the 85-15 (HDA-PhDA)BiI₅ has superior film coverage on FTO compared to the other hybrid bismuth–halide materials. It can also be noted that the 85-15 (HDA-PhDA)BiI₅ layer alone is photoconductive, as the current density values measured under 1 Sun illumination are of larger magnitude than those measured in the dark.

3.4 Conclusions

In the work presented in this chapter, a series of hybrid organic–inorganic bismuth–halide materials that contained divalent organic cations were studied as stable alternatives to those incorporating conventional monovalent organic cations employed in perovskite PVs. Information regarding structure–PV property relationships and ideal solution-processing conditions within the series of bismuth–halide materials were investigated. Appreciable steady-state PL at room temperature for each of the bismuth–halide materials were measured. Time-resolved PL measurements were performed, and PL lifetimes of the materials were either shorter than the instrument response time or are just barely longer than the instrument response time. From TRMC measurements on three of the bismuth–halide materials it was determined that, for the one-dimensional materials, charge-carrier trapping lifetimes were ~10 ns and charge-carrier recombination lifetimes were 300-400 ns, which is comparable to that of conventionally-used methylammonium lead iodide. TRMC measurements on the zero-dimensional material containing

monovalent organic cations, $(\text{FA}_{0.75}/\text{Cs}_{0.25})_3\text{Bi}_2\text{I}_9$, no signal was observed outside the instrument response. This could be attributed to the lack of interconnectivity of the inorganic units, as the material structure is composed of isolated bismuth–iodide bioctahedra.

A similar trend was observed in TA measurements. TA spectra matched well with the steady-state absorption spectra of each of the three materials, which suggested stable exciton formation. TA kinetics of the same three materials were analyzed and it was determined that, for the one-dimensional materials, excitons are long-lived, with lifetimes of 2-3 ns. The exciton binding energy of HDABiI_5 was determined to be ~ 310 meV from TA spectra. This is 100 meV greater than the exciton binding energy of zero-dimensional $\text{MA}_3\text{Bi}_2\text{I}_9$, which can be attributed to the larger size of the HDA moiety. The exciton lifetime of zero-dimensional $(\text{FA}_{0.75}/\text{Cs}_{0.25})_3\text{Bi}_2\text{I}_9$ was much shorter (<100 ps) than the one-dimensional materials, which suggested faster recombination in $(\text{FA}_{0.75}/\text{Cs}_{0.25})_3\text{Bi}_2\text{I}_9$.

3.5 References

- (1) Fabian, D. M.; Ganose, A. M.; Ziller, J. W.; Scanlon, D. O.; Beard, M. C.; Ardo, S. *ACS Appl. Mater. Interfaces* **2018**, manuscript in preparation.
- (2) Eperon, G. E.; Hörantner, M. T.; Snaith, H. J. *Nat. Rev. Chem.* **2017**, *1*, 0095.
- (3) Reid, G. D.; Wynne, K. *Encycl. Anal. Chem.* **2000**, 13644–13670.
- (4) Phuong, L. Q.; Yamada, Y.; Nagai, M.; Maruyama, N.; Wakamiya, A.; Kanemitsu, Y. *J. Phys. Chem. Lett.* **2016**, *7*, 2316–2321.
- (5) Scholz, M.; Flender, O.; Oum, K.; Lenzer, T. *J. Phys. Chem. C* **2017**, *121*, 12110–12116.
- (6) Yang, Y.; Yang, M.; Moore, D. T.; Yan, Y.; Miller, E. M.; Zhu, K.; Beard, M. C. *Nat.*

- Energy* **2017**, *2*, 1–7.
- (7) Yang, Y.; Ostrowski, D. P.; France, R. M.; Zhu, K.; van de Lagemaat, J.; Luther, J. M.; Beard, M. C. *Nat. Photonics* **2016**, *10*, 53–59.
- (8) Yang, Y.; Yang, M.; Zhu, K.; Johnson, J. C.; Berry, J. J.; Lagemaat, J. Van De; Beard, M. C. *Nat. Commun.* **2016**, *7*, 12613.
- (9) Zhou, H.; Chen, Q.; Li, G.; Luo, S.; Song, T. -b.; Duan, H.-S.; Hong, Z.; You, J.; Liu, Y.; Yang, Y. *Science* **2014**, *345*, 542–546.
- (10) Ulbricht, R.; Hendry, E.; Shan, J.; Heinz, T. F.; Bonn, M. *Rev. Mod. Phys.* **2011**, *83*, 543–586.
- (11) Marchioro, A.; Teuscher, J.; Friedrich, D.; Kunst, M.; van de Krol, R.; Moehl, T.; Grätzel, M.; Moser, J.-E. *Nat. Photonics* **2014**, 1–6.
- (12) Pascoe, A. R.; Yang, M.; Kopidakis, N.; Zhu, K.; Reese, M. O.; Rumbles, G.; Fekete, M.; Duffy, N. W.; Cheng, Y. B. *Nano Energy* **2016**, *22*, 439–452.
- (13) Stranks, S. D.; Eperon, G. E.; Grancini, G.; Menelaou, C.; Alcocer, M. J. P.; Leijtens, T.; Herz, L. M.; Petrozza, A.; Snaith, H. J. *Science* **2013**, *342*, 341–344.
- (14) Nie, W.; Tsai, H.; Asadpour, R.; Blancon, J.; Neukirch, A. J.; Gupta, G.; Crochet, J. J.; Chhowalla, M.; Tretiak, S.; Alam, M. A.; Wang, H.; Mohite, A. D. *Science* **2015**, *347*, 522–525.
- (15) Berera, R.; van Grondelle, R.; Kennis, J. T. M. *Photosynth. Res.* **2009**, *101*, 105–118.
- (16) Liang, L.; Wencong, L.; Nianyi, C. *J. Phys. Chem. Solids* **2004**, *65*, 855–860.
- (17) Bartel, C. J.; Sutton, C.; Goldsmith, B. R.; Ouyang, R.; Musgrave, C. B.; Ghiringhelli, L. M.; Scheffler, M. **2018**, *6*, 1–13.
- (18) Collot, L.; Lefèvre-Seguin, V.; Brune, M.; Raimond, J. M.; Haroche, S. *Europhys. Lett.*

- 2007, 23, 327–334.
- (19) Karlin, K. D. *Progress in Inorganic Chemistry, Volume 48*; John Wiley & Sons, Inc.: New York, 1999.
- (20) Nardes, A. M. *On the conductivity of PEDOT:PSS thin films*; Technische Universiteit Eindhoven: Eindhoven, 2007.
- (21) Park, B. W.; Philippe, B.; Zhang, X.; Rensmo, H.; Boschloo, G.; Johansson, E. M. J. *Adv. Mater.* **2015**, 27, 6806–6813.
- (22) APEX2, 2014.
- (23) SAINT, 2013.
- (24) Sheldrick, G. M. SADABS, 2014.
- (25) Sheldrick, G. M. SHELXTL, 2014.
- (26) *International Tables for X-Ray Crystallography*; Vol C.; Kluwer Academic Publishers: Dordrecht, 1992.
- (27) Ito, S.; Murakami, T. N.; Comte, P.; Liska, P.; Grätzel, C.; Nazeeruddin, M. K.; Grätzel, M. *Thin Solid Films* **2008**, 516, 4613–4619.
- (28) Kim, H.-S.; Lee, C.-R.; Im, J.-H.; Lee, K.-B.; Moehl, T.; Marchioro, A.; Moon, S.-J.; Humphry-Baker, R.; Yum, J.-H.; Moser, J. E.; Grätzel, M.; Park, N.-G. *Sci. Rep.* **2012**, 2, 591.
- (29) Savenije, T. J.; Ferguson, A. J.; Kopidakis, N.; Rumbles, G. *J. Phys. Chem. C* **2013**, 117, 24085–24103.
- (30) Hrizi, C.; Samet, A.; Abid, Y.; Chaabouni, S.; Fliyou, M.; Koumina, A. *J. Mol. Struct.* **2011**, 992, 96–101.
- (31) Mousdis, G. A.; Papavassiliou, G. C.; Terzis, A.; Raptopoulou, C. P. *Z. Naturforsch.* **1998**,

53b, 927–931.

- (32) Fabian, D. M.; Ardo, S. *J. Mater. Chem. A* **2016**, *4*, 6837–6841.
- (33) Jain, A.; Voznyy, O.; Sargent, E. H. *J. Phys. Chem. C* **2017**, *121*, 7183–7187.
- (34) Du, M. H. *J. Mater. Chem. A* **2014**, *2*, 9091.
- (35) Xiao, Z.; Meng, W.; Wang, J.; Mitzi, D. B.; Yan, Y. *Mater. Horiz.* **2017**, *4*, 206–216.
- (36) Yu, L.; Zunger, A. *Phys. Rev. Lett.* **2012**, *068701*, 1–5.
- (37) Savory, C. N.; Walsh, A.; Scanlon, D. O. *ACS Energy Lett.* **2016**, *1*, 949–955.
- (38) Ganose, A. M.; Savory, C. N.; Scanlon, D. O. *Chem. Commun.* **2017**, *53*, 20–44.
- (39) Kodzasa, T.; Ushijima, H.; Matsuda, H.; Kamata, T. *Mol. Cryst. Liq. Cryst.* **2000**, *343*, 71–75.
- (40) Noel, N. K.; Habisreutinger, S. N.; Wenger, B.; Klug, M. T.; Hörantner, M. T.; Johnston, M. B.; Nicholas, R. J.; Moore, D. T.; Snaith, H. J. *Energy Environ. Sci.* **2017**, *10*, 145–152.
- (41) Kamminga, M. E.; Stroppa, A.; Picozzi, S.; Chislov, M.; Zvereva, I. A.; Baas, J.; Meetsma, A.; Blake, G. R.; Palstra, T. T. M. *Inorg. Chem.* **2017**, *56*, 33–41.
- (42) Murthy, D. H. K.; Xu, T.; Chen, W. H.; Houtepen, a J.; Savenije, T. J.; Siebbeles, L. D. a; Nys, J. P.; Krzeminski, C.; Grandidier, B.; Stiévenard, D.; Pareige, P.; Jomard, F.; Patriarche, G.; Lebedev, O. I. *Nanotechnology* **2011**, *22*, 315710.
- (43) Colbeau-Justin, C.; Valenzuela, M. A. *Rev. Mex. Fis.* **2013**, *59*, 191–200.
- (44) Norris, D. J.; Sacra, A.; Murray, C. B.; Bawendi, M. G. *Phys. Rev. Lett.* **1994**, *72*, 2612–2615.

CHAPTER 4: DEMONSTRATION OF PHOTOVOLTAIC ACTION AND ENHANCED STABILITY FROM A QUASI-TWO-DIMENSIONAL HYBRID ORGANIC–INORGANIC COPPER–HALIDE MATERIAL INCORPORATING DIVALENT ORGANIC LIGANDS

** In part a compilation of one publication in preparation¹*

4.1 Introduction

Lead–halide hybrid organic–inorganic perovskite (APbX_3) materials are a relatively new class of materials used as photoactive layers in thin-film solar cells.^{2–4} They have tunable bandgaps that allow them to operate efficiently as the photoactive layer in single-junction solar cells or as the photoactive layer in the top cell of a tandem solar cell with silicon.^{5,6} Laboratory-scale solar cells incorporating APbX_3 materials as the photoactive layer have demonstrated impressive efficiencies of $> 20\%$.^{7,8} However, APbX_3 materials incorporate toxic lead and are extremely unstable to moisture and heat.^{9–11} Instability of APbX_3 materials is observed under ambient conditions, in part because the organic halide, AX , dissociates into two water-soluble, low-boiling-point species. For example, when $\text{A}^+ = \text{CH}_3\text{NH}_3^+$ and X^- is a halide, they dissociate into CH_3NH_2 and HX .¹² Exposure to light and dry air has also been reported to decompose APbX_3 materials, especially when incorporated in mesostructured assemblies.¹³

One way to improve stability of APbX_3 materials is to increase the size of the organic A^+ moiety, and therefore decrease the vapor pressure of its deprotonated state, A . However, APbX_3 materials form a three-dimensional (3D) Pb–X network of corner-sharing octahedra and therefore, the ionic radii of Pb^{2+} and X^- dictate the volume of the cuboctahedral voids that limit the allowable size of the organic group to no larger than the isopropylammonium cation.¹⁴ Alternatively, one-dimensional (1D) and two-dimensional (2D) hybrid organic–inorganic materials offer flexibility

to accommodate larger organic groups.^{15–19} However, weaker orbital overlap within the inorganic network in these materials precludes efficient electronic conduction between adjacent 1D chains or 2D sheets and, therefore, overall solar-cell performance.²⁰ One strategy to overcome this limitation is to incorporate divalent organic ligands in the unit cell to serve as bridges between the inorganic chains or sheets. We recently used this strategy to fabricate a photovoltaic that contained a 1D bismuth–iodide hybrid organic–inorganic material with bridging 1,6-hexanediammonium divalent organic ligands (HDABiI₅) as the photoactive layer.²¹

Like 3D APbX₃ materials, which were first reported in 1893 and only in the last decade were used as the photoactive layer in solar cells,^{22,23} 1D and 2D halide-containing hybrid organic–inorganic materials are not new. In terms of 1D materials, Mousdis et al. reported in 1998 the single-crystal structure of HDABiI₅, which they described as a 1D semiconductor.²⁴ This class of bismuth–halide hybrid organic–inorganic materials was further investigated by Mitzi and Brock in the early 2000s,²⁵ and more recently bismuth–halide hybrid organic–inorganic materials have re-emerged as candidates for the photoactive layer in solar cells.^{21,26–33} The body of work on bismuth–halide photoactive materials has shown that these materials have conductivities in the range of 10⁻⁹ – 10⁻² S·cm⁻¹,^{26,29} tunable bandgaps in the visible spectral range, high crystal quality, and superior heat and moisture stability compared to state-of-the-art 3D APbX₃ materials.²¹

Although 1D bismuth–halide hybrid organic–inorganic materials can accommodate larger organic cations in their crystal lattice, which can facilitate control over materials stability, conduction through the inorganic network is limited. This can in part be overcome through use of 2D hybrid organic–inorganic materials, which should still offer flexibility in the allowable size of the organic group as well as superior in-plane conductivity compared to 1D hybrid organic–inorganic materials. The first crystallographic structural data of 2D copper–halide hybrid organic–

inorganic materials incorporating divalent organic ligands were reported in 1988 by Willett et al.³⁴ These copper–halide materials containing diammonium salts, $n(\text{DA}^{2+}(\text{R}^-)_2)$, (i.e. salts of $[\text{NH}_3(\text{CH}_2)_n\text{NH}_3]^{2+}$) consisted of 2D copper–halide sheets arranged in an eclipsed conformation, and materials with $n = 3, 4,$ or 5 were shown to exhibit ferromagnetism.³⁴ Recently, 2D Ruddlesden–Popper halide perovskite materials have emerged as a promising photoactive layer in solar cells.³⁵ While they were reported to be more stable than APbX_3 , to-date only those that contain lead or tin have been reported.^{36–40} A copper–chloride quasi-2D hybrid organic–inorganic material containing 1,4-butanediammonium was investigated by Li and coworkers, and from this study it was found that the organic moiety inhibits a phase transition and amorphization of the crystal structure at high pressure.⁴¹ In 2016, Cortecchia and coworkers reported a series of photoactive materials that consisted of 2D copper–halide sheets with a 2:1 molar ratio of methylammonium monocations (MA^+) to Cu^{2+} .⁴² The sunlight-to-electrical power conversion efficiency of a solar cell using $(\text{MA})_2\text{CuBr}_2\text{Cl}_2$ as the photoactive layer was reported to be 0.017%, with an open-circuit photovoltage of 260 mV.⁴² For stability chloride incorporation in the materials was necessary, because the all-bromide-containing $(\text{MA})_2\text{CuBr}_4$ was extremely hygroscopic.⁴² In a follow-up paper, Cortecchia et al. reported on the incorporation of an organic ligand within a 2D copper–chloride network that contained hydrophobic aromatic units to improve moisture stability.⁴³ To assess the plausibility of using high-molecular-weight divalent organic ligands in 2D copper–halide hybrid organic–inorganic materials for applications in solar cells, a comparative study on novel dicationic and monocationic copper–halide materials was conducted and the results are reported herein.

4.2 Experimental

4.2.1 Preparation of $(\text{HDA})_2\text{CuBr}_{6-x}\text{Cl}_x$ and $(\text{PA})_4\text{CuBr}_6$ Solutions

All chemicals were used as received. 1,6-hexanediammonium bromide (HDABr_2) and 1,6-hexanediammonium chloride (HDACL_2) were synthesized by slow addition of aqueous hydrobromic acid (HBr , 48% in water, Oakwood Chemical) and aqueous hydrochloric acid (HCl , 37% in water, Macron Fine Chemicals), respectively, at room temperature to a solution of 1,6-hexanediamine (98%, Alfa Aesar) dissolved in methanol (at a 2:1 mole ratio of HBr/HCl to 1,6-hexanediamine) at 0 °C with stirring, followed by continued stirring for 30 min. In a similar manner, propylammonium bromide (PABr) was synthesized by slow addition of HBr to a solution of propylamine (98%, Alfa Aesar) dissolved in methanol (1:1 mole ratio of HBr to 1,6-hexanediamine). HDABr_2 , HDACL_2 , and PABr precipitates were recovered by evaporation of solvents at 50 °C under reduced pressure. To purify HDABr_2 , HDACL_2 , and PABr , precipitates were dissolved in methanol, recrystallized from diethyl ether, and finally vacuum dried for 12 h.

$(\text{HDA})_2\text{CuBr}_6$ and $(\text{PA})_4\text{CuBr}_6$ solutions were prepared by mixing powders of the organic precursor (either HDABr_2 or PABr) and CuBr_2 (99%, Alfa Aesar) at a 1:1 molar ratio, but with the organic precursor in slight excess, in 4:1 v/v *N,N*-dimethylformamide to dimethyl sulfoxide (4:1 DMF:DMSO) to make a 1 M solution. For $(\text{HDA})_2\text{CuBr}_5\text{Cl}$ and $(\text{HDA})_2\text{CuBr}_4\text{Cl}_2$ solutions, a 5:1 ratio and 2:1 ratio of HDABr_2 to HDACL_2 were used, respectively. The solutions were stirred at 70 °C inside a nitrogen-filled glovebox, stored in the glovebox until use, and used within two weeks of preparation.

4.2.2 $(\text{HDA})_2\text{CuBr}_6$ Single-Crystal Growth

Approximately 200 μL of a 1 M solution of $(\text{HDA})_2\text{CuBr}_6$ in 4:1 v/v DMF:DMSO was dispensed into a 4 mL vial and this vial was placed uncapped in a 20 mL vial containing ~ 2 mL

dichloromethane and the 20 mL vial was capped. $(\text{HDA})_2\text{CuBr}_6$ single crystals grew overnight in the 4 mL vial via diffusion of dichloromethane.

4.2.3 X-ray Data Collection and Structure Solution for $(\text{HDA})_2\text{CuBr}_6$

A black crystal was mounted on a glass fiber and transferred to a Bruker SMART APEX II diffractometer. The APEX2⁴⁴ program package was used to determine the unit-cell parameters and for data collection (20 sec/frame scan time for a sphere of diffraction data). The raw frame data was processed using SAINT⁴⁵ and SADABS⁴⁶ to yield the reflection data file. Subsequent calculations were carried out using the SHELXTL⁴⁷ program. There were no systematic absences nor any diffraction symmetry other than the Friedel condition. The orthorhombic space group $P2_1/c$ was assigned and later determined to be correct.

The structure was solved by direct methods and refined on F2 by full-matrix least-squares techniques. The analytical scattering factors⁴⁸ for neutral atoms were used throughout the analysis. Hydrogen atoms were included using a riding model.

4.2.4 Materials Processing

All steps of materials deposition and solar cell fabrication were performed in air with 40–60 % relative humidity as described below, unless noted otherwise. All thermal treatments were performed using a hot plate. Fluorine-doped tin-oxide-coated glass (FTO) substrates were cleaned as follows: 1) sonicated in Alconox solution, 2) rinsed with deionized water, 3) rinsed with ethanol, 4) sonicated in ethanol, and 5) dried with nitrogen. To deposit the compact TiO_2 (c TiO_2) layer, a solution of titanium diisopropoxide bis(acetylacetonate) was pipetted onto a cleaned FTO substrate and after a 30 sec wait period the substrate was spun at 2000 rpm (2000 rpm/sec acceleration) for

60 sec. The substrate was subsequently dried at 125 °C and then sintered at 550 °C for 30 min. Nanoparticles of TiO₂ were synthesized following a procedure by Ito et al.⁴⁹ The nanoparticle solution was further diluted in ethanol at a weight ratio of 1:1 TiO₂ nanoparticle solution:ethanol to make a mesoporous TiO₂ (mTiO₂) suspension. The mTiO₂ layer was pipetted on top of the cTiO₂/FTO substrate and after a 30 sec wait period the substrate was spun at 500 rpm (500 rpm/sec acceleration) for 5 sec and then 5000 rpm (5000 rpm/sec acceleration) for 25 sec, dried at 125 °C, and then sintered at 550 °C for 30 minutes. A conventional method was used to deposit the copper–halide-containing solutions, which was adapted from Kim et al.⁵⁰ A filtered copper–halide-containing solution in 4:1 v/v DMF:DMSO was pipetted on top of the mTiO₂/cTiO₂/FTO substrate and after a 60 sec wait period the substrate was spun at 2000 rpm (2000 rpm/sec acceleration) for 60 sec, followed by transfer to a hot plate that was preheated to 100 °C, and the substrate was subsequently annealed at 100 °C for 45 min.

4.2.5 Solar Cell Fabrication

Prior to the FTO cleaning step, a region of the FTO film was etched using 2 M aqueous HCl and Zn powder in order to prevent solar cell shunting upon contact to the top Au electrode. After performing the cleaning steps listed above (*Materials Processing* subsection), FTO substrates were further cleaned using an O₂ plasma treatment for 10 min. Following deposition of the copper–halide-containing solution per the protocol described above (*Materials Processing* subsection), a 50 mM solution of 2,2',7,7'-tetrakis(N,N'-di-p-methoxyphenylamine)-9,9'-spirobifluorene (spiro-OMeTAD) dissolved in toluene was deposited by spin coating at 3000 rpm (3000 rpm/sec acceleration) for 60 sec. The solar cells were left to dry in air for 20 min and then were transferred into a nitrogen-filled glovebox, and 80 nm of Au was thermally evaporated onto

the solar cells at a base pressure of 5×10^{-6} mbar. The complete solar cells had an architecture of Au/spiro-OMeTAD/Cu/mTiO₂/cTiO₂/FTO, where Cu = (HDA)₂CuBr₆, HDACuBr₅Cl, HDACuBr₄Cl₂, or (PA)₄CuBr₆.

4.2.6 Stability Tests

Stability tests were performed in air for (HDA)₂CuBr₆ and (PA)₄CuBr₆ thin films deposited on mTiO₂/cTiO₂/FTO per the protocols above (*Materials Processing and Solar Cell Fabrication* subsections). For the accelerated thermal stability tests, thin films were heated to 100 °C and exposed to ~50 % relative humidity for 16 h. The X-ray diffraction patterns before and after exposure are displayed in Figure 4. For the moisture stability tests, thin films and powders of (HDA)₂CuBr₆ and (PA)₄CuBr₆ were exposed to ~50 % relative humidity. The thin films were monitored over a period of 12 days using transmission-mode ultraviolet–visible electronic absorption spectroscopy. The powders were monitored over a period of 14 days using X-ray diffraction.

4.2.7 Materials Characterization

Electronic absorption spectroscopy measurements were carried out using an Agilent Cary 60 spectrophotometer with a resolution of 1 nm, and Tauc plots were constructed from the measured spectra. Spectra were baseline-subtracted for long-wavelength scattering, and bandgap energies were determined from best-fit lines of the data near the absorption onset. Scanning electron microscopy and energy-dispersive X-ray spectroscopy images were acquired on a FEI Magellan 400L XHR. Absorption coefficients of thin films were calculated based on the average thickness measured from cross-sectional scanning electron microscopy images (740 ± 80 nm). For

thin films, grazing-incidence X-ray diffraction data were collected using a Rigaku Smartlab diffractometer with Cu K_{α} radiation and in parallel-beam geometry. For powders, X-ray diffraction data were collected in Bragg-Brentano geometry. Thermogravimetric analysis data were obtained using a TGA Q500 by TA Instruments. Steady-state photoluminescence spectra were acquired at room temperature using a Cary Eclipse fluorescence spectrophotometer by Agilent Technologies with excitation light at 320-350 nm, matched slit widths of 10 nm, and detection in a right-angle geometry. Films were positioned at $\sim 60^{\circ}$ relative to the detector (i.e. $\sim 30^{\circ}$ relative to the incident excitation light). Data were corrected for the wavelength-dependent response of the detection system.

XPS measurements were performed using a Kratos AXIS Supra photoelectron spectrometer using Al K_{α} radiation. Cu 2p region scans were obtained immediately following sample z-alignment in order to minimize X-ray induced reduction of Cu^{2+} .⁵¹ The XPS data were analyzed using CasaXPS Processing Software. XPS peaks were fit to Gaussian–Lorentzian (80:20) curves. For XPS measurements of the cutoff region (determination of the work function) and valence-band region (determination of the valence-band maximum), Fermi edge calibration was performed with a sputter-cleaned Ag standard to ensure that all energies were referenced to a common Fermi level (0 eV). XPS measurements were performed instead of ultraviolet photoelectron spectroscopy (UPS) measurements because ultraviolet light has been shown to induce significant work-function reduction on transparent-conductive-oxide substrate surfaces.⁵² Work functions were calculated by extrapolating the XPS cutoff region spectra to the x-intercept. In a manner similar to that performed by Schulz et al.,⁵³ the low-energy tail of the valence-band spectrum was used to determine the position of the valence-band maximum relative to the Fermi level. Using the determined optical bandgaps, the conduction-band minimum was calculated for

each copper–halide hybrid organic–inorganic material. The conduction-band minimum of TiO₂ and the valence-band maximum of spiro-OMeTAD were taken from a report by Chilvery et al.⁵⁴ The Fermi level positions with respect to the conduction-band minimum and valence-band maximum suggest that the materials are p-type. Scanning electron microscopy, X-ray diffraction, and X-ray photoelectron spectroscopy (XPS) work was performed in the UC Irvine Materials Research Institute (IMRI).

4.2.8 Electrical Characterization

An ELH-type W–halogen lamp was used inside a nitrogen-filled glovebox as a source of simulated solar illumination. Before measurement of solar cell current density *versus* potential (J – E) behavior and chronoamperometry behavior, the light intensity was measured to be approximately 1 Sun using a calibrated Si photodiode (ThorLabs, Inc., FDS100) positioned at the location of the solar cell. Two-electrode J – E measurements at a scan rate of 100 mV s⁻¹ and chronoamperometry measurements were performed using a Gamry Reference 600 Potentiostat.

Two-electrode impedance spectroscopy data for a complete solar cell consisting of Au/spiro-OMeTAD/HDACuBr₅Cl/TiO₂/FTO were collected at reverse-bias potentials from 0 mV to -500 mV (in 50 mV increments) over frequencies ranging from 2 MHz to 1 Hz. Frequency-dependent data at each DC bias were fit to the standard Randles circuit model (inset of Figure 13b), where C_1 is the interfacial capacitance, R_1 is the charge-transfer resistance, and R_2 is the series resistance.⁵⁵ The flat-band potential (E_{FB}) and doping density (N_A) were obtained by best fits of the C_1 *versus* E data to the following formula,⁵⁶

$$C_1 = \sqrt{\frac{1}{\frac{2}{e\epsilon_r\epsilon_0 N_A} \left(E - E_{\text{FB}} - \frac{k_B T}{e} \right)}}$$

where e is the elementary charge of an electron (1.6×10^{-19} C), ϵ_r is the real part of the relative static permittivity (70, value reported by Lin et al. for methylammonium lead triiodide⁵⁷), ϵ_0 is the permittivity of vacuum (8.854×10^{-14} F·cm⁻¹), k_B is the Boltzmann constant (1.38×10^{-23} J·K⁻¹) and T is the temperature (298.15 K). These data were plotted as the corresponding Mott–Schottky plot (C_1^{-2} versus E) where the flat-band potential was calculated as ($k_B T/e$) less than the x-intercept ($(6.22 \pm 0.03) \times 10^{15}$ cm⁴·F⁻²). The doping density (N_A , cm⁻³) was calculated using the following formula,⁵⁸

$$N_A = \frac{2}{e\epsilon_r\epsilon_0 m}$$

where m is the slope of the Mott–Schottky plot ($(3.6 \pm 0.1) \times 10^{15}$ cm⁴·F⁻²·V⁻¹).

4.3 Results & Discussion

Replacement of organic monocations with half as many organic dications in the syntheses of 2D copper–halide hybrid organic–inorganic materials resulted in the formation of new

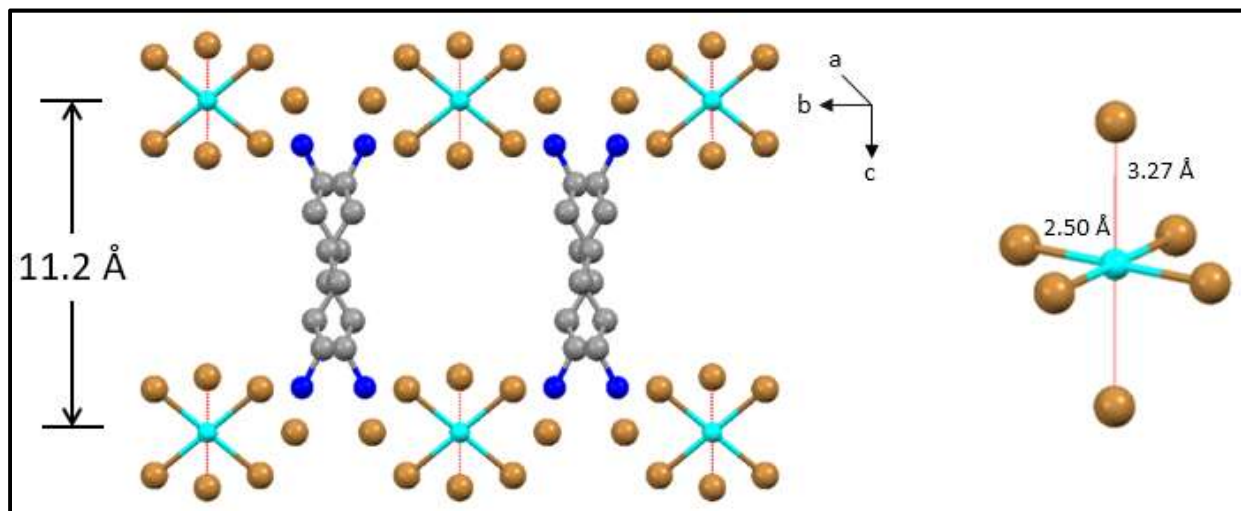


Figure 4.1. Unit cell crystal structure of $(\text{HDA})_2\text{CuBr}_6$ showing the vertical alternation of copper (light blue)–bromide (gold) layers separated by hexanediammonium dications (carbon = silver, nitrogen = dark blue). Hydrogens are omitted for clarity. Shown on the right is a CuBr_6 octahedral unit with the measured Cu–Br bond lengths.

(HDA)₂CuX₆ materials, where HDA is 1,6-hexanediammonium (HDA²⁺). Single crystals of (HDA)₂CuBr₆, in the form of black platelets, were grown and the single-crystal structure of (HDA)₂CuBr₆ was resolved. The unit cell structure is shown in Figure 4.1. (HDA)₂CuBr₆ is monoclinic (space group 14: C2/m), with lattice constants $a = 10.2 \text{ \AA}$, $b = 16.9 \text{ \AA}$, and $c = 11.2 \text{ \AA}$ and unit cell angles $\alpha = 90.0^\circ$, $\beta = 98.8^\circ$, $\gamma = 90.0^\circ$. CuBr₆ octahedra are isolated from each other, but the octahedra arrange in quasi-2D sheets along the ab plane. Equatorial copper–bromide bond lengths are 2.50 \AA and axial copper–bromide bond lengths are 3.27 \AA . This difference in bond lengths can be attributed to Jahn–Teller elongation, which has been observed in analogous materials containing CuBr₆ octahedra.⁵⁹ Table 4.1 shows crystallographic information pertaining to the (HDA)₃CuBr₈ single crystal.

Table 4.1. Crystallographic data for (HDA)₂CuBr₆.

(HDA) ₂ CuBr ₆	
Empirical formula	C ₁₂ H ₃₆ Cu Br ₆ N ₄
Formula weight	779.42
Temperature	88(2) K
Crystal system	Monoclinic
Space group	P2 ₁ /c
a	11.5341(13)
b	17.6726(19)
c	9.6467(11)
α	90 °
β	96.3669(14) °
γ	90 °
Volume	1954.23
Z	2
Crystal color	black

The transmission-mode ultraviolet–visible absorption spectra are shown in Figure 4.2a and displayed as Tauc plots in Figure 4.3a for $(\text{HDA})_2\text{CuX}_6$ materials as well as a control spectrum of a copper–bromide perovskite material incorporating four propylammonium (PA^+) groups per copper atom, $(\text{PA})_4\text{CuBr}_6$. PA^+ was chosen for comparative studies because its C–N core is roughly half the length of that of HDA^{2+} . Each thin film exhibited a lowest-energy indirect bandgap of ~ 1.80 eV (Figure 4.3a), a direct bandgap of ~ 2.05 – 2.10 eV (Figure 4.4), and d–d transitions at

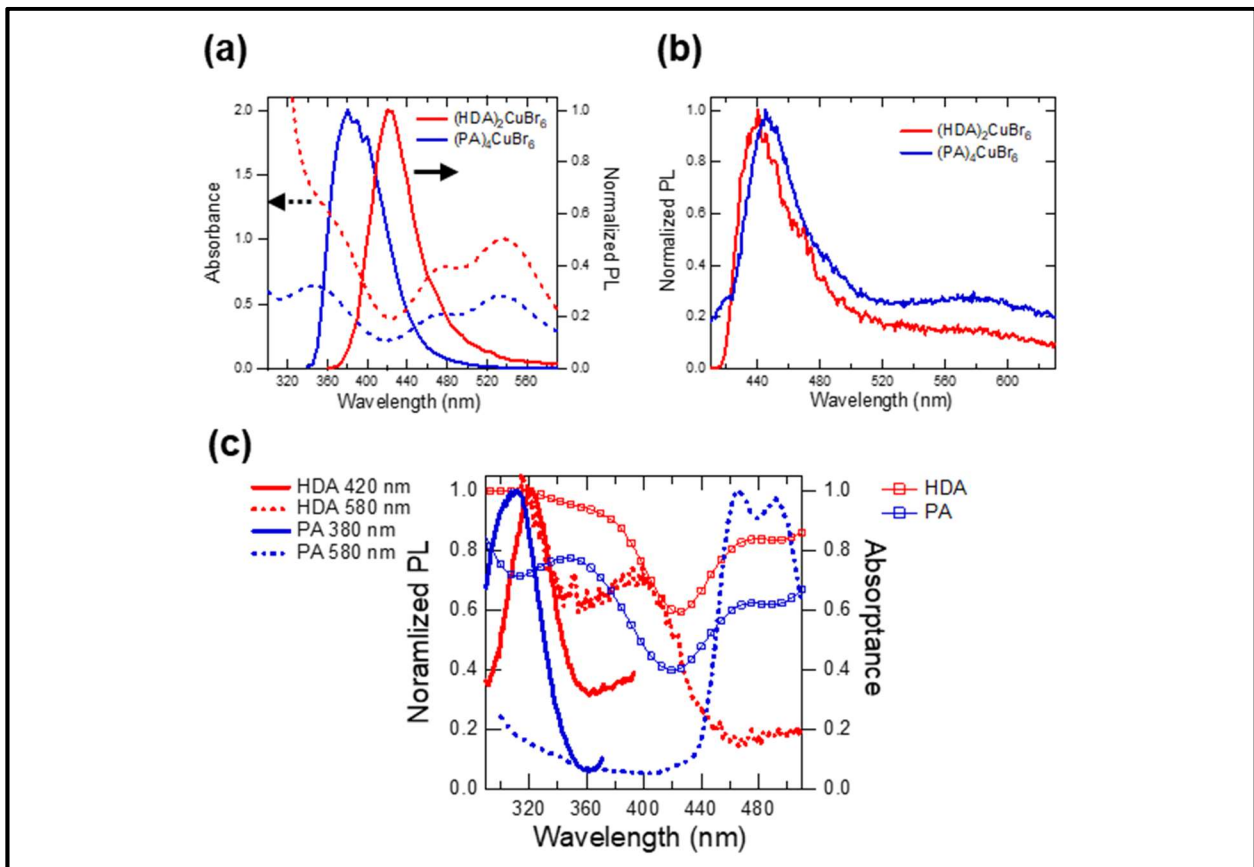


Figure 4.2. (a) Transmission-mode electronic absorbance spectra (dotted traces) and steady-state photoluminescence emission spectra (solid traces, $\lambda_{\text{ex}} \approx 340$ nm) of thin films of $(\text{HDA})_2\text{CuBr}_6$ (red trace) and $(\text{PA})_4\text{CuBr}_6$ (blue trace). (b) Normalized steady-state photoluminescence emission spectra ($\lambda_{\text{ex}} \approx 400$ nm) of thin films of $(\text{HDA})_2\text{CuBr}_6$ (red trace) and $(\text{PA})_4\text{CuBr}_6$ (blue trace), showing a broad tailing region due to emission from an electronic transition with $\lambda_{\text{max}} \approx 580$ nm. (c) Steady-state photoluminescence excitation spectra of $(\text{HDA})_2\text{CuBr}_6$ and $(\text{PA})_4\text{CuBr}_6$ probed at emission peak wavelengths (solid traces) and at 580 nm (dotted traces), with the absorbance spectra of $(\text{HDA})_2\text{CuBr}_6$ (red squares trace) and $(\text{PA})_4\text{CuBr}_6$ (blue squares trace) overlaid.

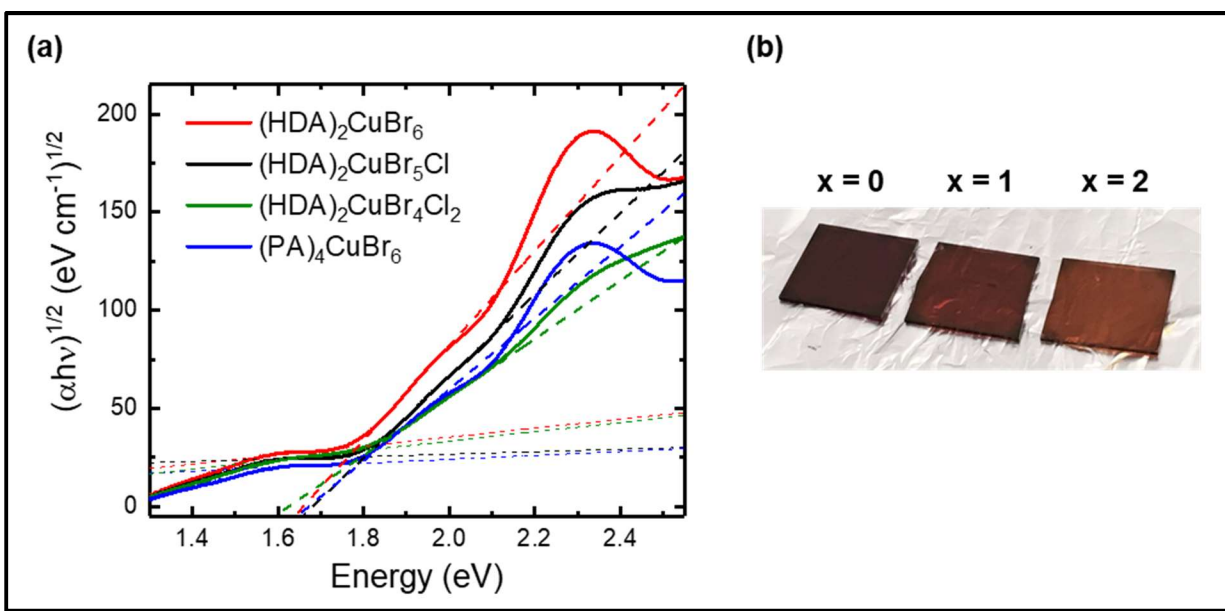


Figure 4.3. (a) Indirect-bandgap Tauc plots of copper-halide hybrid organic-inorganic thin films deposited on glass and incorporating HDA²⁺ with varying halide compositions (black, red, and green traces) or PA⁺ (blue trace). Data are corrected for scattering as described in the *Materials Characterization* subsection. Bold dashed lines represent best fits to the absorption onsets and thin dashed lines represent baselines for the indirect transitions. (b) Digital photograph image of representative freshly-prepared (HDA)₂CuBr_{6-x}Cl_x thin films deposited on glass, with (from left to right) $x = 0, 1, \text{ and } 2$.

~1.60 eV (Figure 4.3a). The indirect bandgap of these materials is ~0.25 eV smaller than that of thin films of HDABiI₅,²⁰ making them more suitable for applications as the photoactive layer in the top cell of a tandem solar cell with silicon.^{4,5} Bandgap energies and molar absorption coefficients are comparable to those reported for monocationic copper-halide perovskite materials.⁴¹ Interestingly, the (PA)₄CuBr₆ thin film exhibited the weakest molar absorptivity of the series, which suggests that incorporation of divalent organic ligands in these materials causes enhancement of their absorption cross sections. Digital photograph images of freshly-prepared (HDA)₂CuBr_{6-x}Cl_x thin films deposited on glass are shown in Figure 4.3b. Analogous digital photograph images of (HDA)₂CuBr_{6-x}Cl_x and (PA)₄CuBr₆ deposited on mesoporous TiO₂/cTiO₂/FTO for solar cell fabrication and testing are shown in Figure 4.5.

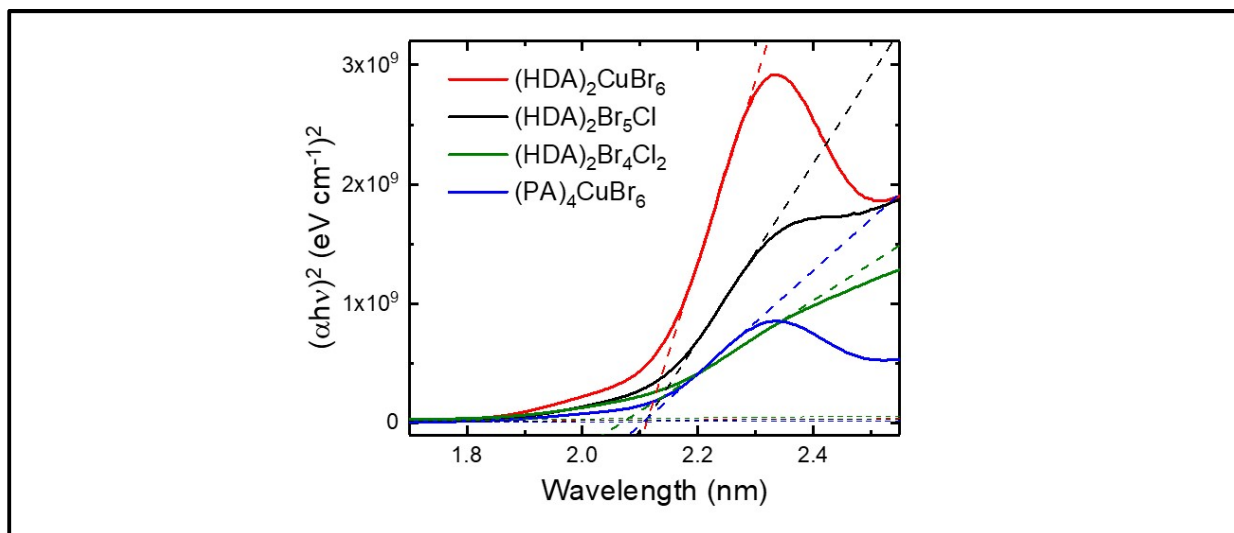


Figure 4.4. Direct-bandgap Tauc plots of copper-halide hybrid organic-inorganic thin films deposited on glass and incorporating HDA²⁺ with varying halide compositions (black, red, and green traces) or PA⁺ (blue trace). Data are corrected for scattering by the same method used in Figure 4.3.

Air-processed solution-cast thin films of (HDA)₂CuBr₆ and (PA)₄CuBr₆ exhibited absorption features that are similar to those of MA₂CuCl_xBr_{4-x} materials as well as steady-state photoluminescence at room temperature. During 330 nm excitation, (HDA)₂CuBr₆ films were emissive with a peak position at 420 nm (Figure 4.2a, red trace) and (PA)₄CuBr₆ films were emissive with a peak position at 380 nm (Figure 4.2a, blue trace). These emission peaks exhibit much smaller Stokes shifts (0.49 eV in (HDA)₂CuBr₆ and 0.31 eV in (PA)₄CuBr₆) than in previously reported MA₂CuCl_xBr_{4-x} materials (1.3 eV), which suggests less electronic and nuclear reorganization in the copper-bromide materials reported herein. When the excitation wavelength was adjusted to lower energy (400 nm), a new broad, weak emission band was apparent at ~580 nm that has not been reported previously for copper-halide hybrid organic-inorganic materials (Figure 4.2b). The weakness of this emission band suggests that the quantum yield for emission is poor or that the electronic transition that gives rise to this emission band has a small absorption cross section at 400 nm or is present at a low concentration in the film (Figure 4.2c, dotted traces versus squares traces). Absorption into low-energy transitions resulted in a tailing of the emission

spectrum out to beyond 620 nm, where $(\text{HDA})_2\text{CuBr}_6$ still exhibited >10% of its maximum emission signal intensity and $(\text{PA})_4\text{CuBr}_6$ still exhibited >20% of its maximum emission signal intensity (Figure 4.2b). Emission in this wavelength region for analogous $\text{MA}_2\text{CuCl}_x\text{Br}_{4-x}$ materials has been attributed to recombination via Cu^+ trap states that likely form during film annealing.⁴¹ likely form during film annealing.

The speciation of atoms near the surface of thin films were characterized by

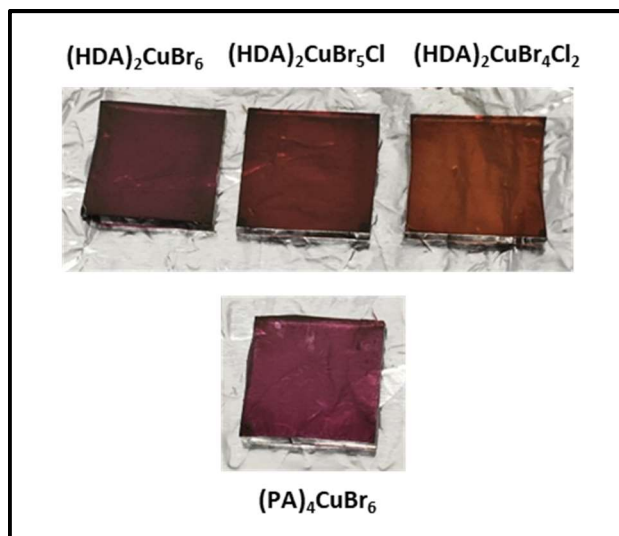


Figure 4.5. Digital photograph images of freshly-prepared $(\text{HDA})_2\text{CuBr}_{6-x}\text{Cl}_x$ (top) with (from left to right) $x = 0, 1,$ and $2,$ and $(\text{PA})_4\text{CuBr}_6$ (bottom) thin films deposited in the mesostructured assembly, $\text{Cu}/\text{mTiO}_2/\text{cTiO}_2/\text{FTO}$, where Cu is the copper-halide light absorber material, mTiO_2 is a mesoporous TiO_2 nanoparticle layer, cTiO_2 is a compact TiO_2 layer, and FTO is a fluorine-doped tin-oxide-coated glass substrate.

X-ray photoelectron spectroscopy. Scans of the $\text{Cu } 2p$ core level binding energy range revealed

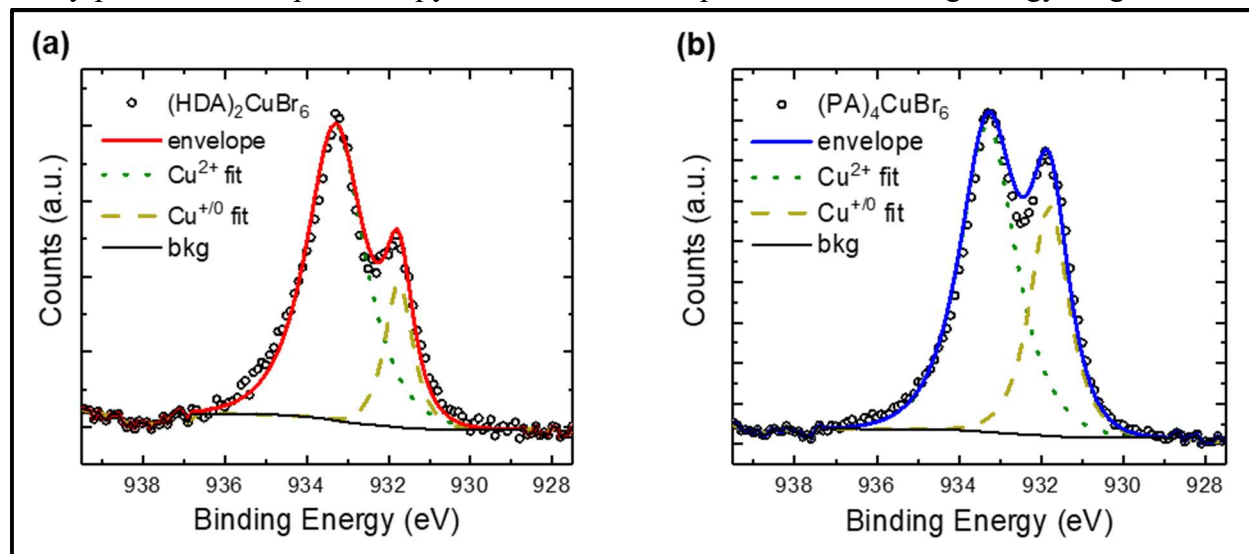


Figure 4.6. X-ray photoelectron spectra of the $\text{Cu } 2p_{3/2}$ region of thin films of (a) $(\text{HDA})_2\text{CuBr}_6$ and (b) $(\text{PA})_2\text{CuBr}_4$ on FTO . Best fits to the $\text{Cu } 2p_{3/2}$ peaks are shown, where envelope is the sum of the Cu^{2+} fit, the Cu^+/Cu^0 fit, and a Shirley background (bkg).

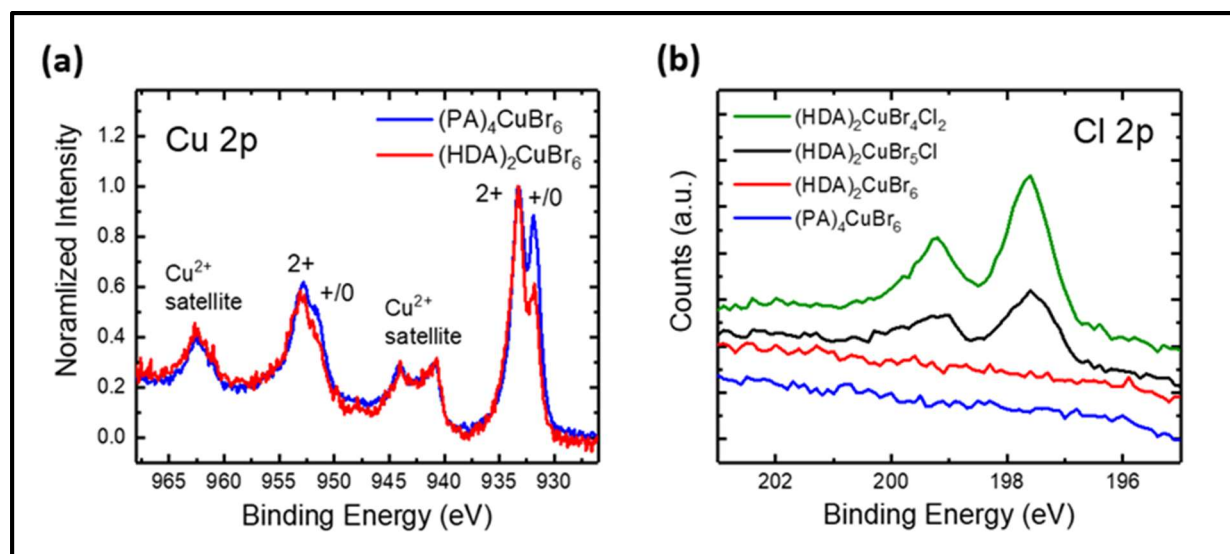


Figure 4.7. X-ray photoelectron spectra of the (a) Cu 2p region and the (b) Cl 2p region of copper-halide hybrid organic-inorganic thin films each deposited on a fluorine-doped tin-oxide-coated glass substrate. Intensities in panel (a) are normalized to the Cu 2p_{3/2} peak that corresponds to Cu²⁺.

the presence of Cu²⁺ and other peak(s) due to Cu⁺ and/or Cu⁰ (Figure 4.6, Figure 4.7a), which is consistent with the absorbance and photoluminescence data. Deciphering between characteristic peaks corresponding to Cu⁺ and Cu⁰ is a challenge because Cu⁺ and Cu⁰ states have very similar binding energies. Peak fitting of the Cu 2p_{3/2} peaks revealed the copper composition profile of (HDA)₂CuBr₆ to be approximately 81% Cu²⁺ and 19% Cu⁺/Cu⁰ (Figure 4.6a) and for (PA)₄CuBr₆, approximately 66% Cu²⁺ and 34% Cu⁺/Cu⁰ (Figure 4.6b). These data suggest that reductive degradation of the inorganic precursor material, CuBr₂ occurred during thin-film fabrication. Scans of the Cl 2p region were performed on the series of materials, which revealed near-surface speciation of chloride in the (HDA)₂CuBr₄Cl₂ and (HDA)₂CuBr₅Cl samples and no observed chlorine species in the (HDA)₂CuBr₆ and (PA)₄CuBr₆ samples (Figure 4.7b). Following continued X-ray exposure, through measurements of survey spectra and other core level binding energy regions, the (HDA)₂CuBr₆ thin film contained approximately 75% Cu²⁺ and 25% Cu⁺/Cu⁰ (Figure 4.8a) and the (PA)₄CuBr₆ thin film contained approximately 60% Cu²⁺ and 40% Cu⁺/Cu⁰ (Figure

4.8b), which marked a $\sim 6\%$ increase in near-surface Cu^+/Cu^0 for both thin films. The small magnitude of these X-ray-induced changes provide evidence that there is Cu^+/Cu^0 present in both thin films before exposure to the X-ray beam. The larger percentage of reduced copper species in thin films of $(\text{PA})_4\text{CuBr}_6$ supports observations of faster degradation of the Cu^{2+} -containing $(\text{PA})_4\text{CuBr}_6$ thin films in comparison to the Cu^{2+} -containing $(\text{HDA})_2\text{CuBr}_6$ thin films. Scans of the C 1s, N 1s, and Br 3p core level binding energy ranges for thin films of $(\text{HDA})_2\text{CuBr}_6$ and $(\text{PA})_4\text{CuBr}_6$ were also performed (Figure 4.9). For both samples, the C 1s region spectra reveals the presence of two peaks, which correspond to C–C bonds and C–N bonds in the organic groups. The N 1s region spectrum contains a peak at 401.2 eV, which is consistent with the N 1s peak position for MAPbX_3 materials and is attributed to the nitrogen atoms in the ammonium groups.⁶⁰ Strong Br 3p peaks were observed in $(\text{HDA})_2\text{CuBr}_6$ and $(\text{PA})_4\text{CuBr}_6$ thin films due to their large bromide content.

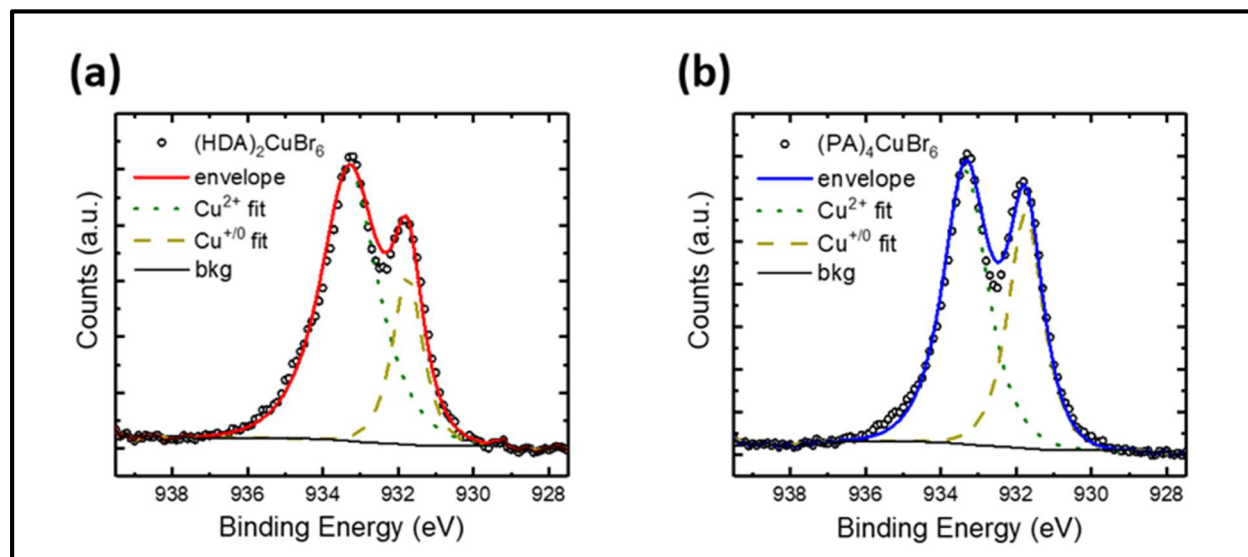


Figure 4.8. Best fits to the Cu $2p_{3/2}$ peaks of the X-ray photoelectron spectra of thin films of (a) $(\text{HDA})_2\text{CuBr}_6$ and (b) $(\text{PA})_4\text{CuBr}_6$ thin films each deposited on a fluorine-doped tin-oxide-coated glass substrate following continued X-ray exposure, where envelope is the sum of the Cu^{2+} fit, the Cu^+/Cu^0 fit, and a Shirley background (bkg).

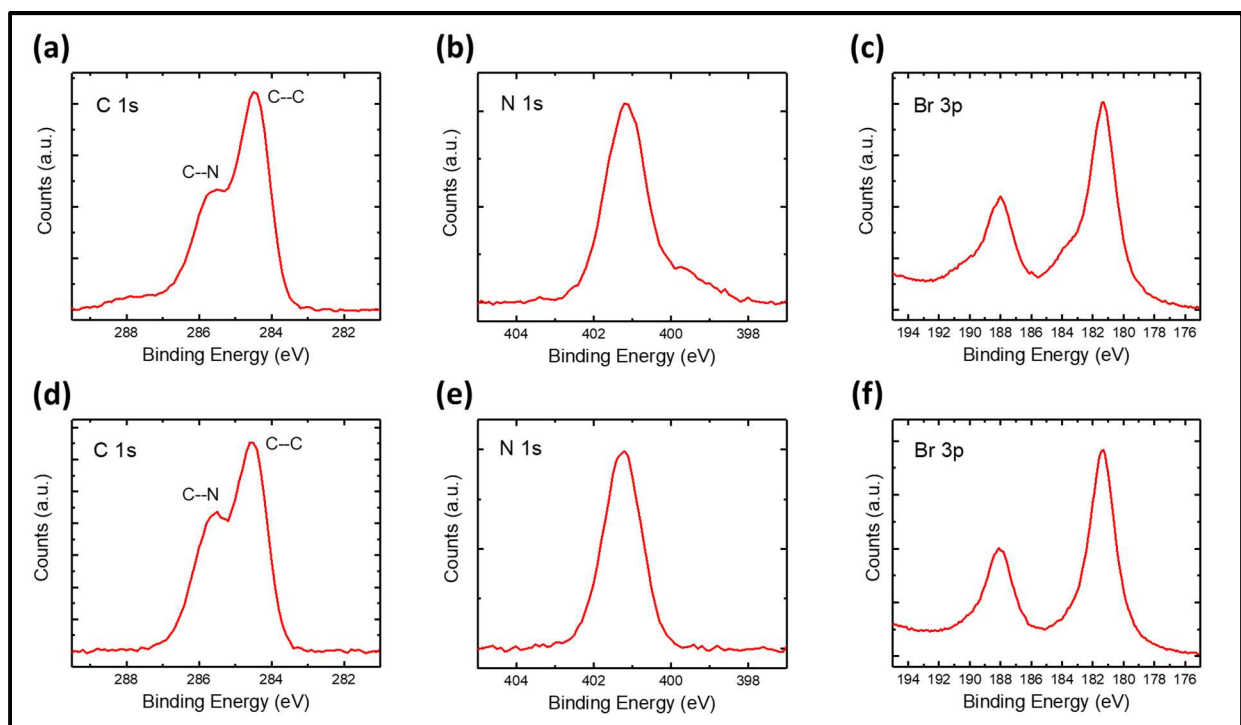


Figure 4.9. Scans of the (a), (d) C 1s, (b), (e) N 1s, and (c), (f) Br 3p core level binding energy regions for thin films of $(\text{HDA})_2\text{CuBr}_6$ (top row) and $(\text{PA})_4\text{CuBr}_6$ (bottom row), each deposited on a fluorine-doped tin-oxide-coated glass substrate.

Evaluation of crystallinity and thermal stability were performed using grazing-incidence X-ray diffraction. X-ray diffraction patterns of freshly-prepared thin films of dicationic $(\text{HDA})_2\text{CuBr}_6$ (Figure 4.10, solid red line) and analogous monocationic $(\text{PA})_4\text{CuBr}_6$ (Figure 4.10, solid blue line) show strong preferential orientation in the [001] direction, which is similar to the patterns reported by Cortecchia et al.⁴¹ This indicates that the quasi-2D copper-halide sheets are oriented in-plane with the FTO substrate. The observation of larger higher-order peaks in the $(\text{HDA})_2\text{CuBr}_6$ pattern in comparison to the $(\text{PA})_4\text{CuBr}_6$ pattern indicates that there is a greater amount of ordering at each Bragg reflection condition in the $(\text{HDA})_2\text{CuBr}_6$ thin film.⁶¹ Because the c -axis is orthogonal to the quasi-2D copper-halide sheets, the value of c is the sheet spacing and can be determined from the two-theta values. For $(\text{HDA})_2\text{CuBr}_6$, the (001) peak occurs at two-theta = 7.80° , which indicates a sheet spacing of 11.3 Å. This value is consistent with the sheet

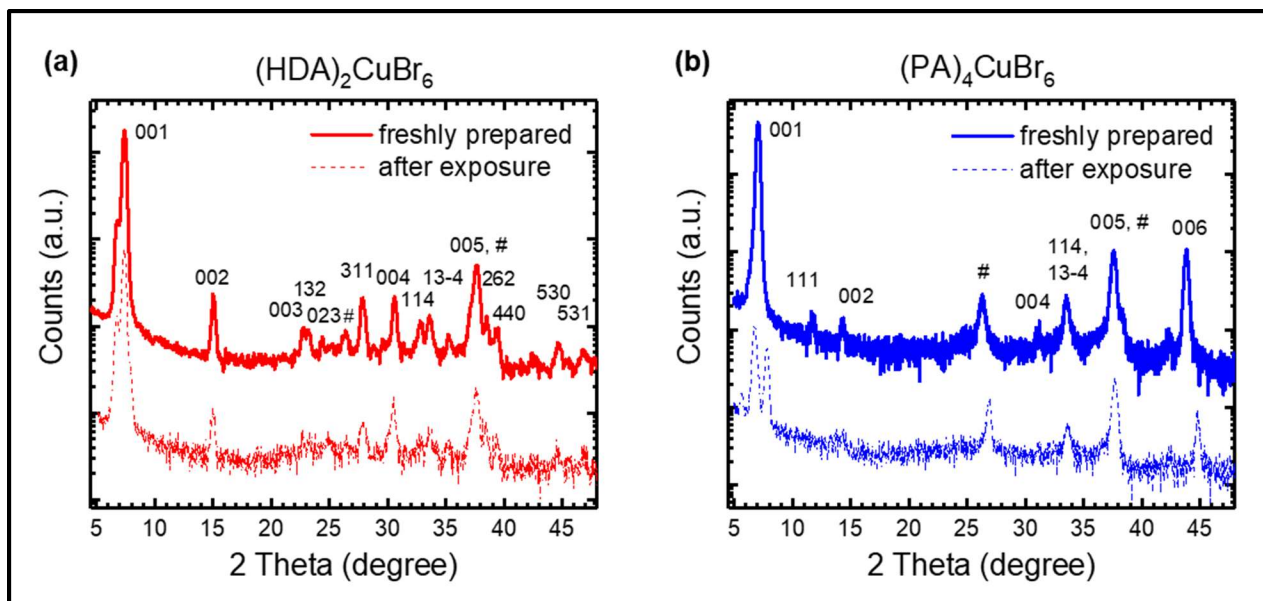


Figure 4.10. Grazing-incidence X-ray diffraction patterns of thin films of (a) $(\text{HDA})_2\text{CuBr}_6$ (red) and (b) $(\text{PA})_4\text{CuBr}_6$ (blue) when freshly-prepared (solid traces) and after exposure to 100 °C and ~50% relative humidity for 16 h (dashed traces). # denote peaks associated with the underlying fluorine-doped tin-oxide-coated glass substrate.

spacing determined from single-crystal X-ray diffraction, which was 11.2 Å. In comparison, the sheet spacing for $(\text{PA})_4\text{CuBr}_6$ is 12.6 Å, which was calculated from a $(\text{PA})_4\text{CuBr}_6$ (001) two-theta value of 7.04°. The difference between sheet spacing in $(\text{HDA})_2\text{CuBr}_6$ and $(\text{PA})_4\text{CuBr}_6$ is logical

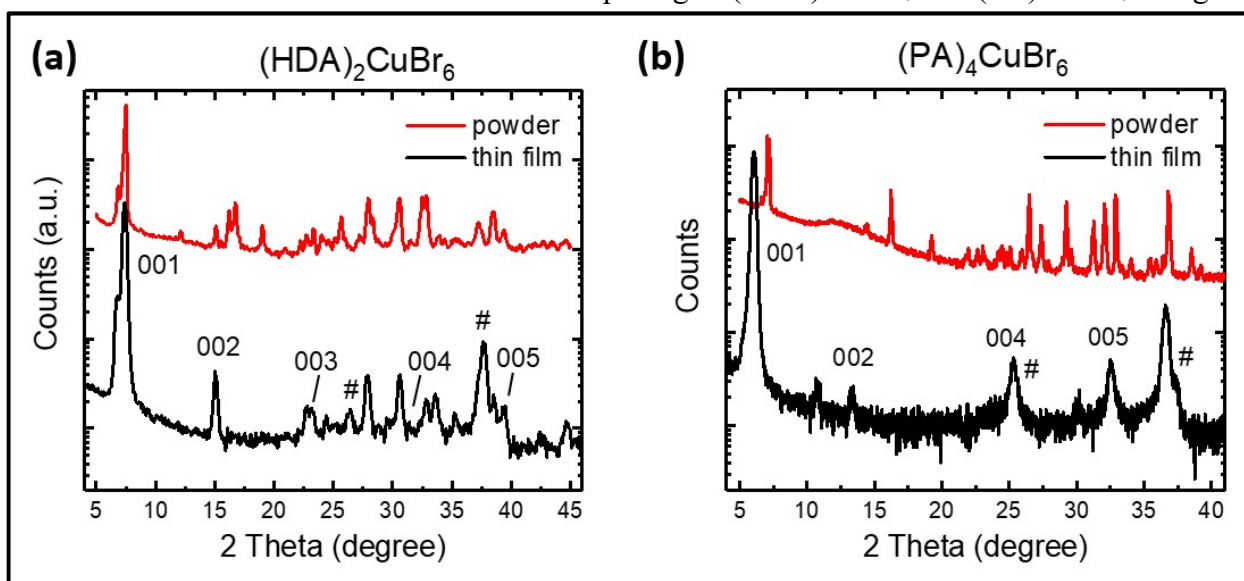


Figure 4.11. Powder X-ray diffraction patterns and thin-film X-ray diffraction patterns for (a) $(\text{HDA})_2\text{CuBr}_6$ and (b) $(\text{PA})_4\text{CuBr}_6$.

based on the slightly larger size of four PA^+ in comparison to two HDA^{2+} . A comparison of powder versus thin-film X-ray diffraction patterns for both $(\text{HDA})_2\text{CuBr}_6$ and $(\text{PA})_4\text{CuBr}_6$ are shown in Figure 4.11. Unlike for $(\text{HDA})_2\text{CuBr}_6$, the largest-intensity peak for the $(\text{PA})_4\text{CuBr}_6$ powder occurred at a larger two-theta value relative to that of the thin film, which is speculated to be due to water molecules present in $(\text{PA})_4\text{CuBr}_6$ powder, which would suggest $(\text{PA})_4\text{CuBr}_6$ is more hygroscopic than $(\text{HDA})_2\text{CuBr}_6$ since they were processed in nominally identical manners.

Accelerated thermal stability tests on thin films of $(\text{HDA})_4\text{CuBr}_6$ resulted in minimal changes in the grazing-incidence X-ray diffraction pattern (Figure 4.10a) and absorption spectrum (Figure 5a, red data) in comparison to changes observed for thin films of $(\text{PA})_4\text{CuBr}_6$ after the same treatment (Figure 4.10b and Figure 4.12a, blue data). For $(\text{PA})_4\text{CuBr}_6$ thin films, the (001) peak intensity decreased significantly, the (001) peak shifted to 6.70° , and new peaks emerged at

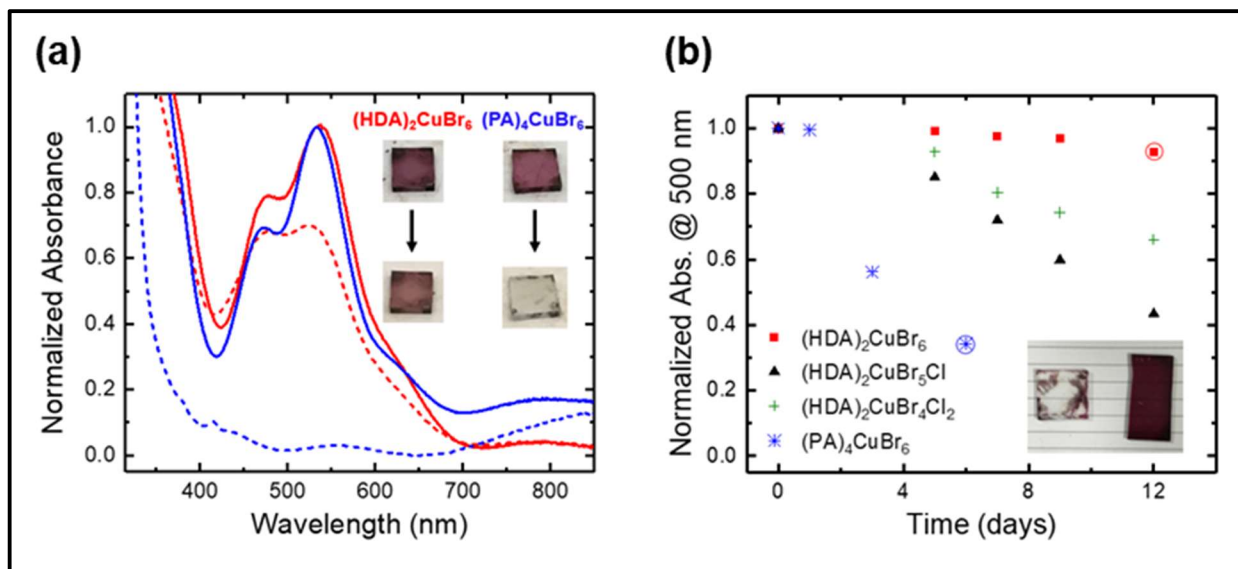


Figure 4.12. (a) Transmission-mode absorption spectra of thin films of $\text{HDA}_2\text{CuBr}_6$ (red) and $(\text{PA})_4\text{CuBr}_6$ (blue) freshly-prepared (solid lines) and after exposure to 100 °C and ~50% relative humidity for 16 h (dashed lines), each corrected for background scattering. Inset: Digital photograph images of the thin films before and after exposure. (b) Normalized absorbance at 500 nm as a function of time for copper-halide perovskite thin films at room temperature and 50% relative humidity. Inset: Digital photograph image of $(\text{PA})_4\text{CuBr}_6$ after 6 days (left; blue circle in main figure) and $\text{HDA}_2\text{CuBr}_6$ after 12 days (right; red circle in main figure).

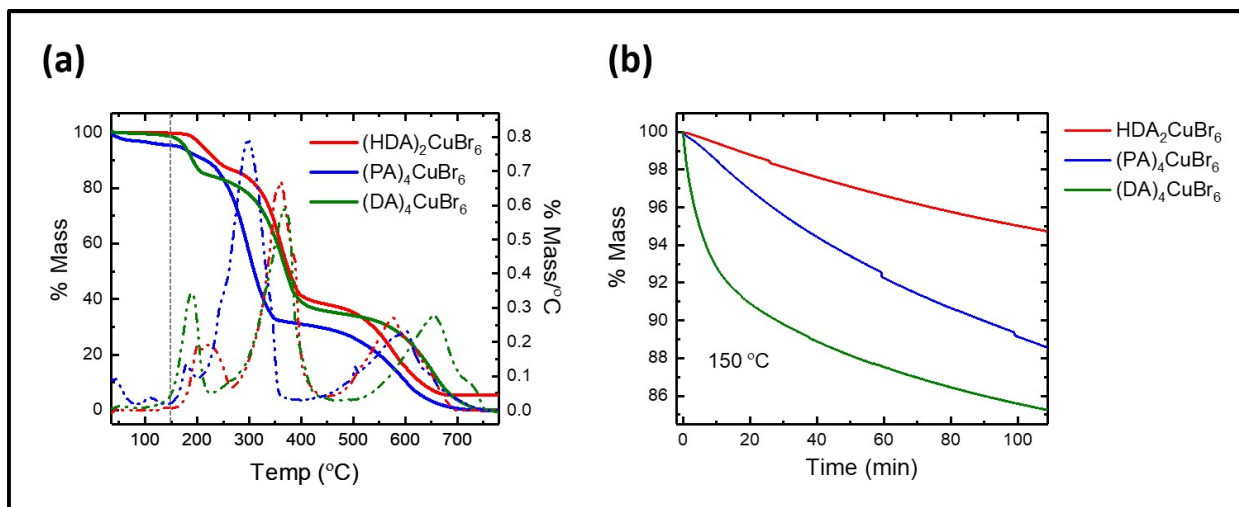


Figure 4.13. (a) Temperature-dependent thermogravimetric analysis of $(\text{HDA})_2\text{CuBr}_6$, $(\text{PA})_4\text{CuBr}_6$, and $(\text{DA})_4\text{CuBr}_6$ powders. The solid curves correspond to the % mass remaining (left axis) and the dashed curves correspond to the derivative of the % mass with respect to temperature (right axis). The gray dotted vertical line corresponds to the temperature used in panel b. (b) Isothermal thermogravimetric analysis at 150 °C as a function of time.

two-theta values of 5.66° and 7.80° . Accelerated thermal stability tests using thermogravimetric analysis on powders under an inert atmosphere showed similar trends when performed on $(\text{HDA})_2\text{CuBr}_6$ and $(\text{PA})_4\text{CuBr}_6$ (Figure 4.13) and when performed directly on bromide salts of the dicationic and monocationic organic moieties, i.e. HDABr_2 and PABr precursor powders (Figure 4.14). The same thermogravimetric analyses were performed on the material $(\text{DA})_4\text{CuBr}_6$, where DA^+ is the 1-decylammonium monocation ($\text{C}_{10}\text{H}_{21}\text{-NH}_3^+$), and the DABr precursor powder. Protonated decylamine was chosen for comparative thermal stability tests because of the similar boiling point of decylamine (217°C) to 1,6-hexanediamine (204°C). The results show that copper-bromide materials as well as precursor powders containing HDA can withstand the greatest amount of thermal input (Figure 4.13 and 4.14). These data suggest that for hybrid organic-inorganic materials that can accommodate organic moieties with a net charge of 2+ per formula unit, the presence of divalent organic ligands in the unit cell enhances stability, even in cases where a monovalent organic precursor is slightly less volatile than a divalent organic

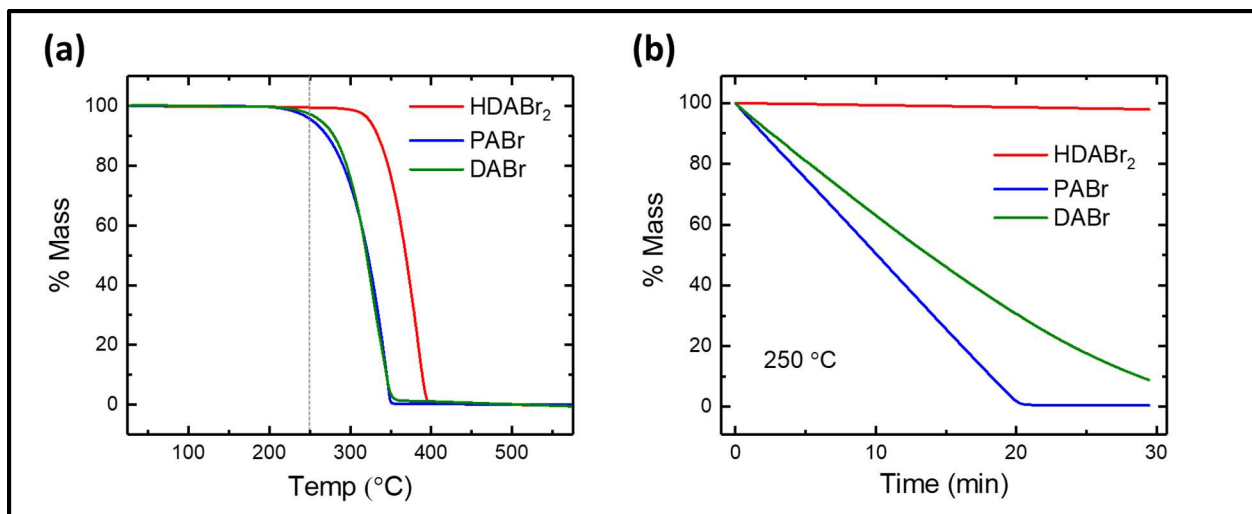


Figure 4.14. a) Temperature-dependent thermogravimetric analysis of HDABr₂, PABr, and DABr precursor powders. The gray dotted vertical line corresponds to the temperature used in panel b. (b) Isothermal thermogravimetric analysis at 250 °C as a function of time.

precursor. Cortecchia et al. reported that partial substitution of bromide for chloride in (MA)₂CuBr₄ improved crystallinity and moisture tolerance.⁴¹ However, Lichty et al. reported that chloride-containing phases should be more soluble in water at room temperature than bromide-containing phases, which may accelerate the degradation process of the chloride-containing

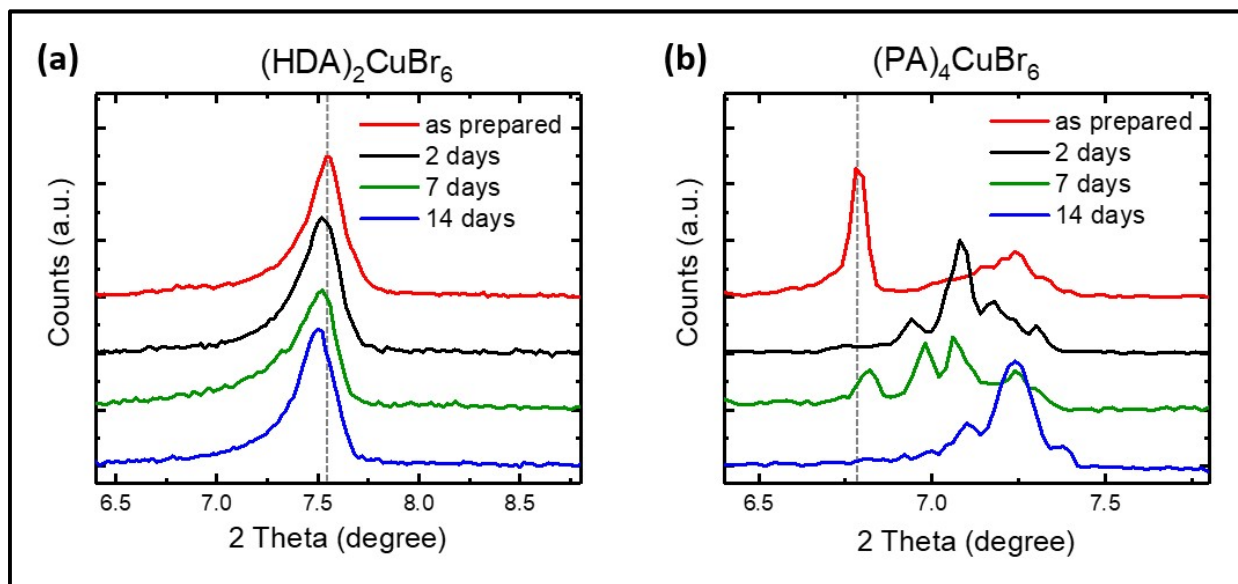


Figure 4.15. Powder XRD of (a) (HDA)₂CuBr₆ and (b) (PA)₄CuBr₆ during moisture stability tests at the indicated number of days into the tests. The position of the (001) peak for the freshly-prepared thin film is labeled with a gray dotted vertical line.

films.⁶² Herein, moisture stability studies on thin films of $(\text{HDA})_2\text{CuBr}_{6-x}\text{Cl}_x$, $0 \leq x \leq 2$, and $(\text{PA})_4\text{CuBr}_6$ indicated a trend consistent with aqueous solubility where thin films of $(\text{HDA})_2\text{CuBr}_6$ were more tolerant to ambient moisture (Figure 4.12b and Figure 4.15).

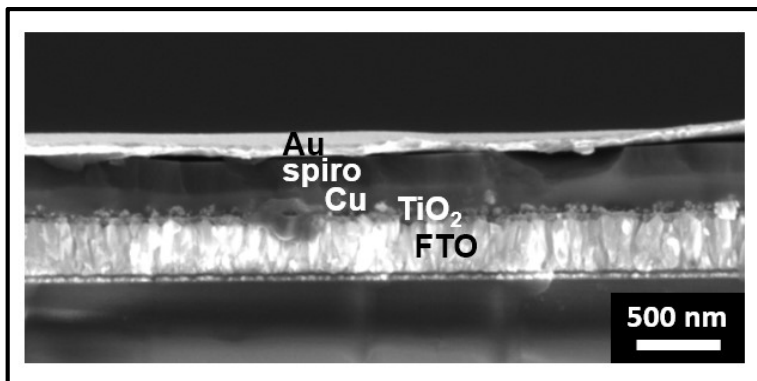


Figure 4.16. Cross-sectional scanning electron micrograph of a representative solar cell containing $(\text{HDA})_2\text{CuBr}_5\text{Cl}$ as the photoactive layer, and where spiro is spiro-OMeTAD, TiO_2 is a compact TiO_2 layer, and Cu is $(\text{HDA})_2\text{CuBr}_5\text{Cl}$.

Solar cells were fabricated from the 2D $(\text{HDA})_2\text{CuBr}_{6-x}\text{Cl}_x$ materials. All of the material layers were deposited in air except for the gold top contact. A cross-sectional SEM image of a representative solar cell containing $(\text{HDA})_2\text{CuBr}_5\text{Cl}$ as the light-absorbing layer is shown in Figure 4.16. This SEM image reveals that the $(\text{HDA})_2\text{CuBr}_5\text{Cl}$ layer is smooth, continuous, and,

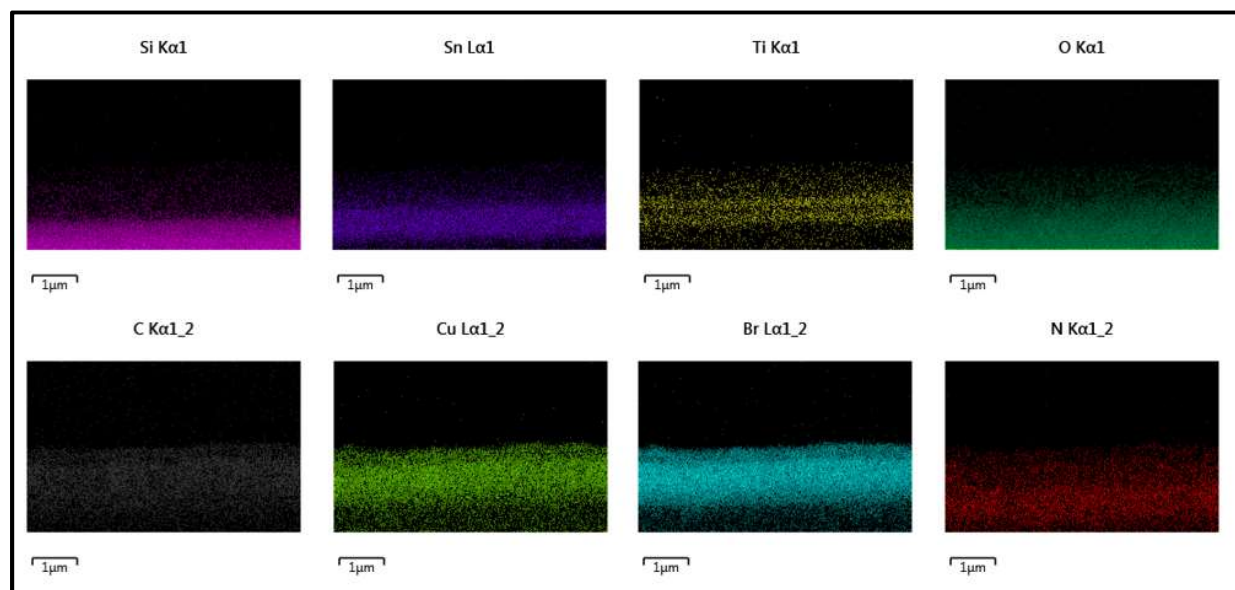


Figure 4.17. Energy-dispersive X-ray spectroscopy mapping data of a thin-film cross section of $(\text{HDA})_2\text{CuBr}_6/\text{mTiO}_2/\text{cTiO}_2/\text{FTO}$, where mTiO_2 is a mesoporous TiO_2 nanoparticle layer, cTiO_2 is a compact TiO_2 layer, and FTO is a fluorine-doped tin-oxide-coated glass substrate.

average, roughly 200 nm thick. The mesoporous TiO₂ scaffold is not visible as it is coated by the (HDA)₂CuBr₅Cl layer. Energy-dispersive X-ray spectroscopy mapping data of the (HDA)₂CuBr₆ thin-film cross section are shown in Figure 4.17 and they support the location of elements within the (HDA)₂CuBr₆, TiO₂, and fluorine-doped tin-oxide-coated glass (FTO) layers.

The photovoltaic performances of these materials as solar cells are shown in Figure 4.18a. Solar cells containing (HDA)₂CuBr₅Cl as the photoactive layer yielded the most promising photovoltaic performance, which may be attributed to the improved crystallinity due to partial substitution of bromide for chloride.³⁶ The champion solar cell, with an active area of 0.25 cm², exhibited an open-circuit photovoltage (V_{oc}) of 240 mV, a short-circuit photocurrent density (J_{sc}) of ~30 $\mu\text{A cm}^{-2}$, and a fill factor of 0.30, resulting in a light-to-electrical power conversion efficiency of ~0.002 %. A similar-sized champion solar cell containing (HDA)₂CuBr₆ exhibited a

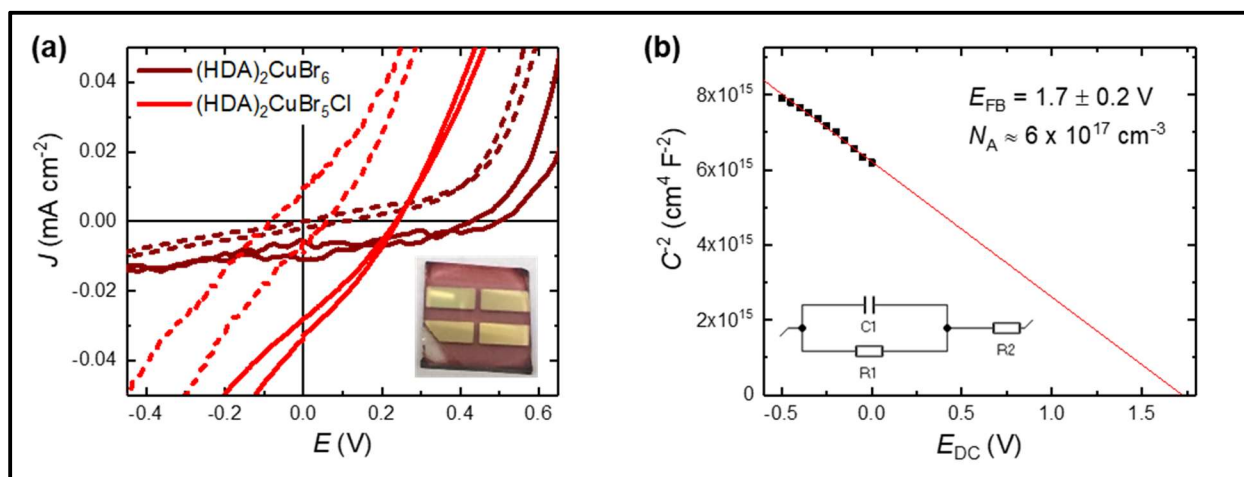


Figure 4.18 (a) J - E behavior for solar cells consisting of Au/spiro-OMeTAD/Cu/TiO₂/FTO, where Cu is (HDA)₂CuBr₆ (red traces) or (HDA)₂CuBr₅Cl (brown traces). Solid traces represent measurements under 1 sun irradiance and dashed traces represent dark measurements. Inset: digital photograph image of a complete solar cell. (b) Impedance spectroscopy data, presented as a Mott-Schottky plot, for a solar cell consisting of Au/spiro-OMeTAD/(HDA)₂CuBr₅Cl/TiO₂/FTO, and with the calculated flat-band potential (E_{FB}) and dopant density (N_A). Inset: standard Randles circuit used to model the impedance spectroscopy data.

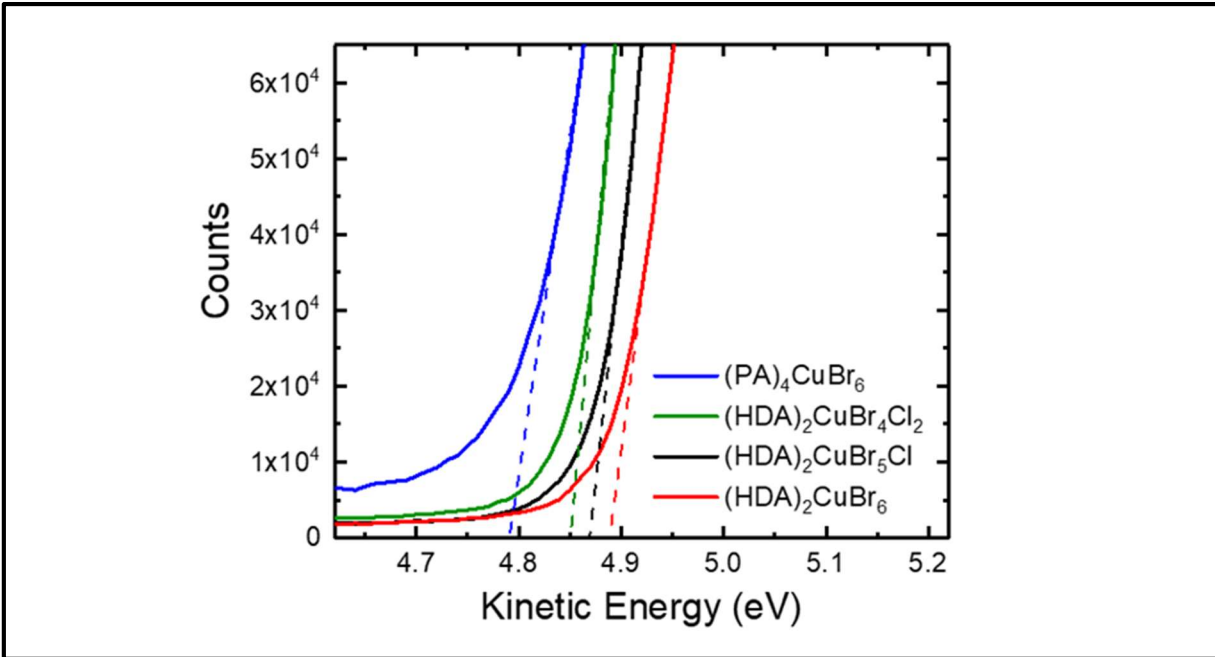


Figure 4.19. Low-intensity X-ray photoelectron spectra of the cutoff region to determine work functions of copper–halide hybrid organic–inorganic materials each deposited on a fluorine-doped tin–oxide-coated glass substrate.

much larger V_{oc} of > 400 mV, but a significantly smaller J_{sc} of $\sim 10 \mu\text{A cm}^{-2}$. Two-electrode impedance spectroscopy was used to determine the flat-band potential and doping density of $(\text{HDA})_2\text{CuBr}_5\text{Cl}$. A non-linear least-squares best fit of the $C-E$ data, depicted in the form of a Mott–Schottky plot (Figure 4.18b), indicates a flat-band potential of 1.7 ± 0.2 V and a doping density of $\sim 6 \times 10^{17} \text{ cm}^{-3}$. Calculations are provided in the *Electrical Characterization* subsection of the experimental section of this chapter. The maximum valence band energies of $(\text{HDA})_2\text{CuBr}_{6-x}\text{Cl}_x$ materials were calculated based on low-intensity X-ray photoelectron spectroscopy data reporting on the work function (Figure 4.19) and the valence band (Figure 4.20). From these measurements it was determined that the spiro-OMeTAD/ $(\text{HDA})_2\text{CuBr}_6$ interface and the $(\text{HDA})_2\text{CuBr}_6/\text{TiO}_2$ interface are responsible for combined losses in photovoltage that exceed 750 mV (Figure 4.21). Therefore, the electron-transport layer and hole-transport layers of $(\text{HDA})_2\text{CuBr}_{6-x}\text{Cl}_x$ -based solar cells can be optimized in order to achieve larger V_{oc} values. The

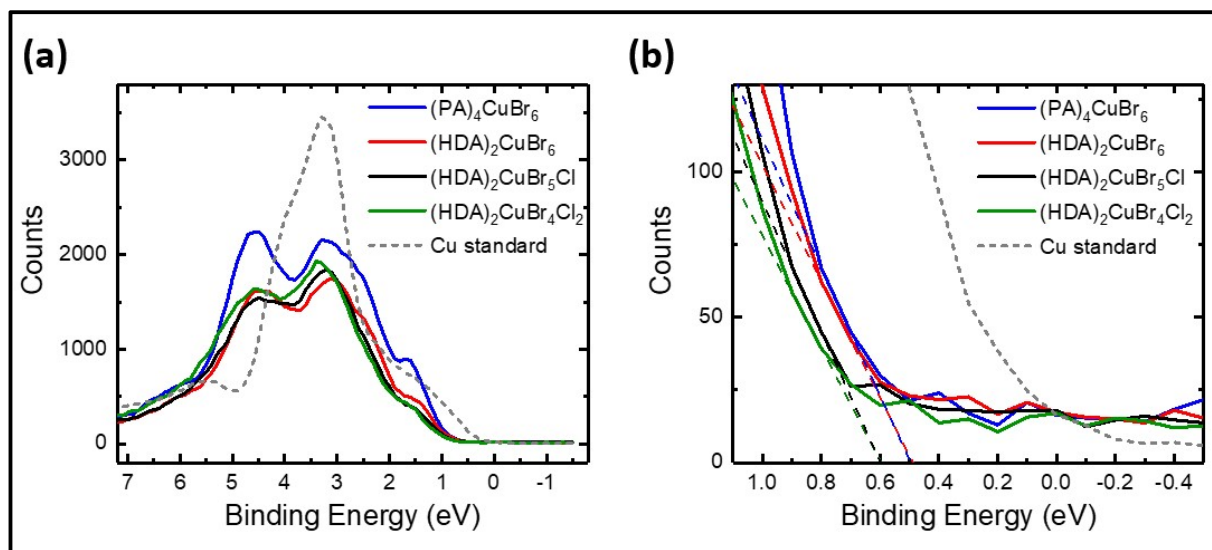


Figure 4.20. X-ray photoelectron valence-band spectra of copper–halide hybrid organic–inorganic materials each deposited on a fluorine-doped tin–oxide-coated glass substrate showing (a) the entire valence-band region and (b) the valence-band position relative to the work function of the copper standard (set to 0.0 eV).

energy difference between the conduction-band minimum and Fermi level in $(\text{HDA})_2\text{CuBr}_5\text{Cl}$ is 1.2 eV, which is in modest agreement with the flat-band potential calculated from Figure 4.18b. Additional analysis associated with the X-ray photoelectron spectroscopy data is provided in the *Materials Characterization* subsection of the experimental section.

4.4 Conclusions

With the aim to mitigate materials instability and toxicity, new 2D copper–halide hybrid organic–inorganic materials incorporating divalent organic ligands were synthesized and characterized. Electronic absorption spectra suggested indirect optical bandgaps of ~ 1.8 eV and photoluminescence spectra indicated the presence of emissive Cu^+ trap states. X-ray photoelectron spectroscopy data confirmed surface elemental composition of these materials and supported the faster degradation during sample processing observed for $(\text{PA})_4\text{CuBr}_6$ in comparison to $(\text{HDA})_2\text{CuBr}_6$, possibly due to reduction of Cu^{2+} to Cu^+/Cu^0 . Grazing-incidence X-ray diffraction

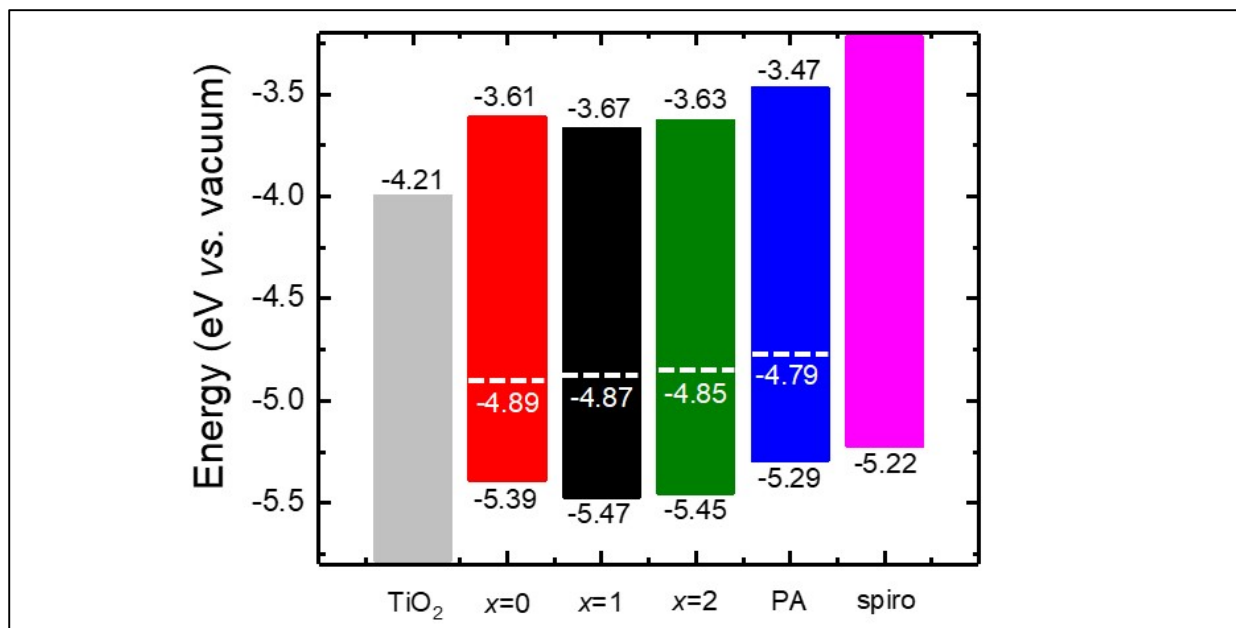


Figure 4.21. Energy-level diagram of $(\text{HDA})_2\text{CuBr}_{6-x}\text{Cl}_x$ thin films, with $x = 0$ (red), $x = 1$ (black), and $x = 2$ (green), as well as a $(\text{PA})_4\text{CuBr}_6$ thin film (blue), each deposited on a fluorine-doped tin-oxide-coated glass substrate. Valence-band maxima (Figure 4.20) and work functions (Figure 4.19) were determined by X-ray photoelectron spectroscopy measurements. The conduction-band minimum of each copper-halide hybrid organic-inorganic material was calculated as described in the Materials Characterization subsection. The conduction-band minimum of TiO_2 and valence-band maximum of spiro-OMeTAD were taken from a report by Chilvery et al.³²

data confirmed crystallinity and indicated preferential orientation in the [001] direction such that the copper-halide sheets were oriented in-plane with the substrate.

$(\text{HDA})_2\text{CuBr}_6$ demonstrated superior stability to heat and moisture in comparison to analogous monocationic copper-halide materials, $(\text{PA})_4\text{CuBr}_6$ and $(\text{DA})_4\text{CuBr}_6$. Photophysical measurements on $(\text{HDA})_2\text{CuBr}_5\text{Cl}$ solar cells demonstrated a champion photovoltage in excess of 400 mV and a champion photocurrent of $\sim 30 \mu\text{A cm}^{-2}$, which are similar to reported values for analogous state-of-the-art materials containing organic monocations.

4.5 References

- (1) D. M. Fabian, J. W. Ziller, S. Ardo, *J. Mater. Chem. A*, 2018, manuscript in preparation.

- (2) S. I. Seok, M. Grätzel and N.-G. Park, *Small*, **2018**, 201704177.
- (3) G. E. Eperon, M. T. Hörantner and H. J. Snaith, *Nat. Rev. Chem.*, **2017**, *1*, 95.
- (4) T. Leijtens, K. Bush, R. Cheacharoen, R. Beal, A. Bowring and M. D. McGehee, *J. Mater. Chem. A*, **2017**, *5*, 11483.
- (5) S. Albrecht, M. Saliba, J. P. Correa Baena, F. Lang, L. Kegelmann, M. Mews, L. Steier, A. Abate, J. Rappich, L. Korte, R. Schlattmann, N. Mohammad K., A. Hagfeldt, M. Grätzel and B. Rech, *Energy Environ. Sci.*, **2016**, *9*, 81–88.
- (6) K. A. Bush, A. F. Palmstrom, Z. J. Yu, M. Boccard, R. Cheacharoen, J. P. Mailoa, D. P. McMeekin, R. L. Z. Hoye, C. D. Bailie, T. Leijtens, I. M. Peters, M. C. Minichetti, N. Rolston, R. Prasanna, S. Sofia, D. Harwood, W. Ma, F. Moghadam, H. J. Snaith, T. Buonassisi, Z. C. Holman, S. F. Bent and M. D. McGehee, *Nat. Energy*, **2017**, *2*, 17009.
- (7) M. A. Green, Y. Hishikawa, E. D. Dunlop, D. H. Levi, J. Hohl-Ebinger and A. W. Y. Ho-Baillie, *Prog. Photovoltaics Res. Appl.*, **2018**, *26*, 3.
- (8) M. Saliba, T. Matsui, J.-Y. Seo, K. Domanski, J.-P. Correa-Baena, M. K. Nazeeruddin, S. M. Zakeeruddin, W. Tress, A. Abate, A. Hagfeldt and M. Gratzel, *Energy Environ. Sci.*, **2016**, *9*, 1989.
- (9) B. Saparov and D. B. Mitzi, *Chem. Rev.*, **2016**, *116*, 4558.
- (10) A. H. Slavney, R. W. Smaha, I. C. Smith, A. Ja, D. Umeyama and H. I. Karunadasa, *Inorg. Chem.*, **2017**, *56*, 46.
- (11) T. Leijtens, G. E. Eperon, N. K. Noel, S. N. Habisreutinger, A. Petrozza and H. J. Snaith, *Adv. Energy Mater.*, **2015**, *5*, 1500963.
- (12) R. K. Misra, S. Aharon, B. Li, D. Mogilyansky, I. Visoly-Fisher, L. Etgar and E. A. Katz, *J. Phys. Chem. Lett.*, **2015**, *6*, 326.

- (13) N. Aristidou, I. Sanchez-Molina, T. Chotchuangchutchaval, M. Brown, L. Martinez, T. Rath and S. A. Haque, *Angew. Chem., Int. Ed.*, **2015**, *54*, 8208.
- (14) M. Becker, T. Klüner and M. Wark, *Dalt. Trans.*, **2017**, *46*, 3500.
- (15) K. Liang, D. B. Mitzi and M. T. Prikas, *Chem. Mater.*, **1998**, *10*, 403.
- (16) D. B. Mitzi, K. Chondroudis and C. R. Kagan, *Inorg. Chem.*, **1999**, *38*, 6246.
- (17) D. B. Mitzi, *Inorg. Chem.*, **2000**, *39*, 6107.
- (18) I. C. Smith, E. T. Hoke, D. Solis-Ibarra, M. D. McGehee and H. I. Karunadasa, *Angew. Chem., Int. Ed.*, **2014**, *53*, 11232.
- (19) D. Cao, C. C. Stoumpos, O. K. Farha, J. T. Hupp and M. G. Kanatzidis, *J. Am. Chem. Soc.*, **2015**, *137*, 7843.
- (20) R. K. Misra, B.-E. Cohen, L. Iagher and L. Etgar, *ChemSusChem*, **2017**, *10*, 3712.
- (21) D. M. Fabian and S. Ardo, *J. Mater. Chem. A*, **2016**, *4*, 6837.
- (22) H. L. Wells, *Anorg. Chem., Int. Ed.*, **1893**, *3*, 195.
- (23) A. Kojima, K. Teshima, Y. Shirai and T. Miyasaka, *J. Am. Chem. Soc.*, **2009**, *131*, 6050.
- (24) G. A. Mousdis, G. C. Papavassiliou, A. Terzis and C. P. Raptopoulou, *Z. Naturforsch.*, **1998**, *53b*, 927.
- (25) D. B. Mitzi and P. Brock, *Inorg. Chem.*, **2001**, *40*, 2096.
- (26) R. E. Brandt, R. C. Kurchin, R. L. Z. Hoye, J. R. Poindexter, M. W. B. Wilson, S. Sulekar, F. Lenahan, P. X. T. Yen, V. Stevanovi, J. C. Nino, M. G. Bawendi and T. Buonassisi, *J. Phys. Chem. Lett.*, **2015**, *6*, 4297.
- (27) A. J. Lehner, D. H. Fabini, H. A. Evans, C.-A. Hébert, S. R. Smock, J. Hu, H. Wang, J. W. Zwanziger, M. L. Chabynyc and R. Seshadri, *Chem. Mater.*, **2015**, *27*, 7137.

- (28) B. W. Park, B. Philippe, X. Zhang, H. Rensmo, G. Boschloo and E. M. J. Johansson, *Adv. Mater.*, **2015**, *27*, 6806.
- (29) M. Lyu, J. H. Yun, M. Cai, Y. Jiao, P. V. Bernhardt, M. Zhang, Q. Wang, A. Du, H. Wang, G. Liu and L. Wang, *Nano Res.*, **2016**, *9*, 692.
- (30) R. Hoye, R. E. Brandt, A. Osherov, V. Stevanovic, S. D. Stranks, M. W. B. Wilson, H. Kim, A. J. Akey, R. C. Kurchin, J. R. Poindexter, E. N. Wang, M. G. Bawendi, V. Bulovic and T. Buonassisi, *Chem. - A Eur. J.*, **2016**, *22*, 2605.
- (31) A. H. Slavney, T. Hu, A. M. Lindenberg and H. I. Karunadasa, *J. Am. Chem. Soc.*, **2016**, *138*, 2138.
- (32) G. Volonakis, M. R. Filip, A. A. Haghghirad, N. Sakai, B. Wenger, H. J. Snaith and F. Giustino, *J. Phys. Chem. Lett.*, **2016**, *7*, 1254.
- (33) K. K. Bass, L. Estergreen, C. N. Savory, J. Buckeridge, D. O. Scanlon, P. I. Djurovich, S. E. Bradforth, M. E. Thompson and B. C. Melot, *Inorg. Chem.*, **2017**, *56*, 42.
- (34) R. Willett, H. Place and M. Middleton, *J. Am. Chem. Soc.*, **1988**, *110*, 8639.
- (35) C. C. Stoumpos, D. H. Cao, D. J. Clark, J. Young, J. M. Rondinelli, J. I. Jang, J. T. Hupp and M. G. Kanatzidis, *Chem. Mater.*, **2016**, *28*, 2852.
- (36) H. Tsai, W. Nie, J.-C. Blancon, C. C. Stoumpos, R. Asadpour, B. Harutyunyan, A. J. Neukirch, R. Verduzco, J. J. Crochet, S. Tretiak, L. Pedesseau, J. Even, M. A. Alam, G. Gupta, J. Lou, P. M. Ajayan, M. J. Bedzyk, M. G. Kanatzidis and A. D. Mohite, *Nature*, **2016**, *536*, 312.
- (37) M. Safdari, P. H. Svensson, M. T. Hoang, I. Oh, L. Kloo and J. M. Gardner, *J. Mater. Chem. A*, **2016**, *4*, 15638.

- (38) C. C. Stoumpos, C. M. M. Soe, H. Tsai, W. Nie, J.-C. Blancon, D. H. Cao, F. Liu, B. Traoré, C. Katan, J. Even, A. D. Mohite and M. G. Kanatzidis, *Chem*, **2017**, *2*, 427.
- (39) D. H. Cao, C. C. Stoumpos, T. Yokoyama, J. L. Logsdon, T.-B. Song, O. K. Farha, M. R. Wasielewski, J. T. Hupp and M. G. Kanatzidis, *ACS Energy Lett.*, **2017**, *2*, 982.
- (40) Z. Wang, A. M. Ganose, C. Niu and D. O. Scanlon, *J. Mater. Chem. A*, **2018**, *6*, 5652.
- (41) Q. Li, S. Li, K. Wang, Z. Quan, Y. Meng and B. Zou, *J. Phys. Chem. Lett.*, **2017**, *8*, 500.
- (42) D. Cortecchia, H. A. Dewi, J. Yin, A. Bruno, S. Chen, T. Baikie, P. P. Boix, M. Grätzel, S. Mhaisalkar, C. Soci and N. Mathews, *Inorg. Chem.*, **2016**, *55*, 1044.
- (43) D. Cortecchia, C. Soci, M. Cametti, A. Petrozza and J. Martí-Rujas, *ChemPlusChem*, **2016**, *81*, 1.
- (44) APEX2, 2014.
- (45) SAINT, 2013.
- (46) Sheldrick, G. M. SADABS, 2014.
- (47) Sheldrick, G. M. SHELXTL, 2014.
- (48) International Tables for X-Ray Crystallography; Vol C.; Kluwer Academic Publishers: Dordrecht, 1992.
- (49) Ito, S.; Murakami, T. N.; Comte, P.; Liska, P.; Grätzel, C.; Nazeeruddin, M. K.; Grätzel, M. *Thin Solid Films* **2008**, *516*, 4613.
- (50) Kim, H.-S.; Lee, C.-R.; Im, J.-H.; Lee, K.-B.; Moehl, T.; Marchioro, A.; Moon, S.-J.; Humphry-Baker, R.; Yum, J.-H.; Moser, J. E.; Grätzel, M.; Park, N.-G. *Sci. Rep.* **2012**, *2*, 591.
- (51) Chusuei, C. C.; Brookshier, M. A.; Goodman, D. W. *Langmuir* **1999**, *15*, 2806.

- (52) Schlaf, R.; Murata, H.; Kafafi, Z. *J. Electron. Spectrosc. Relat. Phenom.* **2001**, *120*, 149.
- (53) Schulz, P.; Edri, E.; Kirmayer, S.; Hodes, G.; Cahen, D.; Kahn, A. *Energy Environ. Sci.* **2014**, *7*, 1377.
- (54) Chilvery, A. K.; Guggilla, P.; Batra, A. K.; Gaikwad, D. D.; Currie, J. R. *J. Photon. Energy* **2015**, *5*, 053093.
- (55) Dualeh, A.; Moehl, T.; Tétreault, N.; Teuscher, J.; Gao, P.; Nazeeruddin, M. K.; Grätzel, M. *ACS Nano* **2014**, *8*, 362.
- (56) Gelderman, K.; Lee, L.; Donne, S. W. *J. Chem. Ed.* **2007**, *84*, 685.
- (57) Lin, Q.; Armin, A.; Chandra, R.; Nagiri, R.; Burn, P. L.; Meredith, P. *Nat. Photon.* **2014**, *9*, 106.
- (58) Bard, A. J.; Faulkner, L. R. *Electrochemical Methods: Fundamentals and Applications*, 2nd ed.; John Wiley & Sons, Inc.: New York, 2001.
- (59) K. Halvorson and R. D. Willett, *Acta Crystallogr.*, **1988**, *C44*, 2071.
- (60) J. Yan, X. Ke, Y. Chen, A. Zhang and B. Zhang, *Appl. Surf. Sci.*, **2015**, *351*, 1191.
- (61) A. R. West, *Basic Solid State Chemistry*, John Wiley & Sons, Inc., New York, 2nd ed., 1999.
- (62) D. M. Lichy, *J. Am. Chem. Soc.*, **1903**, *25*, 469.

CHAPTER 5: LOW-DIMENSIONAL LEAD–HALIDE PEROVSKITE MATERIALS INCORPORATING DIVALENT ORGANIC LIGANDS

** In part a compilation of one publication in preparation¹*

5.1 Introduction

Two-dimensional (2D) lead–halide perovskites incorporating divalent organic ligands have an advantage over three-dimensional (3D) lead–halide perovskites with regard to the inherent stability of the organic moiety.² Due to their structural dimensionality, the low-dimensional lead–halide perovskites are most likely better suited for use in light-emitting diodes as opposed to solar cells for their emissive properties yet inferior charge-carrier conduction.^{3–5} The structural confinement of the low-dimensional lead–halide perovskites results in excitonic behavior (i.e.

exciton binding energies are not negligible), and as a result, charge-carrier diffusion lengths are substantially lower than those of 3D lead–halide perovskites.⁶ If the structural dimensionality is 2D the material behaves like quantum films, if it is 1D the material behaves like

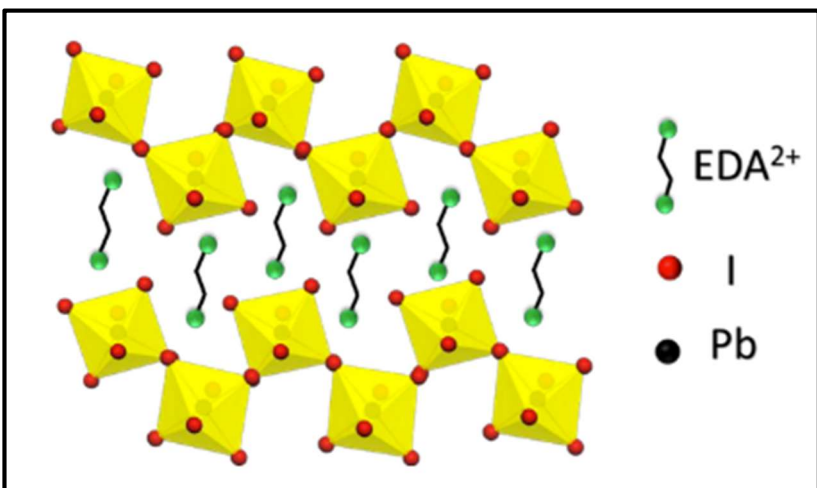


Figure 5.1. Proposed structure of the two-dimensional lead–halide perovskite ethylenediamine lead iodide (EDAPbI₄) viewed along the plane of the $n=1$ sheets of PbI₆ octahedra. From Zhang, T.; Dar, M. I.; Li, G.; Xu, F.; Guo, N.; Grätzel, M.; Zhao, Y. *Sci. Adv.* **2017**, *3*, e1700841. Reprinted with permission from AAAS.

quantum rods or wires, and if it is 0D the material behaves like quantum dots.⁷ Strategies have been employed, however, to lower the exciton binding energies of 2D perovskites such that the absorption and electronic confinement are like those of 3D perovskites.⁸ It has been shown that incorporation of a small amount of the 2D perovskite EDAPbI₄ stabilizes the α phase of the 3D perovskite CsPbI₃ to avoid the undesirable phase change to the non-perovskite γ -phase of CsPbI₃ (Figure 5.1).⁹

Time-resolved photoluminescence (TRPL) has been used to measure free-charge-carrier kinetics in perovskite materials.^{10–14} TRPL measurements have been performed on perovskite single crystals as well as polycrystalline thin films. Notably, PL lifetimes of 3D perovskite thin films have been shown to exceed 8 μ s¹¹ and charge-carrier recombination centers are predominantly located on the surface of crystallites rather than in the bulk of the crystallites.¹² In addition, it has been determined through TRMC and TRPL measurements that perovskite thin films deposited in the planar architecture exhibited higher charge-carrier mobilities and slower recombination compared thin films deposited in the mesostructured architecture.¹³ This difference was attributed to the larger average crystallite size in planar films vs. mesostructured films.¹³

Time-resolved terahertz spectroscopy (TRTS) is a useful technique for measuring free-charge-carrier generation and decay in novel materials and technologies for solar energy conversion.^{15,16} Time-resolved terahertz spectroscopy (TRTS) probes photoconductivity of a sample, where the photoconductivity is the product of the mobility and the concentration of charge carriers.¹⁷ A schematic of the TRTS experimental setup is shown in Figure 5.2.¹⁸ TRTS, much like transient absorption spectroscopy (TAS), is a pump–probe technique. TRTS requires generation of ultrafast optical pump and terahertz probe pulses that are synchronized. To accomplish this, a fraction of the pulses used to generate and detect the probe pulses is split to produce an optical

pump pulse. The terahertz pulse is delayed with respect to the optical pump pulse, the sample is photoexcited by the pump pulse, and the sample attenuates, delays, and distorts the terahertz pulse according to its complex photoexcited permittivity. As a result, kinetic processes that occur in the terahertz region can be probed. The delay time between the optical pump and terahertz probe pulses

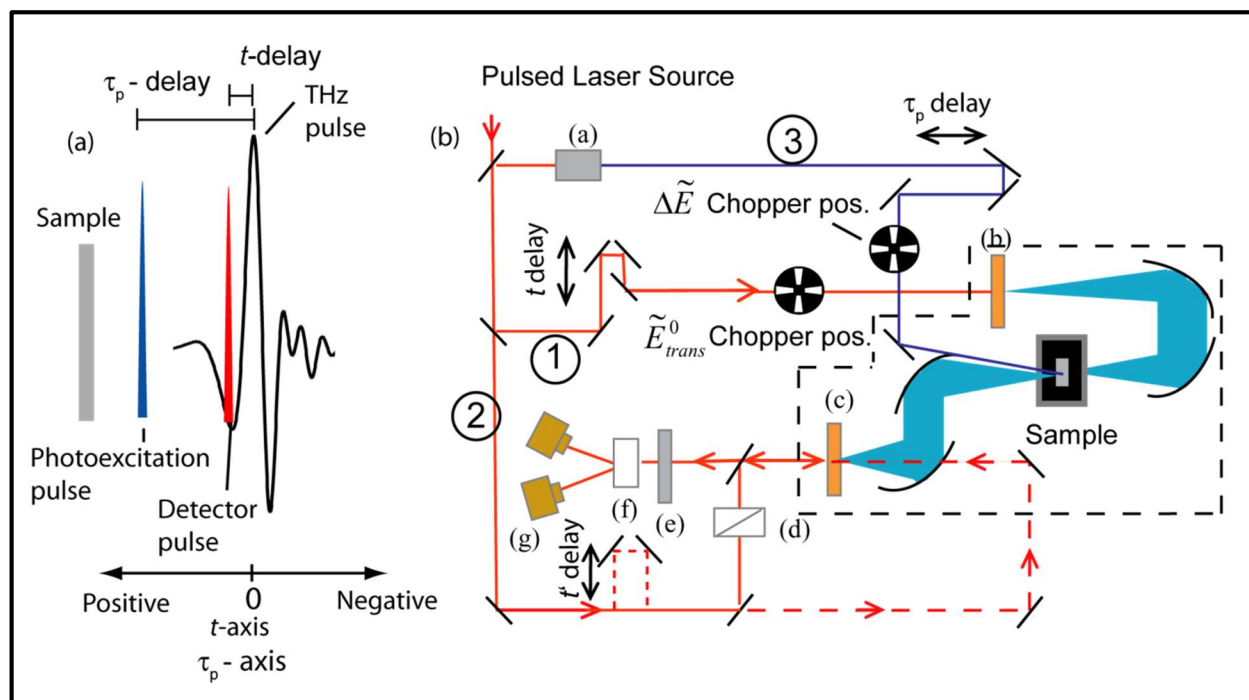


Figure 5.2. (a) A schematic representation of time-resolved terahertz (THz) spectroscopy (TRTS). There is a THz pulse, detector pulse, and photoexcitation pulse. THz pulses are generated via optical rectification of <100 fs pulses from an amplified Ti:Sapphire laser (fundamental wavelength = 800 nm) operating at a repetition rate of 1 kHz. (b) A diagram of the experimental setup of TRTS. The numbers correspond to the beam path of the THz pulse (1), the detector pulse (2), and the photoexcitation pulse (3). Key components are the pulsed laser source (a), THz generation crystal (b), detector crystal (c), near-IR linear polarizer (d), $\frac{1}{4}$ waveplate (e), beam-splitting polarizer (f), and balanced photodiodes (g). The THz pulse is focused onto the sample and overlapped with a visible pump pulse. THz radiation spans frequencies ~ 0.1 to 3 THz, or 3 mm to 100 microns, as a result, the THz radiation is typically focused down to approximately ~ 5 mm. One cannot then focus the visible pump pulse tighter than ~ 1 cm to ensure uniform excitation of the sample. In practical terms this implies that the size of the samples investigated be large (but not necessarily thick) and the necessary pulse energies for photoexcitation are higher even if the photon density is not then typically used for visible pump-probe measurements. Reprinted with permission from Beard, M.C.; Blackburn, J. L.; Heben, M. J. *Nano Lett.*, **2008**, *8*, 4238–4242. Copyright 2008 American Chemical Society.

can be varied, which allows for the study of carrier injection, cooling, decay, and trapping processes.

Amplified Ti:Sapphire laser systems are commonly used as laser sources, but unamplified Ti:Sapphire lasers or synchrotrons can also be used if different photon fluences or photon energies are desired. Amplified Ti:Sapphire laser systems can provide high energy, <100 fs pulses at kilohertz repetition rates with wavelengths that are tunable by nonlinear optics and optical parametric amplifiers. For samples that are expected to produce a large change in terahertz transmission per photon and whose longest time constants are on the order of nanoseconds, it is possible to perform TRTS with just a high repetition rate Ti:Sapphire oscillator. On the other hand, for samples requiring very high photon flux, free-electron lasers or synchrotron sources can be used. THz radiation spans frequencies of 0.1 to 3 THz, which corresponds to wavelengths of 3 mm to 100 microns. As a result, the THz radiation is focused down to ~5 mm. To ensure uniform excitation of the sample, visible pump pulse cannot be focused down to smaller than ~1 cm, implying that the sample size be large. The sample thickness, however, does not need to be large; as the system is set up to measure THz transmission, the sample can be any thickness so long as it transmits THz radiation.

Low-dimensional lead-halide perovskites may also show promise for use in spintronics technologies.¹⁹⁻²¹ The spin-dependent optical response of lead-halide perovskites suggests a method to control spin states, which is a prerequisite for quantum computing based on spin.²¹ Spin splitting in lead-halide perovskites may also be strong enough to aid in long charge-carrier lifetimes.²⁰ However, calculations on lead-halide perovskites have concluded that spin splitting is very sensitive to organic cation orientation and inorganic structural distortion.²⁰ It is hypothesized that the presence of a bulky organic cation moiety may result in improper orientation to observe

the spin splitting effect. In addition, a low-dimensional or distorted inorganic framework may inhibit the observation of spin splitting.

5.2 Experimental

5.2.1 Preparation of Hybrid Organic–Inorganic Lead–Iodide Solutions

All chemicals were used as received. Diammonium dihydroiodide salts were synthesized by slow addition of hydriodic acid (57% in water, stabilized with 1.5% hypophosphorous acid, Sigma-Aldrich) to the diamine of choice dissolved in methanol. The hydriodic acid to diamine molar ratio was 2:1, with hydriodic acid in slight excess. As an example, to synthesize 1,6-hexanediamine dihydriodide (HDA•2HI), 260.9 mg of 1,6-hexanediamine (98+%, Alfa Aesar) was dissolved in 5 mL methanol, and then 1 mL hydriodic acid was added slowly at 0 °C with stirring, followed by stirring for an additional 30 min. HDA•2HI precipitate was recovered by evaporation of solvents at 40 °C with a rotary evaporator. The precipitate was rinsed with diethyl ether, and vacuum dried at 60 °C for at least 12 h. HDAPbI₄ solution was then prepared by mixing HDA•2HI and PbI₂ (99.999%, Sigma-Aldrich) powders at an approximately 1:1 mole ratio, with HDA•2HI in slight excess, in an anhydrous mixture of 4:1 (v/v) DMF:DMSO at 70 °C inside a nitrogen-filled glovebox. The HDAPbI₄ solution was stored in the glovebox until use and was used within one week of preparation.

MAPbBr₃ solution was prepared by mixing methylammonium bromide (MABr, 98%, Sigma-Aldrich) and PbI₂ (99%, Sigma-Aldrich) powders at approximately a 1:1 mole ratio, but with MABr in slight excess, in an anhydrous mixture of 4:1 (v/v) DMF:DMSO at 70 °C inside a nitrogen-filled glovebox. The MAPbBr₃ solution was stored in the glovebox until use and was

used within one week of preparation. All powders were combined for solution preparation inside a nitrogen-filled glovebox.

5.2.2 Materials Processing

Materials deposition and thin-film annealing were performed in a nitrogen-filled glovebox. All substrates were cleaned as follows: 1) sonication in Alconox solution, 2) rinse with deionized water, 3) rinse with ethanol, 4) sonication in ethanol, and 5) dry with nitrogen. The substrates were further cleaned by UV/ozone treatment for 10 min. A conventional spin-coat method was adapted from Kim et al.²² and used for depositing the hybrid organic–inorganic lead–iodide solutions. For this method, a filtered 0.5 M solution in 4:1 (v/v) DMF:DMSO was pipetted on top of the substrate and then the substrate was spun at 6000 rpm (6000 rpm/s acceleration) for 60 s, followed by rapid transfer to a hot plate that was preheated to 100 °C and subsequent annealing at 100 °C for 45 min. For all deposition methods, the photoactive layer solution was dispensed on the substrate at a volume of 17.5 $\mu\text{A}/\text{cm}^2$. For X-ray diffraction (XRD) measurements, the substrate used was fluorine-doped tin oxide coated glass (FTO). For transmission, reflection, steady-state photoluminescence (PL), and time-resolved photoluminescence (TRPL) measurements, the substrate used was glass. For time-resolved terahertz spectroscopy (TRTS) and transient absorption spectroscopy (TAS), the substrate used was quartz.

5.2.3 Ultrafast Laser Spectroscopy

Time-resolved photoluminescence spectroscopy measurements were performed using the time-correlated single photon counting technique. Excitation light was generated by a Fianium SC-450-PP laser operating with an average power of 15.5 μW at a repetition rate of 10 MHz and a

wavelength of 450 nm selected by a Fianium AOTF system. A 470 nm long pass filter was used to remove scattering from the excitation source. The emission was detected using a Hamamatsu streak camera with a wavelength range of 200-900 nm and response of < 20 ps. To compare traces, data were shifted and normalized so that maximal values of 1 occurred at $t = 0$ ns. Samples were measured under ambient conditions.

TAS measurements were performed using a Coherent Libra Ti:sapphire ultrafast laser (800 nm, pulse duration ~ 100 fs, ~ 4 mJ/pulse, and 1 KHz repetition rate) and a Helios Ultrafast System pump-probe TA spectrometer. In this system, the 800 nm fundamental beam is split into two beams, one of which becomes the pump beam and the other becomes the probe beam. One beam is sent to a TOPAS optical parametric amplifier to generate the pump pulse with a tunable wavelength, and its intensity is attenuated by two neutral density filters. The other beam is focused into a sapphire crystal to generate a white light continuum probe beam. The pump-probe delay is tuned by a delay line (Thorlabs). The pump and probe beams are focused and overlapped onto the sample. The pump excitation pulse power is measured using a power meter, and pump fluence was calculated to be 0.29–1.16 mJ/cm². The probe beam size is ~ 130 μ m and the pump beam size is ~ 1 mm. Samples were measured under ambient conditions.

The experimental setup for TRTS measurements is described as follows. The optical pulse beam (1 KHz repetition rate, <100 fs pulse duration, 4.5 mJ/ pulse energy, $\lambda = 800$ nm wavelength) is provided by an amplified Ti:Sapphire laser (Coherent Libra) which consists of a regenerative amplifier seeded by a mode-locked oscillator. The amplifier output is split to feed an optical parametric amplifier (Light Conversion Ltd., TOPAS-C), which generates excitation pulses that serve as the optical pump to photo-generate carriers in the sample. The pump excitation pulse power is measured using a power meter, and pump fluence was calculated to be 0.27 mJ/cm². A

second part of the beam is used to generate single cycle terahertz pulses by optical rectification in a ZnTe non-linear crystal. The terahertz probe beam is focused on the sample using mirrors. The transmitted terahertz pulses are detected in the time domain through free-space electro-optic sampling. A third part of the initial pump beam is used as a gating beam and guided over a delay line onto a ZnTe detector crystal. By varying the time delays between the optical pump pulse, the terahertz probe pulse, and the gating, amplitude and phase changes of the terahertz single-cycle pulses can be recorded. Amplitude changes of the terahertz pulses upon photo-excitation were measured on balanced large-area silicon photodiodes on a time scale of up to 1.5 ns with sub-picosecond time resolution. Samples were contained in an unsealed chamber kept under a constant flow of nitrogen.

5.2.4 Characterization

Grazing-incidence XRD data were collected using a Rigaku Smartlab diffractometer with Cu K α radiation and in parallel beam geometry. Transmission and reflection spectra were obtained using an integrating sphere in a Shimadzu UV-3600 ultraviolet-visible-near-infrared spectrophotometer. Absorption was calculated by assuming Absorbance = 1 – Transmittance – Reflectance. Steady-state photoluminescence (PL) was measured with a Horiba Jobin Yvon Model FL-1039/40 Fluorolog, a Horiba Jobin Yvon iHR320 spectrograph, and a Horiba Jobin Yvon SPEX Instruments S.A. Group Spectrum One G35 CCD camera. A monochromatized Xe lamp was used as the excitation source.

Transmission, reflection, steady-state PL, TRPL, TAS, TRTS spectroscopy, and grazing-incidence XRD measurements were performed in the Chemistry and Nanoscience Center at the National Renewable Energy Laboratory.

5.3 Results & Discussion

An extensive analysis on low-dimensional $n=1$ lead-iodide perovskite materials incorporating divalent alkylammonium cations was performed. The materials under investigation contained divalent cations of varying alkyl chain length: two-carbon ethylenediamine (EDA), four-carbon butanediamine (BDA), and six-carbon hexanediamine (HDA). These materials are hypothesized to be 2D $n=1$ perovskites, where $n=1$ means there is just one layer of Pb-I octahedra that comprise the sheets, which are separated by the organic ligands. Absorption spectra of the series of low-dimensional hybrid lead-iodide materials as thin films are shown in Figure 5.3a. It is clear from the absorption spectra that the absorption onset red-shifts as the size of the organic moiety decreases. The resulting red-shift in the absorption onset indicates bandgap narrowing, which is also observed in 3D hybrid lead-halide materials as size of the organic moiety decreases. The absorption spectra of BDAPbI₄ and HDAPbI₄ exhibit a single exciton peak whereas EDAPbI₄ exhibits two exciton peaks, one at a longer wavelength and one at a shorter wavelength than the exciton peaks of BDAPbI₄ and HDAPbI₄. This suggests the presence of a mix of a 2D phase and a one-dimensional (1D) or zero-dimensional (0D) phase in the EDAPbI₄ thin film.

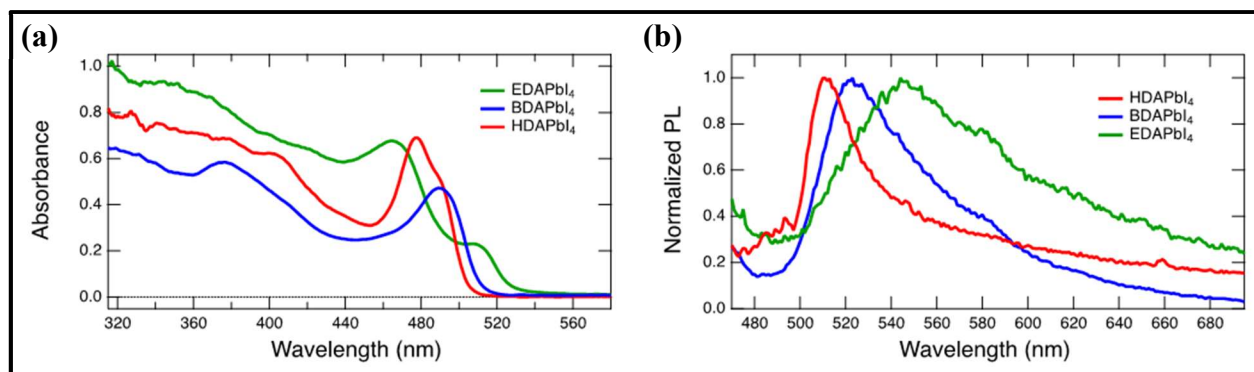


Figure 5.3. (a) UV-Visible absorption spectra and (b) steady-state emission spectra ($\lambda_{\text{ex}} = 400$ nm) of hybrid lead-halide material thin films.

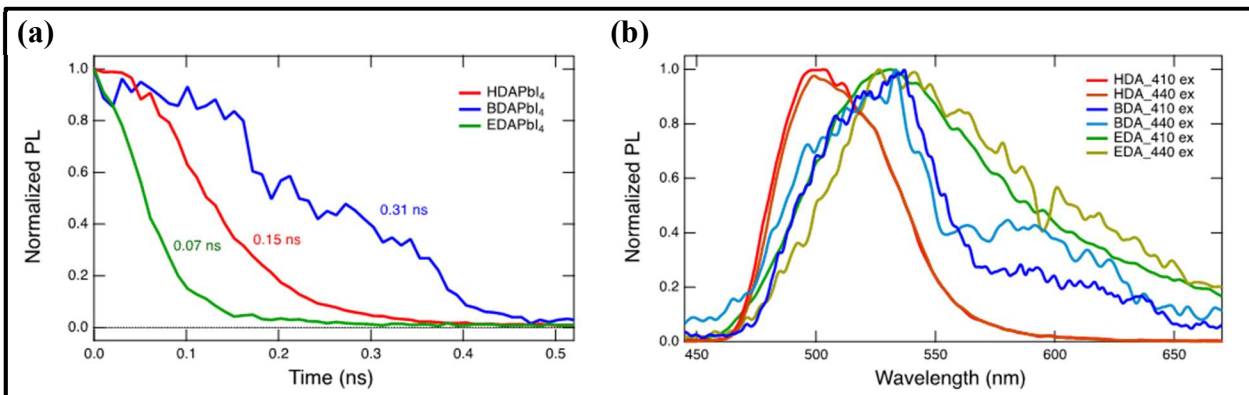


Figure 5.4. (a) Time-resolved photoluminescence kinetic traces and (b) time-resolved photoluminescence emission spectra of hybrid lead-halide thin films at 410 nm excitation.

Steady-state PL spectra of thin films of the low-dimensional lead-iodide materials showed that HDAPbI₄ has the narrowest emission whereas EDAPbI₄ has the broadest emission, which supports the notion that the 2D sheets of lead-iodide octahedra are most isolated from each other in HDAPbI₄ and the sheets of lead-iodide octahedra are closest to each other in EDAPbI₄ (Figure 5.3b). The PL emission peaks also red-shift with decreasing size of the organic moiety, following the trend of the absorption spectra. TRPL measurements on these thin films were also performed (Figure 5.4). It was determined from kinetic data that BDAPbI₄ films exhibited the longest lifetime and the TRPL emission spectra matched well with the steady-state emission spectra (Figure 5.2b). TRPL emission spectra were acquired at excitation wavelengths of 410 nm 440 nm and there was no wavelength-dependent shift of the emission observed, indicating that the TRPL signal was not due to Raman scattering from the samples and was in fact due to emission from the thin films. It is also evident that for each material thin film there is no wavelength dependence of the steady-state emission across excitation wavelengths of 400 nm–460 nm (Figure 5.5).

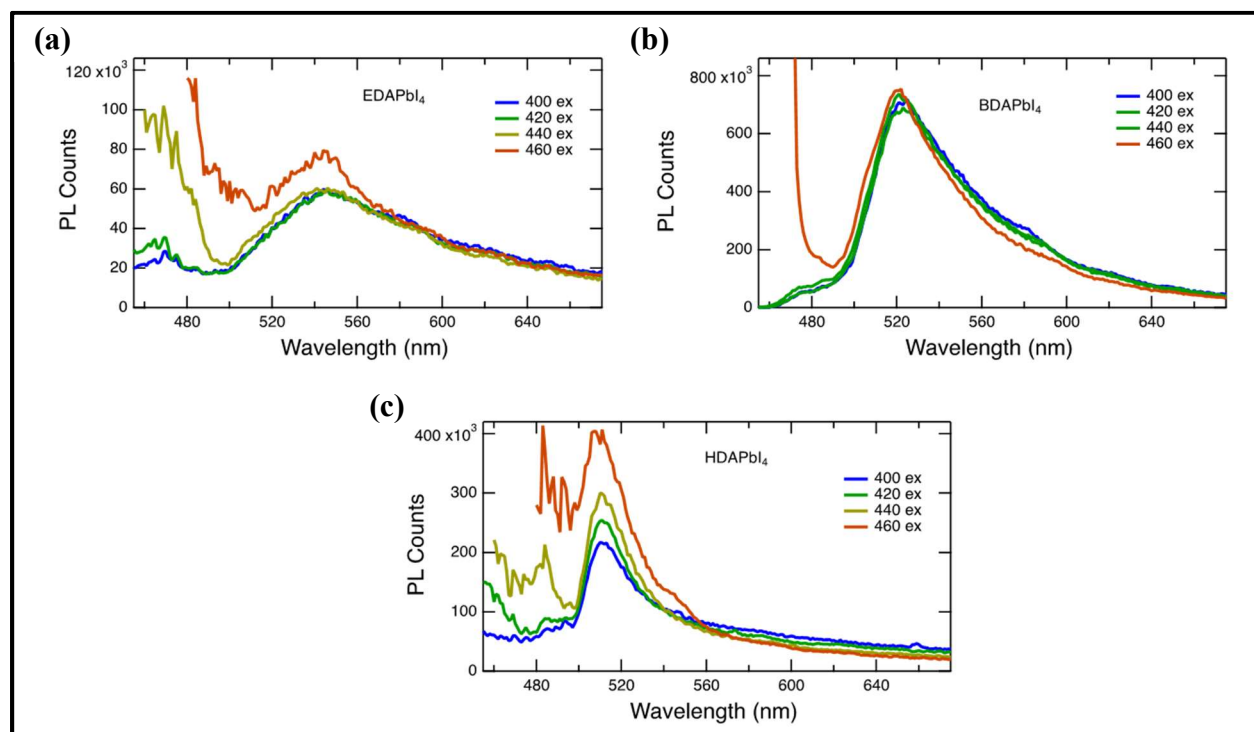


Figure 5.5. Steady-state emission spectra of (a) EDAPbI₄ and (b) BDAPbI₄, and (c) HDAPbI₄ thin films showing no spectral shifts when varying the excitation wavelength.

From grazing-incidence XRD measurements of thin films, it was determined that BDAPbI₄ is the most <110>-oriented film compared to EDAPbI₄ and HDAPbI₄ (Figure 5.6). This indicates that the sheets of lead-iodide octahedra align perpendicular to the underlying substrate, which suggests that BDAPbI₄ has superior through-plane conductivity and thus would be best suited for use in solar cells out of the series of materials. EDAPbI₄ and HDAPbI₄ is more <100>-oriented, wherein lead-iodide sheets align parallel to the substrate. It is hypothesized that charge-carrier collection will be better in the more <110>-oriented BDAPbI₄ in comparison to the more <100>-oriented EDAPbI₄ and HDAPbI₄. For EDAPbI₄, a strong peak at $\sim 6^\circ$ indicates a unit cell dimension of 14 Å, meaning the unit cell of EDAPbI₄ is larger than the unit cells of both BDAPbI₄ and HDAPbI₄. This does not make sense as EDA is smaller than both BDA and HDA. It is hypothesized that the structural dimensionality of EDAPbI₄ is in fact 1D/0D or a mix of 2D and 1D/0D, which supports the conclusion made from absorption spectral data.

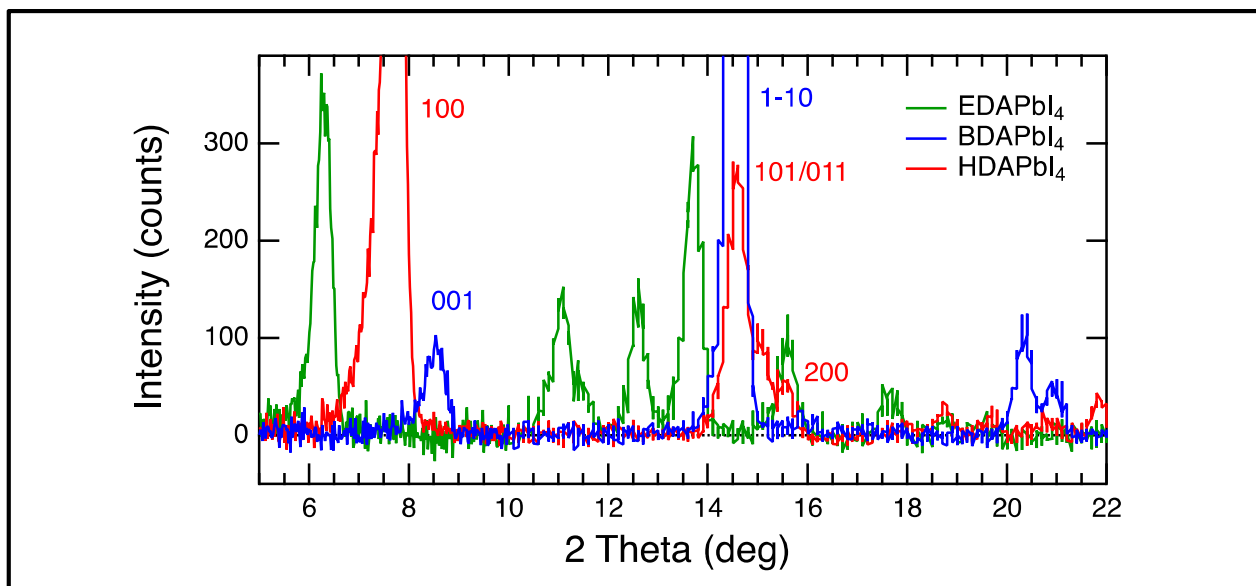


Figure 5.6. Grazing-incidence XRD patterns of hybrid lead-halide material thin films incorporating either ethylenediamine (EDA, green trace), butanediamine (BDA, blue trace), or hexanediamine (HDA, red trace).

Visible-probe TAS measurements were also conducted on this series of materials. Upon excitation with 400 nm laser light, the spectra (Figures 5.7b, 5.8b, and 5.9b) follow the second derivative of the absorption spectra, which can be attributed to trapped-carrier induced Stark effects, which is commonly observed in quantum-confined structures that undergo excitonic absorption processes.²³ This behavior is thus expected in these low-dimensional materials. The observed trapped-carrier induced Stark effect can be explained by an overlap of two absorption band onsets that is due to a split density of states in the conduction band.²³ For such conditions the

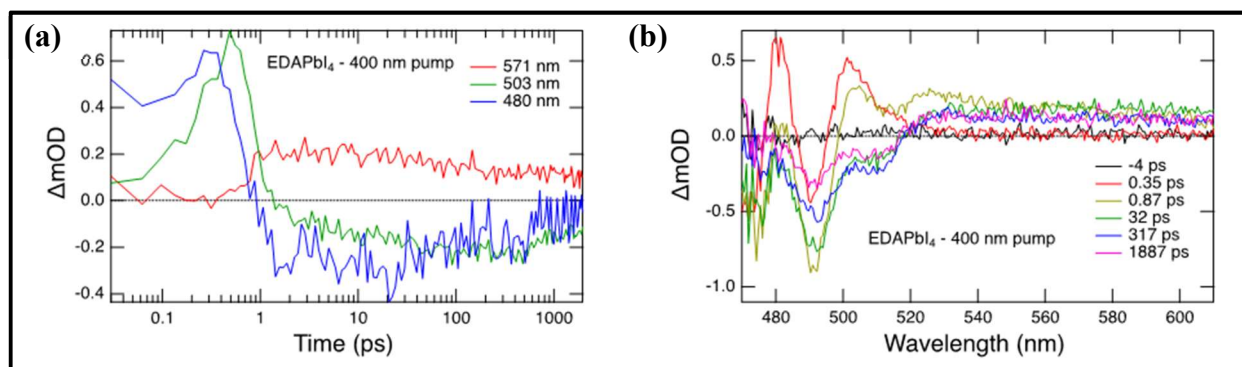


Figure 5.7. Transient absorption (a) kinetic traces and (b) spectra of a thin film of EDAPbI₄ at 400 nm excitation.

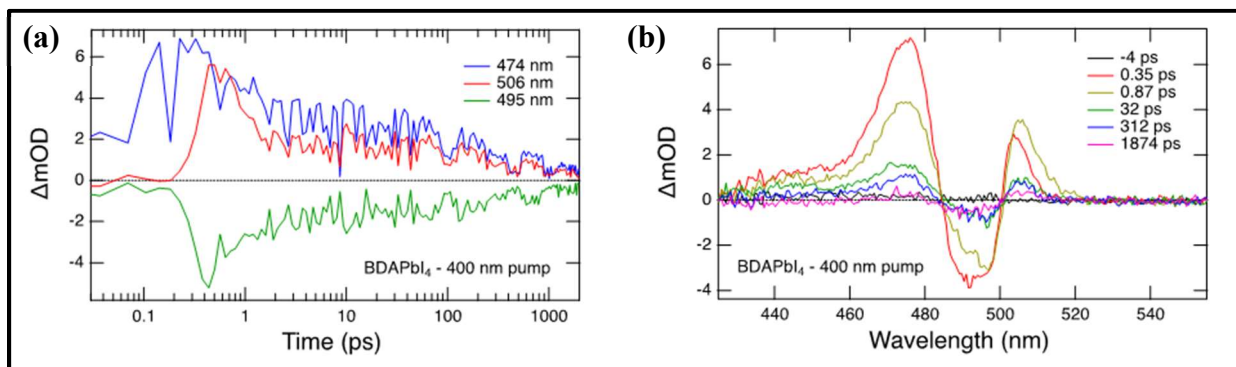


Figure 5.8. Transient absorption (a) kinetic traces and (b) spectra of a thin film of BDAPbI₄ at 400 nm excitation.

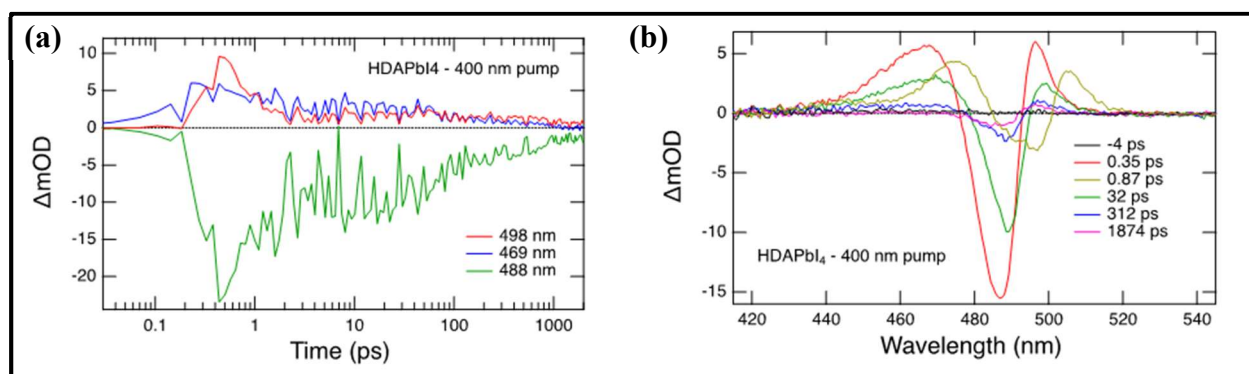


Figure 5.9. Transient absorption (a) kinetic traces and (b) spectra of a thin film of HDAPbI₄ at 400 nm excitation.

Stark effect will result in a repulsion of the transitions giving rise to a second-derivative-type feature in the TA spectrum. The lower-energy exciton-induced absorption peaks have maxima of 503 nm for EDAPbI₄, 506 nm for BDAPbI₄, and 498 nm for HDAPbI₄. In each case, these peaks are convoluted by the overlap of the exciton bleach at 492 nm for EDAPbI₄, 495 nm for BDAPbI₄, and 488 nm for HDAPbI₄. The exciton binding energy can be estimated as the difference in the exciton-induced absorption (exciton IA) features. From TA spectra (Figures 5.7b, 5.8b, and 5.9b), exciton binding energies were determined to be ~100 meV for EDAPbI₄, ~140 meV for BDAPbI₄, and ~160 meV for HDAPbI₄. These exciton binding energies are substantially smaller than that of HDABiI₅ (310 meV) determined in Chapter 3. This can be rationalized by the greater structural dimensionality of the lead-iodide perovskites (2D) compared to 1D HDABiI₅.

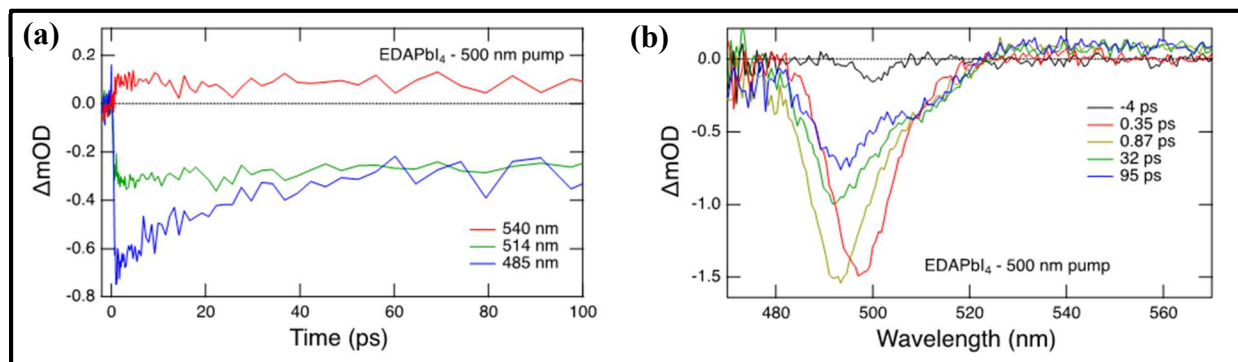


Figure 5.10. Transient absorption (a) kinetic traces and (b) spectra of a thin film of EDAPbI₄ at 500 nm excitation.

For each material thin film, the TA kinetics from exciting with 400 nm laser light showed both a fast decay component and a slow decay component (Figures 5.7a, 5.8a, and 5.9a). The fast decay component can be attributed to a dissociation of a subpopulation of bound excitons to electrons and holes. TA kinetics from exciting with 500 nm laser light showed only one decay component (Figures 5.10a, 5.11a, and 5.12a). This can be attributed to the dissociation of a subpopulation of excitons into electrons and holes that is only accessible when exciting with excess energy above the exciton band. The exciton-induced absorption features are less prominent in the spectra for 500 nm excitation (Figures 5.10b, 5.11b, and 5.12b) due to the generation of a smaller population of excited-state species compared to the generated population upon 400 nm excitation.

TRTS measurements were also performed on these materials, and free-carrier vs. exciton kinetics were distinguished (Figure 5.13). It was found that terahertz lifetimes follow the trend of

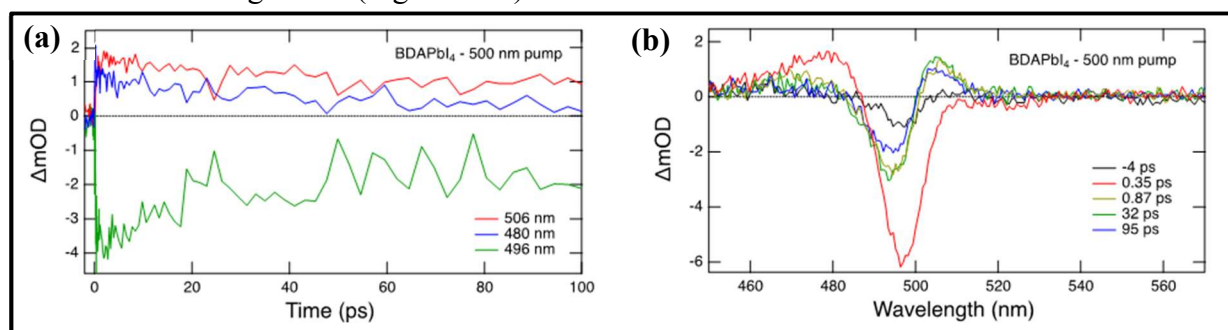


Figure 5.11. Transient absorption (a) kinetic traces and (b) spectra of a thin film of BDAPbI₄ at 500 nm excitation.

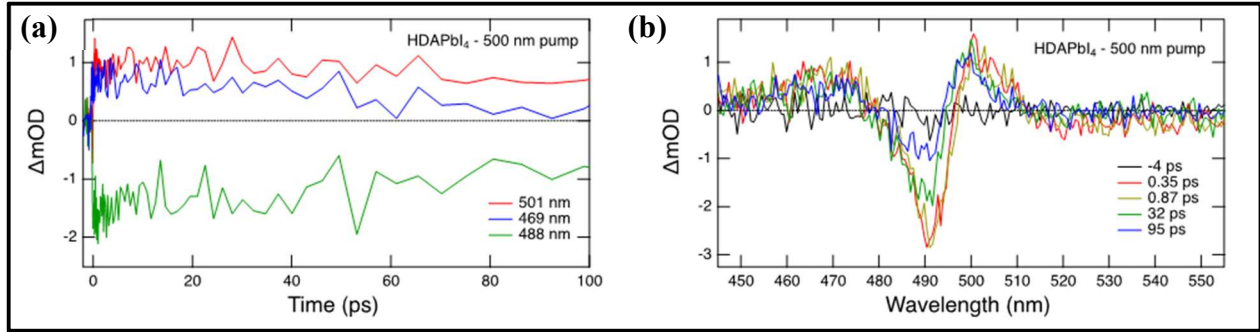


Figure 5.12. Transient absorption (a) kinetic traces and (b) spectra of a thin film of HDAPbI₄ at 500 nm excitation.

the PL lifetimes. The kinetic traces are best fit to biexponential decay functions, as there is a short-lived free-carrier component and long-lived free-carrier/exciton component. In most cases, the TRTS technique is sensitive to detection of only free carriers and not excitons, but for materials that are largely excitonic in nature, such as these 2D $n=1$ lead-halide perovskites, it is not surprising that excitons contribute to part of the signal.²⁴ Lifetimes of the EDAPbI₄ thin film were $\tau_1 = 0.55$ ps and $\tau_2 = 6.5$ ps. Lifetimes of the BDAPbI₄ thin film were $\tau_1 = 1.6$ ps and $\tau_2 = 68$ ps. Lifetimes of the HDAPbI₄ thin film were $\tau_1 = 0.9$ ps and $\tau_2 = 15$ ps. BDAPbI₄ has the longest

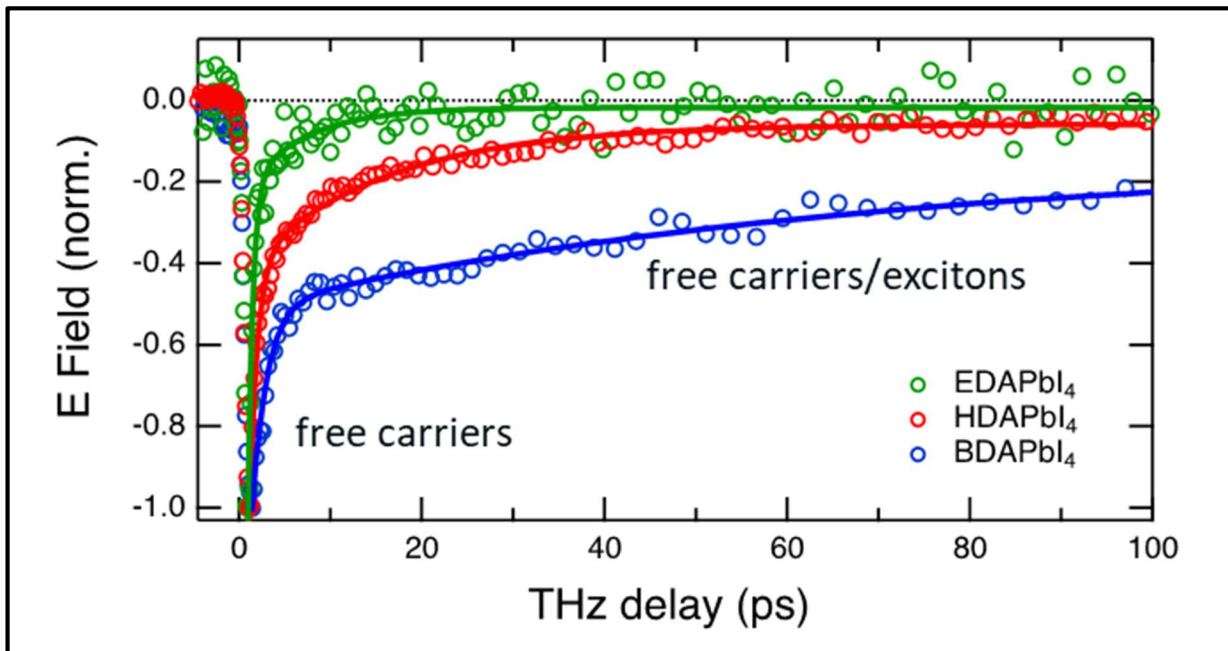


Figure 5.13. Terahertz pump scans showing the charge-carrier kinetics of the hybrid lead-halide material thin films.

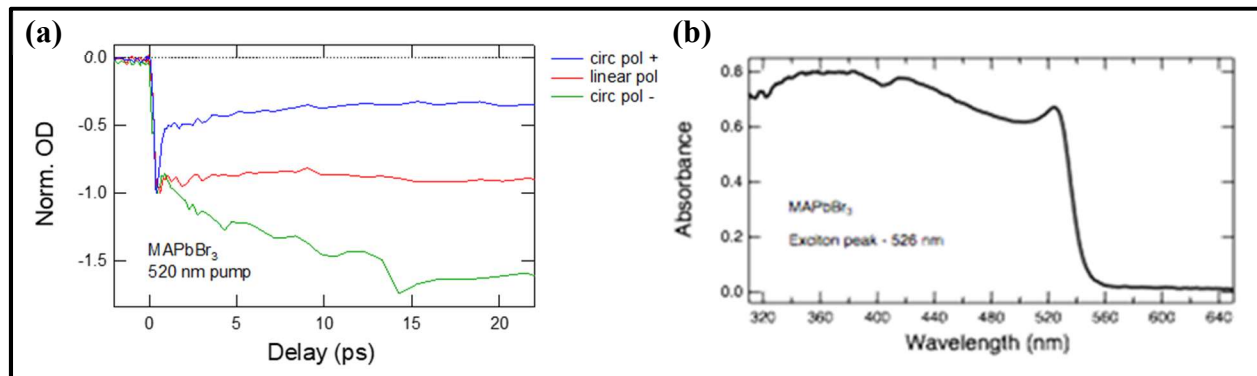


Figure 5.14. (a) Transient absorption spectra of a freshly-prepared MAPbBr₃ thin film excited with 520 nm laser light.

lifetimes due to the smaller size of the organic moiety in comparison to 2D HDAPbI₄ and due to the 2D nature of the inorganic network compared to the mixed 2D and 1D/0D nature of the inorganic network of EDAPbI₄. EDAPbI₄ has the shortest lifetimes, indicating that the structural dimensionality has a greater influence on charge-carrier lifetimes than does the size of the organic moieties in hybrid lead-halide materials.

Spin dephasing measurements were also performed to elucidate spin lifetimes. To measure spin dephasing, TAS measurements of thin films were carried out using linearly polarized excitation light (Figure 5.14a, red trace) and both directions of circularly polarized excitation light (Figure 5.14a, blue and green traces). Spin dephasing behavior of a thin film of MAPbBr₃ was observed when probing the exciton bleach at 537 nm and spin lifetimes of 2–6 ps were measured. In order to measure this behavior, it was necessary to excite the thin film with laser light of slightly higher energy than the exciton peak. For this reason, 520 nm pump laser light was chosen to excite into the exciton band with a peak of 526 nm (Figure 5.14b). The observed bleach was probed, and the bleach had a maximum intensity at 537 nm. It was crucial that the sample was freshly prepared to observe this spin dephasing behavior.

Figure 5.15 presents data of a thin film of MAPbBr₃ that had been prepared and kept outside an inert atmosphere for roughly three months. Although there were no apparent changes

in film quality or color, no evidence of spin dephasing behavior was observed when probing the exciton bleach peak. Unfortunately, these measurements were not successful even on freshly prepared 2D lead-

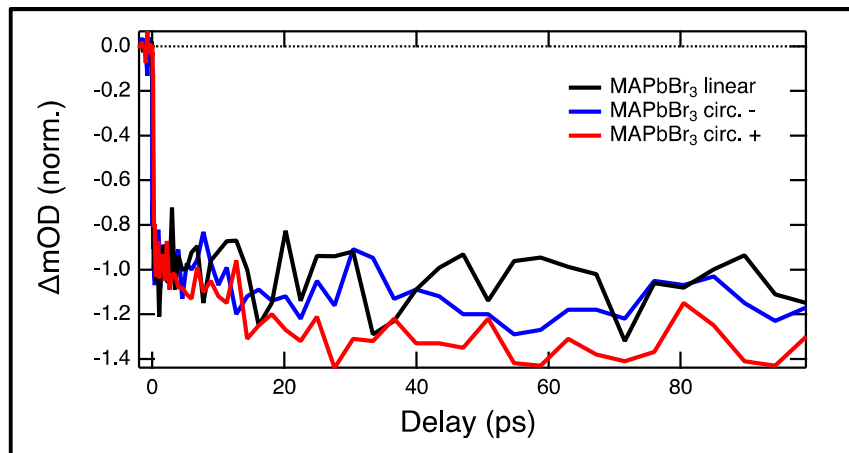


Figure 5.15. Transient absorption spectra of a MAPbBr₃ thin film that has been stored in a container in air for roughly three months.

iodide perovskite thin films, which may be due to spin lifetimes being too fast to detect, or due to the spin decay being convoluted by the exciton bleach decay at early delay times (Figure 5.16). This result supports the hypothesis that a combination of bulky organic cations and a distorted/low-dimensional inorganic framework inhibit the observation of spin splitting.

Probe scans from TRTS measurements are shown in Figure 5.17. The MAPbBr₃ film shows high terahertz photoconductivity (Figure 5.17, black trace), as expected for a 3D Pb-X material, which is indicated by the probe scan being 180° out of phase to a probe scan performed without laser excitation (Figure 5.17, gray trace). The low-dimensional lead-halide thin films show only small or negligible phase

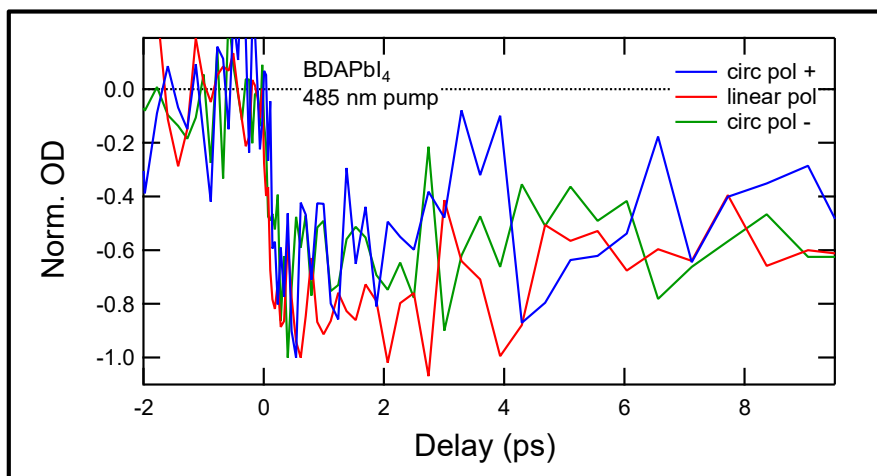


Figure 5.16. Transient absorption spectra of a freshly-prepared BDAPbI₄ thin film at 485 nm excitation, probing the exciton bleach peak at 496 nm.

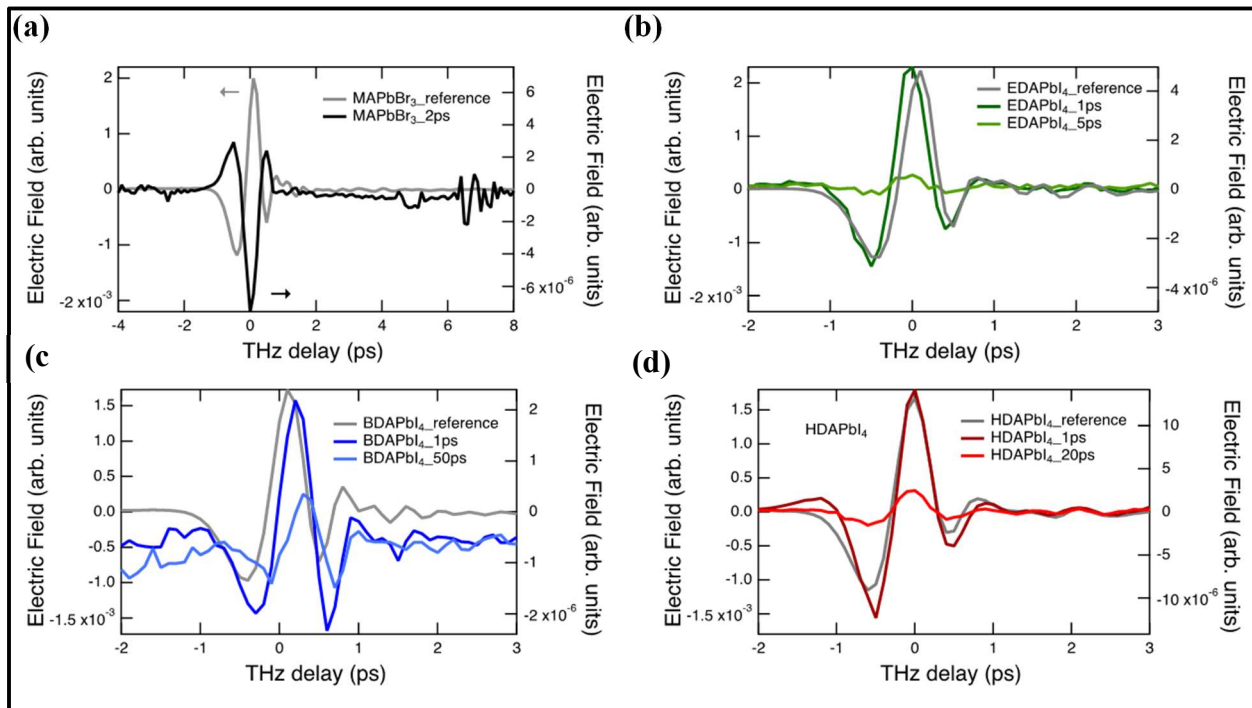


Figure 5.17. Terahertz probe scans of thin films of (a) MAPbBr₃, (b) EDAPbI₄, (c) BDAPbI₄, and (d) HDAPbI₄.

shifts in comparison to reference scans. This suggests that photoconductivities are low and phonon effects dominate in these materials, which is expected for lower-dimensional quantum-confined structures.

5.4 Conclusions

An extensive analysis on 2D lead-halide perovskite materials incorporating divalent alkylammonium cations of varying alkyl chain length was performed. Absorption measurements showed that absorption onsets red-shift with decreasing size of the organic moiety. The absorption spectrum of EDAPbI₄ suggests a phase with structural dimensionality of 1D/0D as the peak does not follow the trend of 2D BDAPbI₄ and HDAPbI₄. Steady-state PL spectra showed that HDAPbI₄ has the narrowest emission whereas EDAPbI₄ has the broadest emission, which supports the notion that the sheets of lead-iodide octahedra are the most isolated from each other in HDAPbI₄ and the

sheets are closest to each other in EDAPbI₄. The PL emission peaks also red shift with decreasing size of the organic group, following the trend of the absorption spectra. From TRPL measurements on these materials it was determined that BDAPbI₄ films exhibited the longest lifetime and the emission spectra matched well with the steady-state emission.

Grazing-incidence XRD of thin films showed that BDAPbI₄ is the most <110>-oriented film, meaning sheets of lead-iodide octahedra are perpendicular to the substrate, which suggests that BDAPbI₄ has superior through-plane conductivity and thus would be best for use in solar cells. Visible-probe TA measurements on these materials showed that the materials exhibited a trapped-carrier induced Stark effect, which is behavior that has been observed in materials that undergo excitonic absorption processes. In each of the materials, the TA kinetics from exciting with 400 nm laser light showed both a fast decay component and a slow decay component, whereas TA kinetics from exciting with 500 nm laser light only showed one decay component. This could be attributed to a dissociation of a subpopulation of excitons into electrons and holes that is only accessible when exciting with excess energy above the exciton band. From TA spectra, exciton binding energies were determined to be ~100 meV for EDAPbI₄, ~140 meV for BDAPbI₄, and ~160 meV for HDAPbI₄.

From THz spectroscopic measurements it was found that free-carrier lifetimes probed by THz radiation followed the trend of the PL lifetimes, where BDAPbI₄ showed the longest free-carrier lifetimes due to the smaller size of the organic moiety in comparison to HDAPbI₄ and due to the 2D structural dimensionality of BDAPbI₄ compared to the mixed 2D and 1D/0D structural dimensionality of EDAPbI₄. Spin decoherence measurements were unfortunately not successful on the 2D lead-halide perovskite materials, which may be due to spin lifetimes being too fast to detect, or due to the spin decay being convoluted by the exciton bleach decay at early delay times.

This work represents promising materials discovery of low-dimensional lead–halide perovskites that, if studied further, could prove promising for use in light-emitting diodes and quantum computing.

5.5 References

- (1) Fabian, D. M.; Beard, M. C.; Ardo, S. *J. Phys. Chem. C* **2018**, manuscript in preparation.
- (2) Safdari, M.; Svensson, P. H.; Hoang, M. T.; Oh, I.; Kloo, L.; Gardner, J. M. *J. Mater. Chem. A* **2016**, *4*, 15638–15646.
- (3) Vassilakopoulou, A.; Papadatos, D.; Koutselas, I. *Appl. Mater. Today* **2016**, *5*, 128–133.
- (4) Yuan, Z.; Zhou, C.; Tian, Y.; Shu, Y.; Messier, J.; Wang, J. C.; Van De Burgt, L. J.; Kountouriotis, K.; Xin, Y.; Holt, E.; Schanze, K.; Clark, R.; Siegrist, T.; Ma, B. *Nat. Commun.* **2017**, *8*, 1–7.
- (5) Chen, P.; Bai, Y.; Lyu, M.; Yun, J.-H.; Hao, M.; Wang, L. *Sol. RRL* **2018**, *1700186*, 1700186.
- (6) Park, J.; Reid, O. G.; Rumbles, G. *J. Phys. Chem. B* **2015**, *119*, 7729–7739.
- (7) Nozik, A. J.; Beard, M. C.; Luther, J. M.; Law, M.; Ellingson, R. J.; Johnson, J. C.; Arrays, Q. D. *Chem. Rev.* **2010**, *110*, 6873–6890.
- (8) Smith, M. D.; Pedesseau, L.; Kepenekian, M.; Smith, I. C.; Katan, C.; Even, J.; Karunadasa, H. I. *Chem. Sci.* **2017**, *8*, 1960–1968.
- (9) Zhang, T.; Dar, M. I.; Li, G.; Xu, F.; Guo, N.; Grätzel, M.; Zhao, Y. *Sci. Adv.* **2017**, *3*, e1700841.

- (10) Chen, Q.; Zhou, H.; Song, T.-B.; Luo, S.; Hong, Z.; Duan, H.-S.; Dou, L.; Liu, Y.; Yang, Y. *Nano Lett.* **2014**, *14*, 4158–4163.
- (11) DeQuilettes, D. W.; Koch, S.; Burke, S.; Paranjli, R. K.; Shropshire, A. J.; Ziffer, M. E.; Ginger, D. S. *ACS Energy Lett.* **2016**, *1*, 438–444.
- (12) Stewart, R. J.; Grieco, C.; Larsen, A. V.; Maier, J. J.; Asbury, J. B. *J. Phys. Chem. Lett.* **2016**, *7*, 1148–1153.
- (13) Pascoe, A. R.; Yang, M.; Kopidakis, N.; Zhu, K.; Reese, M. O.; Rumbles, G.; Fekete, M.; Duffy, N. W.; Cheng, Y. B. *Nano Energy* **2016**, *22*, 439–452.
- (14) Dunfield, S.; Moore, D. T.; Klein, T.; Fabian, D. M.; Christians, J. A.; Dixon, A. G.; Dou, B.; Ardo, S.; Beard, M. C.; Shaheen, S. E.; Berry, J. J.; van Hest, M. F. A. M. *ACS Energy Lett.* **2018**, *3*, 1192–1197.
- (15) Ponceca Jr, C. S.; Sundström, V. *Nanoscale* **2016**, *8*, 6249–6257.
- (16) Ponceca Jr, C. S.; Tian, Y.; Sundström, V.; Scheblykin, I. G. *Nanotechnology* **2016**, *27*, 082001.
- (17) Marchioro, A.; Brauer, J. C.; Teuscher, J.; Grätzel, M.; Moser, J.-E. *Proc. SPIE* **2013**, *8811*, 881108.
- (18) Beard, M. C.; Blackburn, J. L.; Heben, M. J. *Nano* **2008**, *8*, 2–6.
- (19) Juarez-Perez, E. J.; Sanchez, R. S.; Badia, L.; Garcia-Belmonte, G.; Kang, Y. S.; Mora-Sero, I.; Bisquert, J. *J. Phys. Chem. Lett.* **2014**, *5*, 2390–2394.
- (20) Niesner, D.; Wilhelm, M.; Levchuk, I.; Osvet, A.; Shrestha, S.; Batentschuk, M.; Brabec, C.; Fauster, T. *Phys. Rev. B - Condens. Matter Mater. Phys.* **2016**, *117*, 126401.

- (21) Yang, Y.; Yang, M.; Zhu, K.; Johnson, J. C.; Berry, J. J.; Lagemaat, J. Van De; Beard, M. *C. Nat. Commun.* **2016**, *7*, 12613.
- (22) Kim, H.-S.; Lee, C.-R.; Im, J.-H.; Lee, K.-B.; Moehl, T.; Marchioro, A.; Moon, S.-J.; Humphry-Baker, R.; Yum, J.-H.; Moser, J. E.; Grätzel, M.; Park, N.-G. *Sci. Rep.* **2012**, *2*, 591.
- (23) Norris, D. J.; Sacra, A.; Murray, C. B.; Bawendi, M. G. *Phys. Rev. Lett.* **1994**, *72*, 2612–2615.
- (24) Beard, M. C. **2018**, Personal Communication.